

Early-Stage Development of a Multifunctional Liposomal Drug Delivery System for Glioblastoma Therapy

Zur Erlangung des akademischen Grades einer
DOKTORIN DER NATURWISSENSCHAFTEN (DR. RER. NAT.)

von der KIT-Fakultät für Chemieingenieurwesen und Verfahrenstechnik des
Karlsruher Instituts für Technologie (KIT)
genehmigte

DISSERTATION

von

Larissa Jessica Lubitz
aus Wiesbaden

Tag der mündlichen Prüfung: 04.12.2024

Erstgutachter: Priv.-Doz. Dr. Gero Lenewit

Zweitgutachter: Prof. Dr. Jürgen Hubbuch

Häufig las ich an dieser Stelle
„Für meine Eltern“.

Auch ich möchte an dieser Stelle meinen Eltern danken mir diesen Weg ermöglicht zu
haben.

Gemacht habe ich es jedoch

Für mich selbst.

Doch Forschung strebt und ringt, ermüdend
nie, nach dem Gesetz, dem Grund, Warum
und Wie.“

Johann Wolfgang von Goethe

Acknowledgment

This thesis was written in the context of my scientific work at ABNOBA GmbH within the Eurostars-2 project RELIEF, in cooperation with the Institute of Mechanical Process Engineering and Mechanics (MVM) of the Karlsruhe Institute of Technology (KIT), in the years 2020 to 2024.

First of all, I would like to express my special thanks to my supervisor, Priv.-Doz. Dr. Gero Leneweit, for the trust he has placed in me, for providing and financing the interesting research topic, for the always inspiring conversations and discussions, and for his commitment and support in the preparation of the joint publications and this thesis. I would also like to thank you for the opportunity to present my results at national and international conferences and for the trust you have placed in me to grow with additional tasks, such as laboratory organization or the supervision of students. I would particularly like to emphasize the RELIEF project as the framework for my doctoral thesis. Thanks to you, Mr. Leneweit, I was able to be part of this European research project. I was able to gain considerable expertise during my time abroad with our cooperation partners. I was also able to grow through other challenges of an exceptional kind - not forgetting the new building including the move and the water damage with an improvised laboratory.

Further, I would like to thank Prof. Dr.-Ing. Jürgen Hubbuch for kindly acting as co-lecturer and for his interest in my dissertation.

I would also like to take this opportunity to thank Dr. Harden Rieger and Dr. Christoph Heyder. Thank you very much for your support, time and encouragement with questions or ideas.

My thanks also belong to my companions and fellow sufferers in the laboratory. Even though we were still unknown to each other and had identical professional backgrounds, we immediately harmonized both, professionally and personally, and mastered the hurdles of the early days together. It is still a pity not to have finished the journey together with you. Thank you, dear Katharina Friedly. I would also like to thank you, dear Josanna Kaufman and Moritz Haffner – or rather Bosy and Morice. Whether it was a professional exchange, jokes and nonsense or emotional support – you were always at my side. Interns became not only colleagues but also friends. I will never forget all our sushi escalations, “Mekong Mittwoch” or other food comas. Thank you for allowing me to grow through you. I always look back fondly on our time together and it will always bring a smile to my face. During my time at ABNOBA GmbH, I also had the pleasure of working with many dedicated students. Namely, these are Marlene Fritsch, Luisa Bortone, Ulf Garbe, Jasmin Friederich, Lisa Klingel, Leonie Görden, Amelie Waller, Nico Dirks, Niklas Walter, Maya Litzig, Laura Dickhäuser, Eray Cetin and Nico Senia. I thank you for the time spent together in the lab, the active support and the joint discussions as a stimulus for new ways and ideas.

Additionally, I want to thank Kirsten Ullman and Simon Buchheiser for their support “from afar” and the warm welcome I received during my visits to KIT, even though I was an “exotic from another field”. I would also like to thank the administrative staff, Mrs. Keiderling-Schlegel and Mrs. Peter. They not only provided answers to many administrative questions but also the necessary “therapy sessions” when nerves were on edge.

Not to forget, my thanks also go to all my dear “Pappenheimer” – Friends, who became my family of choice. Dear Jonathan Wohlfahrt, Sabine Ziebura, Denis Hirsch, Roland Ebert, Tobias Cillien, Julian Gurske, Nathalie and Nils Kolb – Thanks that we found each other during our studies and that even after more than a decade our friendships are the same as they were on day 1. Special thanks go to my “Türk” and shrink Yaser Mansuroğlu.

Finally, my greatest debt of gratitude is owed to my parents, without whose support this career would never have been possible.

Liebe Mami, lieber Papi,
Danke ♥

Summary

The number of cancer cases is constantly rising and the prognosis for glioblastoma patients in particular remains poor despite all the progress made. Brain tumors are not only often inoperable but also inadequately treatable, as chemotherapeutics cannot effectively cross the blood-brain barrier. Liposomes, as spherical carrier systems made of phospholipids, offer a way of transporting active substances in a targeted and efficient manner. Current developments aim to achieve the production of asymmetric liposomes based on two inverse perfluorocarbon (PFC) nanoemulsions. The different structure of the phospholipid layers of an asymmetric liposome makes it possible, on the one hand, to protect active ingredients from rapid degradation and, on the other hand, to deliver them specifically to the site of action through versatile surface modification.

The pressure-dependent homogenization of perfluorocarbon-in-water (PFC/W) nanoemulsions shows two transitions from laminar flow to turbulence when investigating the flow of mixed suspensions of liposomes and emulsion droplets (PFC droplets). These were identified by calculating the Reynolds numbers in the interaction chambers. The first transition occurs between 750 bar and 1,000 bar, the second between 1,500 bar and 1,750 bar. Only the first turbulence transition influences the droplet size significantly, due to the high shear rate. The results show that the particle size decreases more with laminar flow, which is due to different particle distributions in rectangular channel cross-sections. In laminar flow, the particles are concentrated in a rectangular ring around the center in a high shear zone, while in turbulent flow they are concentrated in the corners and diagonals of the channel in low shear zones. Only liposomes can be broken down into smaller particles over the entire pressure range from 250 bar to 2,000 bar, while the PFC droplet size can only be reduced at ≤ 750 bar.

Investigations on the number of cycles show that droplet break-up only occurs for the first 15 cycles. At 25 cycles, the droplet size increases due to the high rate of recoalescence, as the particles tend to merge. The break-up of the liposomal bilayers into emulsifying monolayers occurs at a constant rate from 5 cycles to 25 cycles.

The formulation parameters also have a strong influence on emulsification. For example, as the cholesterol content in the emulsifier lipid composition increases, the particle size increases. The optimum emulsifier concentration is 5 mM, which results in an ideal ratio of the lipid concentration to volume of the dispersed phase of 2 mM / 1 % (v/v). In this case, the emulsifier molecules form a monolayer around the PFC droplet. Higher ratios lead to inhomogeneous distributions or multilayers of phospholipids. A larger dispersed volume increases the particle size without affecting the size distribution. The length of the fatty acid chain of the phospholipid should be selected on the basis of the phase transition temperature given possible recoalescence of the droplets or inefficient vesicle disruption. A higher Zeta potential as well as a higher molecular surface area of the phospholipids in a bilayer reduce the particle size and increase the relative number of particles. Zwitterionic phospholipids are less efficient than anionic phospholipids in breaking down liposomes into emulsifying monolayers. The viscosity ratio of the dispersed to the continuous phase significantly influences the particle size, their distribution and the proportion of remaining liposomes. However, this correlation only applies to the variation of the viscosity ratio with the aid of cyclic perfluorocarbons. The lowest possible ratio of the viscosities of the two phases is preferable.

The PFC/W nanoemulsion forms the outer phospholipid layer in the production of asymmetric liposomes, which can be modified for targeted transport. Modification with glucose increases the cellular uptake of liposomes, especially in human glioblastoma cells U-87 MG, despite lower expression of the glucose transporter 1 (GLUT1) compared to murine cerebral endothelial cells bEnd.3, which respond more sensitively than glioblastoma cells to glucose deprivation by increasing GLUT1 expression. The reason for the lower sensitivity of glioblastoma cells to glucose deprivation is their ability to use alternative energy sources such as lactate.

Murine bEnd.3 cells differentiate the cellular uptake of liposomes based on their surface modifications, whereas U-87 MG cells do not. The rate of the liposomal uptake is highly

variable in bEnd.3 at high lipid concentrations, whereas U-87 MG cells only show differences at low and medium concentrations. Modification with succinimide increases cellular uptake presumably by receptor-mediated mechanisms, especially in bEnd.3 cells.

Modification of the liposomal surface with apolipoprotein E3 (ApoE3) increases cellular uptake via the low-density lipoprotein receptor-related protein 1 (LRP1) in murine bEnd.3 cells and human U-87 MG cells, but less so in F98 cells. Comparative studies show that ApoE3-modified liposomes achieve similar saturation levels in U-87 MG and F98 cells, despite different LRP1 expression and uptake rates. A c(RGD)-modification of liposomes improves cellular uptake, particularly in endothelial cells, which is mediated via the integrin $\alpha_v\beta_3$ receptor. In tumor cells, U-87 MG cells show consistent cellular uptake despite increasing lipid concentration or increasing incubation time. In contrast, the F98 cells show a significantly lower liposomal internalization compared to U-87 MG cells, which is in a concentration- and time-dependent increasing manner.

However, not only the modification of the liposomal surface for a targeted therapy is of great importance, but also its hydrophilization for shielding the carrier system in the blood system is of high relevance. The preparation of anticoagulant heparin fragments and their covalent binding to various liposomal anchors has been successfully demonstrated as well as their hemocompatibility with human whole blood. Heparinization of the liposomal surface is a conceivable alternative to the current standard polyethylene glycol (PEG).

Initial investigations on the emulsion-based production of asymmetric liposomes showed promising results in terms of particle size, storage stability and encapsulation efficiency. They offer enormous potential as a platform for a liposomal drug delivery system for targeted therapy and encapsulation of active ingredients specifically adapted to different types of tumors.

Zusammenfassung

Die Zahl der Krebserkrankungen ist stetig steigend und die Prognose insbesondere für Glioblastompatienten trotz aller Fortschritte weiterhin schlecht. Gehirntumoren sind nicht nur häufig inoperabel, sondern auch unzureichend zu therapieren, da Chemotherapeutika die Blut-Hirn-Schranke nicht effektiv überwinden können. Liposomen als kugelförmige Trägersysteme aus Phospholipiden, bieten eine Möglichkeit, Wirkstoffe zielgerichtet und effizient zu transportieren. Moderne Technologien erlauben die Herstellung asymmetrischer Liposomen auf Basis von zwei inversen Perfluorocarbon (PFC)-Nanoemulsionen. Der unterschiedliche Aufbau der Phospholipidschichten eines asymmetrischen Liposoms ermöglicht es einerseits Wirkstoffe vor einem schnellen Abbau zu schützen, aber auch andererseits durch vielseitige Oberflächenmodifikation gezielt an den Wirkort zu bringen.

Die druckabhängige Homogenisierung von Perfluorocarbon-in-Wasser (PFC/W) Nanemulsionen zeigt bei der Untersuchung der Strömung von gemischten Suspensionen aus Liposomen und Emulsionströpfchen (PFC-Tröpfchen) zwei Übergänge von laminarer Strömung zu Turbulenz in unterschiedlichen Kanalabschnitten. Diese wurden durch Berechnung der Reynolds-Zahlen in den Interaktionskammern identifiziert. Der erste Übergang tritt zwischen 750 bar und 1.000 bar auf, der zweite zwischen 1.500 bar und 1.750 bar. Nur der erste Turbulenzumschlag beeinflusst die Tröpfchengröße signifikant, aufgrund der hoher Scherrate. Die Ergebnisse zeigen, dass die Partikelgröße bei laminarer Strömung stärker abnimmt, was auf unterschiedliche Partikelverteilungen in rechteckigen Kanalquerschnitten zurückzuführen ist. Bei laminarer Strömung konzentrieren sich die Partikel in der Mitte, während sie bei turbulenter Strömung in den Ecken und Diagonalen des Kanals konzentriert sind. Nur Liposomen können über den gesamten Druckbereich von 250 bar bis 2.000 bar in kleinere Partikel zerlegt werden, während die PFC-Tropfengröße nur bei ≤ 750 bar verringert werden kann.

Untersuchungen zur Zyklenzahl zeigen, dass ein Tropfenaufbrechen nur bei den ersten 15 Zyklen stattfindet. Bei 25 Zyklen nimmt die Tröpfchengröße aufgrund hoher Rekoaleszenzrate zu, da die Partikel zur Verschmelzung neigen. Das Aufbrechen der liposomalen Doppelschichten in emulgierende Monoschichten erfolgt mit einer konstanten Rate von 5 Zyklen bis 25 Zyklen.

Die Formulierungsparameter beeinflussen die Emulgierung ebenfalls stark. So zeigt sich mit steigendem Cholesterolgehalt in der Emulgatorzusammensetzung eine steigende Partikelgröße. Das Optimum der Emulgatorkonzentration liegt bei 5 mM, was ein ideales Verhältnis der Lipidkonzentration zum Volumen der dispersen Phase von 2 mM / 1 % (v/v) ergibt. Nur dann bilden die Emulgatormoleküle eine Monoschicht um den PFC-Tropfen. Höhere Verhältnisse führen zu inhomogenen Verteilungen oder Multischichten der Phospholipide. Ein größeres dispergiertes Volumen erhöht die Partikelgröße, ohne die Verteilung zu beeinflussen. DPPC ist Emulgator aufgrund seiner resultierenden kleinen Emulsionströpfchen zu bevorzugen. Ein höheres Zeta Potential sowie eine höhere molekulare Oberfläche der Phospholipide in Bilschichten verringern die Partikelgröße und erhöhen die relative Partikelanzahl. Zwitterionische Phospholipide sind weniger effizient als anionische hinsichtlich des Aufschlusses von Liposomen zu emulgierenden Monoschichten. Das Viskositätsverhältnis der dispersen zur kontinuierlichen Phase beeinflusst die Partikelgröße, deren Verteilung und den Anteil verbleibender Liposomen maßgeblich. Diese Korrelation gilt jedoch nur für die Variation des Viskositätsverhältnisses mit Hilfe von zyklischen Perfluorocarbonen. Ein möglichst niedriges Verhältnis der Viskositäten beider Phasen ist zu bevorzugen.

Bei der Herstellung asymmetrischer Liposomen bildet die PFC/W Nanoemulsion die äußere Phospholipidschicht, welche für einen zielgerichteten Transport modifiziert werden kann. Eine Modifikation mit Glucose erhöht die zelluläre Aufnahme der Liposomen, insbesondere bei den humanen Glioblastomzellen U-87 MG, trotz niedrigerer GLUT1-Expression verglichen zu den murine zerebralen Endothelzellen bEnd.3. Diese reagieren sensibler als Glioblastomzellen auf einen Glucoseentzug, indem sie die Expression des GLUT1 steigern. Ursache für die geringere Sensitivität der Glioblastomzellen auf den Glucoseentzug ist deren Nutzung alternativer Energiequellen wie beispielsweise Lactat.

Murine bEnd.3 Zellen differenzieren die zelluläre Aufnahme von Liposomen basierend auf deren Oberflächenmodifikationen, während dies U-87 MG Zellen nicht auftritt. Die Geschwindigkeit der Liposomenaufnahme ist bei bEnd.3 bei hohen Lipidkonzentration,

stark variierend während U-87 MG Zellen lediglich bei niedrigen und mittleren Konzentrationen Unterschiede zeigen. Eine Modifikation mit Succinimid erhöht die zelluläre Aufnahme vermutlich durch Rezeptor-vermittelte Mechanismen, insbesondere bei bEnd.3 Zellen.

Eine Modifikation der liposomalen Oberfläche mit Apolipoprotein E3 (ApoE3) steigert die zelluläre Aufnahme über den Low Density Lipoprotein Receptor-related Protein 1 (LRP1) Rezeptor bei murinen bEnd.3 Zellen und humanen U-87 MG Zellen, hingegen weniger bei F98 Zellen. Vergleichende Untersuchungen zeigen, dass ApoE3-modifizierte Liposomen ähnliche Sättigungswerte bei U-87 MG und F98 Zellen erreichen, trotz unterschiedlicher LRP1-Expression und Aufnahmeraten. Eine c(RGD)-Modifikation der Liposomen verbessert insbesondere bei Endothelzellen die zelluläre Aufnahme, welche über den Integrin α_v -Rezeptor vermittelt wird. Bei den Tumorzellen zeigen U-87 MG Zellen eine trotz steigender Lipidkonzentration oder Steigerung der Inkubationszeit gleichbleibende zelluläre Aufnahmen. Die F98 Zellen hingegen zeigen eine deutlich geringere liposomale Internalisierung, welche sowohl konzentrations- als auch zeitabhängig steigend ist.

Doch nicht nur die Modifikation der liposomalen Oberfläche für eine zielgerichtete Therapie ist von großer Bedeutung, auch deren Hydrophilisierung zur Abschirmung des Trägersystems im Blutsystem ist von hoher Relevanz. Die Präparation gerinnungshemmender Heparin-Fragmente, deren kovalente Bindung an verschiedene liposomale Anker, sowie deren Hämkompatibilität mit menschlichem Vollblut konnte erfolgreich gezeigt werden. Die Heparinisierung der liposomalen Oberfläche ist eine denkbare Alternative für den derzeitigen Standard Polyethylenglycol (PEG).

Erste Versuche zur emulsionsbasierten Herstellung asymmetrischer Liposomen zeigten vielversprechende Ergebnisse hinsichtlich der Partikelgröße, Lagerungsstabilität sowie der Einkapselungseffizienz. Sie bieten ein enormes Potential als Plattform eines liposomalen Trägersystems für eine zielgerichtete Therapie und die Verkapselung von Wirkstoffen speziell angepasst an verschiedene Arten von Tumoren.

Table of Contents

1	Introduction and Objective	1
1.1	Introduction	1
1.2	Objective	4
2	Theoretical Background	7
2.1	Surfactants	7
2.1.1	Structure and Function	7
2.1.1.1	Hydrophilic-Lipophilic Balance	8
2.1.1.2	Critical Micelle Concentration	9
2.1.2	Phospholipids	10
2.1.2.1	Glycerophospholipids	10
2.1.2.2	Sphingophospholipids	13
2.2	Emulsions	14
2.2.1	Structure and Types of Emulsions	14
2.2.2	Preparation of Emulsions	15
2.2.3	Mechanisms of Instability	17
2.2.4	Perfluorocarbons as Dispersed Phase	19
2.3	Liposomes	20
2.3.1	Definition and Categorization	20
2.3.2	Structure and Components	21
2.3.2.1	Phospholipids	22
2.3.2.2	Cholesterol	22
2.3.3	Pharmaceutical Application of Liposomes	23
2.3.3.1	Approved Liposomal Formulations	25
2.3.4	Surface Modifications of Liposomes	26

2.3.5	Established Manufacturing Procedures	28
2.3.5.1	Preparation of Asymmetric Liposomes Based on Nanoemulsions	29
2.4	Glioma	31
2.4.1	Epidemiology and Classification	31
2.4.2	Diagnosis.....	32
2.4.3	Therapy	32
2.5	Blood-Brain Barrier	34
2.5.1	Structure and Physiological Role.....	34
2.5.2	Drug Delivery	36
2.5.2.1	Active and Passive Targeting	37
2.6	Hemo- and Immunocompatibility	43
2.6.1	Immune- and Complement-System	43
2.6.1.1	Immune System	43
2.6.1.2	Complement System.....	44
3	Materials and Methods	49
3.1	Materials	49
3.1.1	Phospholipids	49
3.1.2	Chemicals and Reagents	50
3.1.3	Buffers and Solutions	53
3.1.4	Disposables and Glass Products.....	53
3.1.5	Devices and Software.....	56
3.1.6	Cell Culture.....	58
3.1.6.1	Media, Solutions and Antibodies.....	58
3.1.6.2	Cell Lines	59
3.2	Methods.....	60
3.2.1	Preparation and Characterization of Nanoemulsions	60
3.2.1.1	Thin-Film Method.....	60
3.2.1.2	Preparation of Nanoemulsions.....	61
3.2.1.3	Sucrose Gradient.....	62
3.2.2	Preparation and Characterization of Liposomes.....	63
3.2.2.1	Preparation of Symmetric Liposomes	63
3.2.2.2	Post-Modification of Liposomes	64
3.2.2.3	Analysis of Symmetric Liposomes	68
3.2.3	Cell Culture.....	78

3.2.3.1 Cell Handling	78
3.2.3.2 Cell Staining	79
3.2.3.3 Cellular Uptake Assay	80
3.2.3.4 Cytotoxicity Assay	81
3.2.4 Hemo- and Immunocompatibility	82
3.2.4.1 Factor Xa Assay	82
3.2.4.2 Complement Factor ELISAs	82
3.2.5 Analytical Methods	85
3.2.5.1 Dynamic Light Scattering.....	85
3.2.5.2 Zeta Potential Measurement	87
3.2.5.3 UV/VIS Spectroscopy	89
3.2.5.4 Fluorescence Spectroscopy	90
3.2.5.5 Size Exclusion Chromatography	91
3.2.5.6 FACS.....	92
4 Process Optimization of a PFC/W Nanoemulsion	95
4.1 Effect of Pressure on Homogenization of Mixed Liposomes and Emulsion Droplets.....	95
4.2 The Geometry of the Interaction Chambers and Calculation of Reynold Numbers.....	102
4.3 Preparative Separation of Particle Species	103
4.4 Investigation on Different Numbers of Homogenization Cycles N_c	106
4.5 Conclusion.....	109
5 Formulation Optimization of a PFC/W Nanoemulsion	115
5.1 Investigations on the Emulsifier	116
5.1.1 Variation of the Cholesterol Percentage.....	116
5.1.2 Variation of the Total Lipid Concentration	117
5.1.3 Variation of the Emulsifier Concerning the Phospholipid Head Group and Chain Length.....	120
5.2 Investigations on the Dispersed Phase.....	124
5.2.1 Variation of the Proportion of the Dispersed Phase	124
5.2.2 Variation of the Viscosity Ratio Between the Phases by Varying the Perfluorocarbon.....	125

5.3 Conclusion	129
6 Liposomal Surface Modifications for Targeting Aspects	131
6.1 Succinimide- and Glucose- Modifications for Elevated Uptake	131
6.1.1 Characterization and Stability of Liposomes.....	132
6.1.2 Expression Levels of GLUT1 in Endothelial and Cancer Cells under Different Glucose Concentrations.....	133
6.1.3 Cellular Uptake of Succinimide- or Glucose-modified Liposomes in Endothelial Cells.....	134
6.1.4 Cellular Uptake of Succinimide- or Glucose-modified Liposomes in Glioblastoma Cells.....	137
6.1.5 Expression Levels of 5-HT ₇ in Endothelial and Cancer Cells Under Normal Cultivation Conditions	138
6.1.6 Cellular Viability After Treatment with the Liposomal Formulations ..	139
6.1.7 Discussion and Conclusion	140
6.2 Surface Modifications with ApoE3 and c(RGD)	145
6.2.1 Characterization and Stability of Liposomes.....	146
6.2.2 Expression Levels of LRP1 and Integrin α_v in Endothelial and Cancer Cells	148
6.2.3 Cellular Uptake of ApoE3-Modified Liposomes	150
6.2.4 Cellular Uptake of c(RGD)-Modified Liposomes.....	154
6.2.5 Discussion and Conclusion	158
7 Conclusions and Outlook	159
7.1 Conclusions	159
7.2 Outlook.....	161
References	163
Appendix	201
A1 Process Optimization of a PFC/W Nanoemulsion Based on Membrane Extrusion	201
A2 Process Optimization of a PFC/W Nanoemulsion Based on High-Pressure Homogenization.....	212
A3 Formulation Optimization	222
A4 Succinimide- and Glucose-Modified Liposomes	229

A5 ApoE3- and c(RGD)-Modified Liposomes	233
A6 Surface Modification using Heparin as an Alternative to PEG.....	240
A7 Asymmetric Liposomes as Proof-of-Concept	258
A8 Calculations for Conjugation and Conjugation Efficiency	264
A9 Buffers, Lipid Films and Dilutions	272
A10 Calibration Curves	283
Abbreviation List	289
List of Symbols	295
List of Publications and Conferences	299

Chapter 1

Introduction and Objective

1.1 Introduction

20 million. This number represents the people worldwide diagnosed annually with cancer (WHO Global Cancer Observatory 2022). In other words, this corresponds to a quarter of the population of Germany. Even more alarming is the number of deaths caused by cancer every year – 10 million (Bray et al., 2024). From a global perspective, one in five people will develop cancer in their lifetime, of which one in nine men and one in twelve women will die from it (Bray et al., 2024). The situation in Germany is even worse – here, one in two people will develop cancer in their lifetime, and one in four men and one in five women will die from it (Ronckers et al., 2023). Frightening and sobering statistics. In Looking at the total number of cancer cases in Germany, around 500,000 people are diagnosed with cancer and around half of them (230,000 people) die every year (Ronckers et al., 2023). And these numbers are steadily rising. Over the last three decades, the number of cancer patients worldwide has risen by almost 80 % (Zhao et al., 2023). According to a prognosis by the United Nations, there will be 35 million patients worldwide by 2050 (Bray et al., 2024). This would reflect another increase of 75 %.

But why are these numbers constantly rising?

Reasons for this include not only the steady aging and growth of the population, unhealthy living conditions such as the consumption of alcohol and tobacco or increasing air pollution, but also improved diagnostics. Preventive actions reduce the risk of devel-

oping the disease. These include, for example, vaccinations against the human papillomavirus (HPV), which reduce the risk of cervical cancer. Improved early diagnosis through highly sensitive genetic and blood tests allows a diagnosis to be confirmed even before imaging techniques can detect a tumor. In addition, immunological procedures and genetic analyses enable more precise diagnostics, allowing for more targeted and effective treatment. Scientific understanding of the development of cancer is also constantly growing, thus opening the door to innovative "personalized" therapies such as checkpoint inhibitors. In addition, more tolerable treatments improve the quality of life and more precise surgical interventions using the latest techniques increase the chances of survival (BMBF Krebsforschung 2020).

Despite all the progress and milestones in cancer research in recent decades, the prognosis for glioblastoma is very low. According to the Robert Koch Institute, the number of new cases of tumors of the central nervous system (CNS) in 2020 was around 7,300, while the number of deaths was 6,000. In women, glioblastomas represent 68.1% of CNS tumors, while in men, the figure is slightly higher at 71.1 % (Ronckers et al., 2023).

However, why is glioblastoma treatment such a difficulty?

The unique tumor phenotype (Kesarwani et al., 2019; Wakimoto et al., 2012) and also the high aggressiveness of the tumor itself (Soroceanu et al., 2013) are some of the reasons for the poor prognosis of glioblastoma. However, the existence of the blood-brain barrier (BBB) is the biggest obstacle to overcome for efficient therapy (Abbott et al., 2006, 2010). It is the most challenging and rate-limiting factor for an effective drug transport into the brain (Alam et al., 2010). Physiologically, the BBB is more a biochemical than a physical barrier (Bernacki et al., 2008) that protects the brain from toxins and pathogens. To give an idea of scale, approximately 98 % of all small molecules and 100 % of all large macromolecules are retained at the BBB (Pardridge, 2005). However, to preserve the integrity of the BBB, it is of paramount importance to develop a drug delivery system (DDS) modified with ligands for targeted transport to the BBB or glioma cells (Oller-Salvia et al., 2016).

Among all these different DDS, liposomes should be given the most attention - but why?

Their high membrane permeability, non-toxicity, biocompatibility, and biodegradability (Barenholz, 2001), as well as their simple methods for surface modification with various ligands, such as endogenous molecules, antibodies or cell-penetrating peptides (Dai et al., 2018; He et al., 2019; Mellinger et al., 2023; Oller-Salvia et al., 2016; Wang et al., 2021), render liposomes particularly advantageous. In addition, liposomes represent an effective non-invasive strategy to transport hydrophilic, lipophilic or amphiphilic drugs across the BBB by surface modification (Alam et al., 2010; Samad et al., 2007).

However, it is not only the modification of liposomes for targeted drug delivery that is of great importance. Another key aspect is the compatibility of administered DDS with human blood to avoid thrombotic events as well as the shielding from the human immune system. Everyone is aware of the increased risk of thrombosis during a flight, which is up to 4 times higher (Rabe et al., 2019). In cancer patients, however, the risk is up to 7 times higher (DKFZ Thrombose bei Krebs, 2023).

In addition, liposomes are an interesting DDS not only because of the various established preparation methods but also due to the preparation of liposomes by centrifugation of a water-in-oil emulsion, as already shown by Pautot et al. 2003 (Pautot et al., 2003). The liposomes resulting from this method show an asymmetry in their lipid composition of the inner and outer layers. The centrifugation of two inverse perfluorocarbon nanoemulsions as a further development of the principle according to Träuble and Grell from 1971 enables an individual "design" of both liposomal leaflets depending on the needs of the API and the intended coating (Träuble and Grell, 1971). This special preparation procedure offers the opportunity to produce optimized liposomes that offer the best conditions for the API to be transported.

To achieve this objective, numerous questions and open aspects still need to be investigated.

1.2 Objective

This work is intended to build on the previously outlined points to demonstrate and further develop the versatility of a liposome as a carrier system in the manner of a "Trojan horse". Both the innovative production of liposomes with an asymmetric bilayer by optimizing a perfluorocarbon-in-water nanoemulsion and the preparation of various surface modifications of liposomes for active targeting and for hemo- and immunocompatibility are the main points of focus of this work.

(1) Development of a Temporarily Stable Perfluorocarbon-in-Water Nanoemulsion

One aspect of this work aims to develop a temporarily stable PFC/W nanoemulsion with the intention of further processing into asymmetric liposomes in which the composition of the outer lipid layer results from the emulsion. The emulsification of the perfluorocarbon takes place with the aid of phospholipids, whereby it must be considered that these are present in the form of a liposomal suspension. When PFCs are added, the phospholipids are distributed in two different conformations: firstly, the monolayer state, in which the PFC pots are emulsified, and secondly, in the liposomal bilayer state. An analytical separation of the liposomes and PFC droplets can be performed using a sucrose gradient due to their density differences. This is of enormous importance, as the main focus in the development of the PFC/W nanoemulsion is on the smallest possible PFC droplets in high yield with the lowest possible proportion of remaining liposomes.

a. Investigations on the Influence of Manufacturing Parameters on a PFC/W Nanoemulsion

The focus is on the preparation of the nanoemulsion using high-pressure homogenization, which has been used in industry for many decades to optimize the product properties of food, beverages and pharmaceuticals. Numerous mechanical effects have already been investigated (Floury et al., 2004; Gupta et al., 2016; Jaegers et al., 2022; G. Kolb et al., 2001; Marie et al., 2002; Olson et al., 2004) and also summarized in various reviews (Jafari et al., 2008; McClements and Jafari, 2018; Schultz et al., 2004). The special characteristics of the PFC/W nanoemulsion due to the

presence of two different particle species therefore require a basic understanding of the vesicle and PFC-droplet break-up, which should be enabled by this subsection.

b. Investigations on the Influence of Formulation Parameters on a PFC/W Nanoemulsion

(i) Variations of the Continuous Phase Concerning the Emulsifier

(ii) Variations of the Disperse Phase Based on the PFC

The two main components of the emulsion, phospholipids as emulsifiers and perfluorocarbons as the disperse phase, are the focus of the investigations. The selection of PFCs as dispersed phase is based on their physicochemical properties. In contrast to typical oils, they do not exhibit miscibility and solubility for phospholipids, which means that the formation of a gel phase at the phase boundary can be avoided and phase transfer during centrifugation for the production of asymmetric liposomes is not subsequently affected (Scartazzini and Luisi, 1988; Ushikubo and Cunha, 2014). Most PFCs are inert, very stable, biocompatible and have already been proven for use in pharmaceutical emulsions (Keipert, 2006; Vorob'ev, 2009). The study focuses on the influence of different volume fractions of PFCs as a dispersed phase, as well as the influence of viscosity by using different PFCs on the resulting particle sizes and also proportions of particle species.

The influence of phospholipids as emulsifiers will be examined in more detail in various studies. A variation of the concentration used, the head group and also the chain length form the framework for this.

(2) Investigation of different liposomal coatings

In the case of liposomal surface coatings, a distinction must be made depending on their intended function.

a. Investigation of liposomal ligands of different structures and uptake mechanisms

The standard therapy for the treatment of a tumor includes the use of chemotherapeutic agents, which have the disadvantage of not acting selectively on cancer cells alone, but also affecting healthy cells. One way to reduce toxic side effects and the therapeutically necessary dose is to specifically target the tumor. This can be

achieved, for example, by using different surface structures (ligands) for targeted transport of the DDS. The testing of different ligands with different structures (small molecular, peptide and protein) and cellular uptake mechanisms is the focus of this work.

b. Investigation on fragmented heparin as an alternative to PEG for STEALTH coating

Immunoprotective coatings are essential to avoid activation of the innate immune system and rapid excretion. However, such coatings can also enable long circulation of the carrier system for passive and active targeting. The current gold standard for STEALTH coating is polyethylene glycol (PEG), which has several disadvantages that have not yet been eliminated. These include the so-called ABC effect (accelerated blood clearance), which describes the accelerated blood excretion after repeated injections due to the formation of anti-PEG-IgM antibodies. The lack of biodegradability of PEG and the obstruction of cellular uptake and endosomal escape (also known as the "PEG dilemma") are also reasons that demand the development of an alternative STEALTH coating.

(3) Proof-of-Concept of Asymmetric Liposomes

Asymmetric liposomes represent the link between the two main topics of this thesis – the PFC/W nanoemulsion and the different liposomal surface coatings. Initial investigations into the liposomal size after production and the influence of post-processing employing membrane extrusion, storage stability, encapsulation efficiency and the degree of asymmetry should serve as a platform for further projects.

Chapter 2

Theoretical Background

2.1 Surfactants

Surfactants are not solely relevant for the chemical industry, but are also of great importance for food technology, the cosmetics industry and the pharmaceutical industry.

2.1.1 Structure and Function

Concerning the structure of surfactant molecules, one fundamental aspect has to be noted: they always consist of two parts; a lipophilic (apolar) fat-soluble part and a hydrophilic (polar) part that is miscible with water.

The lipophilic part (surfactant tail) comprises one or more aliphatic, straight or branched, aromatic or even alkyl aromatic hydrocarbon or fluorocarbon chains. The hydrophilic part (surfactant head) contains one or more polar groups, which can be ionic or non-ionic. Due to their amphiphilic character, they tend to accumulate at phase boundaries (Rosen, 2004), which: 1) improves the wettability of a liquid, 2) stabilizes an emulsion or foam or 3) promotes dispersion of a solid in a liquid (Khalfallah, 2024; Tehrani-Bagha and Holmberg, 2013). They are therefore used as washing, lubricating and dispersing agents or for the production of foams, among others. They are also used as additives in the paper, plastics, leather and paint industries. Within the scope of this work, they are used to form and stabilize emulsions.

Figure 1 illustrates the broad classification of surfactants based on their molecular weight. They can be divided into low-molecular and polymeric, with the former being further classified according to the charge structure of the head groups. Accordingly, they are divided into non-ionic, ionic (anionic or cationic) or amphoteric.

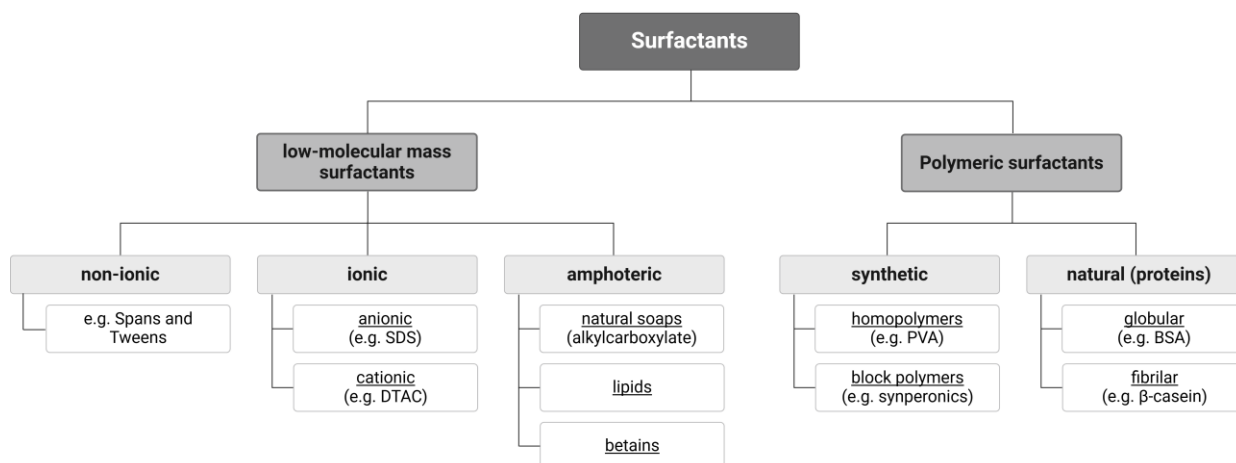


Figure 1: Classification of surfactants (Khalfallah, 2024) (created with BioRender.com).

2.1.1.1 Hydrophilic-Lipophilic Balance

The hydrophilic/lipophilic balance (HLB) is a numerical parameter that was introduced by Griffin in 1949 (Griffin, 1949). It is used to determine the hydrophilic power of a surfactant and is strongly linked to its solubility, which makes it possible to estimate it in different solvents (Griffin, 1955). The HLB value can be calculated with Griffin's empirical method using the equation 1:

$$HLB = 20 * \left(1 - \frac{M_l}{M}\right) + 20 \quad \text{Eq. 1}$$

Where M_l reflects the molar mass of the lipophilic part and M corresponds to the molar mass of the entire molecule.

The Griffin scale ranges from 0 to 20, where higher values indicate greater water-solubility of the surfactant. This Griffin standardized scale shows that: 1) for values of 0 – 9 an oil-soluble surfactant is present, which can be used for W/O emulsions in terms of application technology and 2) for values of 10 – 20 a water-soluble surfactant is present with the property of stabilizing O/W emulsions. However, it is important to note that the Griffin approach does not apply to all surfactants, as counterionic – in the case of ionic

surfactants – or other functional groups are not taken into account. For anionic and cationic surfactants, the method proposed by Davies in 1957 can therefore be used, although it is less common (Davies, 1957). The method according to Davies provides for a calculation from numerical values for the individual chemical groups of a molecule, whereby the influence of the various interacting groups is weighted (Table 1).

Table 1: Categorization of surfactants based on the HLB value (Davies, 1957).

Surfactant properties	HLB value	Solubility
Defoamer	1.5 - 3	lipophilic
Water-in-oil emulsifier	3 - 6	
Wetting	7 - 9	
Oil-in-water emulsifier	8 - 18	hydrophilic
Detergent	13 - 15	
Peptizer-solubilizer	15 - 18	

2.1.1.2 Critical Micelle Concentration

The critical micelle concentration is defined as the concentration above which the interface of two phases is saturated with surfactant molecules, leading to the formation of aggregates (micelles) (IUPAC, 2014). The surface tension is no longer altered above this concentration. A schematic representation is shown in Figure 2.

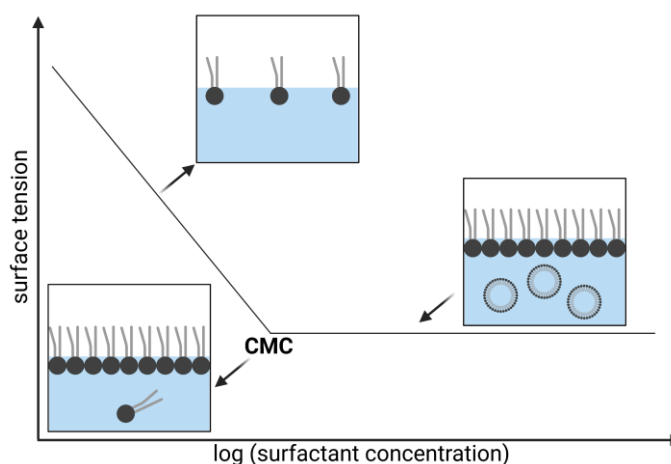


Figure 2: Schematic representation of the adsorption of surfactants at the water-air interface. As soon as the interface is completely covered with surfactants, micelles are formed in the continuous phase. This time point is referred to as the critical micelle concentration (Mishra et al., 2021)

(created with BioRender.com).

Micelle colloids are thermodynamically stable and can assume different geometries depending on the shape of the surfactant (Ghosh et al., 2020). For example, cone-shaped surfactants form a spherical micelle, wedge-shaped surfactants form a rod-like micelle and a disk-shaped bilayer is the result of cylindrical surfactants. Among the aforementioned micelle colloids, the simplest aggregate type is a spherical micelle formed by cone-shaped surfactants, since the cross-sectional area of the hydrated head group exceeded the diameter of the tail. The aggregation number, i.e. the number of molecules involved in a spherical micelle, is 50 – 100 with an average diameter of 5 – 10 nm. Another type of micelle colloids are wormlike or cylindrical ones, which are formed by the addition of strongly binding counterions. This causes the effective head group area to be reduced. It should also be mentioned that wormlike micelles can often contribute to increasing the viscosity of a solution. The third type of aggregates that forms in water are bilayers - very similar to vesicles. In this case, two molecules with the non-polar parts facing each other, form pairs that stack side by side. Due to the orientation of the head groups towards the outside, both sides of the layer are polar and the inside of the layer is non-polar. In contrast, vesicles can be regarded as a bilayer with a smaller curvature, which is closed at the ends (Ghosh et al., 2020).

2.1.2 Phospholipids

Phospholipids are naturally occurring surfactants. Alongside fatty acids, triglycerides, lipopolysaccharides, isoprenoids (steroids) and others, they belong to the group of lipids, which refers to all fats and fat-like substances. Phospholipids are the main component of eukaryotic cell membranes and can mainly be divided into sphingolipids and glycerophospholipids, which will be discussed in more detail below.

2.1.2.1 Glycerophospholipids

The structure is derived from 1,2-Diacyl-*sn*-glycero-3-phosphate, with the phosphate residue of the backbone forming the polar head group together with esterified alcohol. The most frequently occurring alcohols are choline (PC), ethanolamine (PE), glycerol (PG) and inositol (PI) (Figure 3). Depending on their type, the head groups can be charged or neutral (zwitterionic) at physiological pH values and thus significantly determine the polarity of the phospholipids. The hydrophobic part of the phospholipid usually consists of

one or two fatty acid chains, which have different compositions depending on their origin – such as egg yolk, soybean or animal organs. Fully synthetic fatty acids are also available so that a precise fatty acid composition is defined.

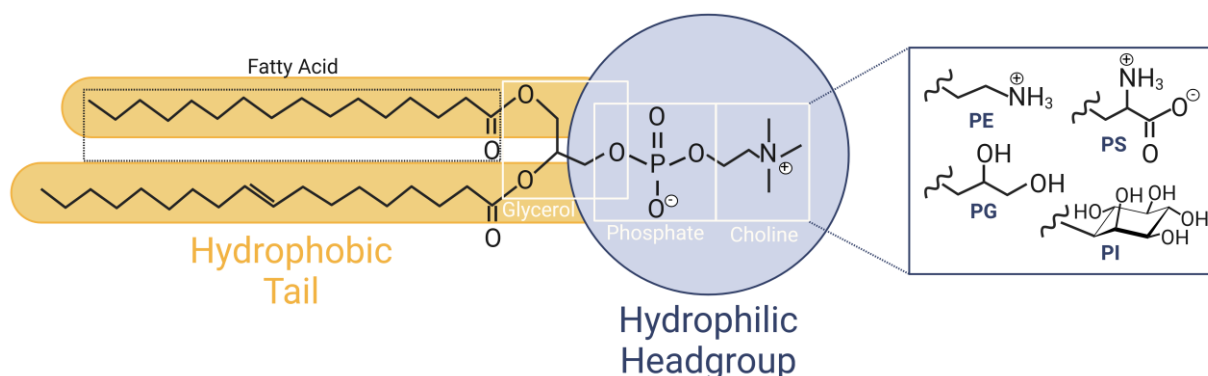


Figure 3: Schematic representation of glycerophospholipids. They consist of a glycerol backbone with two esterified fatty acids and a polar head group of phosphate and variable alcohol residue (PE: phosphatidylethanolamine; PS: phosphatidylserine; PG: phosphatidylglycerol; PI: phosphatidylinositol) (Drescher and van Hoogevest, 2020) (created with BioRender.com).

Phospholipid membranes can occur in several states, with two main states being described (Chapman, 1975) (Figure 4). The transition from the occurs at the so-called phase transition temperature T_m . Firstly, the highly ordered gel state ($L\beta$) in which the fatty acid chains are rigid and immobile. All phospholipid hydrocarbon chains are present in an all-trans configuration, so there is a perpendicular arrangement to the plane of the bilayer, leading to an almost ideal anisotropy of the acyl chains. This state occurs when the temperature T is below the phase transition temperature T_m ($T < T_m$), which remarks the temperature where the phospholipids change from the $L\beta$ state to the $L\alpha$ state on the other hand state. In the liquid-circular phase ($L\alpha$), the fatty acid chains are in constant motion, making the membrane more flexible and increasing its permeability. This state is always present when the $T > T_m$ and is found in almost all physiological membranes (Chen et al., 2013). The structure of the bilayer is maintained due to electrostatic interactions of the polar head group and the hydrophobic interactions of the acyl chains (of the phospholipids). Due to the improved mobility of the fatty acids, the cross-sectional area increases ($6.0 - 7.2 \text{ nm}^2$) while their thickness decreases ($4.0 - 4.5 \text{ nm}$) (McElhaney, 1976). The phase transition temperature depends on the length of the acyl chains, their degree of saturation and the hydrophilic head group itself. Membranes composed of phospholipids with long-chain, predominantly saturated fatty acids are more rigid and generally have a higher membrane thickness (Rawicz et al., 2000).

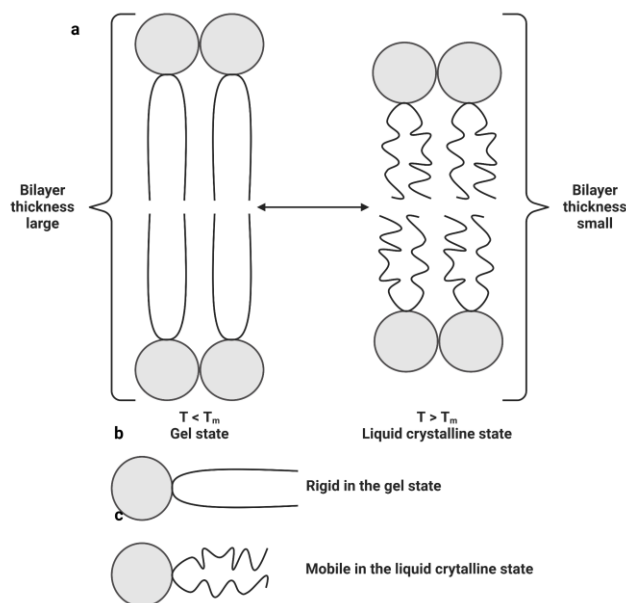


Figure 4: Schematic overview of a phospholipid's thermotropic gel-to-liquid crystalline phase transition. Representation of a) the transition of a phospholipid bilayer whereby the thickness of the bilayer in the gel state is greater than in the liquid crystalline state, b) the lipid structure in the gel state, i.e. at a temperature below the transition temperature and c) the lipid structure in the liquid crystalline state, i.e. at a temperature above the transition temperature at which the mobile acyl chains are hinged to the carbonyl carbon of the glycerol backbone (Eze, 1991) (created with BioRender.com).

Due to their amphiphilicity, phospholipids have emulsifying, wetting and self-organizing properties. They can therefore stabilize emulsions (Yang et al., 2013), improve the hydrophilicity of hydrophobic drugs due to their wetting properties (Haynes, 1992) and also serve as drug carrier systems in the form of liposomes (Cullis and de Kruijff, 1979). The modification of phospholipids by functional groups enables the conjugation of various ligands, fluorescent dyes or other functional groups (Chapter 2.3.4).

Phospholipids can form micelles above the critical micelle concentration in aqueous or oily environments, whereas in oily environments they are reverse micelles (Figure 5). Due to their amphiphilicity, they can align themselves at the phase boundary with the corresponding alignment of their functional groups and thus act as a surfactant. The hydrophilic head groups or lipophilic fatty acid chains are oriented towards the outer phase, whereby phospholipids with short fatty acid chains above the CMC form micelles in an aqueous environment. In contrast, longer fatty acid chains above the critical aggregate concentration (CAC) form bi-layer structures. The boundary between micelle formation and bi-layer formation depends on the hydrophilic head group. It lies between 6 carbon atoms (for PE) and 12 carbon atoms (for PG) (Kleinschmidt and Tamm, 2002).

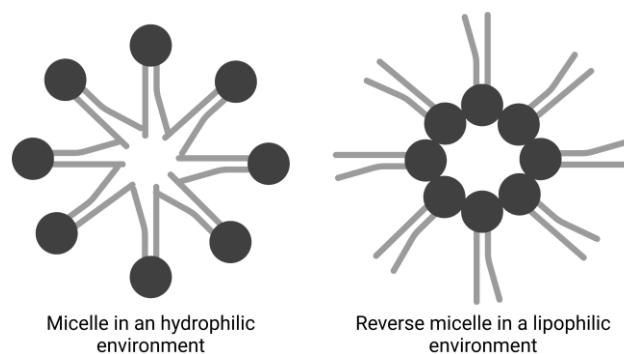


Figure 5: Arrangement of phospholipids above the CMC in a hydrophilic (aqueous) or lipophilic (oily) environment (created with BioRender.com).

2.1.2.2 Sphingophospholipids

Sphingomyelins, also known as sphingophospholipids, are classified as both, phospholipids and sphingolipids. In contrast to glycerophospholipids, sphingomyelins are not composed of a glycerol skeleton, but instead of a sphingosine skeleton to which one fatty acid chain and one choline residue are attached. Sphingomyelin is therefore similar in structure and biological function to phosphatidylcholine (PC). Both representatives make up more than 50 % of all phospholipids found in biological membranes (Barenholz and Thompson, 1999; Lasic, 1993). From a chemical point of view, the carbonyl group acts as a hydrogen bond acceptor and the additional hydroxyl group as a hydrogen bond donor. This structure allows sphingomyelin to form stable membranes via so-called "hydrogen bonds" (Lasic, 1993; Tirri et al., 1978). Compared to phosphatidylcholine, these interactions lead to significantly higher phase transition temperatures of the sphingomyelin membrane ($T_m = 39 - 46\text{ }^{\circ}\text{C}$).

2.2 Emulsions

Emulsions are defined as the liquid-liquid case of a colloidal system of two immiscible liquids that form a homogeneous mixture through the input of external energy. One liquid is present as a droplet (dispersed phase), which is dispersed in a second liquid (continuous phase). The liquids are usually an oil – hydrophobic and non-polar – and an aqueous phase, which is hydrophilic and polar (Bibette et al., 1999; Köhler and Schuchmann, 2012). The addition of surfactants allows for improved stability of the emulsion, and this can be short-term in the range of min or long-term for years. The interfacial tension between the two liquids is the dominant force for the interactions in an emulsion. An emulsifier therefore minimizes the energy required to maintain the interface between the droplets and the continuous phase (Köhler and Schuchmann, 2012). Depending on the composition of the two liquids, different flow behavior can be generated, resulting in a wide range of applications. For example, emulsions are used as lubricants in the food and pharmaceutical industries as well as in cosmetics production and the plastic industry (Mason et al., 2006).

2.2.1 Structure and Types of Emulsions

Emulsions can be categorized according to various criteria. For example, based on the size of the dispersed phase present or on the expansion of the dispersed and continuous phase. When classifying by size, emulsions with a droplet size of 1 – 1,000 μm are defined as macroemulsions. They have a milky-white appearance and are thermodynamically unstable (Schubert and Armbruster, 1989). In contrast, there are micro- and nanoemulsions, whose droplet size is in a range of 10 – 200 nm. Nanoemulsions can appear “quasi-transparent” in visible light at low emulsifier concentrations.

If categorization is based on morphology, two main types can be distinguished. If the continuous phase is aqueous and the disperse phase is an oil, it is referred to as a "direct", "water-based" oil-in-water emulsion (O/W) (Figure 6a). In this case, the surfactant is usually water-soluble. If, however, the continuous phase is oily and the disperse phase is aqueous, it is an "inverse", "oil-based" water-in-oil (W/O) emulsion (Figure 6b). In this instance, the oil phase typically dissolves the surfactant.

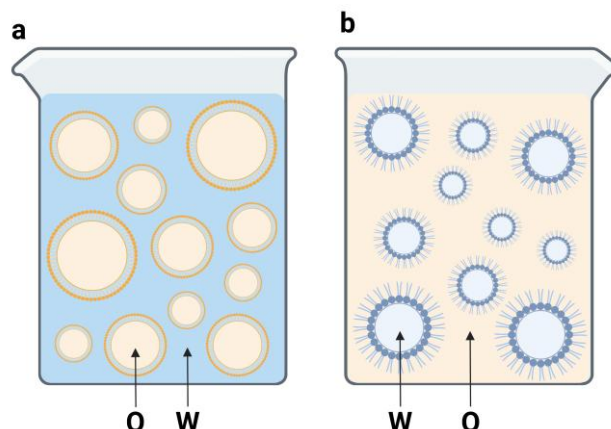


Figure 6: Schematic representation of the structure of different emulsion types. The blue color reflects the aqueous phase (W), the yellow color the oil phase (O). (a) oil-in-water type emulsion (O/W) and (b) water-in-oil type emulsion (W/O) (Köhler and Schuchmann, 2012) (created with BioRender.com).

Emulsions can be analyzed by optical methods such as microscopy using contrast agents. For nanoemulsions, however, methods such as DLS, X-ray scattering, CryoTEM or REM are necessary due to their small droplet size (Mason et al., 2006). The droplet size distribution is one of the most important parameters of an emulsion, since rheology, haptics and also appearance are dependent on the number of droplets, their size, and distribution. This is indirectly influenced by the concentration or volume of the dispersed phase.

2.2.2 Preparation of Emulsions

The preparation of emulsions requires an energy input that enables droplet formation in the two-phase system and causes an enlargement of the interface. The energy input is usually provided by mechanical energy - mostly in the form of shear force. Whether the shear is sufficient depends not only on the flow, but also on the tensile stress of the droplets and the interface created. Many different methods are available for this purpose, the most commonly used being ultrasound and high-pressure homogenization.

The emulsification process takes place in several steps (Figure 7). First, a crude emulsion is formed by premixing, whereby the disperse and continuous phases are roughly mixed and large droplets are present. For this step, a rotor-stator mixer such as the Ultra-Turrax® is often used, with gravity being created between a stationary and a moving wall. Pre-emulsification leads to emulsions with a droplet size of up to one micrometer. To produce smaller droplets, further dispersing by high shear forces is required (Mason et

al., 2006; Schuchmann and Danner, 2004). High-pressure homogenization (HPH) can be used for this purpose, creating extremely high shear forces in the impact chambers suitable for nanoemulsions. The geometry of the channel or the impact chamber are the decisive factor in addition to the pressure. Comminution to the desired droplet size can be achieved by multiple circulation of the emulsion through the channel. When using ultrasound for emulsification, the sonotrode generates cavitation at the tip. In the medium, there are temporal and local pressure barriers (so-called acoustic pressure). This depends on the ambient pressure and the pressure generated by the amplitude of the probe. Small air bubbles filled with vapor form below the probe's tip, which expand and ultimately collapse due to the difference between the internal bubble pressure and the ambient pressure. Ultrasound can be introduced into a system continuously via a flow cell or directly via an ultrasonic horn or bath (Gogate and Kabadi, 2009). During the preparation of an emulsion, newly created interfaces must be coated with emulsifier immediately after dispersion in order to avoid direct separation. Diffusion of the emulsifier is of great importance as the dispersed droplets are in strong motion due to the dispersion process and frequently collide.

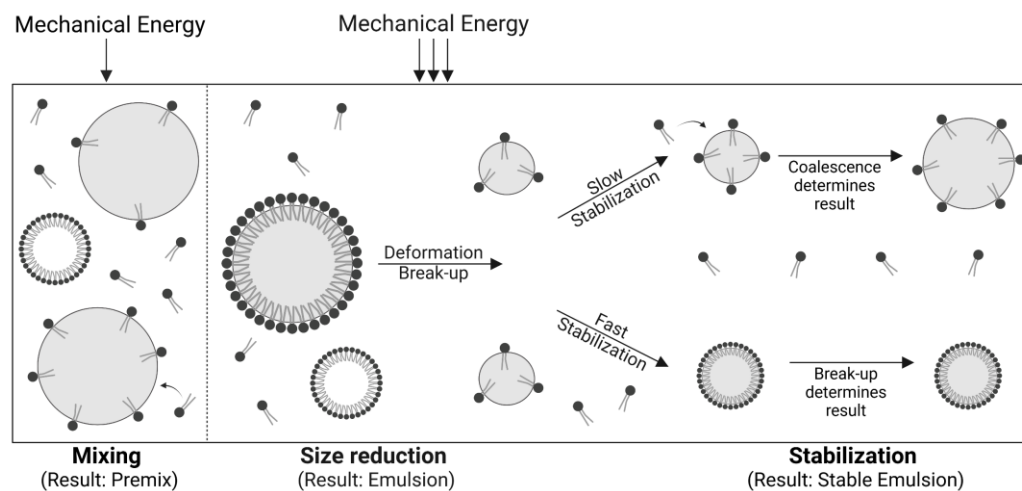


Figure 7: Stages of the preparation of an emulsion. After a preceding mixing step by introducing mechanical energy, an emulsion is formed by size reduction. The addition of the emulsifier to stabilize the emulsion can follow fast or slow kinetics (Schuchmann and Danner, 2004) (created with BioRender.com).

Figure 7 schematically illustrates the production phases of an emulsion: 1) premixing of the individual components to form a coarse dispersed raw emulsion, 2) fine emulsification by droplet break-up when the critical deformation is exceeded and 3) stabilization of the newly formed interfaces.

2.2.3 Mechanisms of Instability

Emulsified droplets tend to reunite to form a uniform phase, as the "droplet state" is not thermodynamically stable (Köhler and Schuchmann, 2012). Combining the droplets reduces the surface area until finally, both original liquid phases are present. Emulsifiers can be used to prevent this. An emulsifier covers the interfaces and lowers the interfacial tension between the fluids due to its amphiphilic structure with polar and hydrophobic sides in the respective medium. This effect is mainly responsible for the stabilization of the emulsion. However, other effects such as the viscosity of the continuous phase, the dispersed phase fraction, the density difference of the fluids, the droplet size and distribution, the steric hindrance, the surface charge due to the emulsifier and the osmotic pressure are also relevant. Figure 8 shows the various mechanisms of emulsion instability, with Ostwald ripening and coalescence being of the greatest importance. Ostwald ripening describes the self-running ripening process of colloids from small to larger droplets due to diffusion - small droplets migrate to larger droplets. Thus, this is the natural aging of the emulsion. The prerequisite for this process is always a slightly inhomogeneous droplet distribution. Diffusion is set in motion since smaller droplets have a greater vapor pressure compared to larger droplets and strive to compensate for this difference in a closed system. Ostwald's ripening can be avoided, for example, by adding salts to change the osmotic pressure, as this changes the capillary pressure at the same time. Another surface-reducing process is coalescence. It describes the merging of two droplets as they collide. The impact probability plays a decisive role here. It depends on the size of the droplet, the viscosity of the medium and the number of droplets in the continuous phase. If there are a large number of droplets (dispersion phase proportion) in the continuous phase, the probability of two droplets colliding is higher. The emulsifier, which coats the droplet, forms the final barrier in the event of a collision - either sterically through long molecular groups or electrostatic repulsion with the same charge. The zeta potential describes the charge at the shear boundary of the particles or droplets, as can be derived from the DLVO theory (Derjaguin, Landau, Verwey, Overbeek) (see Chapter 3.2.5). There is always a thin film of the other phase between two droplets of one phase. As soon as this film decreases to a thickness of a few nanometers, the van der Waals attraction between the two droplets causes the film to break through. The probability of coalescence is therefore proportional to the area of the film of the continuous phase and

can be described in more detail by the proportionality coefficient ω , which defines the frequency of coalescence per unit area (Dinh et al., 2020).

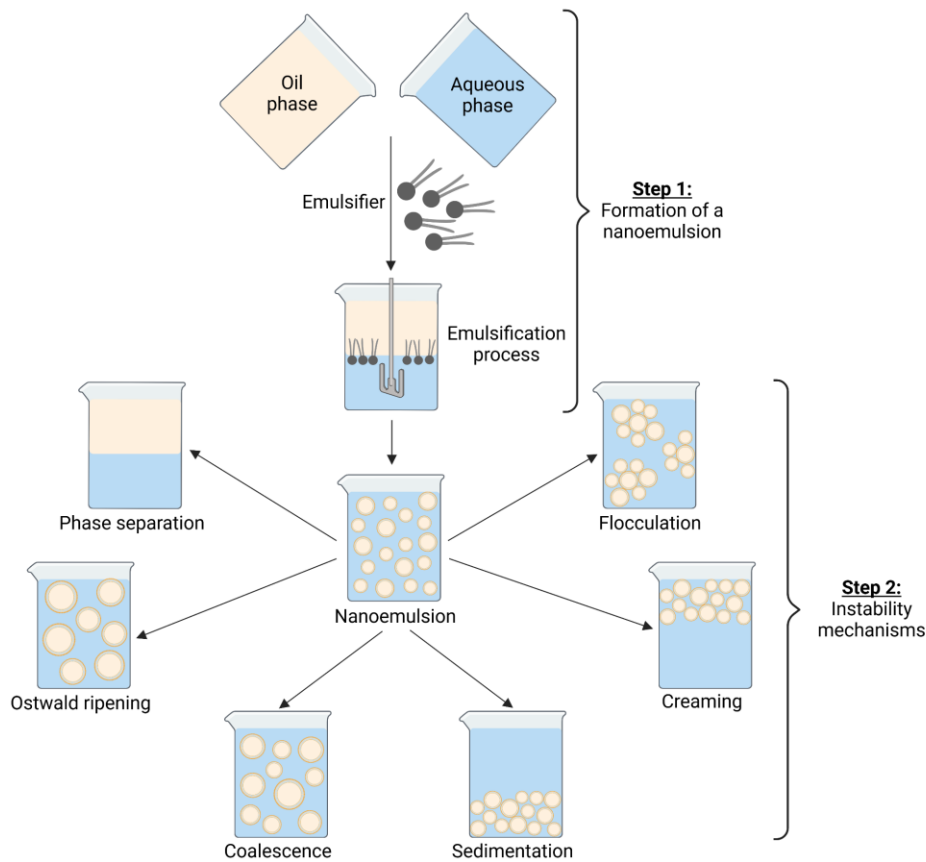


Figure 8: Schematic representation of the preparation and the various instability mechanisms of a nanoemulsion (Hu et al., 2017; Karthik et al., 2017) (created with BioRender.com).

In addition to the mechanisms mentioned above, there are a few more illustrated in Figure 8. These include gravitational separations, which are caused by external forces such as gravity or centrifugal force. If the external force exceeds the Brownian motion, a concentration gradient occurs in the system and the dispersed phase begins to migrate (Tadros, 2013). Gravitational separations are usually reversible by applying a small amount of energy, such as shaking the sample. However, it should be noted that this favors Ostwald ripening, as the droplets are packed much more densely and thus the probability of impact is increased or the diffusion distance is shortened. There are two subtypes of gravitational separation: firstly, creaming, where the dispersed phase migrates upwards if the phase has a lower density, and secondly, sedimentation, where the dispersed phase migrates downwards if it has a higher density. In both cases, complete phase separation can occur. Lastly, flocculation has to be mentioned, whereby

several droplets accumulate without merging with each other. Accumulation is driven by the interactions – the Van der Waals interactions – between the layers on the surface of the droplets (Ravera et al., 2021). Flocculation always happens when the repulsion is not great enough to keep droplets at a distance (Tadros, 2013).

2.2.4 Perfluorocarbons as Dispersed Phase

Perfluorocarbons are organic compounds analogous to hydrocarbons, with the difference that all hydrogen atoms are replaced by fluorine. These compounds do not occur in nature, which is why they are always of synthetic origin (Faithfull and Weers, 1998). Perfluorocarbons have several unique properties. They are clear, odorless liquids whose density can be about twice that of water. In consequence of their structure, they have hydrophobic properties and therefore they are immiscible with water. In addition, they are also lipophobic in most cases. Due to fluorination, they are chemically as well as biologically completely inert and have only low toxicity even at high doses (Janjic and Ahrens, 2009; Krafft and Riess, 2009; Spahn, 1999). PFC-based emulsions are used as oxygen transporters because of their high gas-binding capacity (Riess, 2001; Riess and Krafft, 1998). Approved emulsions were, for example, Fluosol® or Oxygent™ (Keipert, 2006; Lowe, 2006; Vorob'ev, 2009; Weers, 1993). Furthermore, PFC-based emulsions are used for ¹⁹F MRI owing to their extremely preferable nuclear magnetic resonance (NMR) properties and the absence of fluorine in the human organism (Tirota et al., 2015). In addition, PFCs are also used as drug or gene vectors as this allows serum resistance for gene delivery and good stability for drug delivery (Wang et al., 2014, 2016). It should be added that fluorinated liposomes have a prolonged circulation time (Riess, 2009). PFCs are also used in liposome-like fluorinated nanocarriers, so-called dendrimersomes, or in micelles (Klein et al., 2010; Xiao et al., 2016). The latter is significantly more stable as they enhance the cohesion of the hydrophobic core (Matsuoka, 2003; Vierling et al., 2001).

2.3 Liposomes

The early beginnings of liposome research date back to the 1960s, when the British hematologist Bangham first described the formation of closed phospholipid vesicles (Bangham and Hirne 1964, Bangham et al. 1965). These association colloids were initially referred to as "multilamellar smetic mesophases" or "banghasomes" (Deamer 2010). The term "liposomes", which is commonly used today, was introduced by Weissmann (Sessa and Weissmann 1968) and is derived from the Greek words *lipos* (fat) and *soma* (body).

2.3.1 Definition and Categorization

In addition to naturally occurring biomolecules in the nanoscale range, such as DNA, proteins, viruses or antibodies, nanostructures of various types can also be produced in this size range. Nanostructures can be divided into polymeric, inorganic and lipid-based. Liposomes are assigned to the latter subgroup as shown in Figure 9 (Mitchell et al., 2021; Saallah and Lenggono, 2018).

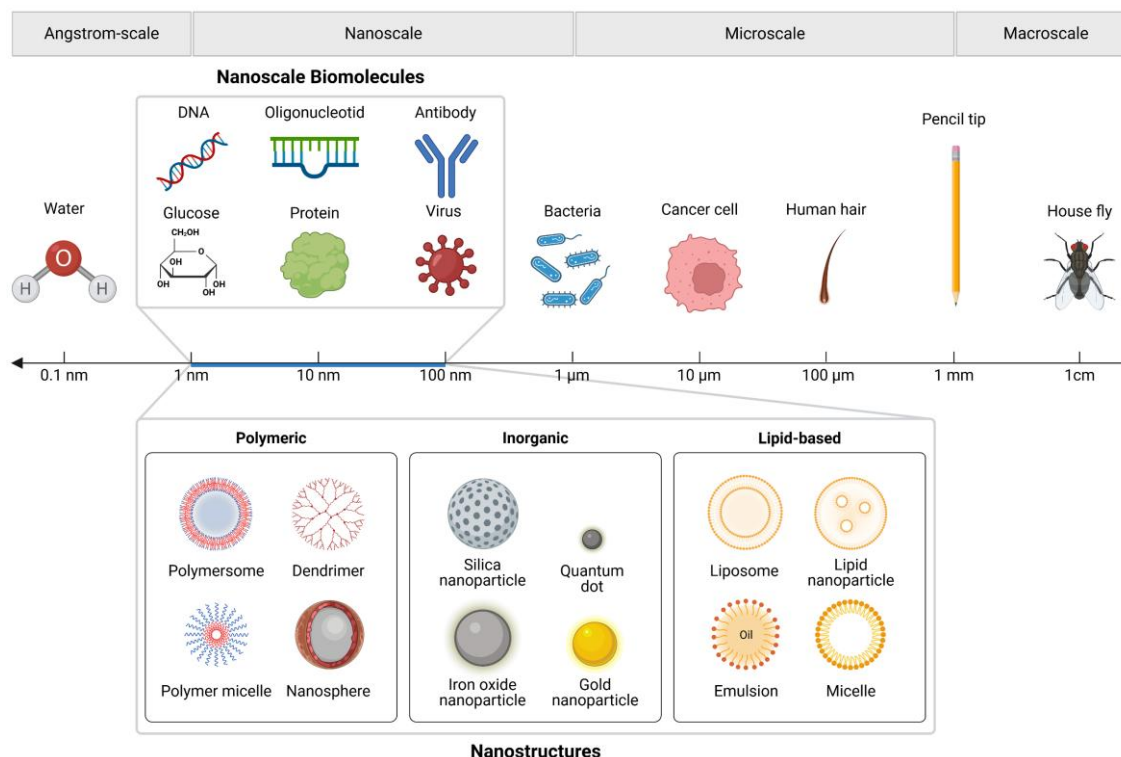


Figure 9: Integration of nanoparticles and biomolecules into the nanoscale. Examples of biological or other reference objects which can be found in the range from nanometers to centimeters (Mitchell et al., 2021; Saallah and Lenggono, 2018) (created with BioRender.com).

2.3.2 Structure and Components

Liposomes are spherical, colloidal vesicles consisting of one or more lipid bilayers as a membrane sheath that encloses an aqueous core. They are formed by spontaneous association (self-assembly) of amphiphilic, water-insoluble molecules after dispersion in an aqueous medium. Phospholipids can be cited as an example of such molecules. The phospholipids are arranged in an aqueous environment in such a way that the hydrophilic head groups are oriented towards the aqueous phase inside and outside the vesicle. The size of the liposomes after spontaneous association (self-assembly) can vary between 20 nm and a few μm . The morphological classification according to size and lamellarity can be seen in Figure 10. "Single-shelled (unilamellar vesicles UV) are divided into small (small ... SUV), large (large ... LUV) and very large (giant ... GUV). "Multi-lamellar" vesicles can in turn be grouped into oligolamellar (OV), multilamellar vesicles (MLV) and multivesicular vesicles (MVV). Below a size of 20 nm, phospholipids form simpler structures, such as micelles, in an aqueous environment due to their strong curvature and size (Figure 5, Chapter 2.1.2).

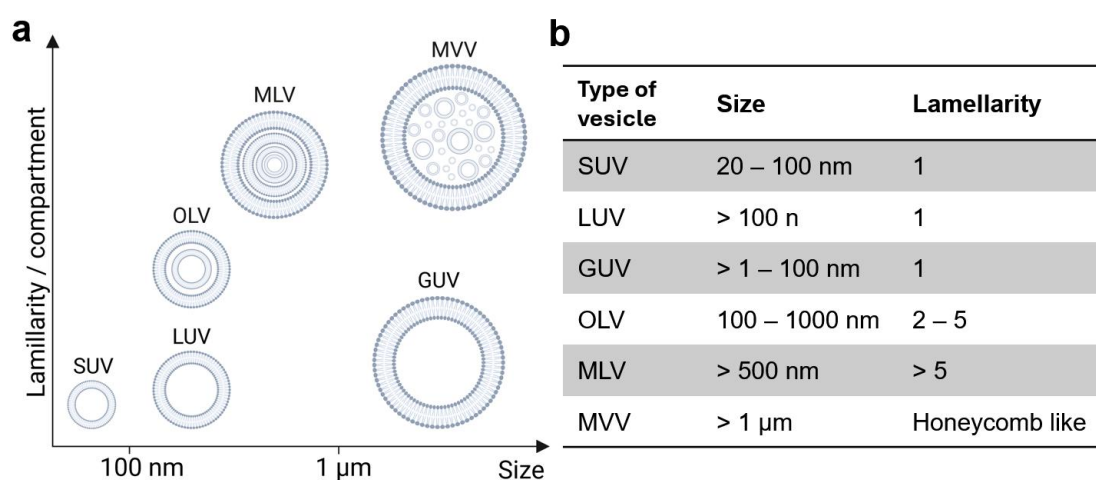


Figure 10: Classifications and structures of vesicles. (a) Classification of liposomal vesicles based on particle size and lamellarity/compartments, (b) the size and lamellarity of various liposomal types (Liu et al., 2022) (created with BioRender.com).

The osmotic pressure can be a factor that influences the shape of the liposomes. If there is a difference in the number of dissolved molecules within the vesicle and the surrounding medium, liposomes either contract, expand or change into a completely different shape. Instead of spheres, ellipses or other elongated plate-like structures can form (Döbereiner et al., 1993).

2.3.2.1 Phospholipids

On account of their amphiphilic character, phospholipids serve as building blocks for physiological membranes, but also for artificial vesicles such as liposomes. Phospholipids are discussed in more detail in Chapter 2.1.2.

2.3.2.2 Cholesterol

Cholesterol is a polycyclic alcohol and, as a steroid from the sterol group, belongs to the lipid-like substances (Figure 11). It is an important component for stabilizing biological membranes and can be incorporated in a proportion of up to 50 mol% (Kirby et al., 1980; Needham and Nunn, 1990). Membrane stabilization is achieved through cholesterol interactions with moving fatty acid chains in the liquid-crystalline ($L\alpha$) phase. In the highly ordered gel phase ($L\beta$), cholesterol leads to a decrease in order, whereby the phase transition temperature T_m decreases and the $L\alpha$ phase persists over a wide temperature range (Lasic, 1993). Thus, the cholesterol content in a liposomal formulation can affect the strength of the liposomal structure (Briuglia et al., 2015). If cholesterol is integrated in the liposomal composition, its hydroxyl group is located next to the carboxyl groups of the ester bonds of the phospholipids (hydrophilic head group). The hydrophobic end and the four-ring structure of the cholesterol are in contact with the hydrophobic fatty acids and thus provide rigidity and support for the membrane.

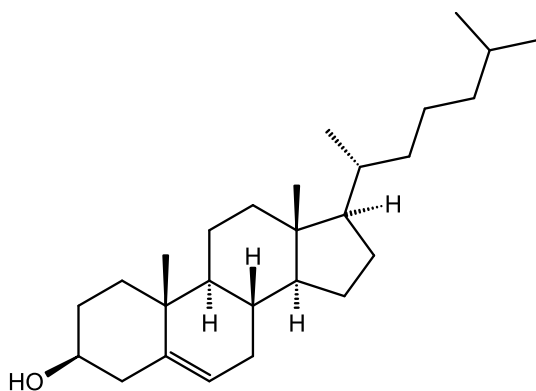


Figure 11: Chemical structure of cholesterol.

2.3.3 Pharmaceutical Application of Liposomes

The potential for using lipid vesicles as membrane models was recognized early on (Bangham et al., 1965; Papahadjopoulos and Watkins, 1967). However, their suitability as DDS was not investigated until the 1970s, with the beginnings of their pharmaceutical use going back to Gregory Gregoriadis (Gregoriadis et al., 1971; Gregoriadis and Rymann, 1972a, 1972b). Liposomes are excellently suited as biocompatible and biodegradable DDS, as the liposomal components (phospholipids and cholesterol) are identical to biological cell membranes. In addition, liposomes are of great interest due to their versatility in terms of size, number of layers and flowability (Liu et al., 2022). In addition to their use from a pharmaceutical point of view, they are also used in the cosmetic field. Liposomes or lipid capsules are utilized in creams for dermal application, in oral preparations such as tablets, for ocular application in the form of eye suspensions or as parenteral injections for tissue-specific application. They are also used in medical diagnostics as signal amplifiers or carriers. Because of their structure, liposomes are suitable for including hydrophilic active ingredients in the aqueous interior and for incorporating lipophilic active ingredients in the bilayer (Figure 12). However, the adsorption of active ingredients via electrostatic interactions on the liposomal surface is also possible.

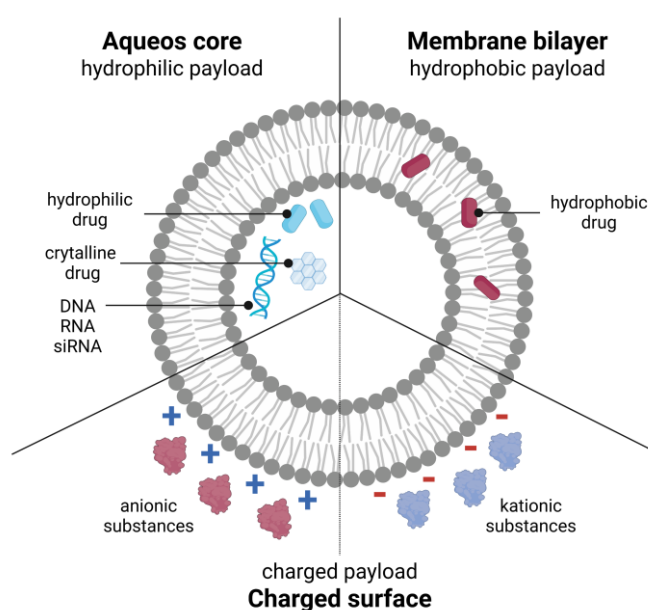


Figure 12: Structural overview of the payload strategies for a liposomal drug delivery system. In addition to active ingredient loading in the aqueous core (hydrophilic APIs), the active ingredient can also be contained inside the membrane (hydrophobic APIs) or outside the membrane (ionic/charged APIs) (Çağdaş et al., 2014) (created with BioRender.com).

The administration of active substances significantly alters their pharmacokinetics in the body. The use of liposomal carrier systems is therefore often aimed at poorly soluble (e.g. Biopharmaceutics Classification System, BCS class II), highly toxic (e.g. cytostatics) or unstable (e.g. proteins) active ingredients. Liposomes can be regarded as a circulating active ingredient depot, as they can release the active ingredient in a somewhat retarded manner. The encapsulation of an active ingredient prevents rapid renal elimination on the one hand and premature degradation and the associated loss of the active ingredient on the other (Allen and Cullis, 2004; Bozzuto and Molinari, 2015). A liposomal-administered drug has a significantly lower distribution volume than a free drug, which is why lower doses are required for therapy (Gabizon et al., 1989; Juliano and Stamp, 1978; Rahman et al., 1986). These advantages lead to an increase in the Therapeutic Index (TI). The TI is defined as the quotient of the toxic dose by the effective dose that produces the desired efficacy (Mayer et al., 1998). Therefore, the TI is a way of describing a drug's safety (Muller and Milton, 2012). The higher the TI, the safer a drug is. The correlations between the form of administration of active pharmaceutical ingredients, side effects, therapeutic efficacy and the TI are shown in Figure 13.

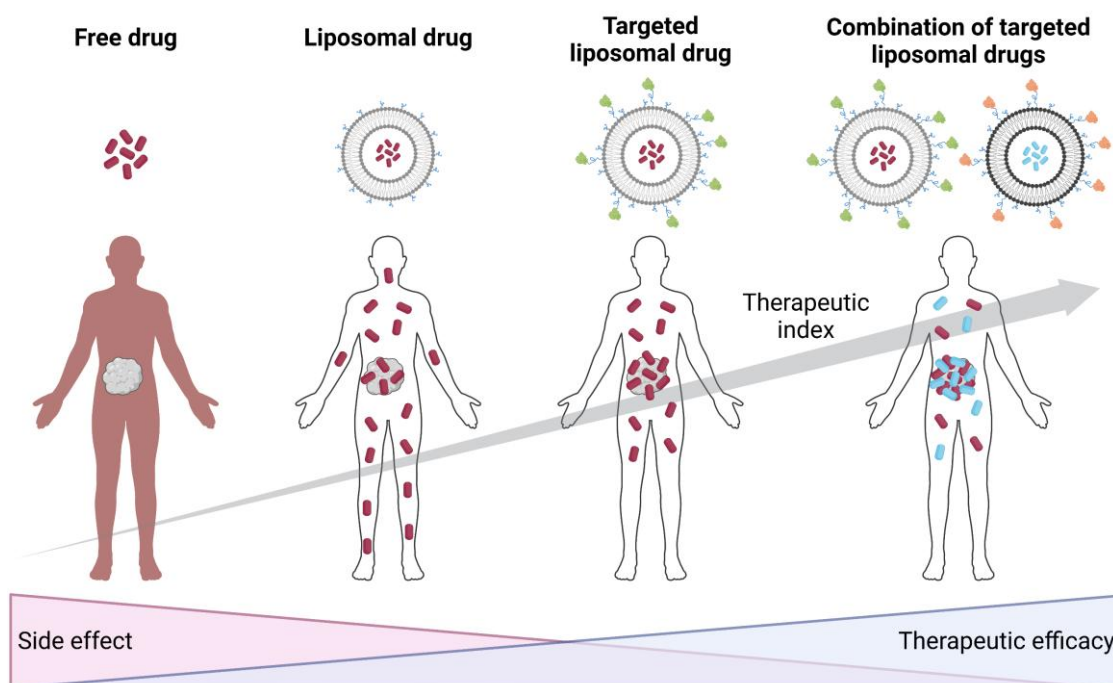


Figure 13: Effects of the type of administration of an API on side effects, therapeutic efficacy and therapeutic index. Free drugs cause the most side effects and have the lowest therapeutic efficiency, as the drug also targets healthy cells. This condition is gradually improved by encapsulation in a liposome, the modification of the liposome into a "targeting drug delivery system" and the combination of various encapsulated and modified API. This increases the therapeutic index of the treatment (Wu et al., 2016) (created with BioRender.com).

2.3.3.1 Approved Liposomal Formulations

In 1995, Doxil® was the first successful milestone of liposome-based products to be launched on the US market (Fan and Zhang, 2013). In addition to their use in cancer therapy, liposomal formulations with drugs for the following main indication groups have since been launched on the market: Fungal infections, pain therapy, immunotherapy and photodynamic therapy. Table 2 classifies 15 approved liposomal products according to their indication. A more detailed list of liposomal formulations approved or undergoing clinical trials, sorted primarily by their basic fatty acid building block, can be found in Table 3.

Table 2: Overview of approved liposomal formulations by trade name and their respective indications.

Indication	Approved pharmaceuticals
Cancer Therapy	Doxil®; Myocet®; DaunoXome®; Depocyt®; Marqibo®; Onivyde®; Mepact®
Fungal Diseases	Abelcet®; Ambisome®; Amphotec®
Analgesics	Exparel®; DepoDure™
Viral Vaccines	Epaxal®; Inflexal®
Photodynamic therapy	Visudyne®

Table 3: Overview of liposomal formulations approved or undergoing clinical trials. Compilation of trade name, active ingredient, administration route, size range and indication (Bulbake et al., 2017).

Trade name	API	Administration	Size [nm]	Indication
Based on Myristoyl Fatty Acids				
Abelcet™ (1995)	Amphotericin B	i.v.	1,600–11,00	Invasive severe fungal infections
Visudyne® (2000)	Verteporfin	i.v.	100	PDT Sensitizer
Arikayce™ (2018)	Amikacin	Oral inhalation	250–300	Antibacterial (Lung infection)
Lipoplatin™ (2017)	Cisplatin	i.v.	110	Non-small cell lung cancer
Ambisome® (1997)	Amphotericin B	i.v.	45–80	Fungal infections
DaunoXome® (1996)	Daunorubicin	i.v.	45	AIDS-related Kaposi's sarcoma
Doxil® (1995)	Doxorubicin	i.v.	87	Ovarian cancer, breast cancer, Kaposi's sarcoma
Onvyx™ (2015)	Irinotecan	i.v.	/	Acute lymphoblastic leukemia

Based on Oleoyl Fatty Acids				
Depocyt® (1999)	Cytarabine	Spinal	20	Neoplastic meningitis
DepoDur™ (2004)	Morphine sulfate	Epidural		Narcotic Analgesic (Pain management)
Epaxal® (1993)	Inactivated hepatitis A virus (strain RGSB)	i.m.	/	Hepatitis A Vaccine
Inflexal®V (1997)	Inactivated hemagglutinine of influenza virus strains A and B	i.m.	/	Influenza Vaccine
Mepact® (2004)	Mifamurtide	i.v.	/	High-grade, resectable, non-metastatic osteosarcoma
Based on Erucoyl Fatty Acids				
Exparel® (2011)	Bupivacaine	i.m.	/	Pain management
Based on Egg Yolk Phospholipids				
Myocet® (2000)	Doxorubicin	i.v.	190	Combination therapy with cyclophosphamide in metastatic breast cancer
Based on Sphingomyelins				
Marqibo® (2012)	Vincristine	i.v.	100	Acute lymphoblastic leukemia
Miscellaneous				
Amphocil® (1993)	Amphotericin B	i.v.	110–114	Severe fungal infections
Amphotec® (1996)	Amphotericin B	i.v.	/	Severe fungal infections

2.3.4 Surface Modifications of Liposomes

The targeted transport of active ingredients to the site of action, as well as aspects of hemo- and immunocompatibility, are decisive for the surface modification of liposomes. An overview of the coating options for active targeting and STEALTH coating is shown in Figure 14.

A STEALTH coating, in most cases a coating with polyethylene glycol (PEG), is necessary to increase the retention time in the body. Non-PEGylated liposomes show rapid elimination from the blood circulation by absorption into the reticuloendothelial system (RES), formerly known as the reticuloendothelial system (RES), whereas the liver is the primary site of uptake. The circulation half-life is less than 30 min (Derksen et al., 1988), which is why uncoated liposomes are unsuitable as a system for targeted therapy. Although the introduction of PEG chains leads to prolonged blood half-lives, it also results in steric hindrance and thus impaired cellular uptake and a lack of endosomal escape (Zalba et al., 2022). In addition to PEG as a synthetic component for surface modification

concerning the introduction of STEALTH properties, the polymer poly(2-methacryloyloxyethyl phosphorylcholine) (PMPC) is also suitable (Adler et al., 2022, 2021). In contrast to the synthetic components, however, coatings can also be made with physiological components such as hyaluronic acid or heparin. In both cases, these are glycosaminoglycans (Adler et al., 2023; Asawa et al., 2021; Hoang Thi et al., 2020; Lee and Spicer, 2000).

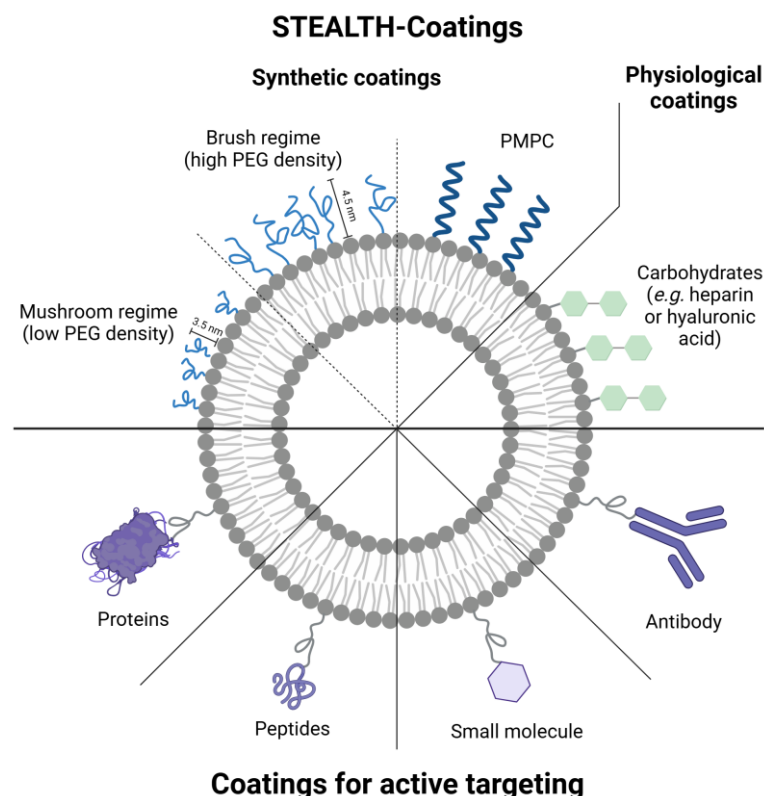


Figure 14: Overview of the various surface modifications of liposomes. The modification is performed with regard to the main aspects: the hemo- and immunocompatibility (STEALTH Coating, upper part) and active targeting (lower part) (Çağdaş et al., 2014) (created with BioRender.com).

Surface modifications are feasible in a variety of manners, as shown in Figure 15. The simplest coupling of ligands can take place via electrostatic interactions in the case of ionic ligands. The preparation of a ligand-phospholipid conjugate (pre-formation) and its incorporation into the liposomes can be achieved by integration into the lipid film or by post-insertion. In the latter case, liposomes and the ligand-phospholipid conjugate are incubated in an aqueous solution, resulting in the incorporation of the conjugate into the outer membrane layer. In addition to pre-formation, post-modification of liposomes is also possible, in which the anchor structures for conjugation are already present in the liposomal formulation and conjugation of the ligand takes place after extrusion of the

liposomes. Conjugation can be carried out as a classical chemical synthesis with reducing agents or as click chemistry according to Kolb, Sharpless and Finn (Kolb et al., 2001). A modification of the surface is also possible based on biotin/avidin or biotin/streptavidin affinity principles. The disadvantage here is a possible crosslinking of several biomolecules on the surface of the DDS due to more than one interacting option per ligand.

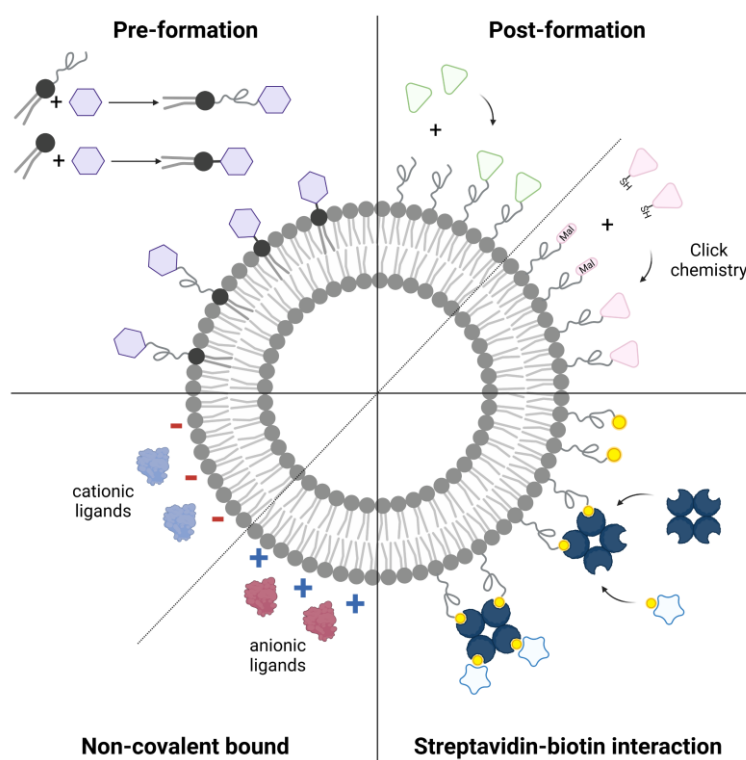


Figure 15: Overview of ligand binding options for the modification of a liposomal drug delivery system
(created with BioRender.com).

2.3.5 Established Manufacturing Procedures

The manufacturing procedure has a significant influence on the size and lamellarity of the liposomes. Therefore, various methods have been developed since their discovery. Depending on the manufacturing process, liposomes with different morphological properties can be produced. The choice of method thus depends not only on the resulting morphology of the liposomes but also on the batch size. The most common methods are summarized in Figure 16. Many of the mechanical methods can be traced back to the film method described by Bangham in 1965 (Bangham et al., 1965). Here, a dispersion of MLVs and MVVs is brought to the desired particle size by applying energy in a further production step after hydration of the thin lipid film. Possible methods for comminution

of the particles include extrusion, ultrasound, or freeze-thaw cycles (Mozafari, 2005). In the case of preparation by detergent removal or from organic solvents, prior film formation can be dispensed with.

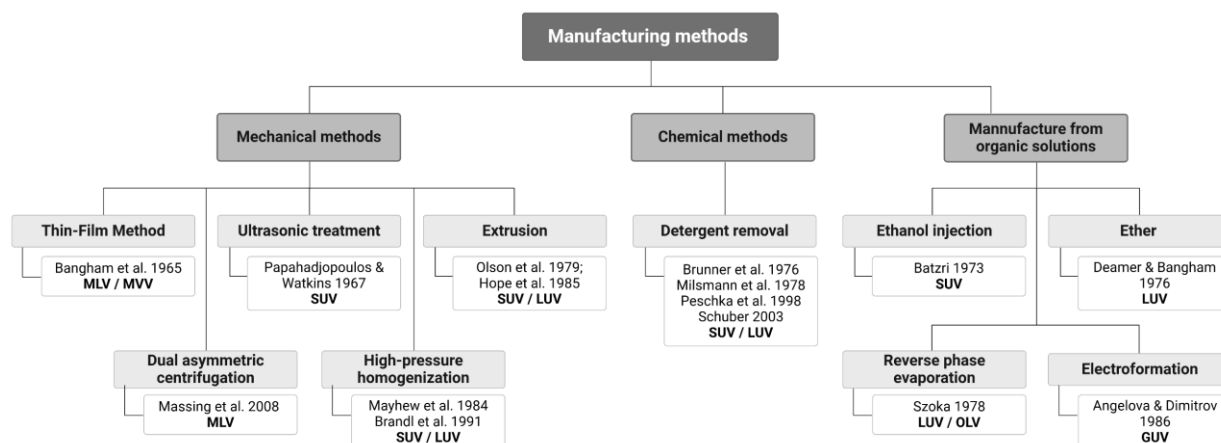


Figure 16: Overview of the most common manufacturing techniques for liposomes. The methods are categorized according to Danilo Lasic (Lasic, 1993) (created with BioRender.com).

In this thesis, the production of symmetrical liposomes, in which the composition of the two lipid layers of the bilayer is identical, was based on the thin film method with subsequent membrane extrusion. A detailed process description can be found in Chapter 3.2.1.2.1. Asymmetric liposomes, in which the composition of both layers of a bilayer is different, are produced using a centrifugation process of two perfluorocarbon nanoemulsions, which is described in more detail below.

2.3.5.1 Preparation of Asymmetric Liposomes Based on Nanoemulsions

In addition to the low encapsulation efficiency (EE), other reasons, such as the complex, wasteful and therefore cost-intensive purification of liposomes due to many process steps, lead to the further development of classic manufacturing processes. The targeted composition and finalization of the inner and outer lipid layer are of enormous interest, as this enables the targeted encapsulation of active pharmaceutical ingredients in the interior on the one hand and protection against the reactions of the immune system and premature release of the liposomal content on the other. On top of this, increased uptake into targeted cells like cancer cells could be achieved using exclusive target structures. This targeted functionalization concerning several aspects can only be achieved using asymmetric bilayers. The first development approaches go back to the 1970s with Träuble and Grell (Träuble and Grell, 1971), who produced liposomes from emulsions in a

benzene phase for the first time and thus provided the basis for Pautot and colleagues (Pautot et al., 2003) for the formation of asymmetric bilayers.

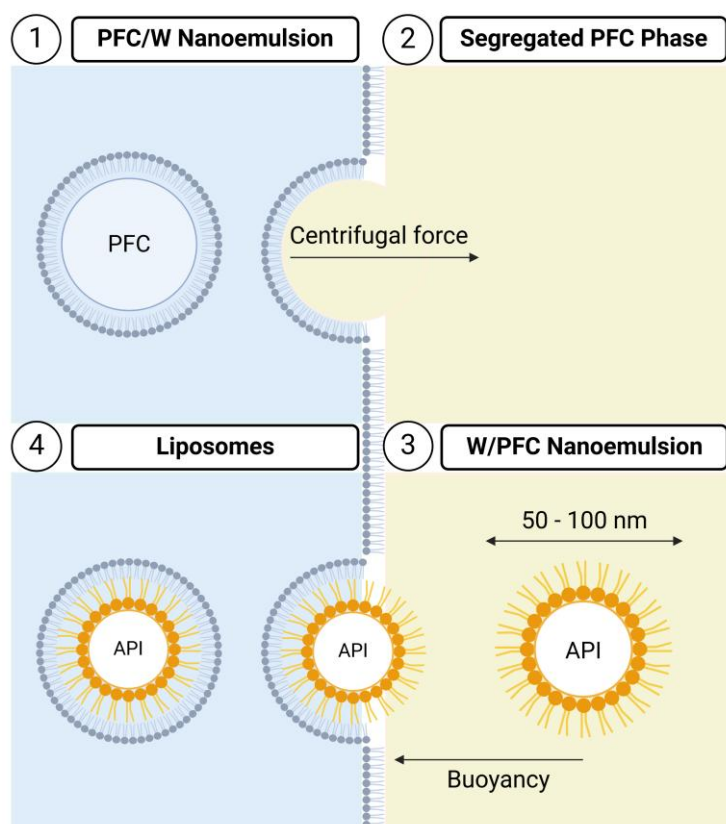


Figure 17: Schematic representation of the single steps of the centrifugation process for the preparation of asymmetric liposomes using two inverse nanoemulsions (created with BioRender.com).

Figure 17 illustrates an adapted process for the production of asymmetric liposomes by centrifugation based on two inverse perfluorocarbon nanoemulsions. In the batch process, a water-in-perfluorocarbon (W/PFC) nanoemulsion is coated with a perfluorocarbon-in-water (PFC/W) nanoemulsion. The centrifugal forces cause sedimentation of the PFC droplets from the upper nanoemulsion due to their density, which is twice that of water for the PFC used. Phospholipids, which stabilize the PFC droplets as a monolayer, are released at the interface and form a monolayer. The headgroups of the phospholipids are oriented toward the upper water phase (Figure 17 Step 1 and 2). At the same time, water droplets are lifted from the lower W/PFC nanoemulsion. The water droplets are also stabilized with a monolayer of phospholipids. The buoyancy of these droplets is also caused by the aforementioned difference in density. During the phase transfer of the water droplets, a second phospholipid layer is formed by phospholipids at the phase boundary (Figure 17 Step 3 and 4).

2.4 Glioma

2.4.1 Epidemiology and Classification

Glioblastoma is the most common form of primary CNS malignancy in adults. It was first described by the German pathologist Dr. Rudolf Virchow (Virchow, 1865). Glioblastoma is considered a rare tumor with an incidence of less than 5 cases (e.g. 3.26 cases in the USA) per 100,000 people (Ostrom et al., 2022). The incidence is currently rising due to the aging population and environmental pollution, but also due to improved diagnostics. Glioblastoma currently accounts for around 14.2 % of all brain and CNS tumors, but as much as 50.1 % of primary malignant brain tumors (Ostrom et al., 2022). The incidence increases with age, with the highest rate found in 75- to 84-year-olds. According to CBTRUS (Central Brain Tumor Registry of the United States), men are 1.6 times more likely to be affected than women. Despite all the advances in diagnostics and therapy, the 5-year survival rate is around 5 %, depending on patient characteristics and tumor histology. Due to the tumor's extremely high tendency to recur, the median survival after a glioblastoma diagnosis is only 8 months (Ostrom et al., 2022).

The classification and grading of gliomas by the WHO was first presented in 1979 by Zülch et al. The current 5th version dates from 2021, in which molecular data was largely implemented (Zülch, 1979). Molecular changes in diagnostics were already introduced in the previous version from 2016. According to the current classification (WHO CNS5), gliomas, glioneuronal and neural tumors form group 1 of tumors. Glioblastoma is graded as Isocitrate dehydrogenase (*IDH*) wild-type grade 4. Within the classification, diffuse gliomas are divided into those that occur mainly in adults ("adult-type") and those that occur in children ("pediatric-type"). Adult-type diffuse gliomas are divided into 3 categories: 1) astrocytoma with *IDH* mutation, 2) oligodendroglioma with *IDH* mutation and 3) glioblastoma *IDH* wild-type; where wild-type means that there is no *IDH* mutation. Glioblastoma *IDH* wild-type CNS WHO grade 4 typically shows necrosis and/or microvascular proliferation, which makes efficient therapy difficult (Louis et al., 2021).

2.4.2 Diagnosis

According to Ohgaki et al., the average age at diagnosis for a primary glioblastoma is 62 years (Ohgaki et al., 2004). The average time from the appearance of the first symptoms to the actual diagnosis is around 6.3 months. For a secondary glioblastoma derived from previously lower-grade gliomas the average age at diagnosis is barely 45 years. If one considers the progression of low-grade gliomas or anaplastic gliomas to a grade 4 glioblastoma, the average time for this is approximately 2 to 5 years (Ohgaki et al., 2004).

Although the symptoms progress rapidly, they are also very varied and often non-specific. Symptoms range from focal neural deficits (40 – 60 %) to headaches (30 – 50 %) and seizures (20 – 40 %) (Hanif et al., 2017). Due to lesions of the brain tissue surrounding the tumor, it becomes necrotic and thus non-functional. Depending on the location of the tumor, the auditory and optic nerves may also be impaired, for example, if the tumor is located in the temporal lobe.

2.4.3 Therapy

The treatment of glioblastoma is considerably more difficult and challenging compared to extracranial tumors due to various aspects such as the presence of the blood-brain barrier (Abbott et al., 2006, 2010), the unique tumor phenotype (Kesarwani et al., 2019; Wakimoto et al., 2012) or the high aggressiveness of the tumor itself (Soroceanu et al., 2013). A complete "cure" for glioblastoma is therefore almost impossible, which is why any therapeutic approach must be considered palliative (Urbańska et al., 2014). Nevertheless, a wide variety of therapies are available to patients. Resection followed by combined radio-chemotherapy is the treatment of choice according to the AWMF (Arbeitsgemeinschaft der Wissenschaftlichen Medizinischen Fachgesellschaften) S2k guideline from 2021 (Wick, 2021). Complete removal of the tumor is barely possible due to the high proliferation rate and the enormous infiltration into the surrounding tissue (Stupp et al., 2005).

The drug temozolomide, belonging to the group of alkylating antineoplastic agents, is the chemotherapeutic agent of choice for the treatment of glioblastoma (Stupp et al., 2005). Temozolomide has a high bioavailability of almost 100 %, with around 20 – 30 % being

able to penetrate the CNS (Diez et al., 2010). The standard dose is 75 mg/m² body surface area per day for 6 weeks with simultaneous adjuvant radiotherapy with 50 – 60 Gray. In addition to the aforementioned beneficial properties of the active substance, it also entails certain problems. For instance, temozolomide has a noticeably short plasma half-life of around 1.8 hours, requiring administration in high doses over a longer period (Amarandi et al., 2022). Furthermore, a prominent level of resistance to temozolomide has been observed in recurrent tumors (Oliva et al., 2010).

As an alternative to the alkylating antineoplastic agent temozolomide, monoclonal antibodies against the vascular endothelial growth factor (VEGF) are available, e.g. bevacizumab (Urbańska et al., 2014). It serves to inhibit tumor-associated angiogenesis and damage the tumor's vessels. As no clear benefit for prolonging overall survival has been demonstrated to date, the monoclonal antibody is sometimes not included in the standard therapy according to the AMWF S2k guideline. More recent therapeutic approaches include so-called “tumor therapy fields” (TTF), in which low-intensity alternating electromagnetic fields can be administered continuously but non-invasively by attaching ceramic gel pads to the skull (Fabian et al., 2019; Lassman et al., 2020). A disruption of the spindle apparatus during cell division is to be induced locally to trigger tumor cell apoptosis. Combined treatment of temozolomide and TTF can extend the median survival by up to 4.5 months (Fabian et al., 2019).

2.5 Blood-Brain Barrier

2.5.1 Structure and Physiological Role

The blood-brain barrier (BBB) represents the interface between the vascular system and the brain (Wong et al., 2013). It is a complex, dynamic system involving biomechanical as well as biochemical factors that separate the vasculature and the brain (Wong et al., 2013). It should therefore be considered a specialized regulatory interface rather than an absolute barrier (Hajal et al., 2021). The BBB prevents the entry of neurotoxic plasma components, blood cells or pathogens into the brain and also regulates the transport of molecules into and out of the CNS, thereby maintaining a tightly controlled chemical composition of the neuronal milieu (Sweeney et al., 2019). The presence of efflux pumps enhances the barrier properties of the BBB by transporting undesired substances from the brain into the systemic circulation (Pulgar, 2019). Selective permeability remains the major obstacle to the treatment of many CNS diseases (Wong et al., 2013) and therefore poses an enormous challenge for drug delivery into the brain (Pulgar, 2019). At the same time, however, many CNS diseases are also associated with a disruption of the BBB, which in turn leads to a change in permeability, modulation of the transport of immune cells, or the spread of pathogens into the brain (Wong et al., 2013). The FDA (Food and Drug Administration) has only approved a few biologics for the treatment of brain diseases. They all have in common a certain inability to cross the BBB (Pardridge, 2017). Even small molecules with a molecular weight of less than 400 Da have difficulty passing the BBB (Pardridge, 2017). There are only a few known exceptions, such as alcohol or caffeine, which can pass through the BBB. A variety of strategies to overcome the BBB have already been investigated and reported. The modulation of the BBB by chemical or physical stimuli to increase permeability (Obermeier et al., 2013) or a possible change of the administration route to intranasal or local administration (Bruinsmann et al., 2019; Chung et al., 2020; Saka et al., 2019) are two strategies to be mentioned here. However, the development of a drug delivery system (DDS) modified with ligands for targeted transport to the BBB is of paramount importance, as it preserves its integrity (Oller-Salvia et al., 2016).

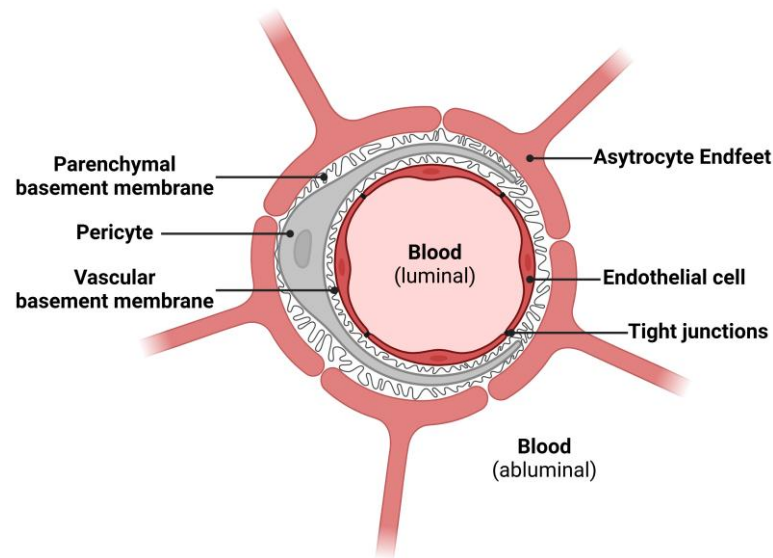


Figure 18: Schematic structure of the blood-brain barrier. The capillaries of the brain consist of a thin monolayer of microvascular endothelial cells held together by tight junctions. These junctions act as physical, metabolic and transport barriers. They are surrounded by the basement membrane (BM), a parenchymatous BM, pericytes and astrocyte endfeet (Neumaier et al., 2021)

(created with BioRender.com).

The capillary network of the human brain covers a total length of approximately 600 km and has a surface area of 15 – 25 m² (Pulgar, 2019; Wong et al., 2013). In this context, the BBB plays a central role. As illustrated in Figure 18, it consists of a thin monolayer of brain microvascular endothelial cells (BMECs), which cover the wall of all brain capillaries and are in close contact with other cells of the neurovascular unit (NU). These primarily include pericytes and astrocytes (Neumaier et al., 2021). Pericytes are discontinuously distributed along the capillary walls and thus surround the BMECs up to ~ 30 %. Hence, they control the capillary diameters and regulate cerebral blood flow (Neumaier et al., 2021; Trost et al., 2016). The endfeet of the astrocytes almost completely (~ 90 %) envelop the capillaries' abluminal side, reinforcing the integrity and tightness of the BBB (Abbott et al., 2010; Neumaier et al., 2021). The inner (vascular) and outer (parenchymal) basement membrane (BM) provide contact points for cell anchoring and thus enable structural support (Neumaier et al. 2021). Both basement membranes consist mainly of proteins of the extracellular matrix (ECM), such as collagen type IV, laminins, nidogen or perlecan. These are secreted by the BMECs or pericytes on the part of the vascular BM or the astrocytes on the part of the parenchymal BM (Kadry et al., 2020; Neumaier et al., 2021). The basement membrane also serves as an anchor for numerous signaling processes. It acts as an additional barrier for transporting substances between the brain and the systemic vascular system (Xu et al., 2019).

In contrast to most peripheral endothelial cells, the BMECs of the BBB lack fenestration (Neumaier et al., 2021). They form close connections with each other through so-called adherens junctions (AJ) and tight junctions (TJ), which seal the intracellular gap and thus severely restrict the paracellular permeability of the endothelium (Figure 19) (Neumaier et al., 2021). Tight junctions (TJs) are dynamic complexes that are formed by the interaction of integral transmembrane proteins (e.g. occludin or claudin) from the BMECs and are anchored to the actin cytoskeleton by membrane-associated cytoplasmic scaffolding proteins (Neumaier et al., 2021). The formation of TJs leads to a physical barrier with a high transendothelial electrical resistance (TEER) of more than $1000 \Omega \times \text{cm}^2$. It exhibits a very low permeability for small polar substances such as sucrose (Neumaier et al., 2021).

2.5.2 Drug Delivery

The concept of "drug delivery" refers to the method or process of administering active pharmaceutical ingredients (API) to enable an effect in humans specifically at the site of action. The various designs of the used DDS can influence the absorption, distribution, metabolism and also excretion (ADME) of an API to achieve the desired therapeutic effects while minimizing side effects (Danhier et al., 2010). The extensive developments of DDS for this purpose include nano- and microparticles as well as transdermal patches, inhalers, implants with drug reservoirs and antibody-drug conjugates (Torchilin, 2010). DDSs are being intensively researched and continuously developed to improve the pharmacokinetics and pharmacodynamics of the API and to enable their transport to the target site (Danhier et al., 2010). Over the past ten years, pharmaceutical research and clinical practice have grown to rely on nanoparticulate pharmaceutical carriers in particular (Torchilin, 2010). Targeted drug delivery, improved solubility, controllable activation and new routes of administration are the top priorities for further development.

The majority of APIs currently available for tumor therapy are extremely toxic and distributed non-specifically in the whole body when administered directly. Given the fact that they are almost equally distributed between tumor cells and healthy tissue in their free form during systemic administration, this leads to considerable damage to healthy tissue and thus restricts clinical application (Alonso and Garcia-Fuentes, 2014). The success of cancer treatment depends primarily on the ability of the therapy to shrink or remove

the tumor without attacking healthy tissue, thereby prolonging survival and improving patient quality of life (Dropcho, 2011; Plenderleith, 1990). Therefore, the encapsulation of chemotherapeutic agents in liposomal nanocarriers has clear advantages as it can limit the uptake of the API into healthy tissue, thereby improving the therapeutic index (Figure 13, Chapter 2.3.3) (Allen et al., 2005).

2.5.2.1 Active and Passive Targeting

The targeting of nanocarriers to the tumor is always a combination of "active" and "passive", as the concept of active targeting cannot be separated from passive delivery to the tumor tissue (Alonso and Garcia-Fuentes, 2014). The various approaches to drug delivery, including passive targeting based on the EPR effect and active targeting, are discussed in more detail below.

2.5.2.1.1 Passive Targeting and the EPR-Effect

Passive targeting, which is mediated by the EPR effect, is based on the assumption of the long-lasting presence of the pharmaceutical carrier in the blood and its accumulation at pathological sites with damaged and leaky vessels, as is the case with tumors, infarcts or inflammation (Torchilin, 2010). The aforementioned EPR effect was first described by Matsumura and Maeda in the late 1980s and early 2000s respectively (Maeda et al., 2001, 2009; Matsumura and Maeda, 1986). Structural changes in vascular pathophysiology provide the opportunity for long-circulating particulate carrier systems to accumulate at the site of action. Since tumor blood vessels are generally characterized by abnormalities such as a high proportion of proliferating endothelial cells, a lack of pericytes and an aberrant basement membrane formation, increased vascular permeability occurs (Danhier et al., 2010). Particles, primarily nanocarriers in the size range of 20 – 200 nm, can thus extravasate and accumulate in the tumor tissue (Danhier et al., 2010), as the pores in the vessel walls, the so-called fenestration, have a size of 10 – 1000 nm (Torchilin, 2010).

2.5.2.1.2 Active Targeting

Active targeting is based on the attachment of specific ligands to the surface of a pharmaceutical carrier system in order to recognize and bind pathological cells, with the aim of increasing cellular internalization (Danhier et al., 2010; Torchilin, 2010). The criterion

for selecting a target structure is its expression in different tissues. For example, it should be overexpressed in tumor tissue and not expressed in normal cells (Danhier et al., 2010).

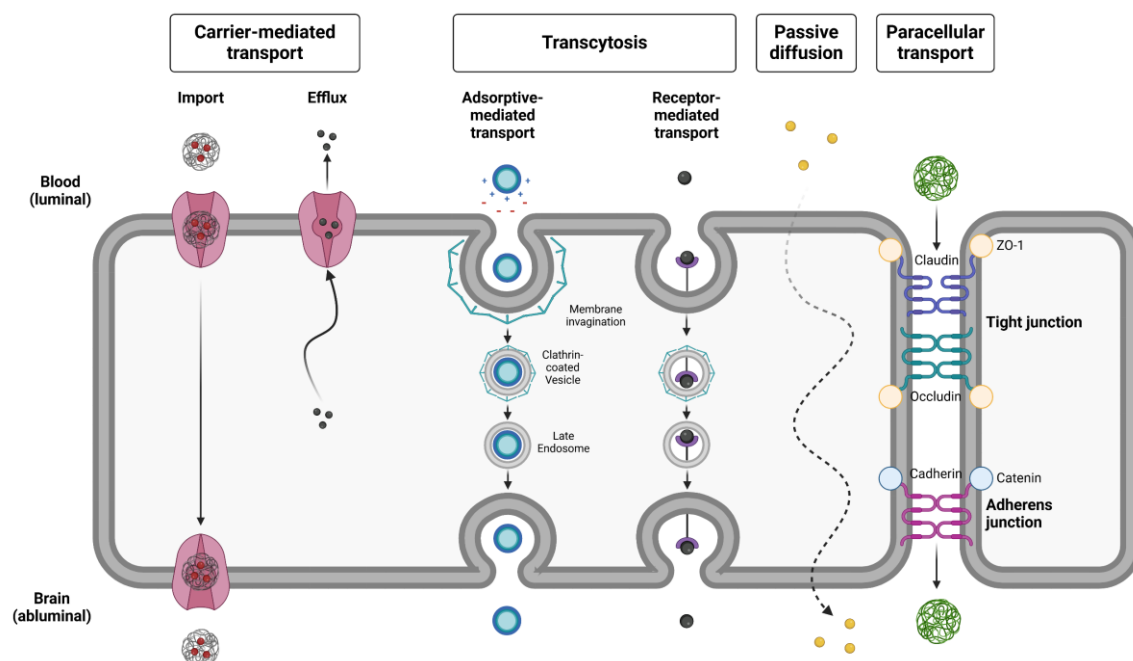


Figure 19: Overview of the different methods of transport through the BBB. Carrier-mediated transport (CMT), transcytosis differentiated into adsorptive-mediated transport (AMT) and receptor-mediated transport (RMT) as well as passive diffusion and paracellular transport (Hersh et al., 2022; Neumaier et al., 2021) (created with BioRender.com).

It is of utmost importance to familiarize oneself with the cellular uptake mechanisms before selecting a suitable target and a corresponding ligand for the transport of an API through the BBB. Cellular uptake can be roughly divided into carrier-mediated transport (CMT) and transcytosis by receptor-mediated transport (RMT) (Figure 19) (Pardridge, 2017). The transporters responsible for CMT are summarized in Table 4. They are either members of the solute carrier (SLC) or the ATP-binding cassette (ABC) transporter family. It should be noted that the influx of nutrients from the blood into the brain is accomplished by the transporters of the SLC family, whereas the efflux from the brain into the blood is accomplished by members of the ABC family. The transport is generally size- and also stereoselective (Lajoie and Shusta, 2015).

The receptors for the RMT occurring at the BBB are also summarized in Table 4. The RMT systems at the BBB can mediate bidirectional transport as well as only the influx in the direction of the blood into the brain or the efflux in the opposite direction. The insulin

receptor (IR) expressed at the BBB mediates the influx of insulin into the brain (Duffy et al., 1988). It should be noted that insulin is present in the brain, although the peptide is not synthesized within the brain due to the absence of the corresponding mRNA (Kojima et al., 2004). The human IR is therefore considered to be the leading target structure as a strategy for overcoming the BBB.

In the case of RMT, cellular internalization takes place in 4 essential steps (Lajoie and Shusta, 2015): 1) the transmembrane receptor at the apical membrane is bound by the circulating ligand, 2) the formation of an intracellular vesicle, which is formed by membrane insertion during endocytosis and contains the receptor-ligand complex, 3) the vesicular and endolysosomal trafficking machinery directs the newly formed intracellular vesicle to its final destination and 4) the vesicle moves to the plasma membrane on the brain side, where the contents of the vesicle are released into the brain parenchyma by exocytosis. This vesicle-based mechanism enables the transport of a large number of endogenous proteins, highlighting RMT is an attractive method for the transport of biologicals into the brain (Descamps et al., 1996). It should be added that in addition to the receptors at the BBB, receptors at the blood-brain-tumor barrier (BBTB), such as the integrin receptor α_v , are also conceivable targets. In high-grade glioma, the function of the BBB is often impaired and BBTB develops in the course of progressive tumor growth and the associated neovascularization (Belykh et al., 2020; Groothuis, 2000).

Table 4: CMT and RMT at BBB (Pardridge, 2017).

Carrier-mediated transporters		
Member of SLC family		Endogenous substrate
GLUT1	= glucose transporter 1	glucose and certain other hexoses
MCT1	= monocarboxylic acid transporter	lactate, pyruvate and ketone bodies
LAT1	= large neutral amino acid transporter	phenylalanine and over 10 other neutral amino acids
CAT1	= cationic amino acid transporter	arginine, lysine and ornithine
CTL1	= choline transporter as choline transporter-like protein-1	choline
CNT2	= sodium-dependent purine nucleoside transporter	adenosine, guanosine, inosine
NBT	= nucleobase transporter	purine bases such as adenine

Receptor-mediated transporters	
IR	Insulin receptor
TfR1	Type 1 transferrin receptor
IGFR	Insulin-like growth factor receptor
LEPR	Leptin receptor
LDLR	Low-density lipoprotein receptor
FcRn	Neonatal Fc receptor
LRP1	LDLR related protein-1

In addition to the commonly monoclonal antibodies (mAbs) or antibody fragments as receptor binding partners, non-antibody ligands such as peptides, proteins or small molecules are also used as ligands - regardless of whether for CMT or RMT (Figure 14 in Chapter 2.3.4) (Danhier et al., 2010).

2.5.2.1.3 Selected Targets

2.5.2.1.3.1 GLUT1

Glucose is the most important monosaccharide in carbohydrate metabolism and serves as the primary energy source in the brain. Since neurons cannot synthesize or store glucose themselves, the transport of glucose across the BBB is essential (McEwen and Reagan, 2004). It is worth mentioning that the glucose consumption of the brain alone accounts for about 30 % of the body's total consumption. The glucose transporter 1 (GLUT1) as a target candidate to overcome the BBB is particularly noteworthy as it is overexpressed on the surface of the BBB (Uchida et al., 2011), as each brain capillary cell expresses about 6×10^6 GLUT1 molecules (Zhang et al., 2021). The CMT itself has a high transport affinity and capacity, with GLUT1 being one of the most efficient transport systems in the human organism.

2.5.2.1.3.2 LRP1

The low-density lipoprotein receptor-related protein 1 receptor (LRP1) is also known as CD91 or $\alpha 2$ -macroglobulin receptor and is a multifunctional scavenger and signaling receptor of the low-density lipoprotein receptor family (Boucher and Herz, 2011; Bruno et al., 2010; Lillis et al., 2008). It binds more than 30 ligands extracellularly – including

apolipoprotein E, α 2-macroglobulin, receptor-associated protein (RAP), A β , proteinase inhibitors, blood coagulation factors, prion protein or aprotinin (Deane et al., 2004b, 2004a; Demeule et al., 2008; Lillis et al., 2008). It is a large single-pass transmembrane receptor with a molecular weight of ~ 600 kDa, which is highly abundant in the CNS including endothelial cells (Spuch et al., 2012). As an endocytotic receptor, it is involved in many cellular processes such as signal transduction and lipid homeostasis (Mao et al., 2017). The LRP1 functions in a dual role (Spuch et al., 2012): 1) as a receptor that intercalates its ligands and becomes like its fast, endocytotic cell transporter and 2) as a transmembrane cell signaling receptor (Pflanzner et al., 2011). Among the ligands mentioned, apolipoprotein E (ApoE) should be emphasized, which, along with ApoB, is an important protein component of lipoprotein particles and thus mediates the interaction with the lipoprotein receptors. The uptake of cholesterol from the bloodstream into nerve cells is mediated by ApoE via LRP1 receptors on the cell surface. This demonstrates that apolipoprotein already plays a central role in brain physiology and that ApoE3, as a widespread isoform, is, therefore, a suitable ligand candidate (Spuch et al., 2012). The tertiary structure of the receptor (LRP1) and the ligand selected for it (ApoE3) are shown in Figure 20.

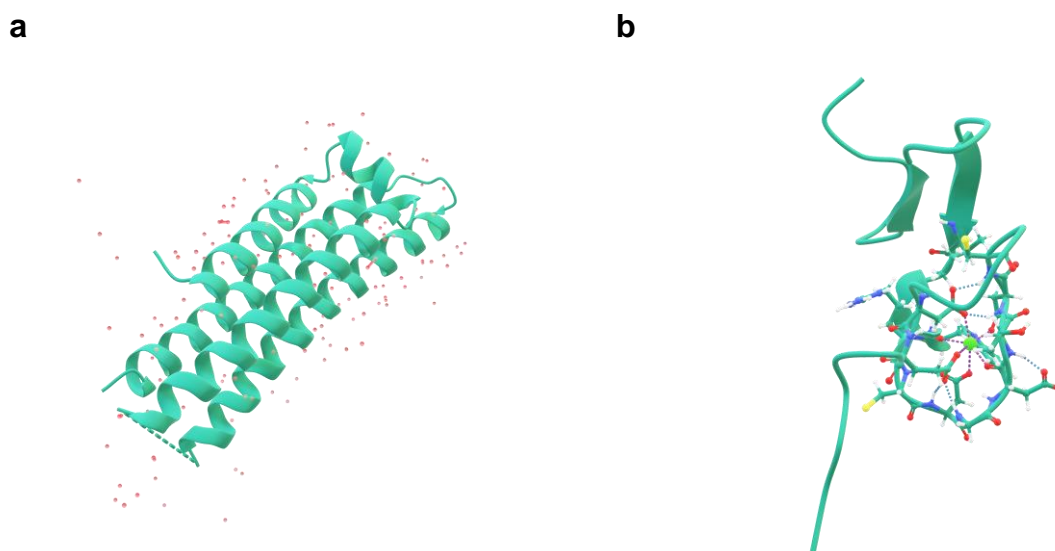


Figure 20: Overview of different protein structures. (a) Tertiary structure of Apolipoprotein E3 (Protein Data Base (PDB) code: 1NFN) and (b) low-density lipoprotein receptor-related protein 1 (LRP1) with bound ligand (PDB code: 1CR8).

2.5.2.1.3.3 Integrin $\alpha_v\beta_3$ Receptor

Extensive vascularization of a highly malignant tumor is crucial for rapid tumor growth (Lebelt et al., 2008; McNamara and Mason, 2012). In addition to angiogenesis of the tumor regions, vascularization also involves the early cooptation of normal cerebral blood vessels (Hardee and Zagzag, 2012; Jo et al., 2012). Integrins are cell surface receptors that are important components of the ECM. Their role depends on environmental factors that can either promote survival or induce apoptosis (Sheikh et al., 2021). The $\alpha_v\beta_3$ receptor from the integrin receptor family is a promising target, as it is overexpressed in the tumor tissue's actively proliferating endothelium and the tumor cells themselves (Danhier et al., 2012a). On the other hand, there is only very low expression in normal blood vessels. The $\alpha_v\beta_3$ receptor (Figure 21) binds several ECM molecules, such as fibrinogen, vitronectin or von Willebrand factor (van der Flier and Sonnenberg, 2001). They all have an RGD motif as a recognition site in common, which was first described by Pierschbacher and Ruoslahti in 1984 (Pierschbacher and Ruoslahti, 1984). This cell adhesion sequence consisting of the three amino acids arginine, glycine and aspartic acid is the smallest that can bind the $\alpha_v\beta_3$ integrin receptor.

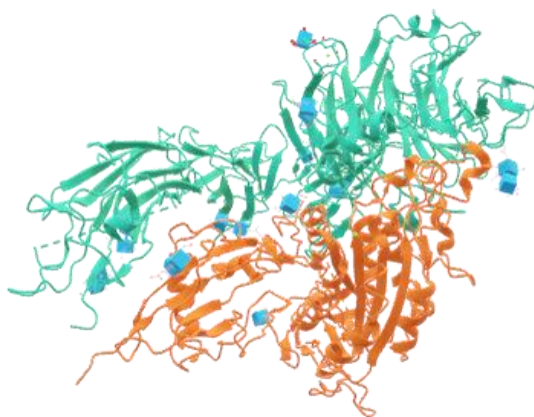


Figure 21: Tertiary protein structure of the integrin receptor. Crystal structure of the extracellular segment of integrin $\alpha_v\beta_3$ with bound ligand (PDB code: 1JV2).

2.6 Hemo- and Immunocompatibility

2.6.1 Immune- and Complement-System

Immunoprotective - also called STEALTH - coatings are successful for all nanomedicines avoiding activation of the innate immune system and rapid excretion as well as allowing long circulation of the carrier system for passive or active targeting. Despite many breakthroughs in the development of new classes of drugs and also delivery systems, no significant improvements have yet been achieved for polyethylene glycol (PEG) coatings, albeit with several obvious drawbacks: 1) accelerated elimination from the blood upon repeated injection due to the formation of anti-PEG IgM antibodies, 2) the lack of biodegradability of PEG, and 3) the impediment of cellular uptake and endosomal escape. The latter effect is also known as the "PEG dilemma" and indicates that STEALTH coating is required to avoid rapid excretion from the blood and to reach the target tissue, while PEG subsequently impedes liposomal uptake and endosomal escape of the drug into the cytosol (Zalba et al., 2022). Alternatives to PEG and modifications of PEG coatings have been preclinically tested, but despite proven benefits, there are currently no clinically available PEG alternatives.

2.6.1.1 Immune System

The human immune system is an intricate biological system made up of several organs, cells, and proteins that cooperate to defend the body against foreign "invaders" and host cells that have changed due to self-non-self-differentiation. The innate and adaptive immune systems make up its two primary subtypes (Abbas et al., 2021).

The innate immune system – as the name suggests – is already present in every human being at birth and is also referred to as non-specific immunity. It is the first line of defense against foreign invaders and consists of barriers such as the skin and mucous membranes, soluble mediators such as the complement system, membrane-bound receptors and innate immune cells like natural killer cells, innate lymphoid cells, dendritic cells and phagocytes (Vollmar et al., 2012). It is basically "preprogrammed" from birth onwards and is mainly based on pattern recognition receptors (PRRs), which frequently recognize pathogenic structures, so-called pathogen-associated molecular patterns (PAMPs). The

PRRs also detect damage-associated molecular patterns (DAMPs), which are endogenous molecules expressed and released by damaged or dying cells (Dunkelberger and Song, 2010). The innate immune system responds quickly to non-self or altered self and in a similar way each time, even with repeated exposure to the same foreign invader.

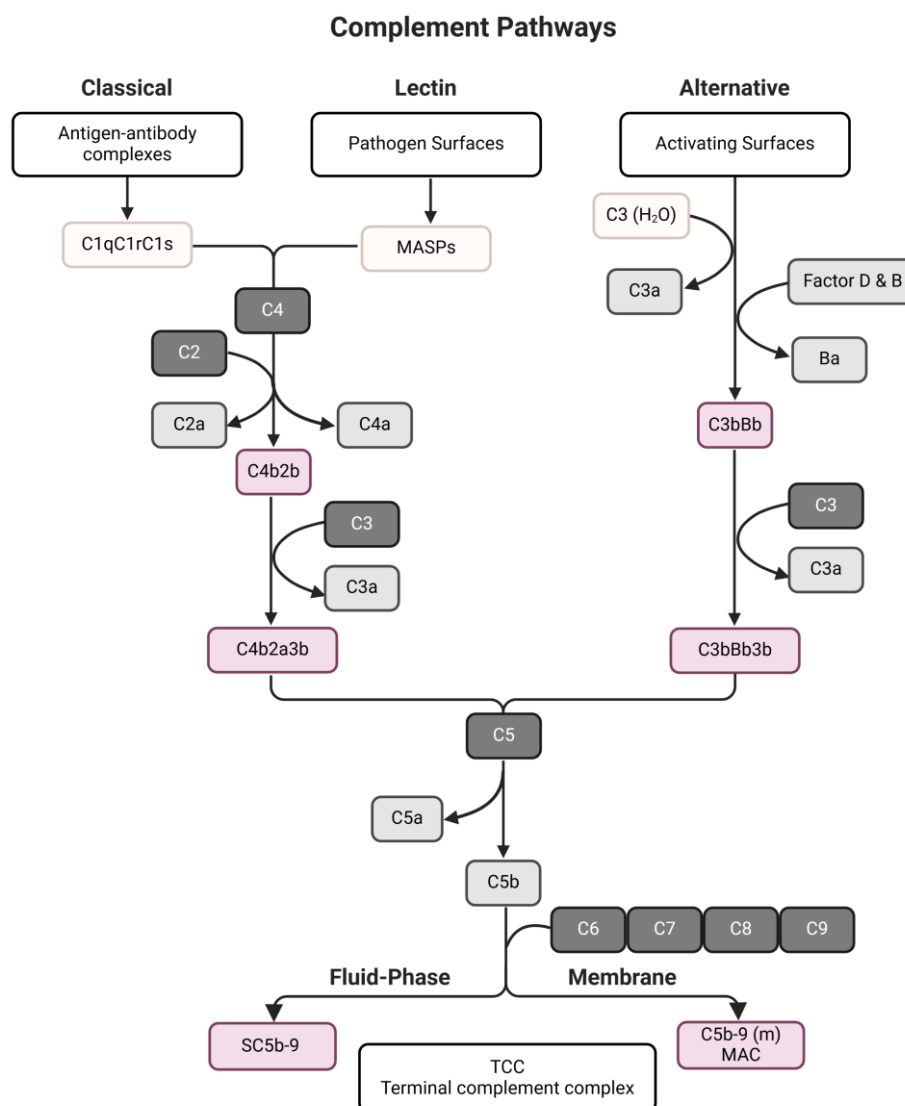
On the other hand, the body can be protected from certain invaders by specialized immune cells like T- and B-cells that are part of the adaptive immune system, also referred to as acquired immunity. It is based on antigen-specific receptors, which are "acquired" in the course of life when the body is exposed to foreign antigens. For instance, the B-cells produce specific antibodies directed against the antigens which the foreign invader expresses. After repeated exposure, adaptive immunity becomes more adept at identifying specific pathogenic structures.

Although the innate and adaptive immune systems perform distinct roles and duties, they are connected through the complement system – in order to work together to defend the body against foreign invaders.

2.6.1.2 Complement System

The complement system is a central component of innate immunity and is "active" in tissues, in plasma and also intracellularly (Merle et al., 2015). It was first discovered in the 1890s when it was shown that a heat-labile substance in human plasma "complements", i.e. supports, antibodies in the lysis of bacteria (Cavaillon et al., 2019). According to current knowledge, the complement system is not just a single substance, but rather an effective, complex and strictly regulated cascade system consisting of over 50 different plasma and cell surface proteins (Nesargikar et al., 2012; Ricklin et al., 2010). The complement system can be initiated via three pathways (Figure 22): firstly, the classical pathway (CP), secondly the lectin pathway (LP) and thirdly the alternative pathway (AP). The complement protein 3 (C3) plays a central role in all three pathways, supporting the cascade activation (Nonaka, 2014; Sahu and Lambris, 2001). Initial activation is triggered by non-self or altered-self surfaces, resulting in subsequent fusion of the three pathways in the downstream stages of the terminal pathway. As the cascade progresses, the signal is amplified and reveals the same effector molecules that are involved in the

elimination of foreign invaders through opsonization, inflammation and lysis (Abbas et al., 2021).



damaged cell membranes, can also start the classical route without the aid of antibodies. C1 then recognizes these substances.

C1 is a multiprotein complex consisting of the pattern recognition molecule C1q and two additional copies of each of the serine proteinases C1r and C1s (Ricklin et al., 2010). C1q binds to fragment crystallizable Fc regions of IgG and IgM). However, when C1q binds to clusters of antibody Fc regions, it undergoes conformational changes that promote the autocatalytic enzymatic activity of C1r. This is followed by the C1r induced cleavage and associated activation of C1s. Once C1s is activated, it proteolytically cleaves C4 into C4a and C4b and C2 into C2a and C2b. C4b and C2b form the C3 convertase C4bC2b on the surface of the pathogen. The C3 convertase in turn cleaves C3 into C3a, an inflammatory mediator, and C3b, an opsonin, and initiates the amplification and downstream effector functions of the complement system, including inflammation, opsonization, phagocytosis and lysis of target cells (Abbas et al., 2021; Murphy and Weaver, 2018).

2.6.1.2.2 Lectin Pathway

The lectin pathway of activation is shown in the center of Figure 22. It is initiated by the binding of pattern recognition molecules such as mannose-binding lectins (MBL), ficolins and collectins to microbial sugars such as mannose, F-acetylglucosamine or fructose. This binding activates mannose-binding lectin-associated serine proteinases (MASPs), which in turn cleave C4 and C2 to initiate the downstream proteolytic steps. These steps are identical to the CP of activation (Garred et al., 2016).

2.6.1.2.3 Alternative Pathway

The alternative pathway (AP) of activation is shown in the right part of Figure 22. While the activation via the CP is specific for antibodies and the activation of the LP is activated by specific sugar groups, Pillemer et al. suggested in 1950s that properdin is a specific initiator of the AP (Pillemer et al., 1954). Properdin is the only known positive regulator of complement to date (Fearon and Austen, 1975; Wirthmueller et al., 1997). In the 1970s, Lachmann et al. proposed the tickover theory, according to which the AP is activated spontaneously. It occurs through non-complementary proteases or interactions with foreign surfaces (Lachmann and Halbwachs, 1975; Lachmann and Nicol, 1973;

Nicol and Lachmann, 1973). A decade later in the 1980s, Pangburn et al. discovered that native C3 can undergo slow spontaneous thioester hydrolysis in solution and form a "C3b-like" molecule – also called C3(H₂O). After the formation of C3(H₂O) in solution by a nucleophilic attack of water molecules on the internal thioester in native C3, a conformational change occurs within the molecule without proteolytic cleavage, leading to the release of the C3a peptide (Pangburn et al., 1981; Pangburn and Müller-Eberhard, 1980). C3(H₂O) can bind factor B in solution in the presence of magnesium ions, which in turn can be cleaved by factor D into Ba and Bb. This subsequently leads to the formation of an initial liquid-phase C3 convertase, C3(H₂O)Bb, which can trigger the AP by cleaving C3 into C3a and C3b (Abbas et al., 2021; Bexborn et al., 2008; Pangburn et al., 1981). Nonetheless, there is ongoing discussion on the AP's initiation mechanism.

The currently most important theories for the activation of the AP are the following (Figure 23): 1) cleavage of C3 into C3a and C3b by non-complementary proteases (Huber-Lang et al., 2018; Johnson et al., 1976), 2) specific and non-specific contact activation of C3 at different surface interfaces leading to conformational changes within C3 to a "C3b-like" molecule, which can form an initial surface-bound C3 convertase (Andersson et al., 2002; Pangburn, 2023) and 3) spontaneous thioester hydrolysis of native C3 to C3(H₂O), again capable of forming an initial C3 convertase in the liquid phase. This C3 tickover mechanism is the most widely described AP activation mode (Abbas et al., 2021; Murphy and Weaver, 2018).

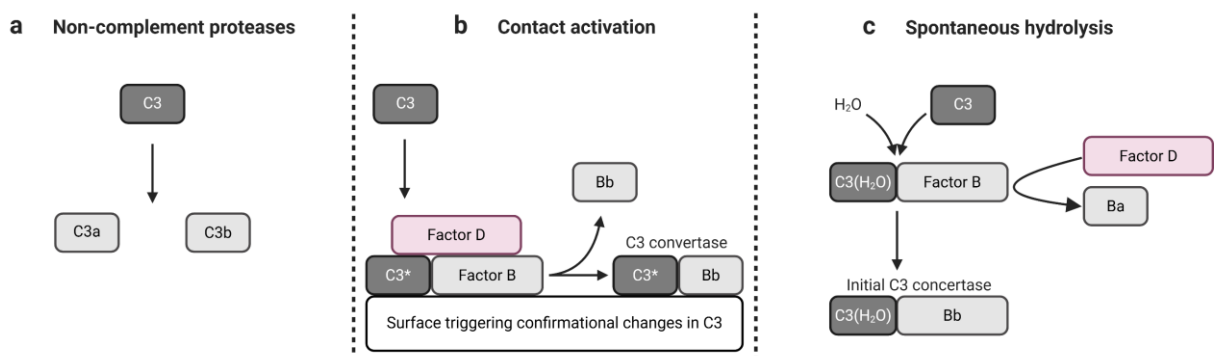


Figure 23: Overview of the current suggested mechanism of initiation of the alternative pathway. (a) tickover of AP by cleavage of C3 to C3a and C3b by non-complement proteases, (b) contact activation of C3 and (c) tickover of C3 by spontaneous hydrolysis of C3 and formation of C3(H₂O) (Abbas et al., 2021; Nilsson et al., 2007) (created with BioRender.com).

2.6.1.2.4 Terminal Pathway

The terminal pathway is shown in the lower part of Figure 22, which is in common for CP, LP and AP. A high local surface density of C3b is generated on the target surface by the C3 convertases' ongoing deposition of C3b. As a result, C3b associates with C3 convertase to promote the formation of C5 convertase (C4bC2bC3b/C3bBbC3bP). The membrane attack complex (MAC, C5b-9) or its liquid phase analog (sC5b.0) is subsequently assembled as a result of the convertase's shift in specificity from C3 to C5 (Berends et al., 2015; Pangburn and Rawal, 2002). The components of MAC, or sC5b-9, are several copies of C9 together with C5b, C5, C6, and C8. They have responsibility for the terminal pathway's downstream complement effects. Target cell lysis results from the MAC's integration into the cell membrane (Abbas et al., 2021).

Chapter 3

Materials and Methods

3.1 Materials

The following subchapters list all phospholipids (Table 5), chemicals (Table 6), buffers and solutions (Table 7), consumables (Table 8), devices (Table 9), and software (Table 10) media, reagents and antibodies for cell culture (Table 11) and cell lines (Table 12) used.

3.1.1 Phospholipids

Table 5: List of phospholipids used.

Chemicals and Reagents	Manufacturer
E80	Lipoid GmbH
DMPC	Lipoid GmbH
DPPA	Lipoid GmbH
DPPC	Lipoid GmbH
DPPG-Na	Lipoid GmbH
DOPS	Lipoid GmbH
DSPC	Lipoid GmbH
DSPE-PEG ₁₀₀₀ -RB	Biopharma PEG Scientific Inc.
DSPE-PEG ₂₀₀₀	Lipoid GmbH

DSPE-PEG ₂₀₀₀ -NH ₂	Biopharma PEG Scientific Inc.
DSPE-PEG ₅₀₀₀ -c(RGD)	Biopharma PEG Scientific Inc.
DSPE-PEG ₅₀₀₀ -Glu	Biopharma PEG Scientific Inc.
DSPE-PEG ₅₀₀₀ -Mal	Biopharma PEG Scientific Inc.
DSPE-PEG ₅₀₀₀ -NHS	Biopharma PEG Scientific Inc.
Lissamine™ Rhodamin B DHPE	Invitrogen, Fisher Scientific GmbH

3.1.2 Chemicals and Reagents

Table 6: List of chemicals and reagents used.

Chemicals and Reagents	Manufacturer
1-Propanol ≥99,5 %	Carl Roth GmbH & Co. KG
1,4-Dioxane ROTIDRY® ≥99,8 %, stabilized	Carl Roth GmbH & Co. KG
2-Iminothiolan ≥98 %	Santa Cruz Biotechnology
2-NBDG ≥98 %	Cayman Chemicals Company
4-Aminophenyl-D-glucopyranoside	Santa Cruz Biotechnology
5,5'-Dithiobis-(2-nitrobenzoic acid) ≥99 %	Santa Cruz Biotechnology
Acetic acid 100 % Ph. Eur.	Carl Roth GmbH & Co. KG
alamarBlue™ HS Cell	Thermo Fisher Scientific
Alcian Blue 8GS	Carl Roth GmbH & Co. KG
Ammonium hydrogen carbonate ≥99 %	Carl Roth GmbH & Co. KG
Ammonium thiocyanate ≥99 %	Carl Roth GmbH & Co. KG
Ampuwa®	Fresenius Kabi
ApoE3, recombinant human	enQuire™ Bio
Argon 4.6 99.99 %	BASI Schöberl GmbH & Co. KG
<i>Bacteroides Heparinase I</i>	New England Biolabs
Biophen Heparin (AT+) Kit	CoaChrom Diagnostica GmbH
BSA	PAN-Biotech GmbH
BSA	Sigma-Aldrich
C3a capture mAb Anti-C3 hybridoma clone 17.3	Innovagen AB
C3a detection mAb	in-house, University Uppsala
C5b-9 capture mAb Anti-complement component antibody (#DIA 011-01)	Bioporto Diagnostics

C5b-9 detection mAb Anti-complement component antibody (#A706)	Quidel Corporation
Cholesterol ≥ 95 %	Carl Roth GmbH & Co. KG
Cholesterol LabAssay™ Kit	Fujifilm Wako Chemicals Europe GmbH
Chloroform ≥ 99 %	Carl Roth GmbH & Co. KG
Citric acid monohydrate for analysis EMSURE®	Supelco (Sigma-Aldrich)
Complement Standard 1	in-house, University Uppsala
Cysteine hydrochloride monohydrate	Thermo Fisher Scientific
D-(+)-Sucrose	Carl Roth GmbH & Co. KG
DiD	AAT Bioquest®
Disodium hydrogen phosphate dihydrate ≥ 98 %	Carl Roth GmbH & Co. KG
DMF, 99.8 %, anhydrous	Sigma-Aldrich
EDTA tetrasodium salt dihydrate ≥ 99 %	Carl Roth GmbH & Co. KG
EDTA disodium salt dihydrate Titriplex® III	Sigma-Aldrich
Ethanol absolute analytical grade	Solveco AB
Ethanol ≥ 70 %	Carl Roth GmbH & Co. KG
Ethanol 99.5 % Ph. Eur. ultrapure	Carl Roth GmbH & Co. KG
Ethanolamine ROTIPURAN® ≥ 99.5 %	Carl Roth GmbH & Co. KG
Ferric (III)-chloride hexahydrate ≥ 98 %	Carl Roth GmbH & Co. KG
fHep-K8C lipid	Synthesized by Yuji Teramura
Fluorescamine	Thermo Fisher Scientific
Fluorescein sodium	Carl Roth GmbH & Co. KG
Glucose Assay-Kit	Sigma-Aldrich
Heparin sodium salt, ≥ 180 I.U./mg, Ph. Eur.	Carl Roth GmbH & Co. KG
Heparin sodium LEO 100 IU/KY/mL stock solution	LEO Pharma A/S
Human ApoE ELISA ^{BASIC} Kit	Mabtech AB
Hydrochloric acid 37 %	Carl Roth GmbH & Co. KG
L-Histidine ≥ 99 %	Carl Roth GmbH & Co. KG
Lipidure CM5206	NOF Corporation
Liquid nitrogen	BASI Schöberl GmbH & Co. KG
Osmosis water	Aquaphore®
PBS Tabs 1X ROTI®Fair pH 7.4 500 mL / 1,000 mL	Carl Roth GmbH & Co. KG
PBS Tabs 10X ROTI®Fair pH 7.4 1,000 mL	Carl Roth GmbH & Co. KG

PBS Tabs 1X pH 7.4 1,000 mL	Medicago Inc.
PFD	abcr GmbH
PFDC	F2 Chemicals Ltd.
PFH	F2 Chemicals Ltd.
PFOB	abcr GmbH
Phenol red	Carl Roth GmbH & Co. KG
PPHP	F2 Chemicals Ltd.
Sephadex G25 fine	Sigma-Aldrich
Silver nitrate ≥ 99 % Ph. Eur.	Carl Roth GmbH & Co. KG
Sodium chloride ≥ 99 %	Carl Roth GmbH & Co. KG
Sodium cyanoborohydride, 99.5 %	Sigma-Aldrich
Sodium dihydrogen phosphate dihydrate ≥ 98 %	Carl Roth GmbH & Co. KG
SDS 20 % solution	VWR International GmbH (Avantor®)
Sodium hydroxide ≥ 98 %	Carl Roth GmbH & Co. KG
Sodium nitrite ≥ 97 %	Carl Roth GmbH & Co. KG
Streptavidin-HRP conjugate	Cytiva
Succinic anhydride ≥ 99 %	Sigma-Aldrich
Sulfuric acid 96 %	Carl Roth GmbH & Co. KG
TAT capture mAb Thrombin-Antithrombin Complex (#TAT-EIA 380R2C)	Enzyme Research Laboratories
TAT detection mAb Thrombin-Antithrombin Complex (#TAT-EIA 330R2D)	Enzyme Research Laboratories
TCEP ≥ 98 %	Carl Roth GmbH & Co. KG
TMB ELISA Substrate	SERVA Electrophoresis GmbH
TMB BioFX One component HRP microwell substrate	SurModics Inc.
Triton X-100	Carl Roth GmbH & Co. KG
Tween® 20	VWR International GmbH (Avantor®)
Tween® 20	Sigma-Aldrich
Zymosan-activated serum, pooled	in-house, University Uppsala

3.1.3 Buffers and Solutions

Table 7: List of buffers and solutions used.

Buffers and Solutions	Concentration / Composition
Ammonium ferro thiocyanate solution	$\text{FeCl}_3 \cdot 6 \text{H}_2\text{O}$ ($c_m = 27,03 \text{ g/L}$) NH_4SCN ($c_m = 30,40 \text{ g/L}$)
Elution buffer SEC	0.25 M NH_4HCO_3 ; 7 % (v/v) 1-propanol
FACS buffer	DPBS 10X with 5 % (v/v) FBS
Freezing medium	Culturing medium with 20 % (v/v) FBS and 5 % (v/v) DMSO
Histidine-Sodium chloride buffer	10 mM; pH 7.4; 0.3 osmol/L
PBS	0.14 M NaCl; 2.7 mM KCl; 10 mM phosphate; pH 7.4
Phosphate buffer	10 mM; pH 7.4, sodium phosphates
Sucrose solution	20 % (w/v); 30 % (w/v); 40 % (w/v); 50 % (w/v); 60 % (w/v)

3.1.4 Disposables and Glass Products

Table 8: List of disposables and glass products used.

Disposables and glass products	Manufacturer
Aspiration pipette	VWR International GmbH (Avantor®)
Beaker cups, PP, Medicine, 30 mL	VWR International GmbH (Avantor®)
Beaker ROTILABO® high/low form various volumes	Carl Roth GmbH & Co. KG
Boiling pebbles Type A	Carl Roth GmbH & Co. KG
Bottle-top filters with PES membrane, 0.2 μm , 500 mL, 75 mm	Nalgene
Caps, MPCnized	in-house, University Uppsala
Cannula Sterican® 18G x 40 mm bluntc	B. Braun Melsungen AG
Cell Culture Flasks, TC-treated T-25 / T -75	VWR International GmbH (Avantor®)
Centrifugal unit VivaSpin® 2, 5000 Da MWCO	Sartorius AG
Centrifuge tubes ROTILABO® without rim 15 / 50 mL	Carl Roth GmbH & Co. KG

Centrifugal tubes 50 mL, MPC-coated	Corning GmbH
Cryogenic Vials, VWR Collection, free-standing, 1.2 mL	VWR International GmbH (Avantor®)
Cuvettes ROTILABO® Polystyrol semi-micro	Carl Roth GmbH & Co. KG
Cuvettes ROTILABO® UV-permeable semi-micro	Carl Roth GmbH & Co. KG
Cuvettes ROTILABO® solvent-resistant semi-micro / macro	Carl Roth GmbH & Co. KG
Cuvettes UV Mirco (z = 15 mm)	BRAND GmbH & Co. LG
Desalting columns Zeba™ Spin 7 kDa MWCO 75 µL / 0,5 mL	Thermo Fisher Scientific
Dialysis membrane Spectra/Por® Biotech CE 1000 Da MWCO 3.5 – 5 kDa MWCO 100 kDa MWCO	Repligen
Dialysis systems Float-A-Lyzer® G2 100 kDa MWCO 1 / 5 mL	Repligen
Dispenser tips Combitips advanced® Biopur® 1 / 10 mL	Eppendorf AG
Eppendorf Tubes® 1,5 / 2 / 5 mL	Eppendorf AG
Folded Capillary Zeta Cells DTS1070	Malvern Panalytical GmbH
Haemacytometre coverslips 0.4 mm	Carl Roth GmbH & Co. KG
Injection needles BD Microlance 3 19G 2" 1.1 x 50 mm	BD GmbH
Loops, heparinized CB Tubing 1/4 x1/16x185 cm 5/B	Medtronics Inc.
Measuring cylinders 50 / 100 / 250 / 500 / 1000 mL	Carl Roth GmbH & Co. KG
Microtitration plates ROTILABO® F-profile, 96-wells	Carl Roth GmbH & Co. KG
Multiwell cell culture plates, flat bottom, TC-treated 6 / 24 / 48 / 96-wells	VWR International GmbH (Avantor®)
MicroWell™ Plates, 96 well, Nunc-Immuno™	Thermo Fisher Scientific
Parafilm®	Amtcor
Pasteur pipettes without cotton plug, 2 mL, 230 mm, tip length: 140 mm	Carl Roth GmbH & Co. KG
Perfusor® Line Type IV Standard	B. Braun Melsungen AG

Pipette tips Low Retention Biosphere® plus 10 / 200 µL	IKA®-Werke GmbH & Co. KG
Pipette tips Finntip™ Flex™ 10 / 200 / 1000 µL	Thermo Fisher Scientific
Pipette tips Finntip™, MPC-coated 5000 µL	in-house, University Uppsala
Pipette tips Finntip™ Extended Length 10 / 200 / 1000 µL	Thermo Fisher Scientific
Pipette tips MAKRO 10 mL	Carl Roth GmbH & Co. KG
Pipette tips SafeSeal SurPhob 10 / 200 / 1000 µL	Biozym Scientific GmbH
Protein LoBind® Tubes 1,5 mL	Eppendorf AG
Reagent reservoirs 25 mL	VWR International GmbH (Avantor®)
Round bottom flask ROTILABO® 50 / 100 / 250 / 500 mL	Carl Roth GmbH & Co. KG
Serological pipette 1 / 2 / 5 / 10 / 25 mL	VWR International GmbH (Avantor®)
Silicon Tubing 2.5 x 1.0 x 4.5 mm	Saint Gobain Life Sciences
Syringe filters PVDF 30 mm 0,22 / 0,45 µm	Carl Roth GmbH & Co. KG
Syringe Injekt® with Luer-Lock fitting 20 mL	B. Braun Melsungen AG
Test tube ROTILABO® 17 mL	Carl Roth GmbH & Co. KG
Volumetric flask BLAUBRAND® class A 50 / 100 / 250 / 500 / 1000 / 2000 mL	BRAND GmbH & Co. KG
Watch glasses ROTILABO®, 100 mm	Carl Roth GmbH & Co. KG
Whatman® Polyester drain disc, Ø 25 mm	Cytiva
Whatman® Nuclepore™ Track-Etched Membranes, polycarbonate, Ø 25 mm / 47 mm 50 / 80 / 100 / 200 / 400 nm	Cytiva

3.1.5 Devices and Software

Table 9: List of devices used.

Device	Manufacturer
Analytical Balance ABT-220 5DNM	KERN & SOHN GmbH
AutoKlav 23	MELAG Medizintechnik GmbH & Co. KG
Block Heater Cole Parmer™ Stuart™	Thermo Fisher Scientific Inc.
Camera Canon EOS 7D	Canon Inc.
Chromatography Laboratory Column Vantage® L	Merck KGaA
Centrifuges 3-16 KL, 3-18 K, 3-30 K	Sigma Laborzentrifugen GmbH
Balance KB1000-2	KERN & SOHN GmbH
Desiccator	Laborbedarf Klobasa GmbH & Co. KG
Dispenser pipette Multipette® M4	Eppendorf AG
Drying cabinet Heraeus T20 250 °C 1N/PE	Heraeus Holding GmbH
Electronic Pipetting Device Accupette	ratiolab® GmbH
Environmental Shaker / Incubator ES20	BioSan
Fluorometer Cary Eclipse VARIAN	Agilent Technologies Inc.
Flow Cytometer LSR II	BD Bioscience®
Fraction Collector LKB-FRAC-100	Pharmacia (GE Healthcare)
Freeze dryer Lyovac GT2	STERIS
Hemocytometer	BRAND GmbH & Co. KG
Hematology Analyzer XP-300, automated	Sysmex Corporation
Incubator DHD AutoFlow 5510 Air Jacketed CO ₂	NuAire Inc.
LAF S1800	Weiss Technik GmbH
Lenses SIGMA 18 – 250 mm 1 – 3.5 – 6.1 Macro HSM	SIGMA Deutschland GmbH
Lipex® Extruder	Northern Lipids
Magnetic Stirrer Rotilabo MH 20	Carl Roth GmbH & Co. KG
Microfluidizer® LV1	Microfluidics (IDEX)
Microliter Syringe GASTIGHT® 1 mL	Hamilton Bonaduz AG
Microscope HF20	Helmut Hund GmbH
Multiwell-Plate Reader Tecan® Sunrise	Tecan Trading AG

Peristaltic Pump PERIMAX12	Spetec GmbH
pH Electrode senTix® 61	WTW GmbH
pH Pocket Device 340 i	WTW GmbH
Pipette Type Finnpiquette™ F2 0.1 – 10 µL 20 – 100 µL 100 – 1000 µL 1 – 10 mL	Thermo Fisher Scientific Inc.
Pipette Type Fisherbrand™ Elite™ 2 – 20 µL	Fisher Scientific GmbH
Pipette Type MICROMAN® E M100E 100 – 1000 µL	Gilson Inc.
Pipette Type IKA PETTE multi 8 10 – 100 µL 20 – 200 µL	IKA®-Werke GmbH & Co. KG
Pipette Type IKA PETTE vario 0.5 – 10 µL 10 – 100 µL 100 – 1000 µL	IKA®-Werke GmbH & Co. KG
Plate Washer BioTek ELx50	Agilent Technologies Inc.
Plate Shaker Titramax 1000	Heidolph Instruments GmbH & Co. KG
Rotary Wheel Fisherbrand™	Fisher Scientific gmbH
Rotavapor® RE 120	BÜCHI Labortechnik AG
Self-build rotor	ABNOBA GmbH
Spectrophotometer 6300-PC Double Beamcc	VWR International GmbH (Avantor®)
Test tube shaker RS-VA 10 Mini Shaker MS1 Vortex Genie® 2	Carl Roth GmbH & Co. KG IKA®-Werke GmbH & Co. KG Scientific Industries Inc.
Thermomixer 5436	Eppendorf SE
Thermo-Shaker PHMP-4	Grant Instruments Ltd.
Thermostat Haake DS5	Haake Technik GmbH
Ultra Turrax® T25 easy clean incl. dispersing tool S25 EC – T – C – 18	IKA®-Werke GmbH & Co. KG
Ultrasonic bath Emmi®-40HC and 30HC	EMAG AG
VACUBOY	INTEGRA BioSciences GmbH
Waterbath Memmert W350 t Unstirred	Memmert GmbH & Co. KG
ZetaSizer ZS90	Malvern Panalytical

Table 10: List of software used.

Software	Supplier
Autodesk Inventor 2017	Autodesk GmbH
BD FlowJo Version 10.9.0	BD Bioscience
Cary Eclipse Simple Reads Version 1.1 (132)	Agilent Technologies Inc.
ChemSketch Version 2022.2.3	Advanced Chemistry Development Inc.
GraphPad Prism 10	GraphPad Software Inc.
UV-Vis Analyst Version 5.44	PROM Vision
Maghellan™ Version 6.6	Tecan Trading AG
Mendeley Reference Manager Version 2.88.0	Mendeley Ltd.
Microsoft Office 365 Apps for Business	Microsoft
RdrOleShell for Tecan Reader Version V 4.50	Tecan Trading AG
ZetaSizer Software Version 7.13	Malvern Panalytical

3.1.6 Cell Culture

3.1.6.1 Media, Solutions and Antibodies

Table 11: List of media, solutions and antibodies for the cell culture used.

Media, solutions and antibodies	Manufacturer
5-HT ₇ antibody (AA 405-433)	antibodies-online GmbH
Accutase®	PAN-Biotech GmbH
BD Pharmingen™ Purified Rat Anti-Mouse CD16/CD32 [Ab93]	BD Biosciences Inc.
BD Pharmingen™ Purified Mouse Anti-Rat CD32 [D34-485]	BD Biosciences Inc.
BD Pharmingen™ Human BD Fc Block™ [Fc1]	BD Biosciences Inc.
decon®-90	Decon Laboratories Limited
DMEM high glucose; CELLPURE® sterile, with glutamine, with pyruvate	Carl Roth GmbH & Co. KG
DMEM low glucose; CELLPURE®, sterile, with stable glutamine, with pyruvate	Carl Roth GmbH & Co. KG
DMEM w/o glucose	PAN-Biotech GmbH
DPBS ROTI®Cell CELLPURE® ready-to-use, sterile, w/o Ca/Mg	Carl Roth GmbH & Co. KG

FBS Supreme	PAN-Biotech GmbH
GLUT1 antibody [EPR3915]	abcam
Integrin α 4 receptor antibody [A-11]	Santa Cruz Biotechnology
LRP1 antibody (A2MR α -2)	Santa Cruz Biotechnology
MEM NEAA	PAN-Biotech GmbH
Penicillin-Streptomycin (10000 U/mL)	PAN-Biotech GmbH
Trypsin-EDTA 10X	BioWest S.A.S
Trypan blue	Carl Roth GmbH & Co. KG

3.1.6.2 Cell Lines

Table 12: List of cell lines used.

Cell line	Cell type	Supplier
bEnd.3 (ATCC CRL-2299™)	Murine brain endothelial cells	American Type Culture Collection
F98 (ATCC CRL-2397™)	Glioblastoma cells from <i>Rattus norvegicus</i>	American Type Culture Collection
U87-MG (ATCC HTB-14™)	Human Glioblastoma cells	American Type Culture Collection

3.2 Methods

3.2.1 Preparation and Characterization of Nanoemulsions

3.2.1.1 Thin-Film Method

For the preparation of a perfluorocarbon-in-water (PFC/W) nanoemulsion, a lipid stock suspension is required to provide the emulsifiers. A 150 mM lipid stock suspension was prepared using the thin film method, whereby a thin lipid film was formed using a rotary evaporator. For this purpose, the required quantities of lipids (Table A 9.6) were weighed into a test tube and dissolved in ethanol or chloroform by using the vortexer and the ultrasonic bath. After transferring the solution to a round bottom flask, it was connected to the rotary evaporator. Oxidation of the lipids was avoided by applying a vacuum. The continuous rotation during the evaporation of the solvent allows the lipid layer to spread evenly and form a thin lipid film until the solvent has completely evaporated. Post-drying for further 30 min and subsequent storage in a desiccator ensured that no organic solvents were left in the lipid film. Rehydration of the lipid film with the respective buffer (His/NaCl or PB) was carried out with the aid of the vortexer and ultrasonic bath until the lipid film was completely resuspended. The vesicles contained in the aqueous lipid stock suspension are LUV, MLC or SUV. A schematic process of the thin film procedure is shown in Figure 24.

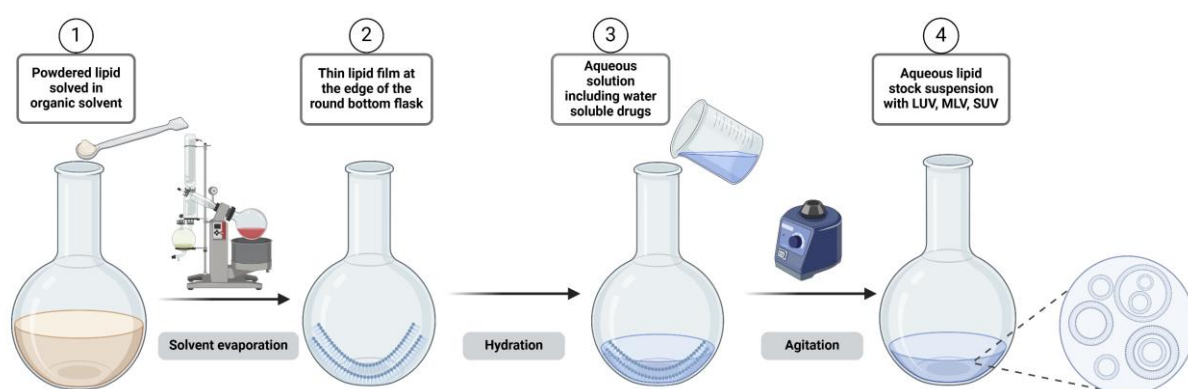


Figure 24: Schematic process for the preparation of a lipid stock suspension. (1) Weighing and dissolving of the required lipids, (2) formation of a lipid film by rotary evaporation, (3) resuspension of the lipid film with buffer and (4) resulting aqueous lipid stock suspension (created with BioRender.com).

3.2.1.2 Preparation of Nanoemulsions

For the further preparation of a PFC/W nanoemulsion, the 150 mM lipid stock suspension was diluted with the appropriate buffer to the desired lipid concentration depending on the experiment (Table A 9.8). A volume of 15 mL was always prepared for this purpose. The lipid vesicles in the buffer were premixed by mixing under high shear with the Ultra-Turrax® at 8,000 rpm for 5 min. Alternatively, the sonotrode can also be used for pre-mixing. The sonotrode was used for 20 min at 60 % and 0.5 cycle. The pre-emulsion was then prepared by adding the desired volume fraction of the respective PFC and mixed again with the UT at 15,000 rpm for 10 min. In the case of the sonotrode, homogenization was first carried out for 10 seconds at 40 % at 1 cycle and then for 20 min at 40 % at 0.5 cycle. For further processing, the volume was adjusted to 12 mL.

3.2.1.2.1 Membrane Extrusion

Membrane extrusion can be used as a method for further homogenization of the PFC/W nanoemulsion. For this purpose, the pre-emulsion was transferred to a syringe and filled into the extruder. The extrusion of liposomes was carried out using track-etched polycarbonate membranes with different pore sizes. Depending on the experimental setup, the emulsion was homogenized for various numbers of membrane passages. The extrusion was performed with different numbers of superimposed membranes and with and without cooling or ultrasound sonication. The exact test parameters are described in more detail in the corresponding chapter in the Appendix A1. The extrusion was done using argon for pressurization in the pressure range from 10 bar to 25 bar.

3.2.1.2.2 High-Pressure Homogenization

High-pressure homogenization can also be used to homogenize the PFC/W nanoemulsion further. For this purpose, immediately after preparing the pre-emulsion, it was transferred to a syringe for further processing on the Microfluidizer® LV1, which was used with a combination of two interaction chambers (F12Y 75 µm and H20Z 200 µm). The emulsion was homogenized for 6 cycles at different homogenization pressures between 250 bar and 2,000 bar, with the process housing being cooled from 1,000 bar. For the cycle number-dependent tests, the emulsions were produced at 1,000 bar with cooling of the process housing. No cooling was used in the series of tests to determine the pressure-dependent volume flow and the emulsion temperature. To prevent lipid oxidation,

all process steps of emulsion preparation using the Ultra-Turrax® and Microfluidizer® LV1 were carried out in an argon atmosphere. The stroke time was measured with a stopwatch and the product temperature at the outlet with an infrared thermometer.

3.2.1.3 Sucrose Gradient

For the analytical separation of the remaining liposomes and the separation of the PFC droplets according to their size, a sucrose gradient was performed (Figure 25). For this purpose, sucrose solutions were layered in ascending concentrations in a 15 mL centrifuge tube by placing one on top of the other up to a total volume of 8.2 mL. Subsequently, 0.8 mL of the PFC/W nanoemulsion was layered dropwise on top and centrifuged for 30 min at 4,000 x g in a swinging bucket rotor. Subsequently, 9 fractions of 1 mL each were removed stepwise from the top and transferred directly into a polystyrene disposable semi-microcuvette for subsequent characterization by dynamic light scattering. To estimate the remaining liposomes in the PFC/W nanoemulsion, fractions 1 and 2 were considered in their proportion of the derived count rate.

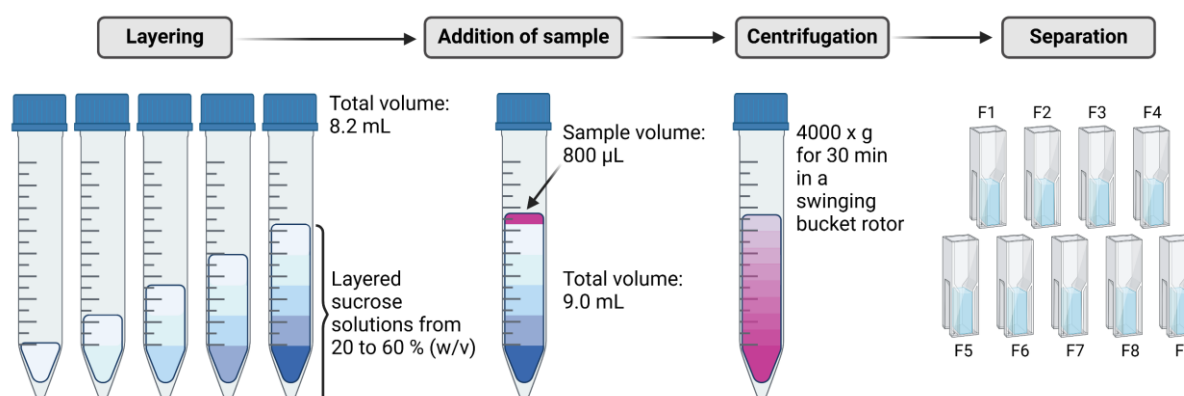


Figure 25: Schematic procedure of the density-based separation of the PFC/W nanoemulsion using the sucrose gradient. The sample is layered on top and centrifuged after layering the sucrose solutions in ascending concentration. Finally, the sample is separated into 9 fractions of 1 mL each starting from the top and characterized using DLS (created with BioRender.com).

3.2.2 Preparation and Characterization of Liposomes

3.2.2.1 Preparation of Symmetric Liposomes

The preparation of symmetrical liposomes was based on the thin film method described in Chapter 3.2.1.1. In contrast to the lipid stock suspension formulation for the PFC/W nanoemulsion, the lipids were first dissolved as a stock solution in organic solvents (Table A 9.9). The necessary volumes of the stock solutions for the various liposomal formulations were then pipetted into a round bottom flask (Table A 9.10). After lipid film formation, resuspension of the lipid film with either His/NaCl or PBS buffer to a total lipid concentration of 20 mM was done. The vesicle suspension was further processed to reduce the vesicle size and lamellarity by membrane extrusion (Figure 26). Extrusion was performed using track-etched polycarbonate membranes with different pore sizes in two steps: a) 5-fold extrusion of liposomes through a membrane with a pore size of 400 nm and b) 20-fold extrusion through a membrane with a pore size of 100 nm. The extrusion was carried out using argon for pressurization in the pressure range of 10 bar to 25 bar.

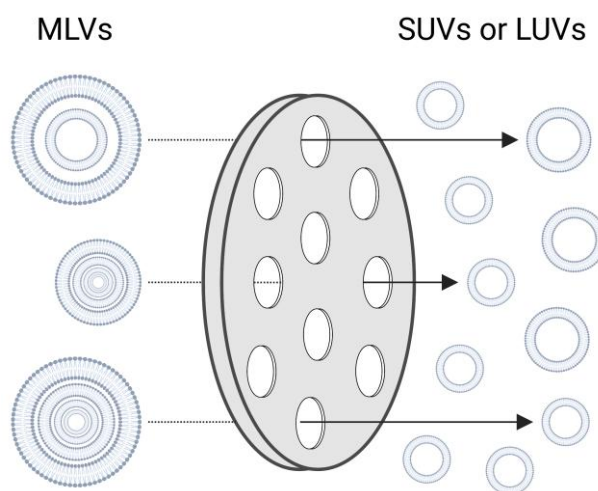


Figure 26: Extrusion of polydisperse multilamellar vesicles through a polycarbonate membrane with a precise pore size (Raemdonck et al., 2014) (created with BioRender.com).

3.2.2.2 Post-Modification of Liposomes

The following chapters describe the procedures for conjugating the individual ligands on the liposomal surface in more detail.

3.2.2.2.1 Glucose

DSPE-PEG5k-NHS was incorporated into the liposomes at 5 mol% to enable the conjugation of 4-Aminophenyl- β -D-glucopyranoside (APG) via an amide bond after liposome formation (Figure 27). This procedure is referred to below as "post-conjugation". The conjugation process was performed by incubating a 10 mg/mL APG solution in a molar ratio of 1.2:1 with the NHS-containing liposomes for 24 h at room temperature (RT) on the rotating wheel. The crude liposomal product was then dialyzed using a tube with a molecular weight cut-off (MWCO) of 100 kDa to remove unreacted APG. The dialysis medium consisted of the same buffer used for liposome preparation and was added outside the dialysis membrane in a 300-fold excess of the sample and replaced after two, four and 24 h. Finally, the liposomal formulations were sterilely filtered through a syringe filter with a pore size of 0.22 μ m.

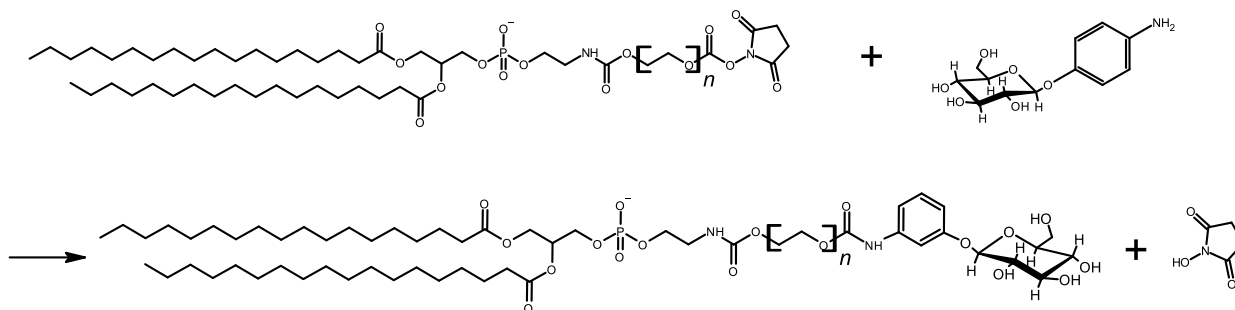


Figure 27: Conjugation reaction of 4-Amino- β -D-glucopyranoside to succinimidyl-phospholipid in aqueous solution (Zhang et al., 2015).

3.2.2.2.2 Apolipoprotein E3

For the conjugation of apolipoprotein E3 after liposome production, DSPE-PEG5k-Mal was incorporated into the liposomes at a concentration of 0.1 mol%. In the following, this process is referred to as "post-conjugation". Conjugation of apolipoprotein E3 (ApoE3) requires prior modification by the Traut reagent (2'-Iminoethiolane), which leads to thiolation of existing primary amino groups on e.g. lysine side chains (Figure 28). Thiolation was achieved by adding a 50-fold molar excess of Traut's reagent. The reagent was used at a concentration of 50 mg/mL in PBS with 5 mM EDTA. After incubation on the

rotation wheel for 2 h under an argon atmosphere, purification was performed using the Zeba™ Spin Column with an MWCO of 7 kDa.



Figure 28: Thiolation of ApoE3 using Traut's reagent.

For post-conjugation of ApoE3 (2 mg/mL in PBS) to the liposomal surface, it was first activated by reducing potential disulfide bonds by a 20-fold molar excess of tris-(2-carboxyethyl)-phosphine hydrochloride (TCEP; 5 mg/mL in PBS) and then incubated with the maleimide-functionalized liposomes at a molar ratio of 1.5:1 for 24 h at RT on the rotary wheel under argon atmosphere. Figure 29 illustrates the reaction scheme of a maleimide-functionalized phospholipid with a thiol group as in modified ApoE3.

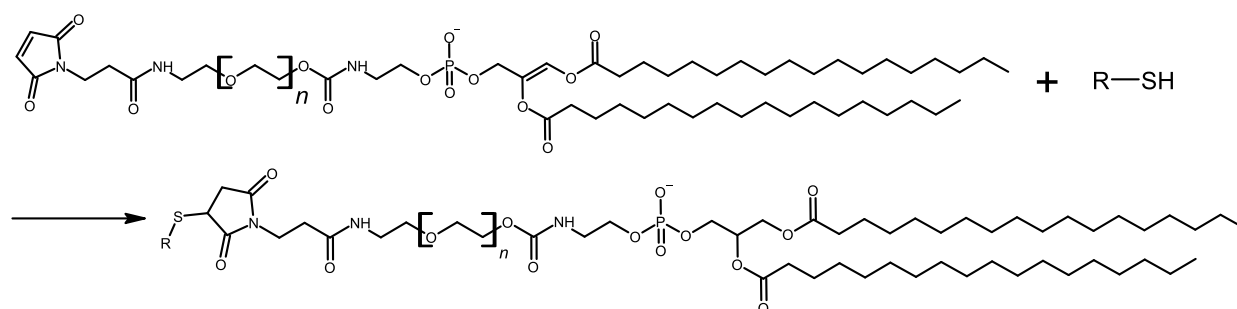


Figure 29: Conjugation reaction of ApoE3 with maleimide-modified phospholipid, which is in this case incorporated into liposomes.

After a 24-h conjugation period, unreacted ApoE3 was removed by dialyzing the liposomal suspension using a tube with a MWCO of 100 kDa. The dialysis medium was added outside the dialysis membrane in a 300-fold excess of the sample and changed after 2 h, 4 h and 24 h. The dialysis buffer consisted of the same buffer that was used to prepare the liposomes. Finally, a syringe filter with a particle size of 0.22 μm was used to sterilely filter the liposomal formulation.

3.2.2.2.3 Fragmented Heparin

In the following sections, the individual steps of heparin fragmentation, fractionation and conjugation are explained in more detail.

3.2.2.2.3.1 Fragmentation of UFH and Subsequent Analytics

Fragmentation of the unfragmented heparin (UFH) was carried out by chemical partial hydrolysis using nitrous acid (Figure 30). For this purpose, the UFH (20 mg/mL in ddH₂O) was mixed with 0.2 M sulfuric acid and 5.0 M sodium nitrite for 15 min at RT on a magnetic stirrer. Hydrolysis was completed by adding 1 M sodium hydroxide solution and adjusting the pH to 7.0. Purification for removing hydrolysis components was carried out by dialysis using a tube with a MWCO of 3.5 – 5 kDa. The dialysis medium used was 2 – 3 L of ddH₂O and replaced after 2 h, 4 h and 24 h. Finally, the samples were freeze-dried for 5 – 7 days at -30 °C. The fragmented heparin (fHep) was placed in the freezer for 24 h and immersed in liquid nitrogen before the start of freeze-drying.

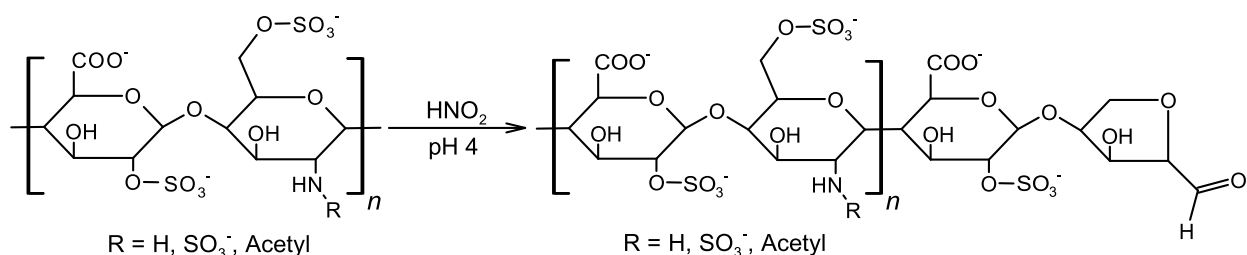


Figure 30: Fragmentation of UFH to fHep.

3.2.2.2.3.2 Fractionation of Fragmented Heparin

In order to separate the fHep into fractions with narrow molecular weight distributions (fragmented fractionated heparin, ffHep), size exclusion chromatography was performed. In the first step, Sephadex G25 fine was used, which had an average swelling volume of 5 mL per gram of substance. A column was prepared as follows: After weighing out the required amount of dry substance, this was swollen with the necessary amount of PBS with 30 % excess overnight in the refrigerator. On the following day, the suspension was slowly poured into the empty column (Vantage® L) and packed by gravity. After adjusting the liquid column and determining the flow rate via a peristaltic pump, it was loaded with 20 mL of a 7.5 mg/mL solution of fHep in PBS. The peristaltic pump was set to 100 rpm and the collection time at the fraction collector at the outlet of the column was set to 4 min. After complete loading, the sample was left on the column for

1 h to adhere and washed with a column volume of PBS. This was followed by elution with 7 % (v/v) 1-propanol in 0.25 M NH_4HCO_3 . In a further step, a part of the fraction eluted last was purified by dialysis (1,000 Da MWCO, dialysis medium ddH₂O) and was applied to a Sephadex G50 fine column for fine separation. Sephadex G50 fine has an average swelling volume of 10 mL per gram of substance and it was packed and calibrated in the same way as the Sephadex G25 fine column. After loading the column with the sample, it was left there for 1 h to adhere and then eluted directly with 7 % (v/v) 1-propanol in 0.25 M NH_4HCO_3 . The settings of the peristaltic pump and the fraction collector were identical to the previous column. To purify the columns, they were washed with two column volumes of 0.2 M sodium hydroxide solution and were set to 20 % (v/v) ethanol for storage. All eluted fractions were finally purified by dialysis (1,000 Da MWCO, dialysis medium ddH₂O) and then freeze-dried. The freeze-drying of the ffHep fractions was performed analogously to the previous chapter.

3.2.2.2.3.3 Conjugation of Fragmented Fractionated Heparin to Liposomes

The conjugation of selected fHep fractions with high activity according to the Factor Xa assay (Chapter 3.2.4.1) was also carried out using the post-conjugation method with conjugation of the aldehyde function of ffHep with a primary amine (Figure 31, lower part). For this purpose, three different phospholipids (DSPE-PEG1k-NH₂, DPPE, DOPS) containing an amine group (Figure 31, upper part) were integrated separately at 5 mol% each into the various liposomal formulations (Table A 9.10). Conjugation of the amine groups of the liposomes with the ffHep was carried out in a mass ratio of 1:3 with the addition of a 50-fold molar excess of sodium cyanoborohydride (6.4 M in PBS). It was executed for 7 days on the rotary wheel at RT in an argon atmosphere. To terminate the reaction, a 20-fold molar excess of succinic anhydride (0.5 M in 1,4-dioxane) was added., followed by a 24-h incubation at RT on the rotary wheel in an argon atmosphere. Finally, the liposomes were purified by dialysis (100 kDa, dialysis medium PBS).

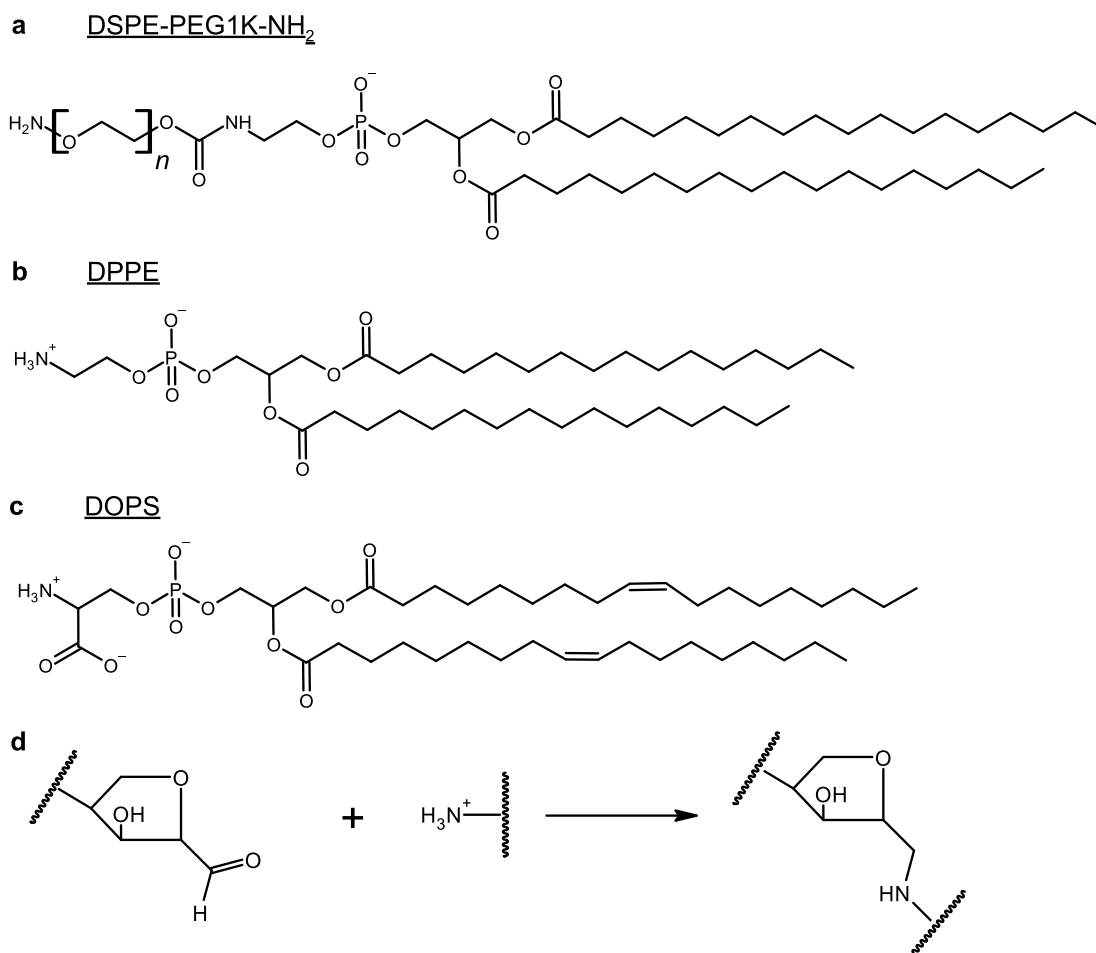


Figure 31: Conjugation of ffHep to the amine groups (d) of different phospholipids (a – c) incorporated into liposomes.

3.2.2.3 Analysis of Symmetric Liposomes

3.2.2.3.1 Ellman's Test

As the conjugation of ApoE3 is carried out by click-chemistry of a sulfhydryl group and the maleimide-functionalized liposome, the Ellmann's test is used to detect and quantify sulfhydryl groups directly after thiolation of ApoE3 and after sterile filtration of the surfaces-modified liposomes. The test was carried out using 0.1 M Tris buffer at pH 8.0. A cysteine hydrochloride stock solution with 1.5 mM in the above-mentioned buffer was prepared to prepare a calibration curve with the following diluted concentration: 0 / 0.25 / 0.5 / 0.75 / 1 / 1.25 mM. Further, 50 μ L of each concentration or the unknown sample was diluted with 150 μ L of the reaction buffer. To start the reaction, 10 μ L of 5,5'-Dithio-bis-(2-nitrobenzoic acid) (DTNB 4 mg/mL in Tris) was added. After incubation at RT for 15 min, the absorbance was measured at 412 nm using UV-permeable semi-micro cuvettes. The determination of the sulfhydryl group concentration of the unknown samples

was carried out utilizing the linearization of the calibration curve (Table A 10.6). The reaction sequence of the detection is shown in Figure 32.

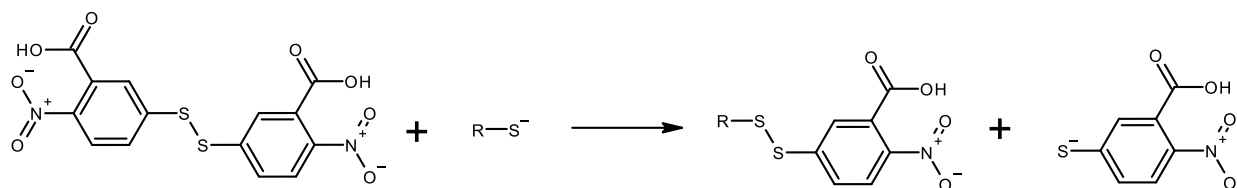


Figure 32: Reaction scheme of Ellman's reagent with thiol groups.

3.2.2.3.2 Lipid Quantification

3.2.2.3.2.1 Cholesterol Assay Kit

The quantification of cholesterol was performed in order to calculate the total lipid concentration of a liposome suspension and was carried out using the LabAssay™ Cholesterol Kit. For this purpose, a calibration curve was prepared using the cholesterol standard at 2 mg/mL. To achieve this, 120 µL of the standard solution was diluted with 120 µL of a 20 % (v/v) sodium dodecyl sulfate solution (SDS). The samples to be analyzed were also diluted 1:2 with the same SDS solution. Both the standard and the samples were heated to 95 °C for 15 min in a block heater. Subsequently, 2 / 4 / 6 / 8 / 10 or 12 µL of the standard solution were pipetted in triplicate into a 96-well plate, as well as 5 µL of the unknown sample as a triplicate. Subsequently, 100 µL of the chromogen substrate from the kit was added to each well and incubated for 5 min under light protection. The absorbance was measured at 600 nm using the microplate reader. The cholesterol concentration of the unknown samples was determined using the linear equation of the calibration curve (Figure A 10.1). The reaction sequence of the detection is shown in Figure 33.

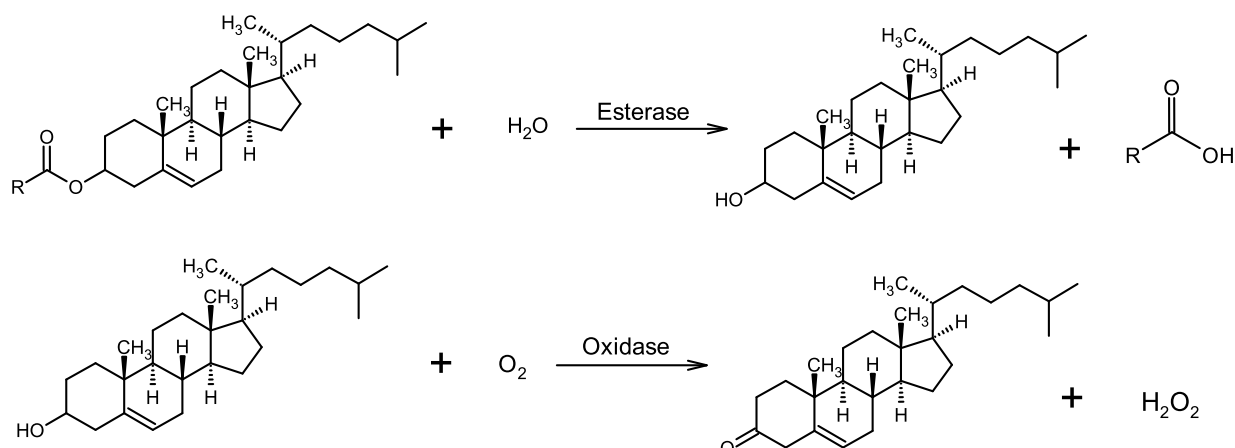
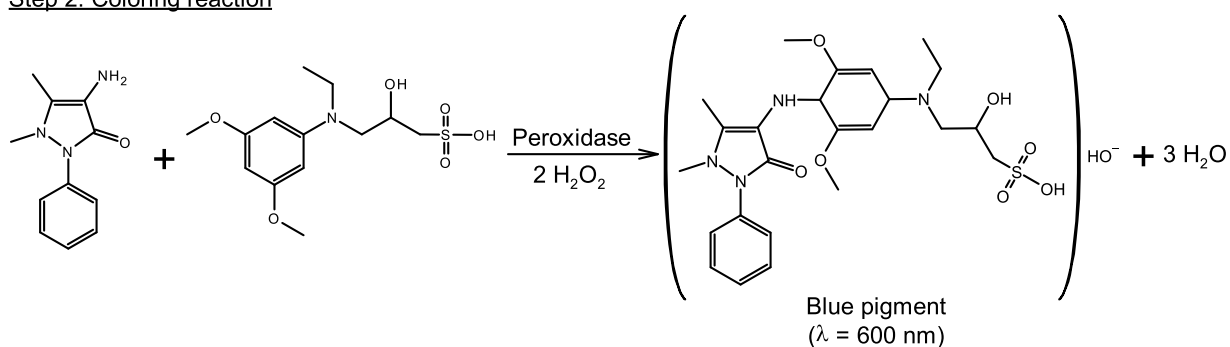
Step 1: Esterase and OxidaseStep 2: Coloring reaction

Figure 33: Detection reaction of cholesterol using the LabAssay™ Cholesterol Kit, where in the first steps enzymatic reactions take place followed by a coloring reaction.

3.2.2.3.2.2 Stewart Assay

As a further method for determining the lipid content and further calculating the total lipid content, the Stewart assay was used for quantification. This is based on the formation of a red-colored complex between a phospholipid head group and ammonium ferro thiocyanate (AF), which is extracted in chloroform. In a first step, a calibration curve was prepared from a 0.1 mg/mL stock solution of the desired phospholipid in chloroform in a concentration range from 0.005 to 0.05 mg/mL. From each standard, 2 mL was mixed with 2 mL of the AF solution containing iron(III) chloride hexahydrate ($c_m = 27.03 \text{ mg/mL}$) and ammonium thiocyanate ($c_m = 30.40 \text{ mg/mL}$) in ddH₂O. The mixture was vortexed for 1 min and incubated for 20 min at RT under light protection. After the removal of the lower chloroform phase, its absorbance was measured at 488 nm using solvent-resistant semi-micro cuvettes. The unknown samples were diluted

with chloroform in advance so that they lay within the concentration range of the calibration curve. The subsequent procedure was identical to the standards. The phospholipid concentration of the unknown samples was determined using the linear equation of the calibration curve (Figure A 10.2 and 10.3). The total lipid concentration was recalculated based on the individual molar ratio of the liposomal composition.

3.2.2.3.3 Glucose Quantification

The quantification of glucose using the Glucose (HK) Assay Kit is based on an enzymatic method whereby glucose is phosphorylated by adenosine triphosphate (ATP) in the first step. This reaction is catalyzed by the hexokinase enzyme. The resulting glucose-6-phosphate (G6P) is then oxidized to 6-phospho-gluconate. This reaction occurs in the presence of oxidized nicotinamide adenine dinucleotide (NAD) and is catalyzed by glucose-6-phosphate dehydrogenase (G6PDH). During this oxidation, an equimolar amount of NAD is reduced to NADH. The resulting increase in absorbance at 340 nm is directly proportional to the glucose concentration. The reaction process is shown in Figure 34.

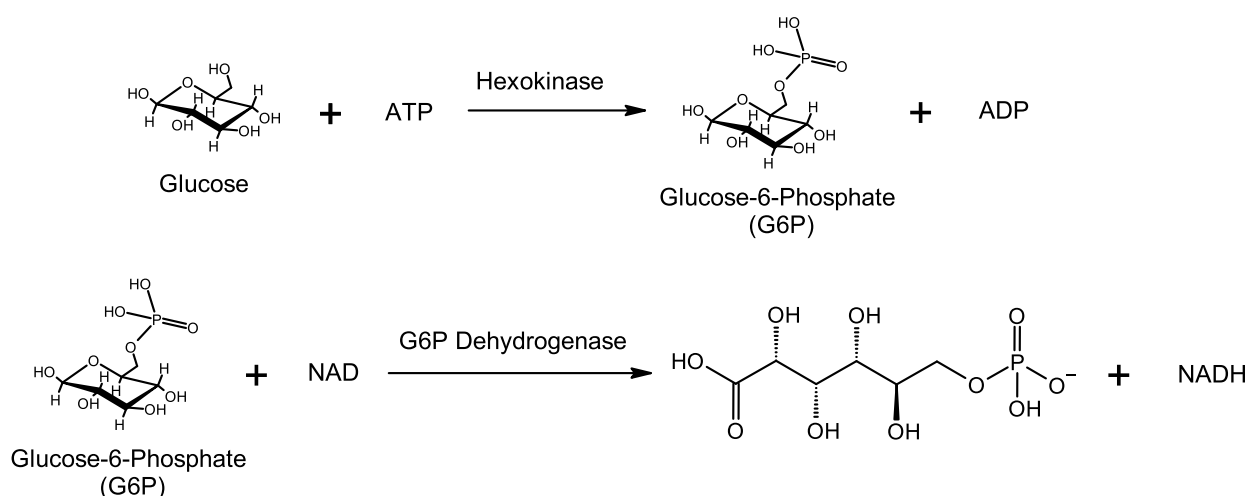


Figure 34: Enzymatic reaction scheme of the quantification of glucose.

To determine the glucose concentration of the liposomal samples, they were diluted with ddH₂O to a glucose concentration of 0.05 – 5 mg/mL. The dilution factor was estimated based on the amount of glucose used for conjugation. A volume containing a corresponding amount of glucose of 0.5 – 50 µg is then taken from this. The three different sample tubes (sample blank, reagent blank and sample) were now prepared for further determination according to Table 13. All tubes were thoroughly mixed using the vortexer and

incubated for 15 min at RT. The absorbance was then measured at 340 nm using polystyrene semi-micro cuvettes.

Table 13: Pipetting scheme for the glucose hexokinase assay kit.

Tube	Assay Reagent [mL]	Sample Volume [μ L]	ddH ₂ O [mL]
Sample Blank	/	Same as for the test	1.0
Reagent Blank	1.0	/	Same as the sample volume for the test
Sample	1.0	10 – 200	/

The evaluation was carried out using the following equation (Eq. 2):

$$c_{Glucose} \left[\frac{mg}{mL} \right] = \frac{(\Delta A) \cdot (TV) \cdot M_w(Glucose) \cdot (DF)}{(\varepsilon) \cdot (d) \cdot (SV) \cdot (Conversion\ factor\ from\ \mu g\ to\ mg)} \quad \text{Eq. 2}$$

whereas

$$\Delta A = A_{Test} - A_{Total\ Blank}$$

$$TV = \text{Total Assay Volume [mL]}$$

$$SV = \text{Sample Volume [mL]}$$

$$M_w(Glucose) = 180.2 \frac{g}{mol} \text{ or } \frac{\mu g}{\mu mol}$$

$$DF = \text{Dilution factor}$$

$$\varepsilon = \text{Millimolar extinction coefficient for NADH at 340 nm; } \left[\left(\frac{mL}{Mol} \right) \left(\frac{1}{cm} \right) \right]$$

$$d = \text{Thickness of the optical path [cm]} = 1\text{ cm}$$

3.2.2.3.4 Apolipoprotein E3 Quantification

The Apolipoprotein E3 (ApoE3) was quantified using the sandwich ELISA principle, whereby the Human Apo E ELISA^{BASIC} Kit was used. In a first step, the 96-well NUNC™ plates were coated with capture antibody E276 (2 mg/mL in PBS) by adding 100 μ g/well. The plate was covered and incubated overnight at 4 – 8 °C. On the following day, the plate was emptied by tapping on paper and then blocked with 200 μ L/well PBS containing 0.05 % (v/v) Tween 20 and 0.1 % (w/v) BSA. The plate was incubated for 1 h at RT on a shaker at 50 rpm. During this time, the dilutions of the standard were prepared according to the following scheme (Figure 35). PBS containing 0.05 % (v/v) Tween 20 was used as incubation buffer.

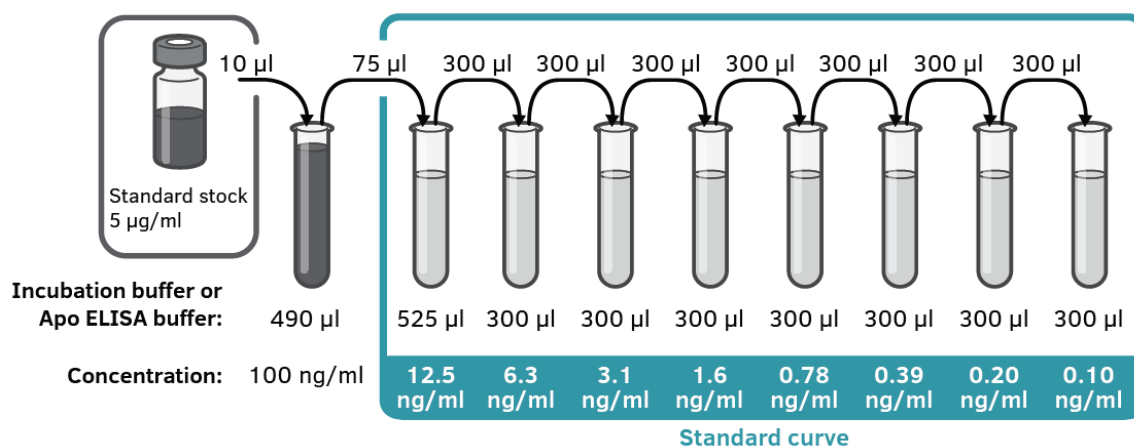


Figure 35: Dilution scheme of ApoE standard according to the manufacturer's instruction.

After 1 h of incubation, the plate was washed 5 times with 300 µL/well each with PBS containing 0.05 % (v/v) Tween 20 - in the following referred to as wash buffer. Subsequently, 100 µL/well of the unknown sample or each standard concentration was pipetted as triplicate and incubated for 2 h at RT on the shaker at 50 rpm. The plate then was washed again three times with 300 µL/well of wash buffer. For detection, 100 µL/well of the detection antibody E887-biotin (1 µg/mL incubation buffer) was added and incubated for 1 h at RT in the shaker at 50 rpm. It was followed by three washing steps with 300 µL/well of the wash buffer each. Then 100 µL of the 1:1000 diluted streptavidin-horseradish peroxidase (HRP) was added and incubated again for 1 h at RT on the shaker at 50 rpm. After three further washing steps, each with 300 µL/well of the wash buffer, 100 µL/well of the 3,3',5,5'-tetramethylbenzidine (TMB) substrate was added and incubated for 15 min at RT on the shaker at 50 rpm for color development. The color reaction was stopped by adding 100 µL/well of 0.2 M sulfuric acid. The absorbance was measured using the microplate reader at 450 nm with 570 nm as the reference wavelength. The ApoE3 concentration of the unknown samples was determined using the linear equation of the calibration line (Figure A 10.6).

3.2.2.3.5 Analysis of ffHep-modified Liposomes

3.2.2.3.5.1 Heparin Quantification using Alcian Blue

The staining of proteoglycans and polysaccharides by Alcian Blue served as the basis for the quantification of heparin on the liposomal surface. In a first step, a calibration curve was created using fHep. For this purpose, a 1:25 dilution of a 10 mg/mL stock solution in ddH₂O was first prepared and then a serial 1:2 dilution was made to obtain a

concentration range from 12.5 µg/mL to 400 µg/mL. The sample was diluted to about 400 µg/mL according to the amount used for conjugation. In a next step, 500 µL of each dilution or of the sample was diluted 1:2 with an Alcian Blue 8GS solution (10 mg/mL in 1 M hydrochloric acid) and incubated for 24 h under light protection to form a precipitate. The excess dye was removed by centrifugation at 10,000 rpm for 10 min at 4 °C and subsequent removal of the supernatant. The precipitate was resuspended in 1 mL of 1 M hydrochloric acid and centrifuged again at 10,000 rpm for 10 min at 4 °C. After removal of the supernatant again, the precipitate was dissolved with 1 mL of the solvent mixture (25 M sodium hydroxide and ethanolamine 1:24 (v/v) by pipetting, vortexing and using the ultrasonic bath for 30 min. After renewed centrifugation at 10,000 rpm for 10 min at 4 °C, 200 µL of the supernatant each sample or standard was pipetted into a 96-well plate as a triplicate determination, whereby the solvent mixture was pipetted as a blank. Finally, the absorbance was measured at 620 nm on the multiplate reader. The heparin concentration of the unknown samples was determined using the linear equation of the calibration line (Figure A 10.8).

3.2.2.3.5.2 *Bacteroides Heparinase I* Assay

An enzymatic assay was used for the qualitative detection of heparin on the liposomal surface. *Bacteroides Heparinase I* is an enzyme that selectively cleaves the glycosidic bond between hexosamines and uronic acids of heparin chains, creating a double bond at the non-reducing end of the uronic acid, which absorbs at 232 nm. For the detection of bound heparin, the sample was diluted to a fHep concentration of 1 mg/mL. Consequently, 10 µL of this dilution was mixed with 10 µL of the *Bacteroides Heparinase* Reaction Buffer and made up to 100 µL with ddH₂O. After adding 1 µL of *Bacteroides Heparinase I*, incubation was carried out at 30 °C on a shaker at 50 rpm, with the absorbance at 232 nm being measured every hour.

3.2.2.3.5.3 Fluorescamine Assay

In addition to the quantification of proteins, fluorescamine can also be used in this case to determine the conjugation efficiency of fHep, as it forms a fluorophore while reacting with primary amines, which are integrated into the liposomes as conjugation anchors (Figure 36). To determine the conjugation efficiency, the sample was first diluted to an amine concentration of 0.5 mg/mL based on the amount of phospholipid used in the

liposomal formulation. A volume of 450 μL of the liposomal sample was mixed with 150 μL of the fluorescamine solution (3 mg/mL in DMSO), and incubated for 15 min at RT. The fluorescence intensity (FI) was measured at an excitation wavelength of 367 nm and an emission wavelength of 470 nm with a slit width of 5 nm.

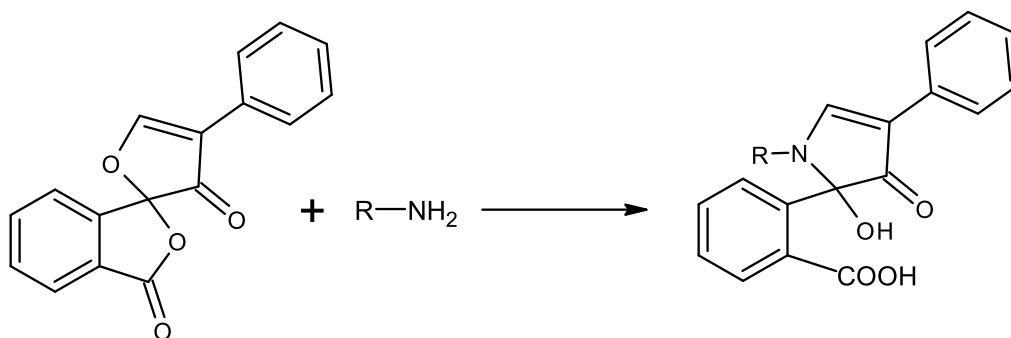


Figure 36: Reaction scheme of fluorescamine with primary amines forming a fluorophore.

The conjugation efficiency was calculated using the following equation (Eq. 3):

$$\text{Conjugation Efficiency [\%]} = \frac{FI_{f\text{Hep-modified liposomes}} * 100}{FI_{\text{unmodified liposomes}}} \quad \text{Eq. 3}$$

3.2.2.3.6 Preparation and Characterization of Asymmetric Liposomes

The preparation of asymmetric liposomes is based on the principle of centrifugation of two inverse nanoemulsions (Chapter 2.3.5.1). The PFC/W emulsion required for this purpose was prepared analogously to Chapter 3.2.1.2.1, whereby the lipid film was generated based on DPPC and cholesterol in a molar ratio of 70:30. To produce the W/PFC nanoemulsion, a 300 mM lipid stock suspension of DMPC and cholesterol (60:40 mol%) was first prepared using the thin film method (Chapter 3.2.1.1), whereby the lipid film was dried in a test tube using a continuous argon stream. The weights of the required lipids can be found in Table A 9.6 and A 9.7. Depending on the subsequent assay, the 300 mM lipid film was rehydrated with PBS or a fluorescein-sodium solution (FluNa 2 g/L in His/NaCl), whereby both the ultrasonic bath and warm water were used for complete resuspension. For the preparation of the W/PFC nanoemulsion, 9.85 mL of the PFC used were stirred using the UT at 25,000 rpm for 3 min while 1.5 % (v/v) of the 300 mM lipid stock suspension was injected for homogenization. For centrifugation step, 10 mL of the W/PFC nanoemulsion was placed in a 50 mL tube, overlaid with 10 mL of the PFC/W

nanoemulsion and centrifuged at 4,000 x g for 5 min at RT. After centrifugation, the liposomes in the upper aqueous phase were separated from the remaining lower PFC phase. A post-processing of the liposomes was achieved by a 5-fold extrusion using a 200 nm membrane and subsequent 5-fold extrusion using a 100 nm. A final sterile filtration of the samples was performed using a syringe filter with a pore size of 0.22 µm.

3.2.2.3.6.1 Determination of Encapsulation Efficiency

FluNa was used as a model substance to determine the liposomal encapsulation efficiency (EE). The VivaSpin® 2 as an ultrafiltration unit with a MWCO of 5,000 Da of the PES membrane was used to determine the EE. In a first step, 1 mL of the sample was added directly to the membrane in a VivaSpin® 2 to remove the unencapsulated dye and centrifuged at 4,000 x g for 1 h at RT. This washing step was repeated after the removal and photometric measurement of the eluate at 495 nm. Subsequently, the liposomes remaining on the PES membrane were cracked to determine the encapsulated FluNa, by adding 1 mL of 2 % (v/v) Triton X-100 in His/NaCl under ultrasonic treatment for 30 min. After renewed centrifugation at 4,000 x g at RT for 1 h, the absorbance of the eluate was measured and the cracking step was then repeated. To determine the EE, two calibration curves of FluNa were prepared in advance, in His/NaCl buffer and in 2 % (v/v) Triton X-100 in His/NaCl buffer (Figure A 10.4 and A 10.5). The FluNa concentration for each process step was calculated using the linear equation of the corresponding calibration curve. The EE was calculated using the following equation (Eq. 4):

$$EE [\%] = \frac{\text{Encapsulated dye} \left[\frac{mg}{mL} \right]}{(\text{Encapsulated dye} \left[\frac{mg}{mL} \right] + \text{Free dye} \left[\frac{mg}{mL} \right])} \cdot 100 \quad \text{Eq. 4}$$

3.2.2.3.6.2 Determination of Bilayer Asymmetry

The degree of lipid bilayer asymmetry was determined using the fluorescamine assay. For this purpose, the phospholipid DOPS (Figure 31), which contains an amine group, was integrated at 5 mol% each into either the PFC/W nanoemulsion for the outer leaflet of the bilayer or into the W/PFC nanoemulsion for the inner leaflet. In a first step, 450 µL of the liposomal sample was mixed with 150 µL of the fluorescamine solution (3 mg/mL in DMSO) and the fluorescence intensity (FI) was measured every 5 min over 30 min. The excitation and emission wavelengths were similar to those in Chapter 3.2.2.3.5.3

($\lambda_{ex} = 367 \text{ nm}$ and $\lambda_{em} = 470 \text{ nm}$ with a slit width of 5 nm). In parallel, FI of cracked liposomes was determined by mixing $450 \text{ }\mu\text{L}$ of a 1:2 dilution of the liposomes with a 4 % (v/v) Triton X-100 in PBS solution with $150 \text{ }\mu\text{L}$ of the fluorescamine reagent and measured identically to the uncracked liposomes. Since fluorescein cannot migrate between the inner and outer phospholipid layers of the liposomes, the FI of the untreated liposomes corresponds to the amount of DOPS in the outer layer. The FI of the cracked liposomes corresponds to the total amount of DOPS in the liposomes. Thus, the asymmetry can be calculated via the ratio of both fluorescence intensities using the following equation (Eq. 5):

$$\text{Bilayer Asymmetry [\%]} = \frac{\text{FI of DOPS}_{\text{outer layer}}}{\text{FI of DOPS}_{\text{total}}} \cdot 100 \quad \text{Eq. 5}$$

3.2.3 Cell Culture

3.2.3.1 Cell Handling

3.2.3.1.1 Cultivation

All three cell lines, murine bEnd.3 brain endothelial cells and both glioma cell lines – rat F98 and human U-87 MG cells were cultured using Dulbecco's Modified Eagle Medium (DMEM) with 4.5 g/L glucose. The culture media were supplemented with 10 % (v/v) FBS, 100 U/mL penicillin, 0.1 mg/mL streptomycin and 0.1 % (v/v) non-essential amino acids (NEAA). All media contained 1 mM sodium pyruvate, low (1.5 g/L) and high glucose (4.5 g/L) medium also contained 4 mM stable glutamine. The DMEM without glucose was supplemented with 4 mM stable glutamine. The cells were cultured in either T25 or T75 culture flasks at 37 °C in an atmosphere of 10 % CO₂ as the medium contains 3.7 g/L sodium bicarbonate.

3.2.3.1.2 Passaging

All three cell lines were passaged, i.e. the cells were isolated, at a confluence of approx. 90 %. In the first step, the culture medium was aspirated, and the cells were washed with 5 mL (T25) or 10 mL (T75) of Dulbecco's Phosphate Buffered Saline (DPBS). To detach the cells from the surface of the cell culture flask, 1 mL or 3 mL of Accutase[®] was added and the flask was incubated for 2-3 min at 37 °C. The resulting cell suspension was diluted with fresh culture medium in the desired ratio and homogenized by pipetting up and down.

3.2.3.1.3 Cell Counting

Light microscopic cell counting was performed using a Fuchs-Rosenthal counting chamber. For this purpose, 100 µL of the cell suspension was diluted 1:2 with 100 µL of 0.2 % (w/v) trypan blue solution. Trypan blue is an anionic diazo dye, which can only penetrate perforated non-intact cell membranes.

Subsequently, 10 µL of the diluted cell suspension was applied to each side of the hemocytometer and the cell number of four large squares was counted, with dead cells stained blue. The cell count of cells alive in the suspension was determined using the following equation (Eq. 6):

$$CC = \emptyset \cdot DF \cdot 10^4$$

Eq. 6

whereby CC is the cell count per mL; \emptyset is the mean cell count per big square; DF is the dilution factor and 10^4 reflects the compartment factor.

3.2.3.1.4 Cell-Freezing and Thawing

For long-term storage, suspended cells were centrifuged for 3 min at 150 x g and the resulting pellet was resuspended in the prepared freezing medium. It consisted of 70 % (v/v) DMEM, 20 % (v/v) FBS and 10 % (v/v) DMSO. The cell suspension was transferred to cryo-vials and placed in the gas phase (-150 °C to -160 °C) of the liquid nitrogen. After 24 h, the vials were transferred to the liquid phase (-196 °C). If necessary, the cells were taken back into culture. This was done by thawing the cell suspension in the cryo-vial in a water bath at 37°C for approximately two min. The cell suspension was then transferred to a 15 mL tube and gradually diluted with pre-warmed culture medium. This served to rapidly inactivate the DMSO in the freezing medium to avoid an osmotic shock of the cells. After centrifugation at 150 x g for 5 min, the supernatant was discarded and the cell pellet was resuspended in a small volume of fresh medium. In the final step, the cells were transferred to a T25 cell culture flask and cultivated in an incubator at 37 °C and 10 % CO₂.

3.2.3.2 Cell Staining

Cells were seeded in 24-well plates with a cell count of 6×10^4 cells/well and incubated for 24 h at 37 °C and 10 % CO₂. DMEM with 4.5 g/L glucose was used as the culture medium for the staining of LRP1, integrin α_v and 5-HT₇. GLUT1 was stained at three different glucose concentrations (0 g/L, 1.5 g/L or 4.5 g/L). After a washing step with DPBS, the cells were detached with Accutase® and transferred to a FACS tube. A cell pellet was formed by centrifugation at 150 x g for 5 min and resuspended in FACS buffer (DPBS with 5 % (v/v) FBS). Subsequent blocking of non-specific Fc-mediated antibody interactions was performed by incubation with anti-mouse or anti-rat CD16/CD32 antibody (1 µg/million cells) or with human Fc-block binding inhibitor (2.5 µg/million cells) for 20 min at room temperature. After removal of the supernatant, the cells were incubated with 4 % (v/v) paraformaldehyde in DPBS for 20 min at room temperature on the shaker.

After washing twice with FACS buffer, the cells were permeabilized by dropwise addition of 2 – 3 drops of 100 % ice-cold methanol and subsequently incubated for 5 min at room temperature on the shaker. After three additional washing steps with FACS buffer, the cells were stained by adding 100 μ L of a 1:200 dilution of the phycoerythrin (PE)-coupled antibody either for GLUT1, 5-HT₇, LRP1 or integrin α_v in FACS buffer. Staining was carried out by incubation in a refrigerator under light-protected conditions for 30 min. The cells were then resuspended in FACS buffer, washed three times and finally resuspended with 500 μ L FACS buffer. The mean fluorescent intensities (MFI) were determined using the BD LSR II flow cytometer by measuring 10^4 single-cell events.

3.2.3.3 Cellular Uptake Assay

Cells were seeded in 48-well plates with a cell count of 3×10^4 cells/well and cultured for 24 h at 37 °C and 10 % CO₂ under complete glucose deprivation for the evaluation of uptake of glucose-modified liposomes. For the uptake evaluation of ApoE3 or c(RGD)-modified liposomes, the culture medium contained 4.5 g/L glucose. After aspiration of the medium, 90 % of the well volume was replaced with the corresponding cell culture medium. Subsequently, 10 % of the well volume was added with the liposomal formulations to be tested, resulting in the final liposomal concentrations of 100 μ M, 500 μ M and 1,000 μ M. The necessary dilutions of the liposomal formulations to a concentration of either 10 mM, 5 mM or 1 mM were prepared in advance with the culture medium (Table A 9.11). In addition, 2-NBDG, a fluorescent analog of glucose, was utilized as a positive uptake control in concentrations of 50 μ M and 150 μ M under starving conditions in separate wells. Incubation was carried out for 1 h or 3 h in an incubator at 37 °C and 10 % CO₂. Cellular uptake of the liposomes was stopped by aspiration of the medium and treatment of the cells with ice-cold DPBS. Cells were detached using trypsin-EDTA, which was diluted 1:10 with DPBS. Subsequently, the trypsin activity was halted by adding cold FACS buffer. The samples were then transferred to FACS tubes and washed 3 times with FACS buffer. The mean fluorescent intensities (MFI) were determined using the BD LSR II flow cytometer by measuring 10^4 single-cell events.

3.2.3.4 Cytotoxicity Assay

In order to prepare dose-response curves for an API, its cytotoxic effect was determined and a sigmoidal fit was used to calculate an inhibitory concentration at which 50 % of the cells have perished (IC_{50}). Within this thesis, the assay was used to evaluate the cytotoxicity of liposomes without encapsulated API. Therefore, cells were seeded in 96-well plates with a cell count of 2×10^4 cells/well and incubated for 48 h at 37 °C and 10 % CO_2 . After 48 h of incubation, the medium was changed, whereby only 90 % of the well volume was replaced with fresh medium. The remaining 10 % was replaced with the corresponding dilutions of the liposomal formulations (Table A 9.11). They were added for the final concentrations of 100 μM , 500 μM and 1,000 μM and incubated for 3 h, according to the uptake assays. Cell viability was determined by adding 10 μL of alamarBlue™ HS reagent, measuring the reducing power of the living cells (Figure 26). It was incubated for 2 h to measure the absorbance on the multiplate reader (wavelength 570 nm and reference wavelength 600 nm). The relative viability was calculated as a quotient of the absorbance of the control well (without treatment) and the absorbance of the wells treated with samples.

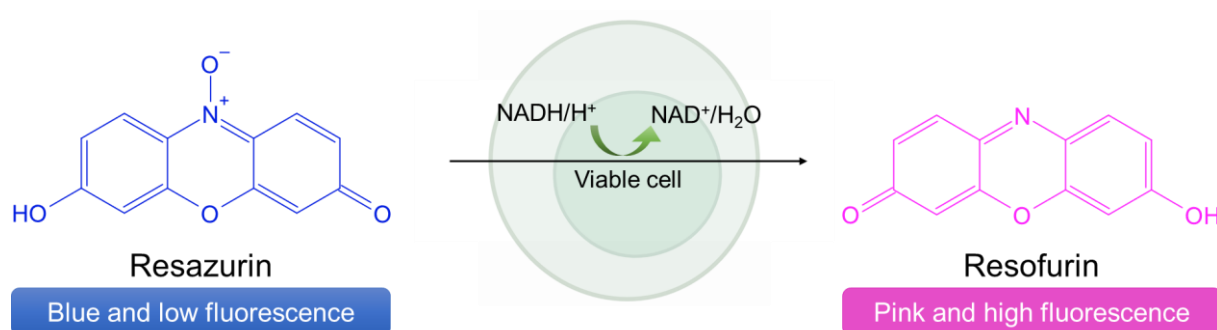


Figure 37: Principle of the alamarBlue™ HS assay. Colorimetric measurement of the converted dye resazurin to resorufin by the metabolic activity of the cell (ABP Biosciences).

3.2.4 Hemo- and Immunocompatibility

3.2.4.1 Factor Xa Assay

To determine the heparin activity of fHep, ffHep and ffHep-modified liposomes, the Bio-phen Heparin (AT+) Assay Kit was used, which is based on a chromogenic anti-Xa kinetic method with the addition of exogenous antithrombin III (ATIII). First, a dilution series of the heparin standard with 100 IU/mL was prepared to establish a calibration curve. Dilution was performed with PBS to the following concentrations: 0.0625 / 0.125 / 0.5 / 0.25 / 0.5 / 1.0 / 2.0 / 40 IU/mL. The samples were also diluted with PBS, 1:5 for the positive control with fHep-K8C or 1:10 for the G25 fractions and ffHep-modified liposomes. The G50 fractions were used undiluted for the assay. For the reaction, the following reagents and volumes per well were pipetted into a 96-well plate: 15 μ L sample or standard, 15 μ L ATIII and 75 μ L of the Factor Xa-specific chromogenic substrate (Sxa-11) pre-warmed to 37 °C. After mixing the components, they were incubated at 37°C for two min. Subsequently, 75 μ L Factor Xa was added to each well and mixed again. After exactly 90 seconds of incubation at 37 °C, the reaction was stopped with 100 μ L citric acid (20 g/L) and the absorbance was measured at 405 nm. As the sample blank, the components are mixed in reverse order to the test, i.e. citric acid, Sxa-11, sample, ATIII and Factor Xa. This sample blank was used for blank correction of the measured values of the samples and the standards. As a high-positive control (HPC), fHep-K8C was used at a concentration of 1 mg/mL in PBS. The heparin activity of the unknown samples was determined using the linear equation of the calibration line (Figure A 10.9).

3.2.4.2 Complement Factor ELISAs

The blood-loop assay was used to evaluate the hemocompatibility of the samples with human whole blood. The blood was drawn directly into an MPC-coated tube via a cannula with a thin tube, ensuring a gas-tight connection to prevent activation of the blood by air bubbles. Immediately after blood collection, 1 mL was placed in a tube filled with 30 μ L 0.34 M EDTA to determine the initial blood values such as the platelet count using the Sysmex Hematology Analyzer (referred to as hemoanalyzer). This was also repeated at the end of the blood collection as a second initial measurement. The tubes were closed

immediately after adding blood and mixed with the EDTA solution by inverting and swirling. For the blood-loop assay, a heparinized blood-collecting tube with a length of 8 cm was rinsed three times with 0.9 % (w/v) sodium chloride solution. Afterward, 1.5 mL of the blood/EDTA mixture was added to the tube, sealed on one side with an MPC-coated cap, and mixed with 30 μ L 20 mM sample or 30 μ L PBS as a negative control. After sealing the tube and incubating for 1 h at 37 °C, the tubes were emptied into a 10 mL disposable beaker for visual assessment of possible clotting of the blood. The treated samples were also characterized using the hemoanalyzer with a focus on the platelet count. To analyze the samples for immunocompatibility, blood samples were centrifuged at 3,200 rpm for 15 min at 4 °C to obtain the blood plasma in the upper phase which was then transferred into a fresh tube for storage at -80 °C.

Table 14: Overview of the complement factor ELISA components.

	C3a	C5b-9	TAT
Capture mAb	anti-C3a 17.3 1:1,000 dilution	anti-C5b-9 E11 1:1,000 dilution	sheep anti-human thrombin 1:400 dilution
Detection mAb	biotinylated anti-C3a-peptide 1:500 dilution	biotinylated anti-human C6 1:2000 dilution	HRP-conjugated anti-human antithrombin 1:500 dilution
Conjugate	HRP-conjugated streptavidin 1:500 dilution		
Substrate	TMB		
Stop solution	1 M sulphuric acid		
Standard	zymosan-activated serum 1:1000, than serial 1:2 dilution		complement standard #1 1:1000, than serial 1:3 dilution
Concentrations	0 / 0.06 / 0.13 / 0.25 / 0.5 / 1 / 2 / 4 / 8 / 16 μ g/L	0 / 1.91 / 3.82 / 7.65 / 15.31 / 30.625 / 61.25 / 122.5 / 245 / 490 / 980 / 1960 μ g/L	0 / 0.01 / 0.03 / 0.083 / 0.25 / 0.75 / 2.22 / 6.67 / 20 / 60 / 180 μ g/L
Measurement	absorbance at 450 nm		

For each ELISA, the 96-well plates (NUNC™) were first coated with the dilution of the corresponding capture mAb (Table 13) by adding 100 µg/well and incubating the plates overnight at 4 – 8 °C in a covered container. On the following day, the plates were emptied by tapping on paper. After adding 200 µL/well of the blocking buffer, the plate was incubated for 1 h at RT on the shaker at 700 rpm. After emptying the plate again, 100 µL/well of the standards or samples were pipetted onto the plate as a duplicate and incubated for 1 h at RT on the shaker at 400 rpm. The plate was then washed three times with 300 µL/well wash buffer each. Subsequently, 100 µL/well of the dilution of the corresponding detection antibody was added and incubated for 1 h at RT on the shaker at 400 rpm. After incubation, the plates were washed again three times with 300 µL/well wash buffer and then completely emptied by tapping out on paper. For the C3a and C5b-9 ELISA, 100 µL/well each of the diluted conjugate HRP-coupled streptavidin was added and incubated for 15 min to 20 min at RT on the shaker at 400 rpm. After washing three times with 300 µL/well wash buffer each and emptying the plates, 100 µL/well of the TMB substrate was added for all ELISA types. After 5 min of incubation under light protection, 100 µL/well of 1 M sulfuric acid was added to stop the color reaction. The absorbance at 450 nm was measured using the microplate reader within 10 – 20 min of adding the sulphuric acid. The corresponding sample concentration was determined using the linear equation of the calibration line (Figure A 10.10 to A 10.12).

3.2.5 Analytical Methods

3.2.5.1 Dynamic Light Scattering

Dynamic light scattering (DLS) was used to characterize the PFC/W nanoemulsions and liposomes in terms of their particle size (Z-Average), particle size distribution (polydispersity index, Pdl) and their relative number of particles (derived count rate, DCR). The measurements were performed using the ZetaSizer Nano ZS90. The principle is based on a particle's Brownian molecular motion. A laser beam (red laser with a wavelength of 633 nm) hits the measuring cell, causing the light to be scattered. Depending on the intensity of the scattered light, the attenuator dampens the laser beam. Using a photomultiplier in a 90° (or 173°) position, the scattered light or the rate of change of the scattered light intensity is recorded over a certain period of time (Figure 38) (Malvern Panalytical, 2013).

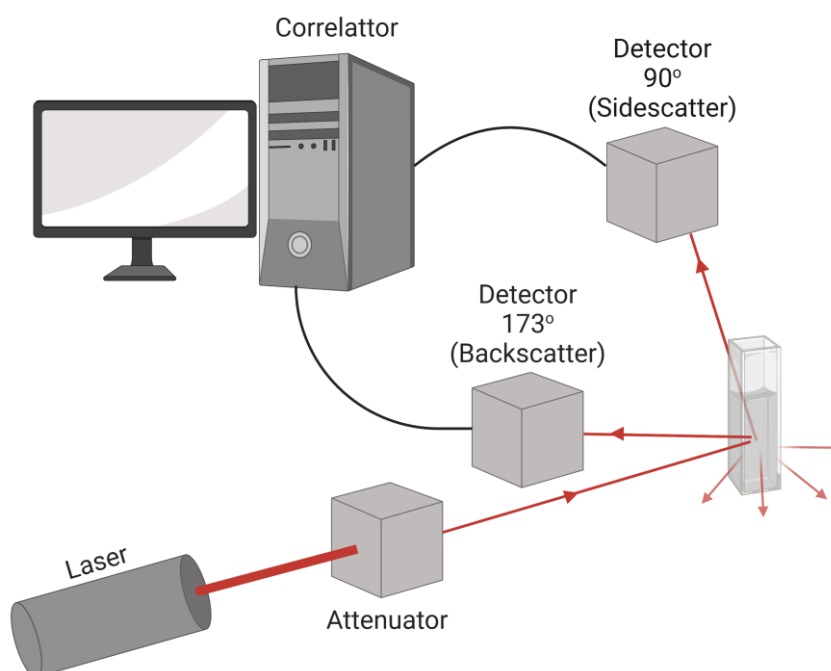


Figure 38: Measuring principle of dynamic light scattering. The laser beam hits the attenuator and is attenuated depending on the scattering behavior of the particles in the sample before the beam hits the measuring cell. The scattered light is recorded by the detector and digitally processed as a signal (Malvern Panalytical, 2013) (created with BioRender.com).

The intensity fluctuation varies depending on the size of the measured particles: the larger a particle, the slower it moves and vice versa. The recorded fluctuation in intensity over a certain period of time is summarized in the autocorrelation function (Stetefeld et al., 2016) (Eq. 7):

$$g(\tau) = A + \sum B \cdot e^{-2q^2 D \tau} \quad \text{Eq. 7}$$

Where τ corresponds to the sample time of the correlator, A reflects the baseline; B is the amplitude of the autocorrelation function; q is the control vector and D is the diffusion coefficient. It can be inferred from the equation that the refractive index is also important, as it is included in the formula of the scattering vector.

The autocorrelation allows various evaluation methods. The simplest is the cumulant analysis according to ISO113321, where the correlation function is fitted using a third-degree polynomial (Eq. 8):

$$\ln(g) = a + b\tau + c\tau^2 + d\tau^3 \quad \text{Eq. 8}$$

Where $b\tau$ is the first, $c\tau^2$ is the second and $d\tau^3$ the third cumulant.

The slope b is used to calculate the diffusion coefficient for the Z-Average, which is converted into the mean droplet diameter. The deviation of the fit from the correlation function is the Pdl, which can assume values from 0 to 1 (particularly polydisperse sample), whereby a Pdl of less than 0.1 describes a monodisperse droplet size distribution (Malvern Panalytical, 2013). The cumulant analysis results in individual mean droplet diameters and is the intensity-based mean value, resulting from the intensity signal. The hydrodynamic radius r_h is therefore calculated using the following equation (Eq. 9):

$$r_h = \frac{k_b \cdot T}{6 \cdot \pi \cdot \eta \cdot D} \quad \text{Eq. 9}$$

Where k_b is the Boltzmann constant; T reflects the temperature, η is the dynamic viscosity of the solvent and D is the diffusion coefficient.

Since the cumulant analysis is no longer suitable for a multimodal distribution, the multi-exponential approach is used instead to calculate the droplet size. Here, too, the intensity-weighted mean value is primarily calculated. The conversion to the volume or number mean is carried out using Mie theory, whereby the refractive index and also the absorption of the sample are necessary. For a sample with two different size populations,

the ratio of the distribution differs depending on the parameter under consideration (Figure 39). The differences between number-weighted and volume-weighted diameters are due to the volume of a sphere, for which d^3 is included in the calculation. In contrast, the intensity-weighted diameter is included from the Rayleigh approximation with d^6 (Riedl, 2006).

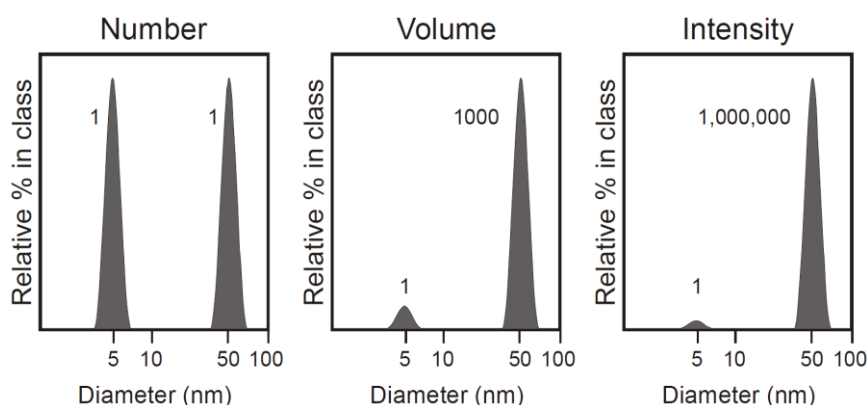


Figure 39: Representation of the number-, volume- and intensity distribution of a bimodal sample with identical parts of small and large particles (Malvern Panalytical, 2013).

3.2.5.2 Zeta Potential Measurement – Electrophoretic Mobility and Laser-Doppler Velocimetry

The following information was all taken from the Malvern Handbook for the ZetaSizer (Malvern Panalytical, 2013). Figure 40 can be used to explain the Zeta potential itself. The liquid layer around a particle always consists of two parts: 1) the inner region, the star layer, in which the ions are strongly bound and 2) the outer diffuse region, in which the ions are less strictly persistent. Thus, there is an electrical double layer around each particle. Within the diffuse layer, however, there is a fictitious boundary in which the ions and particles form a unit. If a particle moves, for example, due to gravity, the ions inside the boundary move with it, while the ions outside the boundary remain unaffected. This boundary is therefore referred to as a "slipping lane". The potential that exists exactly at this boundary is called the Zeta potential (ZP).

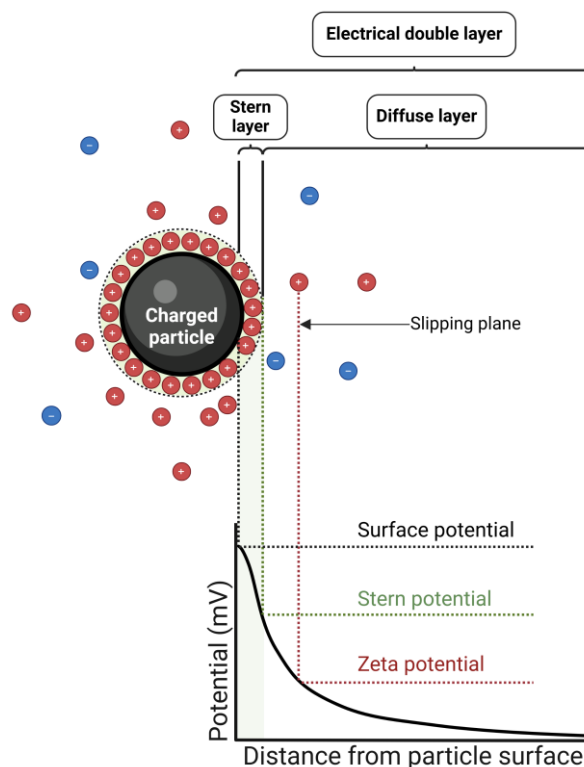


Figure 40: Schematic representation of the electric double layer of a negatively charged particle and the correlating Zeta potential (Drioli and Giorno, 2016; Malvern Panalytical, 2013) (created with BioRender.com).

The ZP indicates the potential stability of a colloidal system. For example, a ZP of ± 30 mV is regarded as a general "dividing line" between stable and unstable suspensions, as the particles repel each other and there is no tendency to flocculate.

The Zeta potential was measured using the ZetaSizer Nano ZS 90, which calculates the ZP by determining the electrophoretic mobility (EM) using the Henry equation. The EM is determined by carrying out electrophoretic experiments on the sample and measuring the velocity of the particles using laser Doppler velocimetry (LDV). Electrophoresis represents the movement of a charged particle relative to the surrounding liquid under the influence of an electric field. If an electric field is applied to the electrolyte, charged particles are attracted in the direction of the electrode with the opposite charge, whereby viscous forces acting on particles counteract this movement. When these two opposing forces are in equilibrium, the particles move at a constant speed. It depends on several factors, such as the viscosity and the dielectric constant of the medium, but also on the ZP. The velocity of a particle in an electric field is generally referred to as its electrophoretic mobility. The Henry equation can be used to calculate the ZP (Eq. 10):

$$U_E = \frac{2 \cdot \varepsilon \cdot \zeta \cdot f(ka)}{3 \cdot \eta} \quad \text{Eq. 10}$$

Where U_E is the electrophoretic mobility; ε is the dielectric constant; ζ is the ZP and η is the dynamic viscosity. $f(ka)$ is the Henry's function, which in this case is 1.5 and is referred to as the Smoluchowski approximation, which is used for aqueous samples.

The measurement of the velocity is carried out using a micro-electrophoresis system, i.e. a capillary with electrodes at both ends to which a potential is applied. LDV is used to measure the velocity of tiny particles in a liquid flow, which move with the velocity of the liquid. In a capillary cell, the receiving optics are focused in such a way that they transmit the scattering of the particles in the cell. The light scattered at an angle of 17° is combined with a reference beam, resulting in a fluctuating intensity signal (Figure 41). The fluctuation rate is proportional to the speed of the particle.

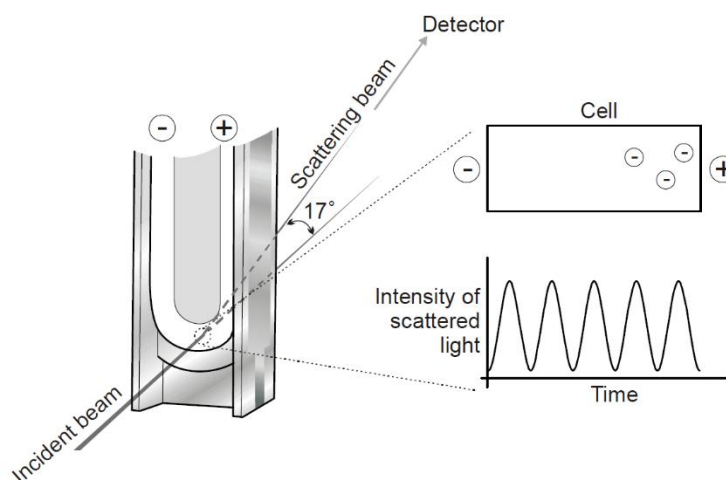


Figure 41: Measuring principle for determining the velocity of a particle in an electrical field in a capillary cell using the Laser Doppler Velocimetry. Illustration of electrophoresis in a micro-electrophoretic system with two electrodes at both ends to which a potential is applied causing the movement of particles in the direction of the electrode with opposite charge (Malvern Panalytical, 2013).

3.2.5.3 UV/VIS Spectroscopy

UV/VIS spectroscopy is used in many assays for quantification and also to generate spectra of a sample. The principle on which the measurement is based utilizes the absorption of molecules in the ultraviolet range (200 – 400 nm) or in the visible range

(400 – 800 nm). Below 190 nm, air begins to absorb the light, which is why measurements in this wavelength range are only possible in an evacuated system. Most spectrophotometers also cover a small area of the "near-infrared range" (NIR) by spectroscopy of the overtones of molecular vibrations. UV/VIS spectroscopy is an electron spectroscopy in which the valence electrons (electrons on the outer shell) are excited. If light with a suitable frequency ν strikes a molecule in the ground state S_0 , it can be absorbed and raise the molecule to an electronically excited state S_1 . The system can return to the ground state through spontaneous emission (Figure 42) (Hesse et al., 2005).

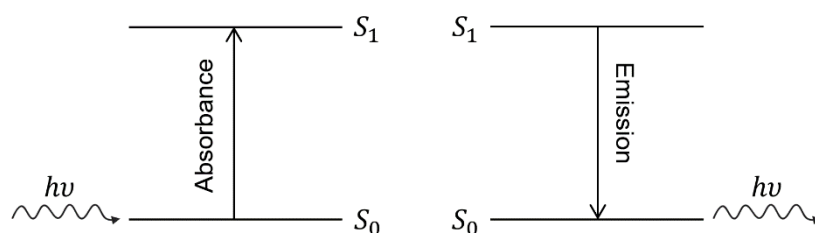


Figure 42: Electron transitions and radiation processes when a molecule is excited with light of a certain wavelength (Hesse et al., 2005).

Quantification by UV/VIS spectroscopy is based on Lambert-Berr's law (Eq. 11):

$$I = I_0 \cdot e^{-\varepsilon dc} \quad \text{Eq. 11}$$

Where the measured intensity I is calculated from the original intensity I_0 , the molar extinction coefficient ε , the thickness of the cuvette d and the concentration c . In most cases, a calibration curve is required to convert the sample absorbance into a concentration (Hesse et al., 2005).

3.2.5.4 Fluorescence Spectroscopy

The basic principle of fluorescence spectroscopy is the ability of molecules to emit the previously absorbed light, whereby a fluorophore must be present in the molecule. Valence electrons are excited to a higher energy state – the so-called singlet S_1 state. The transition of molecules from the thermally relaxed, electronically excited S_1 state or higher ones S_n , back to the ground state S_0 takes place with the emission of radiation, which is defined as fluorescence (Figure 43). The transition can also occur through radi-

ationless deactivation, known as internal conversion. Radiationless spin reversal processes, so-called intersystem crossings, lead to triplet states T_n . A return to the ground state S_0 by radiation emission is called phosphorescence (Hesse et al., 2005).

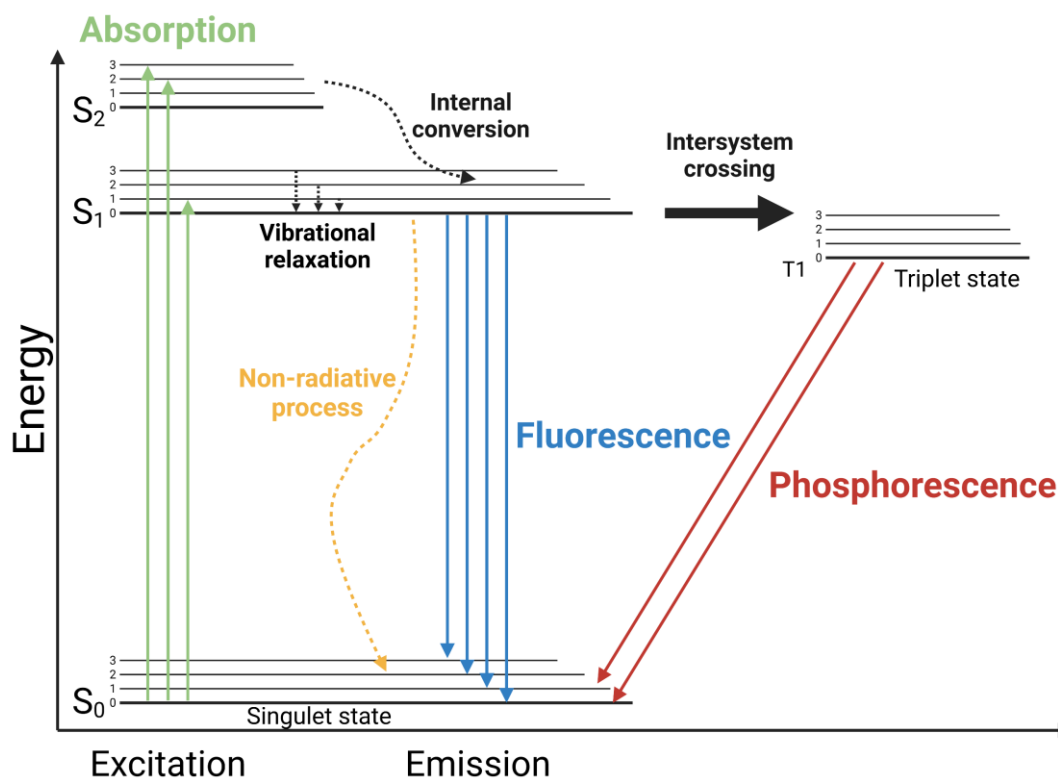


Figure 43: Perrin-Jablonski diagram of fluorescence and phosphorescence, where the number of vibrational energy levels is depicted by 0, 1, 2, etc. (Schweizer et al., 2021) (created with BioRender.com).

3.2.5.5 Size Exclusion Chromatography

Size exclusion chromatography is a form of liquid chromatography in which the molecules in a sample are separated according to their size. The stationary phase usually consists of a gel (matrix) of spherical porous beads with a specific size distribution. Depending on the size of the different particles in a sample, they may or may not penetrate into the pores of the matrix. Smaller particles can diffuse deep into the pores of the matrix when the acid passes through. The molecules trapped in the pores remain longer in the stationary phase before they elute using the elution medium (mobile phase). Large particles elute faster as they are not retained in the matrix. The separation of three particles of different sizes (red = large, orange = medium, yellow = small) is shown schematically in Figure 44. A Gaussian curve and the distance between their elution peaks are a measure of the separation quality (Cytiva, 2020).

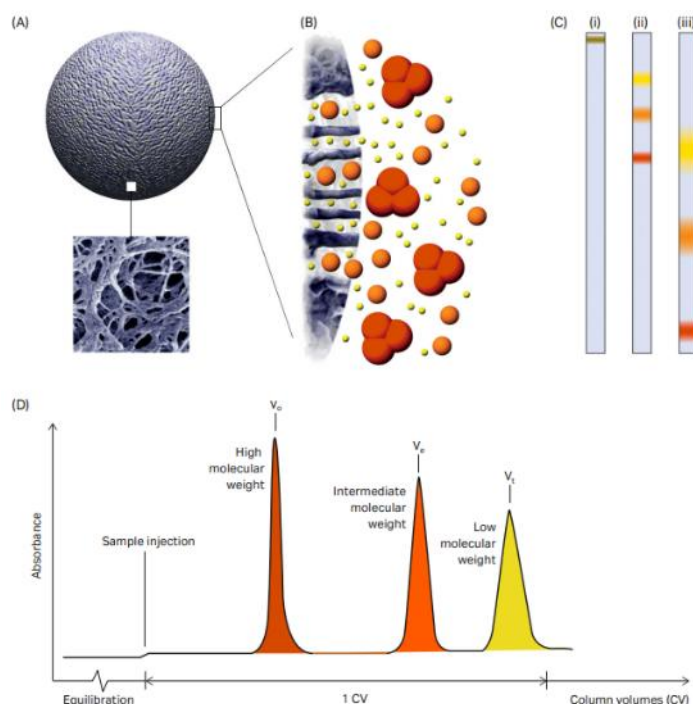


Figure 44: Principle of size exclusion chromatography. (A) Schematic representation of a particle magnified using an electron microscope. (B) Schematic illustration of sample molecules permeating into the pores. (C) A visual representation of separation (i) Sample is added to the column; (ii) the largest molecule (dark orange) is eluted from the column first; (iii) the smallest molecule (yellow) is more delayed than the largest molecule. During chromatography, band widening significantly dilutes the protein zones. (D) representation of a schematic chromatogram (Cytiva, 2020).

3.2.5.6 FACS

Flow Activated Cell Sorting (FACS), also referred to as flow cytometry, is a technology that simultaneously measures and analyzes various physical properties of individual particles - usually cells - as they are transported in a liquid stream and pass individually through a laser. The characteristics that are measured include relative particle size, relative granularity and relative fluorescence intensity. The characteristics are determined by a coupled optical-electronic system, which determines how the cells or particles scatter the incident laser light and emit fluorescence (Adan et al., 2017).

A flow cytometer always includes three main components: fluidics, optics and electronics (Figure 45). The fluidics transports the cells and guides them in a laminar sample flow through the laser beam for analysis. The optical system consists of one or more lasers, whose focused, coherent light illuminates the particles in the sheath fluid, as well as optical filters, which transmit the emerging light signals to the corresponding detectors. The electronic system converts the light signals from the detectors, which can then be

processed by a computer. In addition, flow cytometers can be equipped with a sorting unit in which an electronic system decides when to start sorting by deflecting the particles (Adan et al., 2017).

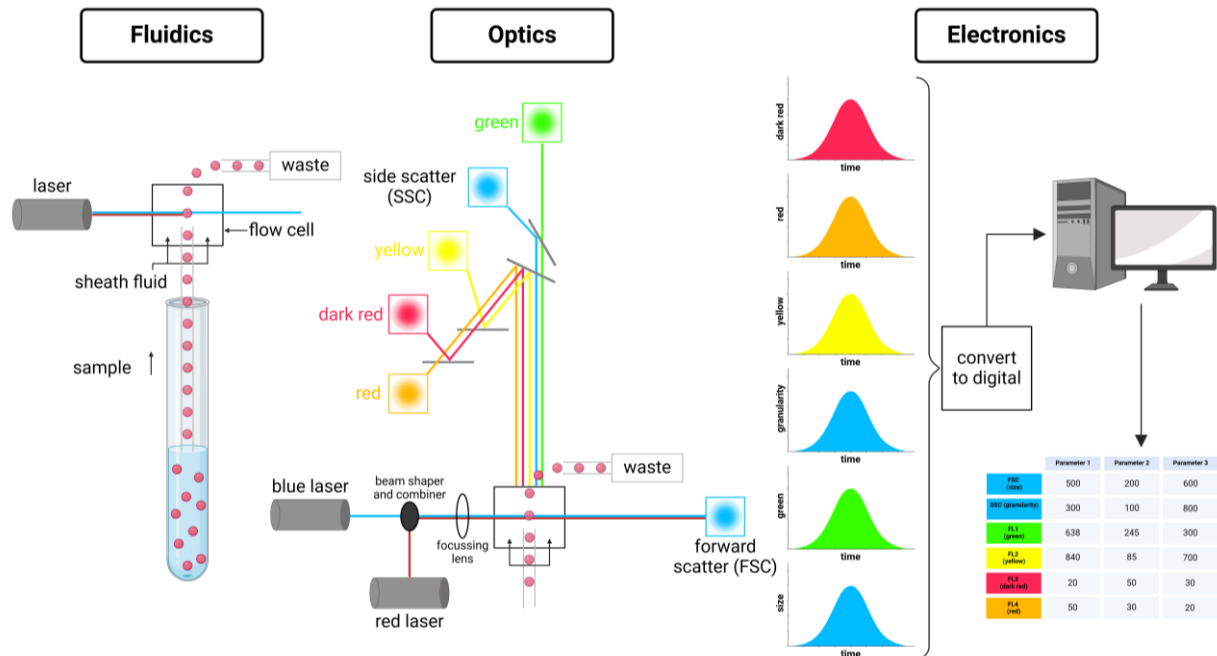


Figure 45: Composition and principle of a flow cytometer consisting of the three compartments fluidics, optics and electronics (Bergquist et al., 2009) (created with BioRender.com).

Chapter 4

Process Optimization of a PFC/W Nanoemulsion¹

In the following chapter, the influence of the pressure and the multiple processing, referred to as the number of cycles, on both particle species in a PFC/W nanoemulsion – liposomes and PFC-droplets – using high-pressure homogenization is investigated and the laminar and turbulent flow effects are clarified in more detail.

4.1 Effect of Pressure on Homogenization of mixed Liposomes and Emulsions

A pre-emulsion consisting of the perfluorocarbon (PFC, 2.5 % (v/v)) in a phosphate-buffered phospholipid/cholesterol suspension (E80/cholesterol 95:5 mol%, 7.5 mM) was prepared by a rotor-stator mixer (15,000 rpm, 10 min). This pre-emulsion was stable enough to be used for the feed of the high-pressure homogenizer without phase separation during influx since high-pressure homogenizers cannot be used with two separated phases in their injection system. However, the parameters used for pre-emulsification only avoided phase separation during influx, but the pre-emulsion was not stable enough to be characterized in size by DLS because of rapid disintegration and separation. The

¹ Content of this section is published in the *Scientific Reports* Journal and adapted for this thesis: L. Lubitz, H. Rieger, G. Leneweit, „Laminar and turbulent flow effects in high-pressure homogenization of liposomes and perfluorocarbon nanoemulsions“; doi: 10.1038/s41598-024-78550-9.

described procedure was chosen with the intention to keep the effect of rotor-stator shear to a minimum and allow high-pressure homogenization to have an almost exclusive effect on droplet break-up during each passage through the homogenization chamber, from now on referred to as 'cycle'. The minimum number of cycles chosen for the emulsification via high-pressure homogenization was 6 cycles since only after this minimum of accumulated passage time a size distribution stable for > 48 h could be achieved. Thus, the conditions used for emulsification were the minimum requirements to characterize the effect of pressure on the size distribution of a PFC stabilized by phospholipids.

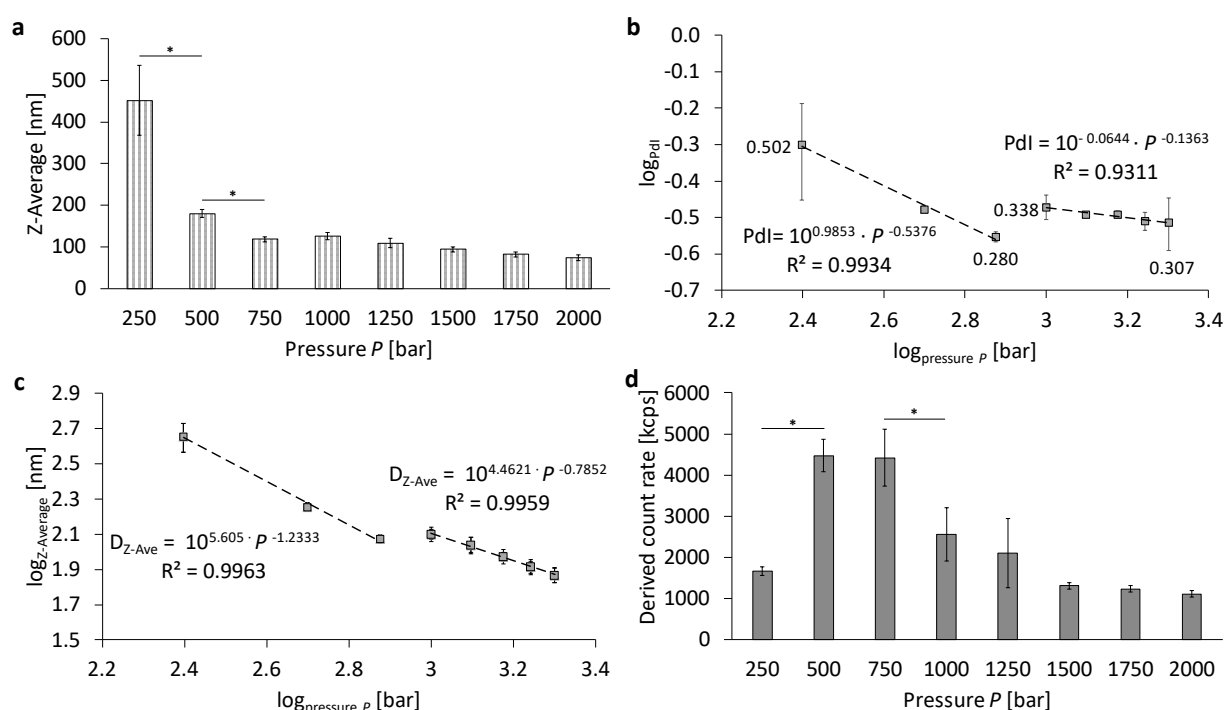


Figure 46: Pressure-dependent characteristics of a PFC/W nanoemulsion after 6 cycles of high-pressure homogenization. Representation of (a) the Z-Ave at linear scale, (b) the logarithmic representation of the Pdl with corresponding values next to the grey squares for 250, 750, 1,000 and 2,000 bar with power-law regressions in two regimes, (c) Logarithmic representation of the Z-Ave with power-law regressions in two regimes, (d) derived count rates (DCR) at a linear scale. The bars or grey squares represent the mean \pm SD, $n = 3$. A one-way ANOVA followed by a two-sample t-test was performed with a significance level for an error probability $*p < 0.05$.

Figure 46 summarizes the particle size, the corresponding Pdl and the derived count rates (DCR) of a PFC/W nanoemulsion processed for 6 cycles at different homogenization pressures. The largest Z-averaged particle size, from now on called 'Z-Ave', is at the lowest pressure 250 bar with $452.2 \text{ nm} \pm 84.2 \text{ nm}$ (Figure 46a). The smallest particle size is achieved after processing at 2,000 bar with a Z-Average of $73.7 \text{ nm} \pm 6.8 \text{ nm}$. Comparing Figure 46a and 46c it becomes apparent that the linear bar plot in Figure 46a

does not fully reveal significant correlations in the resulting particle sizes, only in the lower pressure range $P \leq 750$ bar significant differences can be seen between data points. The pressure-dependent Pdl values (Figure 46b) are also highest at 250 bar with Pdl of 0.502 ± 0.148 . However, the minimum Pdl is not found at 2,000 bar, but at a pressure of 750 bar with 0.280 ± 0.009 . Moreover, it is clearly visible that the Pdl values decrease in two different regimes of homogenization pressures P : in the lower pressure range $P \leq 750$ bar the Pdl decreases with a power-law of $\text{Pdl} \sim 1 / \sqrt{P}$ while in the second regime for $P \geq 1,000$ bar only a very small decrease of Pdl with increasing pressure takes place.

To better visualize and quantify the decay of droplet sizes at higher pressures, the Z-Ave is also presented in a logarithmic plot in Figure 46c. It clearly reveals two regimes of homogenization, but instead of a minimum, it shows a transition in a plateau range between 750 bar and 1,000 bar regarding the size at 750 bar. Logarithmic regressions for the two regimes show a power-law of for the Z-averaged droplet sizes $D_{Z-Ave} \sim P^{-1.233}$ for regime I ($P \leq 750$ bar) and $D_{Z-Ave} \sim P^{-0.7852}$ for regime II ($P \geq 1,000$ bar). This comparison shows that the decrease in Z-Ave with increasing pressure is considerably stronger in the lower-pressure regime I than in the higher-pressure regime II.

In order to elucidate the mechanisms behind the transition from regime I to II, the Reynolds numbers Re are assessed for the different sections of the microfluidic channels causing high-pressure drops by frictional energy dissipation to discriminate ranges of laminar flows and their transition to turbulence. This needs an estimate of the mean flow velocity \bar{u}_i at the cross-sectional area A_i where the subscript $i = A, B$, or C for the Y-channel and D, E, F or G for the Z-channel indicates the cross-section as shown in Figure 48e and 48j deduced from the total volume flow rate Q . This volume flow rate Q is an average in time by dividing the stroke volume V by the total duration Δt of the outflow:

$$\bar{u}_i = \frac{Q}{A_i} \text{ with } Q = \frac{V}{\Delta t} \quad \text{Eq. 12}$$

The Reynolds number Re_i at a specific cross-section of area A_i is defined by a characteristic length D_i which is either the tube diameter if the channel is circular or the hydraulic diameter for a rectangular channel with the smaller side a and the longer side b , and where ν is the kinematic viscosity. So, Re_i and the hydraulic diameters D_B and D_F are defined by:

$$Re_i = \frac{\bar{u}_i \cdot D_i}{\nu} \text{ with } D_B = D_B = \frac{2ab}{a+b} \text{ for the rectangular channels} \quad \text{Eq. 13}$$

Since the manufacturer's manual does not provide a precise geometry of the microfluidic channels used, we opened both the Y- and the Z-channel and display photographs and precisely measured channel dimensions, see Figure 48. In order to estimate the Reynolds numbers Re and the according flow regimes in the complex channel geometry, we used an integrative approach by measuring the total duration of the outlet flow from the instant of the hydraulic pressure discharge. The flow rates displayed in Table 15 are both a spatial and temporal average flowing through a complex microfluidic channel geometry.

Table 15: Reynolds numbers Re in the Y-channel at specific cross section displayed in Figure 48e. The Reynolds numbers are given as arithmetic mean based on the volume flow with its standard deviation; volume flows were measured via the duration of the outlet flow in $n = 3$ independent measurements. Reynolds numbers in bold indicate transition ranges from laminar to turbulent flow in the respective channel section.

Pressure P [bar]	Volume Flow [mL/s]	Reynolds number Re_A at cross-section A	Reynolds number Re_B at cross-section B	Reynolds number Re_C at cross-section C
250	1.85 ± 0.01	2,358	882	737
500	3.22 ± 0.2	4,100	1,533	1,281
750	4.43 ± 0.25	5,645	2,111	1,764
1,000	4.36 ± 0.01	5,549	2,075	1,734
1,250	4.99 ± 0.21	6,349	2,374	1,984
1,500	5.90 ± 0.38	7,514	2,810	2,348
1,750	6.14 ± 0.57	7,822	2,925	2,444
2,000	7.66 ± 0.24	9,752	3,647	3,048

Reynolds numbers Re in the Y-channel at specific cross section displayed in Figure 48e. The Reynolds numbers are given as arithmetic mean based on the volume flow with its standard deviation; volume flows were measured via the duration of the outlet flow in $n = 3$ independent measurements. Reynolds numbers in bold indicate transition ranges from laminar to turbulent flow in the respective channel section.

Section B is a channel segment with a rectangular cross-section where the influx is split at a T-junction, causing a split of the volume flow by half. This results in a drop of the Reynolds number range between 882 (at $P = 250$ bar) and 3,647 (at $P = 2,000$ bar). For

a rectangular channel with cross-section B having an aspect ratio $\alpha = a/b = 0.5 \text{ mm}/1.6 \text{ mm} = 0.3125$, a theoretical analysis by Chang et al. 2012 (Chang et al., 2012) finds the transition Reynolds number to be $Re_{crit, B} = 1,679$. However, Chen et al. 2007 (Chen et al., 2007) show experimentally for $\alpha = 0.333$ that the critical Reynolds number is $Re_{crit. exp.} = 2,528$. This is in accordance with most other experimental results for rectangular channels who find the critical Reynolds number for the onset of a laminar instability to be 5 – 35 % higher than the theoretical analysis by Chang et al. 2012 (Chang et al., 2012). This discrepancy is not a contradiction, since is connected to the fact that unstable fluctuations u' of the linear velocity U are not always detected experimentally in the velocity field $u = U + u'$ when the fluctuation amplitude is still small or would need much longer channels for the convergence of experimental and theoretical findings. Based on this background, it can be concluded that in Figure 46c the distinction of two independent regimes I and II in the Z-Averaged droplet size is caused by the transition from a laminar regime I to a turbulent regime II taking place in section B of the channel geometry.

This interpretation on the physical causes of different modes in droplet homogenization implies that re-laminarization takes place when the turbulent flow from section A impinges as a circular jet at the T-junction forming the entrance of the rectangular channel section B. Experimental measurements by Sano and Tamai (2016) (Sano and Tamai, 2016) and theoretical analyses by Kaewbumrung and Plengsa-Ard (2024) (Kaewbumrung and Plengsa-Ard, 2024) show that re-laminarization of turbulence in a rectangular flow or at an impinging jet is realistic. In these cases, turbulent inflow is relaminarized by the subsequent flow field in case that the latter is governed by laminar flow conditions. But why should the droplet size stop decreasing in the transition range between laminar and turbulent flow? An obvious reason is that the shear rates stop increasing and the friction factor ceases to decrease in the transition range between laminar and turbulent flow (Sano and Tamai, 2016). These correlations thus provide clear indications on the mechanisms of droplet break-up in high-pressure homogenization.

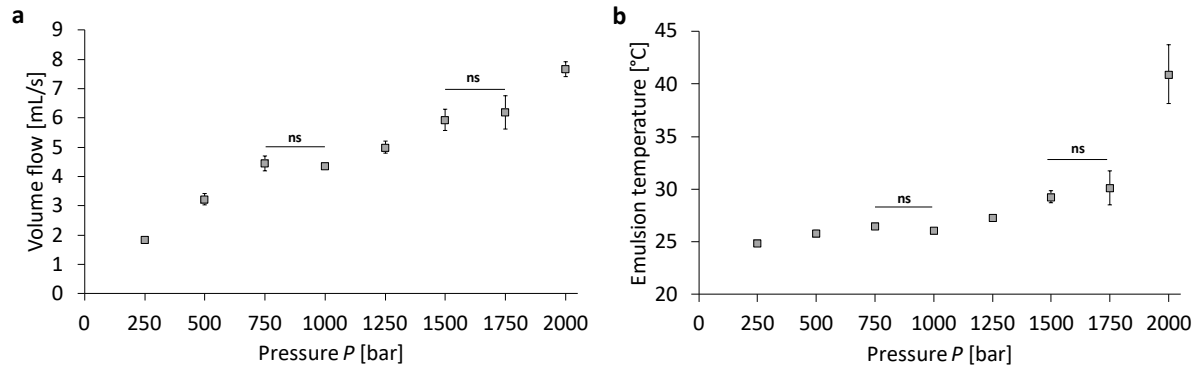


Figure 47: Pressure-dependent volume flow in high-pressure homogenization. Representation of the pressure-dependent (a) volume flow and (b) the temperature-increase of the processed fluids in an uncooled setup of the high-pressure homogenization for a PFC/W nanoemulsion. The dots represent the mean \pm SD, $n = 3$. A one-way ANOVA followed by a two-sample t-test assuming equal variances was performed show a significance level $p < 0.05$ in all neighboring data points except for those indicated as 'non-significant' (ns); $n = 3$.

Following further the pathway of the high-pressure channel, section C also shows a transition range with a corresponding Reynold number $Re_C = 2,348$ at 1,500 bar and $Re_C = 2,444$ at 1,750 bar in Table 15. However, there are no obvious phenomena in Figure 46 that would indicate any transitional effects on Z-averaged droplet sizes or Pdl in the pressure range of 1,500 to 1,750 bar. This is different when studying the increase of the flow rate with increasing pressure in Figure 47a and the temperature increase in Figure 47b measured by infrared thermometry at the outflow of the emulsion from the high-pressure Y- and Z-channels used. Both diagrams show an interruption of the steady increase between 750 bar and 1,000 bar and between 1,500 bar and 1,750 bar. Correlating these facts with the Reynolds number increases in the different sections reveals that there is a quantitative correlation with the laminar-turbulent transitions in: i) section B (for P between 750 bar and 1,000 bar) and ii) section C (for P between 1,500 bar and 1,750 bar). Moreover, there is also a clear correlation between Figure 47a and 47b, which is not self-evident since both figures are based on independent measurements (time duration of outflow vs. temperature of outflow): On the one hand, the volume flow in Figure 47a stops increasing, most likely due to a transitional effect of the flow morphology in a specific section of the pathway, at lower Q in section B and at higher Q in section C. On the other hand, the temperature increase is interrupted at the same transition ranges as is the flow rate Q . This means that when there is also no increase in the fluid transport per unit time, there is an unchanged conductive heat transfer from the fluid

volume, in which frictional energy dissipation takes place to the stainless steel surrounding of the high-pressure channels. However, flow rate and temperature T do not increase completely proportional in the full pressure range as can be seen in the high-pressure range with a very strong increase of T at 2,000 bar.

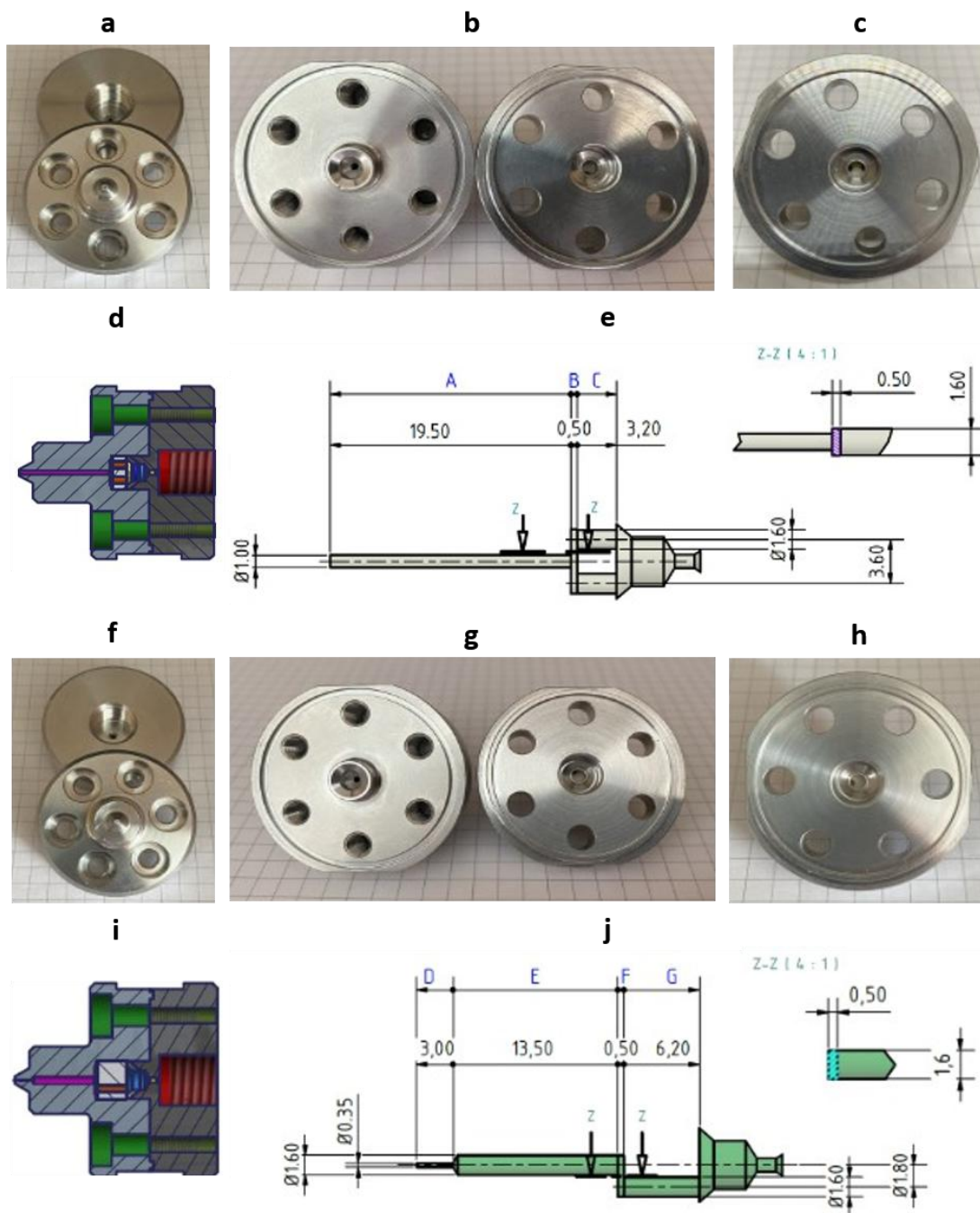


Figure 48: Photographs and CAD drawings of the opened Y- and Z-channel types with the interaction chambers inside. (a – c) Pictures of the Y-channel of type F12Y, (f – h) pictures of the Z-channel of type H20Z, where a and h show the outer surfaces of the channels, b and g show the inner surfaces of the channels, and c and h show a detailed view of both channels focused on the ceramic disc therein. (d and e) Drawings of the Y-channel of type F12Y, (i and j) drawings of the Z-channel, where e and j show a detailed drawing of the dimensions of the Y-channel (e) and Z-channel (j).

Analyzing the Reynolds numbers Re in the Z-channel (H2OZ), it can be found that they are all in the regime of turbulence for all segments D – G and all pressures, except for the circular segments E and G at 250 bar. Transition to turbulence takes place between 250 bar and 500 bar where $Re_{E,G}$ equals 1,474 and 2,562, respectively. However, the laminar shear rate is not very high in these two segments before transition to turbulence. Their maximal wall shear rate is around $9,200 \text{ s}^{-1}$ – much lower than the shear rate in the pre-emulsifying Ultra-Turrax® ($19,300 \text{ s}^{-1}$) and the shear rate in the Y-channel's segment B before the onset of turbulence ($49,800 \text{ s}^{-1}$). Therefore, the laminar-turbulent transitions in the Z-channel do not have a measurable effect on particle homogenization in the studied parameter range. This comparison shows that for a laminar-turbulent transition to become effective, also the shear rate must be in an elevated range in the laminar flow regime. Due to the linear shear gradient in laminar flow and the nonlinear shear gradient in the turbulent flow range, volume-averaged shear is more effective in the laminar range compared to the turbulent range (see discussion section). Another consequence elucidated by the comparison of the flow patterns in the Y and Z-channels is relevant: only the serial arrangement of the Y- and Z-channel causes an enhanced friction and pressure drop in both channels. This higher dissipation shifts the transitions to turbulence to the higher pressure range, in our case between 750 bar – 1,000 bar (segment B) and 1,500 bar – 1,750 bar (segment C). This combination of both flow-induced (shear) and pressure-induced effects (cavitation, vibrations and elasticities of both solid channels and high pressure-induced compressible fluids) cause the homogenization which is presented here.

4.2 The Geometry of the Interaction Chambers and Calculation of Reynold Numbers

In order to obtain precise knowledge of the channel geometry, the high-pressure channels were opened, dimensioned and CAD drawings were designed for illustration purposes. The two image sections of Figure 48a and 48f show the inlet orifice of the Y- and Z-channel, respectively. Surprisingly, the inlet is smaller for the Z-channel than for the Y-channel, although the Z-channel width is specified as $200 \text{ }\mu\text{m}$ according to the manufacturer. The Y-channel is specified with a channel width of $75 \text{ }\mu\text{m}$. Figure 48c shows two

off-centered, laterally symmetric holes in the ceramic disc (left and right) which are characteristic for the Y-channel, whereas Figure 48h shows only one off-centered hole in the ceramic disc, characteristic for the Z-channel (left). Figure 48d shows that the inlet to the interaction chamber is significantly larger for the Y-channel compared to Figure 48i for the Z-channel. In addition, when comparing Figure 48e and 48j (detailed drawing of the channel dimensions), it can be seen that the volume flow for the Y-channel is divided into two parallel tubular channels re-uniting in the interaction chamber.

4.3 Preparative Separation of Particle Species

In order to separate the liposomes that were added as emulsifiers for the perfluorocarbon-in-water emulsion, a density-driven sucrose gradient (20 – 60 % (w/v)) was used. For its use, 0.8 mL of sample was added as top layer above 8.2 mL of the sucrose gradient. After centrifugation (4,000 x g; 30 min), the fractions F1 to F9 were removed by slow and careful pipette aspiration from top to bottom. Figure A 2.16 in the Appendix A2 shows a test run for the separation of liposomes labeled with Lissamine™ Rhodamine DHPE (0.1 mol%), without addition of a perfluorocarbon phase. Here, only fractions F1 (82.8 %), F2 (11.8 %) and F9 (5.4 %) contain the total recovery of the fluorescently labeled phospholipids. The fact that fraction 9 contains liposomes is interpreted as an artefact resulting from the aspiration technique applied to remove the different fractions by pipetting, leaving a thin wall layer which is finally aspirated together with fraction 9. Based on this background, the following analyses are undertaken and interpreted in the way that fractions 1 and 2 contain liposomes while fraction 9 is not interpreted quantitatively as it not only contains some small contamination by liposomes but being the collection basin which is contaminated by the wall layers of all fractions F1 – F8.

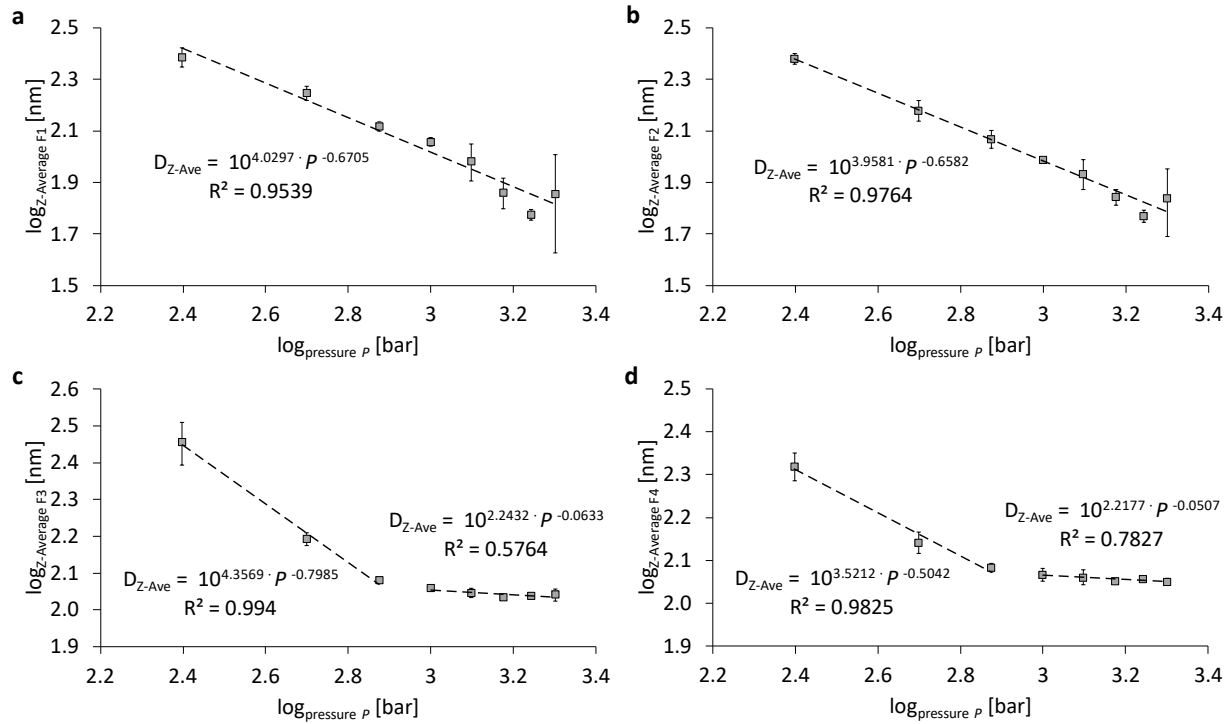


Figure 49: Logarithmic representation of the pressure-dependent particle size (Z-Average) after separation using a sucrose gradient. Representation of the Z-Ave of (a) fraction 1 (F1), (b) fraction 2 (F2), (c) fraction 3 (F3) and (d) fraction 4 (F4). The dots represent the mean \pm SD, $n = 3$.

Figure 49 shows the pressure-dependent particle size after separation of the nanoemulsions using a sucrose gradient. There is a power-law relationship between particle size and homogenization pressure for fraction 1 (Figure 49a) and fraction 2 (Figure 49b), which exclusively contain liposomes and no PFC emulsion droplets. The liposomes' size decrease is: $Z\text{-Ave} \sim P^{-0.65}$, so $D \approx 1/\sqrt[3]{P^2}$ with correlation coefficients of the regression $R^2 > 0.95$. For both fractions, there is a limit of size miniaturization at 1,750 bar at a size of $D \approx 50$ nm. For fraction 3 (Figure 49c) and fraction 4 (Figure 49d), size miniaturization is effective for $P \leq 750$ bar with a power-law exponent of -0.8 and -0.5, respectively. In contrast, for $P \geq 1000$ bar no effect of the pressure P is visible on the Z-averaged droplet sizes with minimum Z-Ave of $107.8 \text{ nm} \pm 1.5 \text{ nm}$ for F3 and $112.7 \text{ nm} \pm 1.8 \text{ nm}$ for F4. For the fractions F5 to F9, shown in Figure A 2.1, the size decrease in the lower pressure range $P \leq 750$ bar still occurs, but without a clearly correlated power-law in this range and without significant size change for $P \geq 1,000$. Minimum Z-averaged sizes in the high-pressure range are: $149.6 \text{ nm} \pm 2 \text{ nm}$ (F5); $176.4 \text{ nm} \pm 4.88 \text{ nm}$ (F6); $179.2 \text{ nm} \pm 3.2 \text{ nm}$ (F7) and $194.7 \text{ nm} \pm 16.9 \text{ nm}$ (F8), see Figure A 2.1.

In addition to the evaluation of the PFC droplet size after separation using a sucrose gradient, the assessment of the count rate percentages is relevant and shown in Figure

50. The maximum Derived Count Rate percentage (DCR%) of the liposomal fractions (F1 + F2) changes from 54.1 ± 2.6 DCR% at 250 bar to 2.2 ± 0.5 DCR% at 2,000 bar. Here, a power-law relationship between pressure and DCR% over the total pressure range can only be seen for fractions 1 plus 2 (Figure 50a) with a correlation of $\text{DCR\%} \sim P^{-1.6335} \approx 1/\sqrt[3]{P^5}$ meaning that the DCR% of the liposomes is approximately reduced to one third upon doubling the pressure. This is the rate by which liposomal phospholipid bilayers are transformed into emulsifying monolayers with increasing pressure. Further, it can be seen that the liposomal fraction is reduced by this power-law regression, irrespective of the changes of the flow regimes as explained for Figure 46 and Figure 47. This means that the transformation of liposomal bilayers into emulsifying monolayers is triggered by the increasing pressure drop, not by flow rates, shear rates or temperature increases, because the latter have transition plateaus, Figure 46 and Figure 47 while Figure 50a does not show such a plateau. A pressure-induced mechanism which destabilizes the integrity of liposomes is cavitation which linearly scales with the static pressure and could therefore be the cause of the transformation of phospholipid bilayers into emulsifying monolayers.

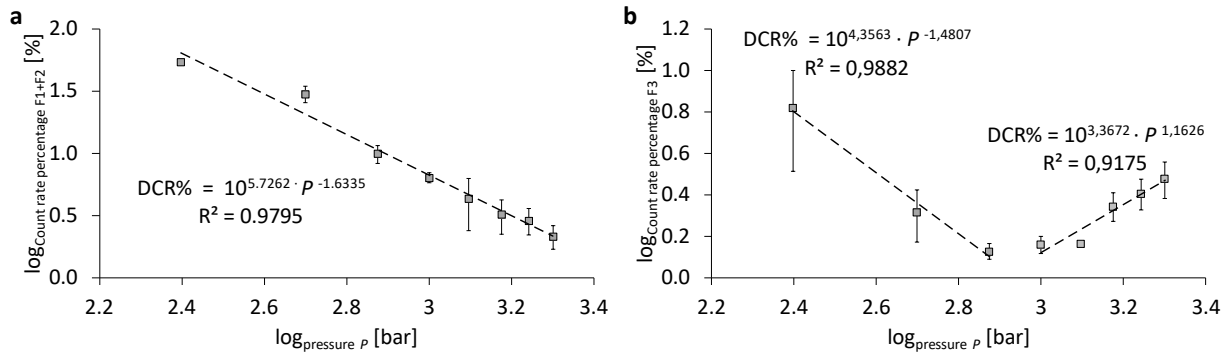


Figure 50: Logarithmic representation of the pressure-dependent count rate percentages of selected fractions after separation using a sucrose gradient. Representation of (a) fraction 1 and fraction 2 in total (F1 + F2) and (b) fraction 3 (F3). The dots represent the mean \pm SD, $n = 3$.

For fraction F3, the decrease in DCR% scales with $P^{-1.4087}$ for $P \leq 750$ bar and with $P^{+1.1626}$ for $P \geq 1,000$ bar. The relative decrease of fraction F3 with a minimum at 750 bar and 1,000 bar is to some extent the consequence of the increase of the DCR in absolute numbers as shown in Figure 46d which means that at pressures of 500 bar and 750 bar the total number of emulsion droplets created is strongly increased. The results for fractions F4 to F9 are shown in Figure A 2.2 in the supplement in their pressure dependency.

Generally, all fractions F4 – F9 increase monotonously with increasing pressure which is a consequence of the conversion of phospholipid bilayers from liposomes (fractions F1 and F2) into monolayers emulsifying F4 – F9 and lead to an increase in their DCR%. Only the fractions F7 – F9 decrease in their DCR% for pressures $P \geq 1,000$ bar as a consequence of the high-pressure homogenization. Figure A 2.3 shows an overview of the DCR% distribution of all 9 fractions as a series of 8 pie charts for the 8 pressures from 250 bar to 2,000 bar.

The analysis of the Pdl dependency on the pressure and the fraction number is based on the data shown in Figure A 2.4. As can be seen for all pressures, the lower fraction numbers have higher $Pdl > 0.15$ while the higher fraction numbers have lower $Pdl \leq 0.15$. For $P = 250$ bar, fractions F1 – F5 are in the high Pdl range, for $P = 500$ bar it is F1 – F4 and for $P = 750$ bar it is F1 – F3. In consequence, this means that in order to homogenize the emulsion fractions F3 – F5, a minimum pressure is needed for the break-up of the smallest emulsion droplets while for the liposomal fractions F1 and F2 their $Pdl \geq 0.25$ for all pressures. In fact, the Pdl is even larger after being treated with higher pressures which is a consequence of the fact that liposomes are strongly decreased in their Z-averaged size while the size distribution is obviously not decreased at the same relative rate as the mean. In essence, emulsion droplets can become increasingly homogeneous with increasing pressure while liposomes cannot (Figure A 2.4), but liposomes decrease stronger in their absolute size (Figure A2.1). Moreover, since liposomes have an absolute minimum in their size of about 20 nm (Cornell et al., 1982; Zhigaltsev et al., 2012), liposomes cannot break up into homogeneously sized fragments but rather preserve a minimum inhomogeneity of their bilayer masses. In contrast, emulsion droplets cannot be broken up into the same droplet sizes as liposomes when using phospholipids as emulsifiers, but the size distributions of emulsions are much narrower than those of liposomes when treated by high-pressure homogenization.

4.4 Investigation on Different Numbers of Homogenization Cycles N_c

Figure 51 shows the effects of several homogenization cycles on a pre-emulsified sample by serial passage through a Y-channel and downstream Z-channel at a fixed homogenization pressure of 1,000 bar. For this purpose, the Z-Ave, the Pdl and the DCR were

determined as emulsion characteristics using DLS. For the Z-Ave of the PFC/W nanoemulsion (Figure 51a), there are significant differences between 5 and 10 cycles, 10 and 15 cycles, 5 and 15 cycles, as well as between 15 and 25 cycles. The smallest Z-averaged particle size is observed at 15 cycles with $84.2 \text{ nm} \pm 5.4 \text{ nm}$. The Z-Ave after 20 cycles is not significantly larger with $91.4 \text{ nm} \pm 4.8 \text{ nm}$. The Pdl after 15 cycles of homogenization is significantly higher than at 10, 20, or 25 cycles, but not strongly different at 0.324 ± 0.017 (Figure 51b). The lowest Pdl values can be found after 20 cycles at 0.263 ± 0.007 and 0.253 ± 0.013 after 25 cycles. Considering the DCR (Figure 51c), it is observed that it significantly decreases from 5 to 15 cycles of processing but does not show significant differences from 15 cycles to 25 cycles.

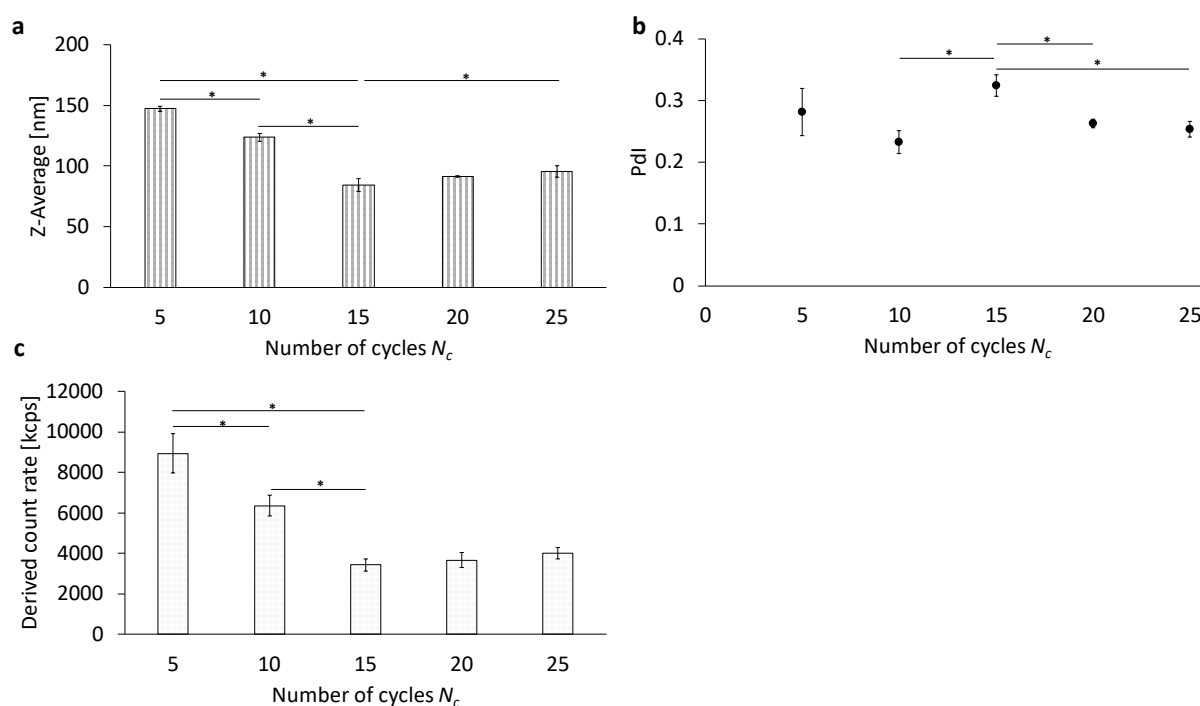


Figure 51: Comparison of different numbers of homogenization cycles N_c . (a) The Z-Average (Z-Ave) (b) the polydispersity index (Pdl) and (c) the derived count rate (DCR) of the PFC/W nanoemulsion after 5, 10, 15, 20, or 25 cycles of homogenization at 1,000 bar. The bars and dots represent the mean \pm SD. A one-way ANOVA followed by a two-sample t-test assuming equal variances was performed at a significance level of $*p < 0.05$; $n = 3$.

Almost identical results for Z-Ave, Pdl and the DCR can be seen after 24 h (Figure A 2.5) and after 48 h (Figure A 2.7) of storage at 4 °C respectively. Figure A 2.6 shows the photographic images of the emulsion replicates after the various numbers of homogenization cycles N_c and subsequent storage at 4°C for 24 h. There is a clear sediment at

cycle numbers $N_c = 15$. Due to the higher density of the perfluorocarbon, it can be concluded that the sediments consist to a large fraction of perfluorocarbons, which, however, have very little difference in their refractive index compared with that of water. Therefore, the white appearance of the sediment must be due to the surface coverage of perfluorocarbon by phospholipids.

To evaluate the particle size distributions of PFC nanoemulsion after different numbers of cycles, separation was carried out using a sucrose gradient. The particle size of fractions F1 to F9 as a function of N_c is shown in Figure 52a. There is an increase in particle size from fraction F3 to F8 for all analyzed cycles, with the particle fractions F1 – F7 being smallest in size after 15 cycles while fractions F8 and F9 show only minor change during the first 15 cycles.

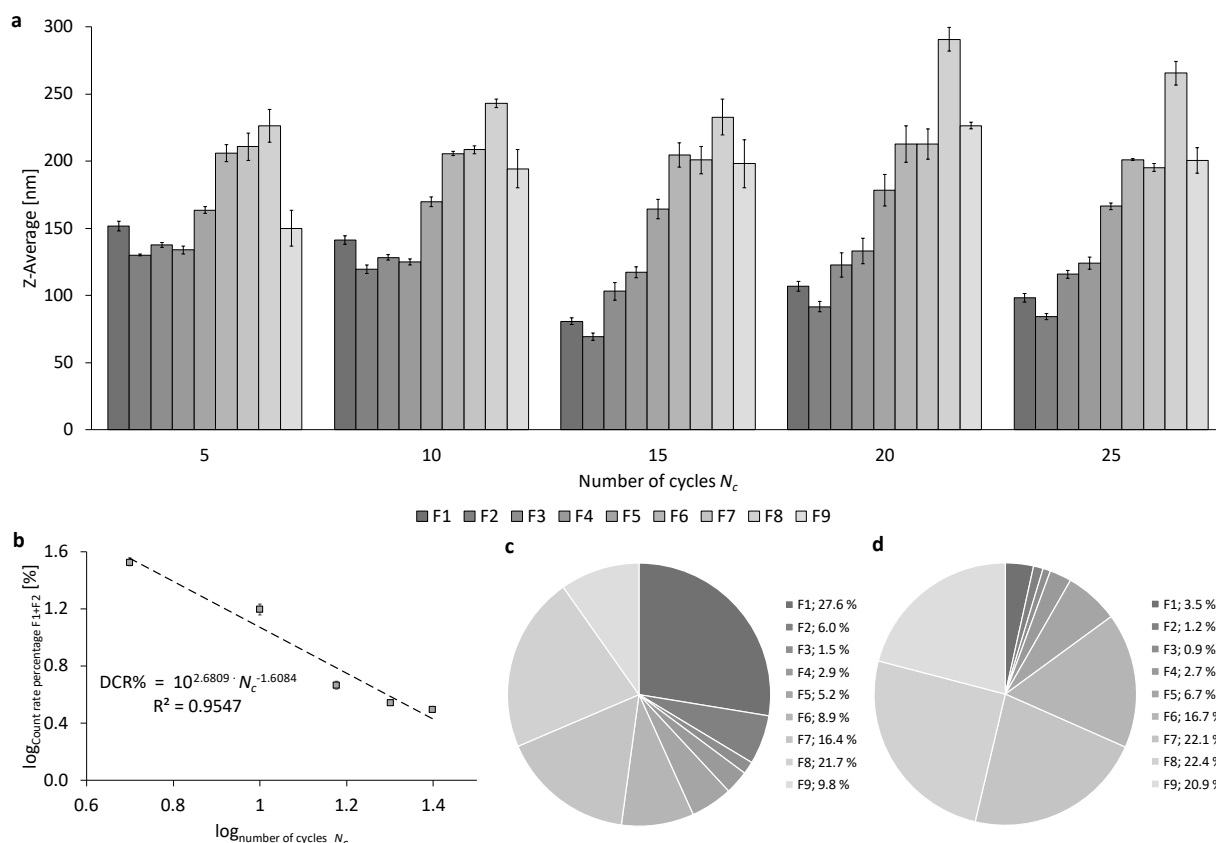


Figure 52: Representation of particle sizes (Z-Average) and DCR% of nanoemulsions after high-pressure homogenization at 1,000 bar with different numbers of cycles N_c , showing the fractions F1 – F9 produced by centrifugation in a sucrose gradient (20 – 60 % w/v). (a) Representation of Z-Ave of PFC droplets in all fractions from F1 to F9, depending on N_c ; (b) logarithmic representation of DCR% for the combination F1 + F2; (c) DCR% of all fractions F1 to F9 of a nanoemulsions homogenized for 5 cycles. (d) Nanoemulsion homogenized 15 cycles. The bars or dots represent the mean \pm SD, $n = 3$.

After 24 h and also 48 h of storage in the refrigerator at 4 °C, there are no significant differences (Figures A 2.8 and A 2.9). Concerning the count rate percentage of fractions F1 and F2 in total, a power-law relationship exists with the DCR% being proportional to the number of cycles N_c , following the regression: $\text{DCR}\% \sim N_c^{-1.6084}$ (Figure 52b) with $\text{DCR}\%(\text{F1} + \text{F2}) = 33.8 \pm 2.2$; 4.7 ± 0.3 ; 3.1 ± 0.1 at $N_c = 5$; 15; 25, respectively. In general, there is a clear change in the DCR%-distribution with an increase in N_c (Figure 52c and 52d). Figure A 2.10 shows the logarithmic representation of the DCR% of fractions F1 and F2 in total after 24 h and 48 h of storage at 4 °C. An overview of the DCR%-distributions depending on N_c directly after production and after 24 h and 48 h of storage can be found in Figures A 2.11 to A 2.15.

4.5 Conclusion

The most obvious discoveries of our study are the two transitions that can be found when studying the flow of mixed suspensions of liposomes and emulsion droplets covered by phospholipids in high-pressure homogenization channels:

The first of these two transitions occurs in the pressure range between 750 bar and 1,000 bar, shown in Figure 46, causing a plateau of the Z-averaged sizes of the particle mixtures and a minimum in the Pdl. This transition is also visible in Figure 47 as a plateau in both the flow rate and temperature with increasing pressure. The second transition in the pressure range between 1,500 bar and 1,750 bar is only visible in Figure 47, causing again a plateau in the flow rate and temperature with growing pressure.

To unravel the origins of these transitions in the respective pressure ranges, the Reynolds numbers Re for the different segments of the Y-channels are shown in Table 15. It can be noticed that transitions from laminar to turbulent flow take place at different pressures for the different segments A, B, and C as shown in Figure 48. In circular segment A, Re_A is already in its transition range at $P = 250$ bar ($Re_A = 2,358$). This means that in the flow range with pressures $P > 250$ bar, turbulent flow is formed in the inflow-bearing segment A of the Y-channel. However, turbulence in this segment is not connected to any of the transition phenomena discussed here. In the rectangular cross-section B, the transition to turbulence occurs between 750 bar and 1,000 bar at $Re_B = 2,111$ and 2,075, respectively. As has been pointed out in the Results section, transition to turbulence in channel flow with an aspect ratio of $\alpha = 0.333$ is very likely to occur between

$Re_{crit, theor.} = 1,679$ (Chang et al., 2012) and $Re_{crit, exp.} = 2,528$ (Chen et al., 2007). Further, it was already clarified that a relaminarization due to the stagnation flow in the T-shaped crossing is very likely, based on experimental results by Sano and Tamai (2016) (Sano and Tamai, 2016) and theoretical analyses by Kaewbumrung and Plengsa-Ard (2024) (Kaewbumrung and Plengsa-Ard, 2024). However, the question remains why only the transition to turbulence in section B of the channel should have an influence on the Z-averaged droplet sizes and not those in sections A and C? This question is studied by a comparison of the shear rates in sections A, B and C at the respective transition Reynolds number Re_{crit} . The maximum laminar shear rate $(\partial u / \partial y)_{max}$ for section B is at $Re_{crit, B}$ ($P = 750$ bar) with $(\partial u / \partial y)_{max} = 49,877 \text{ s}^{-1}$. In contrast, for section A and C these maximum laminar shear rates are $(\partial u / \partial y)_{A max} = 37,726 \text{ s}^{-1}$ and $(\partial u / \partial y)_{B max} = 15,277 \text{ s}^{-1}$ at $Re_{crit, A}$ (@ 250 bar) and $Re_{crit, C}$ (@ 1,500 bar), respectively. This comparison shows that laminar shear stress in the different channels is highest in segment B before the onset of the local transition to turbulence. This comparison clearly explains why segment B is decisive for the minimization of droplet size. The remaining question is why laminar flow has a stronger influence in minimizing droplet sizes compared to turbulent flow? From the pressure exponents it can be seen that the Z-averaged size decreases with $P^{-1.2333}$ in laminar flow, but only with $P^{-0.7852}$ in turbulent flow. This question has to be answered by an analysis of the spatial particle distribution in the rectangular duct cross-section. Studies in laminar flow by Kazerooni et al. (2017) (Kazerooni et al., 2017) and in turbulent flow by Fornari et al. (2018) (Fornari et al., 2018) prove differences in partial segregation and formation of inhomogeneous patterns. In laminar flow, particles are concentrated in a rectangle with a distance between 40 – 90 % from the center of the rectangular duct. In contrast, particles concentrate in the corners, the diagonals and at higher concentrations also the center of turbulent flow in rectangular ducts. As it is also shown by, shear stresses are minimized in these regions (Fornari et al., 2018). This means that particles in laminar flow are transported to a high percentage in high-shear zones while particles in turbulent flow migrate to a much higher proportion into lower-shear zones.

It is relevant to discuss the effect strength of high-pressure homogenization on droplet minimization exerted on the different particle fractions F1 – F9 fractionated by the sucrose gradient (20 – 60 % w/v). As it is shown in Figure 49 and A 2.2, only the liposomal

fractions F1 and F2 are reduced in size over the full pressure range with a correlation between Z-averaged size D and pressure P of $D(F1; F2) \sim P^{-0.67}$. For fractions F3 and F4, the size decrease only occurs for $P \leq 750$ bar with correlations of $D(F3) \sim P^{-0.8}$ and $D(F4) \sim P^{-0.5}$. All fractions F5 – F9 show much lower power-laws of their decrease in size. These findings allow several conclusions:

- a. Only liposomes can be broken into smaller vesicles over the full pressure range and at equal burst rate, leading to a correlation of droplet size D to pressure of $D(F1; F2) \sim P^{-0.67}$.
- b. From the emulsion droplets, only fractions F3 and F4 allow to be considerably reduced in size (with a decreasing rate which scales with $P^{-0.8}$ or $P^{-0.5}$) in the lower pressure range $P \leq 750$ bar. For all other fractions F5 – F9 the power-law exponent is > -0.2 . Moreover, it is apparent that the Z-Ave of fractions F3 are larger than F4. Density fractionation sorts particles of equal density in ascending order of size with increasing sucrose density. Therefore, such inversion can only occur if the density of F3 is (slightly) smaller than that of F4 which is the case for liposome/emulsion aggregates, i.e. the partial attachment of liposomes to emulsion droplets. This scenario is likely since at the lowest pressure of 250 bar, the relative abundance of liposomes (F1 + F2) is $54.1 \text{ DCR}\% \pm 2.6 \text{ DCR}\%$ (Figure A 2.3) which means that at this low pressure, break-up of liposomal bilayers to form emulsifying monolayers is yet very incomplete. In contrast, at 750 bar, the relative abundance of liposomes (F1 + F2) is only $9.9 \text{ DCR}\% \pm 1.7 \text{ DCR}\%$ and at 2,000 bar it is $2.2 \text{ DCR}\% \pm 0.5 \text{ DCR}\%$ (Figure A 2.3). This indicates that emulsification at lower pressures $P < 750$ bar is very incomplete due to the scarcity of emulsifier. Only when most liposomes are broken up, an increase in homogenization pressure leads to a weak decrease of the emulsion droplet sizes $D(F3 - F9) \sim P^{-0.2}$.
- c. In the higher pressure range $P \geq 1,000$ bar, the Z-averaged sizes of the fractions F3 – F9 are of the order of 110 nm (F3); 120 nm (F4); 150 nm (F5); 180 nm (F6); 190 nm (F7); 200 nm (F8), see Figure 49 and A 2.2.
- d. The decrease in the derived count rate (DCR) of fractions F1 and F2 at a rate of $\text{DCR} \sim P^{-1.63}$ shows that doubling the pressure decreases the number of liposomes by 68 DCR%. Correspondingly, the increase of fractions F3 – F9 reflects the break-up of liposomes and their transformation of phospholipid bilayer phases

into emulsifying monolayers with growth rates of about 68 DCR% by doubling the pressure, see Figure A 2.3c.

- e. The polydispersity index Pdl for the different fractions F1 – F9 shows a sharp drop from $Pdl \geq 0.25$ to $Pdl \leq 0.1$ which occurs for F6 at $P = 250$ bar and is shifted to F3 at $P = 750$ bar, see Figure S5. This fact also supports the scenario that the fractions F3, F4 and F5 also contain some aggregates of liposomes with emulsion droplets at low pressures $P < 750$ bar, which makes these fractions more inhomogeneous in their sizes.

In the following, the variation of the number of homogenization cycles N_c is discussed, which sheds more light on the mechanisms of droplet break-up:

- a. The Z-averaged, non-fractionated particle sizes (Figure 51) only decrease for the first 15 homogenization cycles (numbers of cycles $N_c \leq 15$) from 150 to 80 nm and remains constant for $N_c \geq 15$. The following must be taken into account: data with varying N_c are generated at a constant pressure of 1,000 bar while data with varying pressure are taken at $N_c = 6$ and are therefore not comparable in their absolute numbers, only regarding their trends and mechanisms. Considering also the size distribution after fractionation in Figure 52a, it can be concluded that additional homogenization cycles for $N_c > 15$ do not further minimize the sizes of the liposome and emulsion droplet fractions. In contrast, a small increase of the Z-Ave comparing $N_c = 15$ with 25 as can be seen in Figure 51a.
- b. The transformation of the liposome-forming phospholipid bilayers into emulsion monolayers occurs at an equal logarithmic rate of $DCR \sim N_c^{-1.6}$ between 5 cycles and 25 cycles (at constant pressure of 1,000 bar). Roughly speaking, this means that doubling N_c leads to a decrease of the number of liposomes by 67 %.
- c. There is a coincidence in the effect of either doubling of the pressure P exerted on the liposomes or alternatively doubling the N_c which both lead to decrease the DCR% of liposomes by 68% or 67%, respectively. This means that prolonging the shear rates or doubling the shear rates (in the laminar regime where shear rates are proportional to the pressure applied) have the same effect in transforming liposomal bilayers into emulsifying monolayers.
- d. A closer look at the results in Figure 6a reveals that an increase in homogenization cycles beyond 15 cycles results in a small, but significant increase in the

resulting particle size at 25 homogenization cycles. This can be explained by an "over-processing", where the emulsion droplet size increases despite a continued energy input due to a high rate of re-coalescence of new droplets (Desrumaux and Marcand, 2002; Jafari et al., 2007a, 2007b, 2007c; Karbstein and Schubert, 1995; G. Kolb et al., 2001; Olson et al., 2004). It is important to note that the emulsification process is always to be considered as a "balance" of two counteracting sub-processes: droplet break-up vs. re-coalescence (Floury et al., 2004; Perrier-Cornet et al., 2005; Tesch and Schubert, 2002). Freshly produced droplets tend to re-coalesce, i.e. fuse due to thermodynamic instability and incomplete coverage of the interfaces with emulsifier molecules. As a result of Brownian molecular motion and the strong turbulence in the emulsifier systems, the emulsion droplets are subjected to strong relative motion, which leads to droplet collisions (Mohan and Narsimhan, 1997).

As shown here, repetitive cycles of high-pressure homogenization are only effective for a limited number of cycles N_c . For the configuration shown here, 15 cycles are sufficient for the configuration used at a pressure of 1,000 bar. Beyond this threshold, repetitive cycles will not lead to a measurable decrease in the size characteristics of the different particle species and their size fractions. Instead, additional homogenization will progressively lead to increased particle collisions and aggregation effects.

Chapter 5

Formulation Optimization of a PFC/W Nanoemulsion²

In the following chapter, the emulsifying mechanisms of phospholipids during the high-pressure homogenization of perfluorocarbon nanoemulsions are examined in more detail based on the different investigations summarized in Table 16.

Table 16: Chemical composition of emulsions under investigation.

Experimental investigation	Lipids	Composi- tion [mol%]	Lipid concent- ration [mM]	Type of PFC and percentage [% (v/v)]
Variation of cholesterol percent- age	E80/Chol	(100-X):X*	7.5 mM	PPHP, 2.5 % (v/v)
Variation of the total lipid con- centration	E80/Chol	95:5	Y mM**	PPHP, 2.5 % (v/v)
Variation of the fatty acid chain length	DXPC/Chol	60:40	7.5 mM	PPHP, 2.5 % (v/v)
Variation of the phospholipid head group	DPPX/Chol	60:40	7.5 mM	PPHP, 2.5 % (v/v)
Variation of the volume of dis- persed phase	E80/Chol	95:5	7.5 mM	PPHP, Z % (v/v)***
Variation of the volume of dis- persed phase	E80/Chol	60:40	7.5 mM	PFC; 2.5 % (v/v)

* X = 5 / 10 / 20 / 30 / 40 mol%; ** Y = 2.5 / 5 / 7.5 / 15 mM; *** Z = 2.5 / 5 / 10 % (v/v)

² Content of this section is published in the *Soft Matter* Journal and adapted for this thesis: L. Lubitz, H. Rieger, G. Leneweit, „Emulsifying mechanisms of phospholipids in high-pressure homogenization of perfluorocarbon nanoemulsions“; doi: 10.1039/d4sm00828f.

5.1 Investigations on the Emulsifier

5.1.1 Variation of the Cholesterol Percentage

To prepare perfluorocarbon-in-water (PFC/W) nanoemulsions, a pre-emulsion must first be prepared using the Ultra-Turrax® at 15,000 rpm for 10 min. This pre-emulsion, consisting of the perfluorocarbon (PFC, 2.5 % v/v) in a phosphate-buffered phospholipid/cholesterol suspension, was further emulsified by six consecutive runs through the homogenization chamber, also referred to as cycles, at 1,000 bar. The phospholipid component was egg yolk phospholipid with at least 80 % phosphatidylcholine (E80), where the test series focused on varying the corresponding cholesterol content x_{chol} was varied from $x_{chol} = 5$ mol% to 40 mol% (Table 16) as this reflects the physiologically and pharmaceutically relevant range. The results of this variation of the cholesterol content are shown in Figure 53 and A 3.1. Considering the resulting PFC droplet size (Z-Ave, Figure 53a), it can be observed that there is an increasing trend of the Z-Ave with increasing cholesterol content, starting from 10 mol%. The cholesterol dependence of the polydispersity index (Pdl) in Figure 53b, on the other hand, shows a minimum of the Pdl at 20 mol% with 0.320 ± 0.010 and an increase up to 0.470 ± 0.069 at 40 mol%. The derived count rate can be assumed as a relative measure of the number of particles in the emulsion. The DCR shows a maximum at 5 mol% with $5,281 \text{ kcps} \pm 94 \text{ kcps}$ (Figure 53). A comparison of the count rates from 10 mol% to 40 mol% shows a slightly increased droplet count at 20 mol% with $4,223 \text{ kcps} \pm 196 \text{ kcps}$. To evaluate the final PFC/W emulsion, it is important to remove any remaining liposomes from the phospholipid stock suspension from the emulsion. For this purpose, an analytical sucrose gradient with pre-layered sucrose solutions of 20 % (w/v) to 60 % (w/v) is used. After centrifugation for 30 min at $4,000 \times g$ and separation into 9 fractions starting from the top, the liposomes remain in the first two fractions due to their density. For a rough estimate of the proportion of liposomes, the sum of the count rate percentages from both fractions is therefore considered (Figure 53c). There is a linear increase in liposomes in a PFC/W nanoemulsion with 20 mol% to 40 mol%. In total, Figure 53 shows that an increasing cholesterol content in PFC droplets dispersed in water emulsified by lipids leads to larger particles, higher Pdl for $x_{chol} > 30$ mol% and lower particle yields for $x_{chol} > 5$ mol%. Moreover, the emulsification yield, i.e. the conversion rate of phospholipids in

bilayer conformation transformed into emulsifying monolayers is much lower for $x_{chol} > 20$ mol.

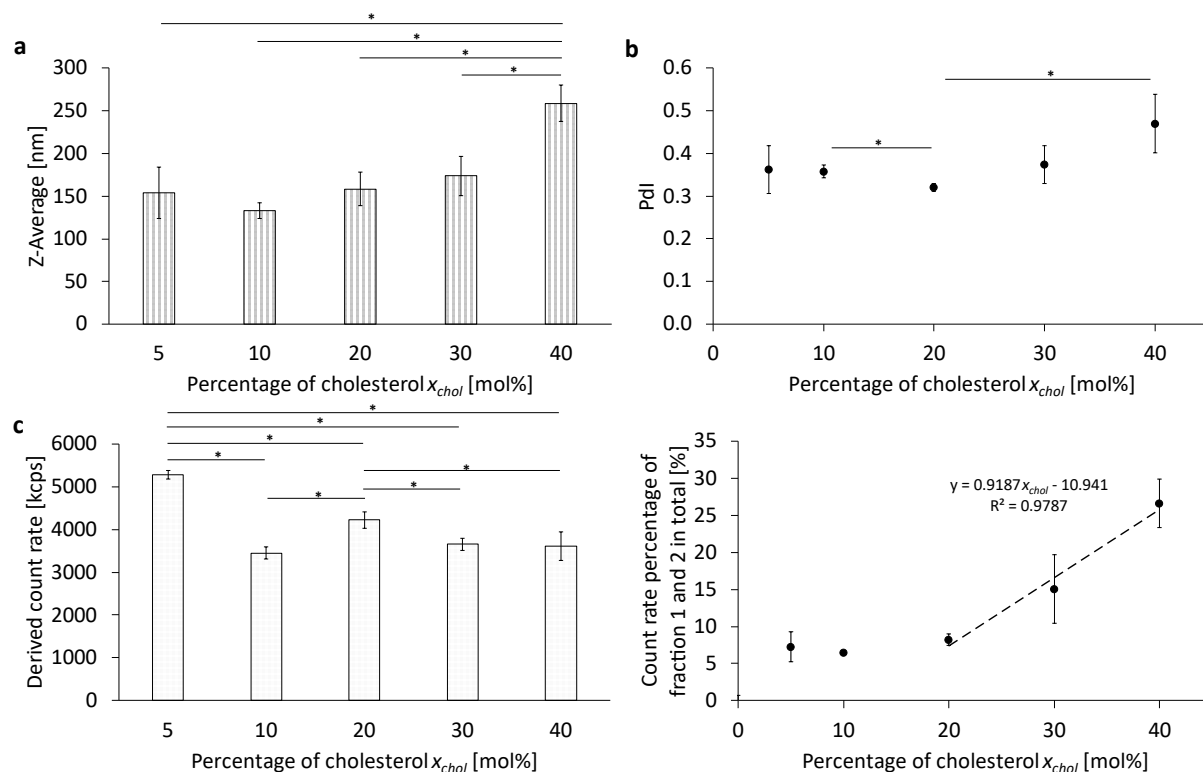


Figure 53: Comparison of different percentages of cholesterol. (a) The Z-Average (Z-Ave) after 6 cycles at 1000 bar without fractionation using a sucrose gradient (b) the corresponding polydispersity index (Pdl), (c) the corresponding derived count rate (DCR) of the PFC/W nanoemulsion and (d) the count rate percentages of fraction 1 and 2 after separation using a sucrose gradient. The bars or dots represent the mean values \pm SD. A one-way ANOVA followed by a two-sample t-test assuming equal variances was performed at a significance level of $*p < 0.05$; $n = 3$.

5.1.2 Variation of the Total Lipid Concentration

Analogously to the variation of the cholesterol content, the total lipid content c_L was varied from $c_L = 2.5$ mM to 15 mM in the PFC/W nanoemulsion in another parameter study (Table 16). The results are shown in Figure 54 and A 3.2.

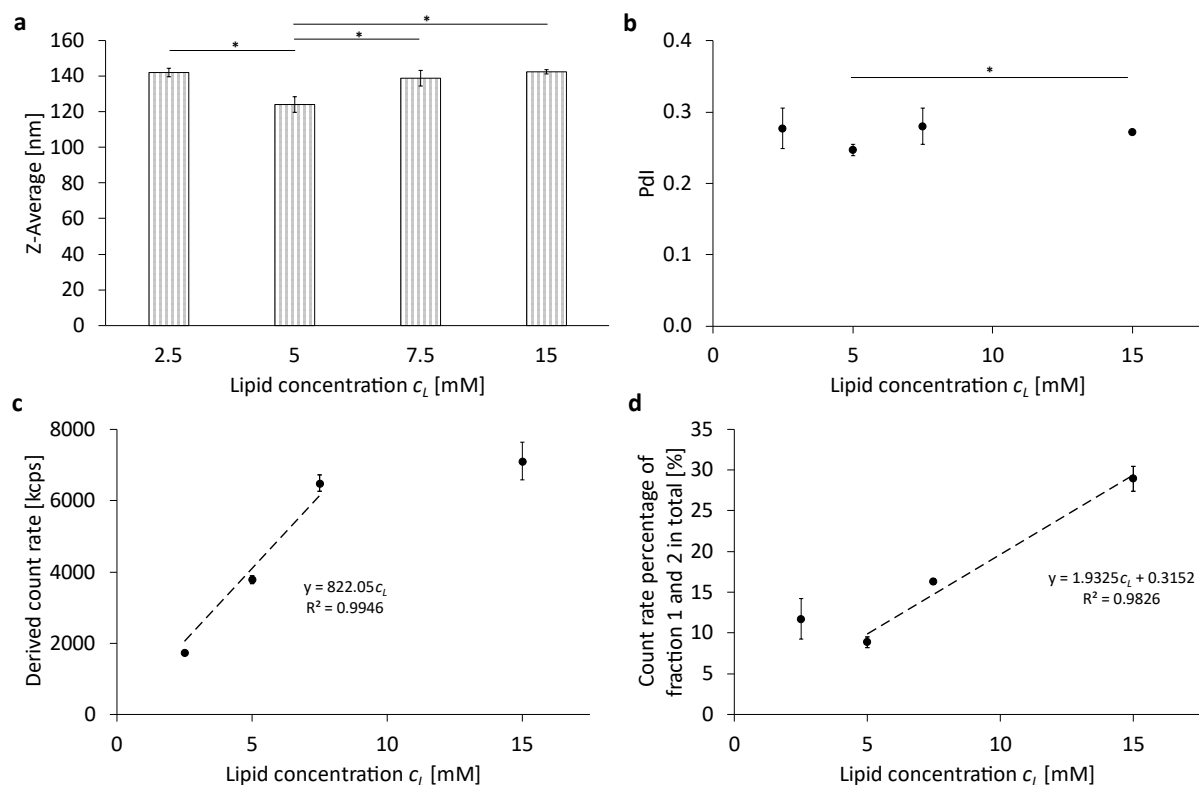


Figure 54: Comparison of different total lipid concentrations. (a) The Z-Average (Z-Ave) after 6 cycles at 1,000 bar without fractionation using a sucrose gradient; (b) the corresponding polydispersity index (Pdl); (c) the corresponding derived count rate (DCR) of the PFC/W nanoemulsion and (d) the count rate percentages of fraction 1 and 2 after separation using a sucrose gradient. The bars or dots represent the mean values \pm SD. A one-way ANOVA followed by a two-sample t-test assuming equal variances was performed at a significance level of $*p < 0.05$; $n = 3$.

A significant minimum in the Z-averaged emulsion drop size (Z-Ave) at $c_L = 5$ mM with a Z-Ave = $124 \text{ nm} \pm 5 \text{ nm}$ can be seen in Figure 54a; the resulting droplet sizes are shown before separation of the nanoparticle species and sizes in a sucrose gradient (Figure 54a). This Z-Ave minimum at $c_L = 5$ mM is about 12.1 % smaller than the mean Z-Ave of all other c_L . A similar result can also be seen in the change of the Pdl in relation to the lipid concentration (Figure 54b). Here, too, there is a minimum of Pdl at 5 mM with 0.247 ± 0.008 , which is about 10.5 % smaller than the mean of all other Pdl. For the derived count rate (DCR, Figure 54c), there is a linear relationship between the DCR and the total lipid concentration from 2.5 mM to 7.5 mM. This relationship indicates two independent processes: for $c_L < 5$ mM there is a shortage of emulsifier, leading to increased drop sizes. For $c_L > 5$ mM, there is an excess of emulsifier, leading to a relative increase in lipids forming bilayers (i.e. liposomes), no longer leading to an increase of emulsifying

monolayers because of the saturation of the droplet surfaces. This can be seen when considering the count rate percentage of fractions 1 and 2 in total, shown in Figure 54d.

Table 17 shows a comparison of lipid molar concentrations with a hypothetical surface area per molecule, calculated by the total surface area of all fractions of emulsion droplets with their fraction-specific size of the Z-Ave and the total volume fraction of the disperse phase, divided by the molar concentration of phospholipids. For the phospholipids, the fractions 1 and 2 are discounted as they do not contribute to emulsification as they persist in their liposomal conformation. Moreover, we apply a yield of 72,48 % of the phospholipids contributing to emulsification, based on phospholipid analysis. For $c_L \geq 5$ mM, a linear relationship to the total lipid concentration is visible which means that doubling c_L leads to a doubling of the relative amount of liposomes among the nanoparticles. The calculation of the hypothetical surface area per molecule is presented in detail in the Table A 3.1.

Table 17: Surface area depending on lipid concentration, considering a minimum surface area per molecule comparable to POPC with $71.0 \text{ \AA}^2/\text{molecule}$ (Klapper et al. 2013).

Lipid concentration [mM]	Hypothetical surface area per molecule [$\text{\AA}^2/\text{molecule}$]
2.5	85.56
5	39.85
7.5	26.36
10	27.69

We approximate the natural blend of the egg yolk phosphatidylcholine E80 by POPC molecules, which have been shown to possess a surface area of about $71.0 \text{ \AA}^2/\text{molecule}$ (Klapper et al., 2013). Therefore, we have to assume that only for the lowest lipid concentration $c_L = 2.5$ mM, a lipid monolayer is formed which is slightly less dense than a phospholipid bilayer of POPC. For $c_L \geq 7.5$ mM, the emulsifiers is apparently forming lipid multilayers. The existence of such multilayers has been proven recently for DPPC and DSPC (Tikhonov, 2020). Since phase boundaries between hydrophilic and hydrophobic phases need an odd number of amphiphilic layers, we have to conclude that multilayers with 3 monolayer leaflets form for $c_L \geq 7.5$ mM while for $c_L = 5$ mM an inhomogeneous

coating of monolayers and triple-layers has to be expected. Summarizing, the phospholipid concentration c_L has an optimum of around 5 mM regarding minimum droplet size and Pdl and maximum emulsification for the given volume V_D of the disperse phase which is $V_D = 2.5 \% (v/v)$. In general terms, this means that a ratio of $c_L / V_D = 2 \text{ mM} / 1 \% (v/v)$ creates an optimum in emulsification efficiency and minimum droplet size and Pdl. Calculations of the total mass of lipids emulsifying PFC droplets allow to conclude that emulsification is only in a monolayer conformation for $c_L / V_D = 1 \text{ mM} / 1 \% (v/v)$ but forms either inhomogeneous mixtures of mono- and triple-layer or homogeneous triple layers $c_L / V_D \geq 2 \text{ mM} / 1 \% (v/v)$.

5.1.3 Variation of the Emulsifier Concerning the Phospholipid Head Group and Chain Length

In another investigation of the various parameters for the formulation of a PFC/W nanoemulsion, the emulsifier itself was varied. On the one hand, the head group of the phospholipid was varied with a constant saturated fatty acid chain length and on the other hand, the reverse case was studied in which the saturated fatty acid chain length was varied with a constant phospholipid head group (Table 16). The phospholipids were selected in relation to already approved pharmaceutical products. Since the studies shown in Figures 53 and 54 were performed with the natural phospholipid blend E80 (containing 80 % egg yolk phosphatidylcholines and 20 % non-cholines), different results have to be expected regarding size ranges, Pdl, and count rates. The results of the chain length variation are summarized in Figure 55 and A3.3. There is a significant maximum particle size (Z-Ave, Figure 55a) for DSPC with $508 \text{ nm} \pm 58 \text{ nm}$. The differences between the shorter-chain phospholipids DMPC and DPPC in terms of particle size and polydispersity (Figure 55b) are not yet significant with the given number of samples tested ($n = 3$) but a trend for a minimum size for DPPC is visible. However, DSPC shows a significant minimum for the Pdl with 0.157 ± 0.102 . The derived count rates (DCR) in Figure 3c show very strong differences between the chain lengths with DPPC being more than doubled compared to DSPC and $> 50 \%$ higher than DMPC. The results in Figure 55c are consistent with those in Figure 55a since smaller Z-Ave necessarily leads to higher count rates at equal volumes of the dispersed phase.

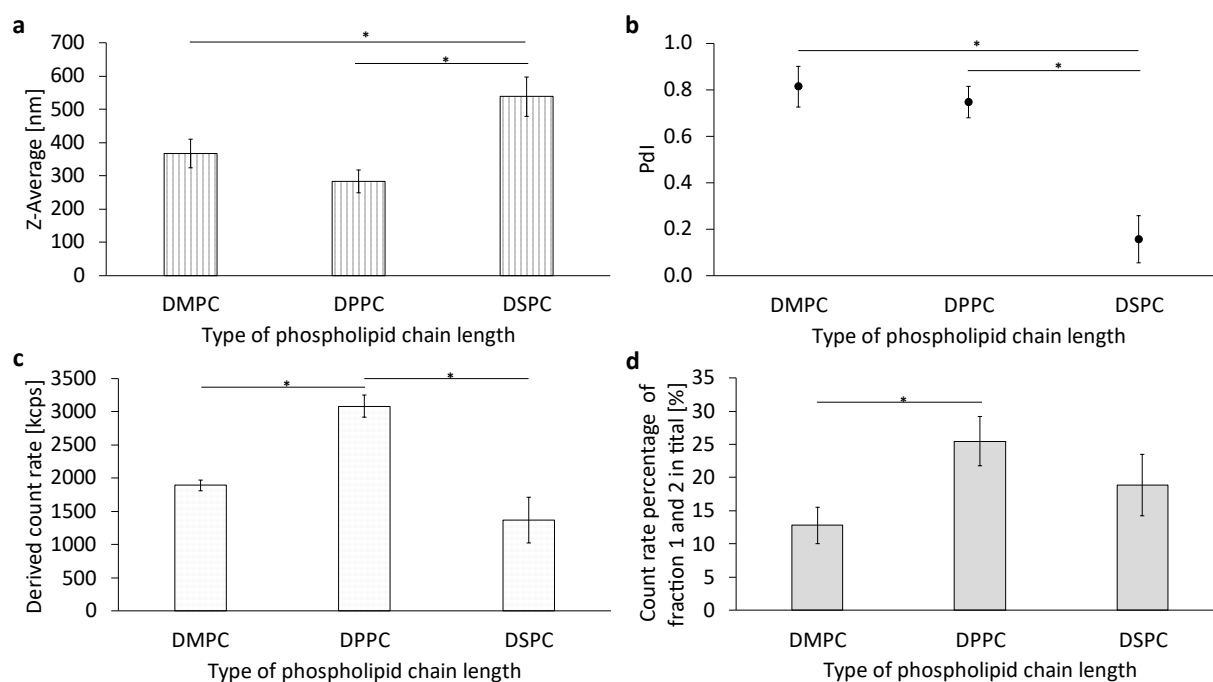


Figure 55: Comparison of different phospholipid chain lengths from 14 to 18 carbon atoms per fatty acid. (a) The Z-Average (Z-Ave) after 6 cycles at 1,000 bar without fractionation (b) the corresponding polydispersity index (Pdl) (c) the corresponding derived count rate (DCR) of the PFC/W nanoemulsion and (d) the count rate percentages of fractions 1 and 2 after centrifugation in a sucrose gradient. The bars represent the mean values with the standard deviation as error bars. A one-way ANOVA followed by a two-sample t-test assuming equal variances was performed at a significance level of $*p < 0.05$; $n = 3$.

The count rate percentages of fractions 1 and 2 shown in Figure 55d reveal a significant difference between DMPC and DPPC. It reflects the fact that DMPC is in the fluid phase at the processing conditions while DPPC is in the gel phase in both monolayer and bilayer conformation. High-pressure homogenization at room temperature (20 °C) leads to a temperature increase due to friction with a final temperature of the nanoemulsion of about 25.8 °C at the processing conditions of 1,000 bar, measured by infrared thermometry at the outlet. This is enough to keep the emulsion above the main transition temperature T_m for DMPC ($T_m = 24$ °C) during processing from the microfluidic channel to the outlet but insufficient for DPPC ($T_m = 41$ °C) and DSPC ($T_m = 55$ °C). The theoretical friction-generated heat by the processing conditions of 1,000 bar is 2.41 K per cycle, i.e. 14.47 K in 6 consecutive homogenization runs. Thus, > 50 % of the generated heat is conducted to the stainless steel tubings of the high-pressure homogenizer. As a conclusion, it can be seen that DPPC produces the smallest nanoemulsion droplets in comparison to DMPC and DSPC. The Pdl of DSPC is the lowest but this fact has to be seen in the context of a Z-Ave which is almost doubled compared to DPPC. The minimum droplet

size of DPPC nanoemulsions is also reflected by a significantly increased derived count rate (DCR). The differences between DMPC, DPPC and DSPC can be interpreted with respect to their main transition temperature which allows DMPC liposomes to transform from the bilayer to the monolayer conformation with a liposomal residue of only about 13 %, but due to the fluidity of its monolayer, droplet coalescence is much more likely, leading to larger droplets.

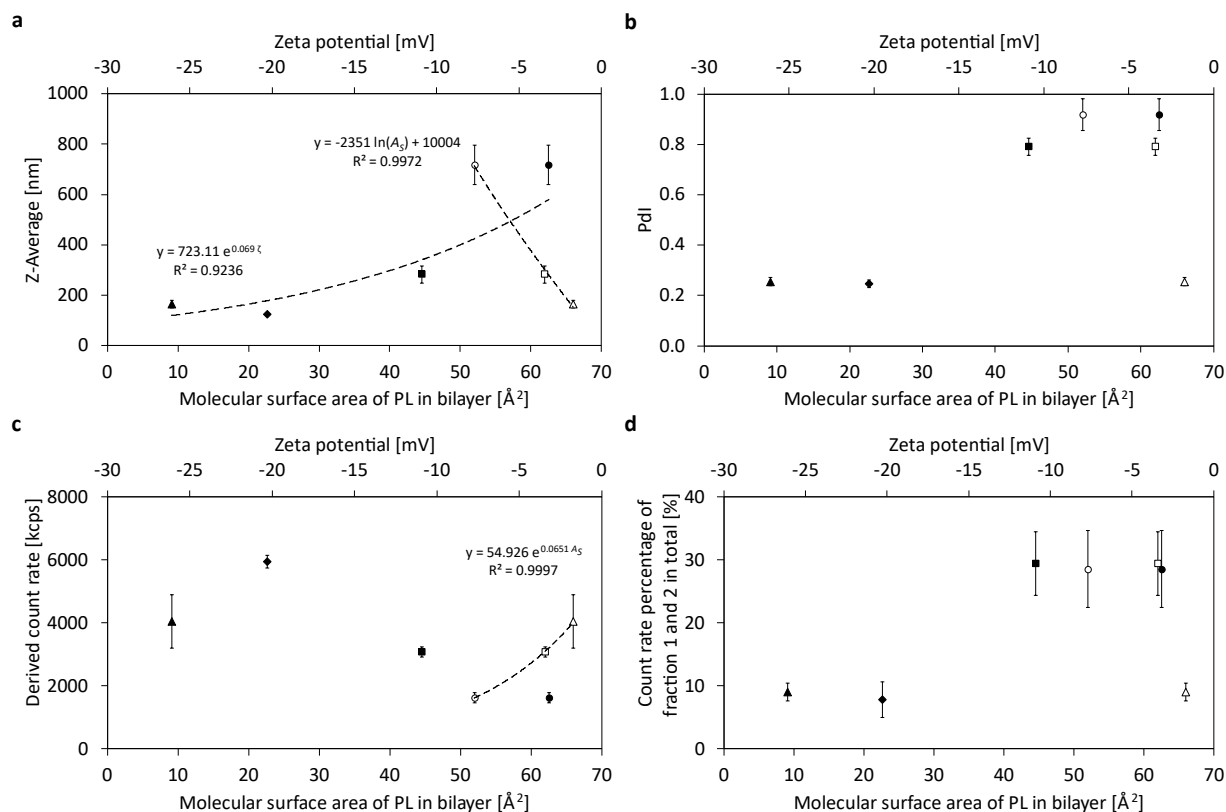


Figure 56: Comparison of the phospholipid head groups DPPE (●○), DPPC (■□), DPPG (▲△) DPPA (◇) correlated to the molecular surface area of the phospholipid in a bilayer or correlated to the Zeta potential. Open symbols indicate the ζ -potentials, closed symbols the respective molecular areas (AS), no literature reference exists for the molecular area of DPPA. (a) The Z-Average (Z-Ave) after 6 cycles at 1,000 bar without fractionation using a sucrose gradient (b) the corresponding polydispersity index (Pdl), (c) the corresponding derived count rate (DCR) of the PFC/W nanoemulsion and (d) the count rate percentages of fraction 1 and 2 after fractionation. The dots represent the mean values \pm SD, $n = 3$.

The results of the head group variation are summarized in Figure 56 and A 3.4. Varying the phospholipid head group reveals a logarithmic relationship between particle size (Figure 56a) and the molecular area for bilayers of the phospholipid head groups of phosphatidylethanolamine (PE), phosphatidylcholine (PC), phosphatidylglycerol (PG) (Kleinschmidt and Tamm, 2002). Bilayer molecular area data for free phosphate (PA)

are not available. On a secondary x-axis, the correlation of the Z-Ave and the Zeta potential (ζ) is shown for all four head groups, DPPE, DPPC, DPPA and DPPG, together with an exponential regression. A linear regression is shown for the polydispersity (Pdl) and the ζ -potential of the four head groups (Figure 56b), proving their correlation. Positive correlations are also found between the derived count rate (DCR) and the magnitude of the ζ -potential and the molecular area (Figure 56c). Looking at the proportion of remaining liposomes in Figure 4d, the head groups can either be regarded in an exponential regression between F1 + F2 percentage vs. ζ -potential. Alternatively, the relationship can also be differentiated into two sub-groups: on the one hand, there are the zwitterionic phospholipids PE and PC, in which a high proportion of liposomes remain in the final nanoemulsion, and on the other hand the anionic phospholipids PG and PA, presented against their ζ -potentials. In the case of DPPG and also DPPA, the proportion of remaining liposomes is significantly lower, i.e. below 10 %, which indicates that liposomal break-up is much more successful by high-pressure homogenization for phospholipids carrying repulsive charges. Summarizing, it can be seen that droplet sizes decrease with increasing ζ -potential and increasing molecular area, the same trend is visible for decreasing Pdl with increasing potential. Contrary, DCR increases with increasing ζ -potential and increasing molecular area. Moreover, the percentage of liposomes persisting the transition into emulsifying monolayers can be assigned to two sub-groups: zwitterionic and anionic phospholipids, the former having high liposomal percentages of almost 30 % while the latter are clearly below 10 %. Thus, higher ζ -potentials and molecular areas lead to lower particle sizes, lower Pdl and smaller fractions of remaining liposomes. These facts indicate that stronger repulsive forces and steric hindrances lead to better emulsifying properties.

5.2 Investigations on the Dispersed Phase

5.2.1 Variation of the Proportion of the Dispersed Phase

In addition to the lipid composition and lipid concentration, it is of interest to vary the dispersed phase of the PFC/W nanoemulsion. For this purpose, the volume fraction of the dispersed perfluorocarbon phase V_D was increased from $V_D = 2.5\%$ (v/v) to 5% (v/v) and up to $V_D = 10\%$ (v/v) (Table 16). Simultaneously, the lipid concentration c_L was kept constant at $c_L = 7.5$ mM, thus producing ratios of $c_L / V_D = 3$ mM; 1.5 mM; or 0.75 mM per 1% (v/v) of disperse phase. The results are summarized in Figure 57 and A 3.5. When looking at the particle size (Figure 57a) after 6 cycles of homogenization at 1,000 bar, a linear relationship between the Z-Ave and the proportion of the dispersed phase can be seen. Thus, the particle size increases with increasing PFC content. In contrast, the Pdl (Figure 57b) and the derived count rate (Figure 57c) show no differences between the different proportions of the dispersed phase. Similarly, there is no difference in the proportion of remaining liposomes between 5% (v/v) and 10% (v/v), but there is a maximum of remaining liposomes at 2.5% (v/v) with $5.7\% \pm 1.0\%$. Thus, the results shown in Figure 57 accurately complement the results from Figure 54 which had proven an optimum of their particle size (Z-Ave) at a ratio of $c_L / V_D = 2$ mM per 1% (v/v) of disperse phase. Clearly, the particle size can be further decreased with an even higher ratio of $c_L / V_D = 2$ mM / 1% (v/v), but this increases the excess amount of liposomes which are not transformed into emulsifying monolayers.

Table 18: Surface area depending on PFC volume percentage.

Volume of dispersed phase V_D [% (v/v)]	Hypothetical surface area per molecule [Å ² /molecule]
2.5	29.69
5	49.67
10	98.92

Table 18 shows the hypothetical surface area per lipid molecule for the varying amounts of the dispersed phase. Analogously to Table 17, it can be concluded that only for a PFC volume percentage of 10% (v/v), a pure monolayer is formed at the emulsions' phase boundaries. This corresponds to a ratio of $c_L / V_D = 0.75$ mM, while for

$c_L / V_D = 1.5 \text{ mM} / 1 \%$ (i.e. 5 % PFC (v/v)), already an inhomogeneous monolayer-multilayer status must be reached while for $c_L / V_D = 3 \text{ mM} / 1 \%$ (i.e. 2.5 % PFC (v/v)), a triple layer is formed.

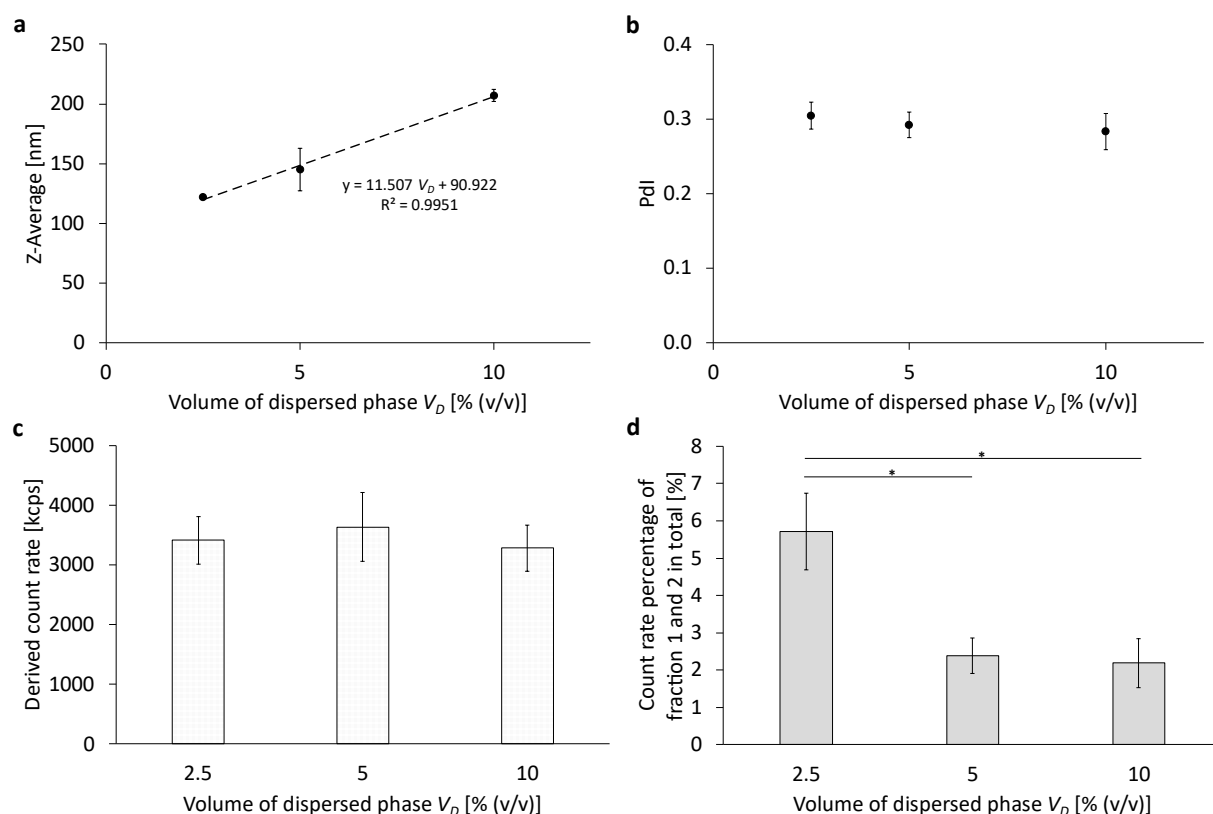


Figure 57: Comparison of different volume percentages of the perfluorocarbon as dispersed phase. (a) The Z-Average (Z-Ave) after 6 cycles at 1,000 bar without fractionation using a sucrose gradient (b) the corresponding polydispersity index (PDI), (c) the corresponding derived count rate (DCR) of the PFC/W nanoemulsion and (d) the count rate percentages of fraction 1 and 2 after fractionation using a sucrose gradient. The bars or dots represent the mean values \pm SD. A one-way ANOVA followed by a two-sample t-test assuming equal variances was performed at a significance level of $*p < 0.05$; $n = 3$.

5.2.2 Variation of the Viscosity Ratio Between the Phases by Varying the PFC

Perfluoroperhydrophenanthrene was used as the dispersed phase in all cases in Figures 53 – 57, which has a dynamic viscosity η of 28.4 mPa·s (Table 19), resulting in a viscosity ratio of continuous to dispersed phase of almost 1:30. For this reason, the viscosity of the dispersed phase was tested in a further series of experiments by changing the perfluorocarbon (Table 16). Table 19 lists the dynamic viscosities as well as the boiling points and densities ρ of the perfluorocarbons used. The limited availability of

perfluorocarbons limits the adjustment of viscosity ratios. The results of varying the viscosity of the dispersed phase are summarized in Figure 58 and A3.6.

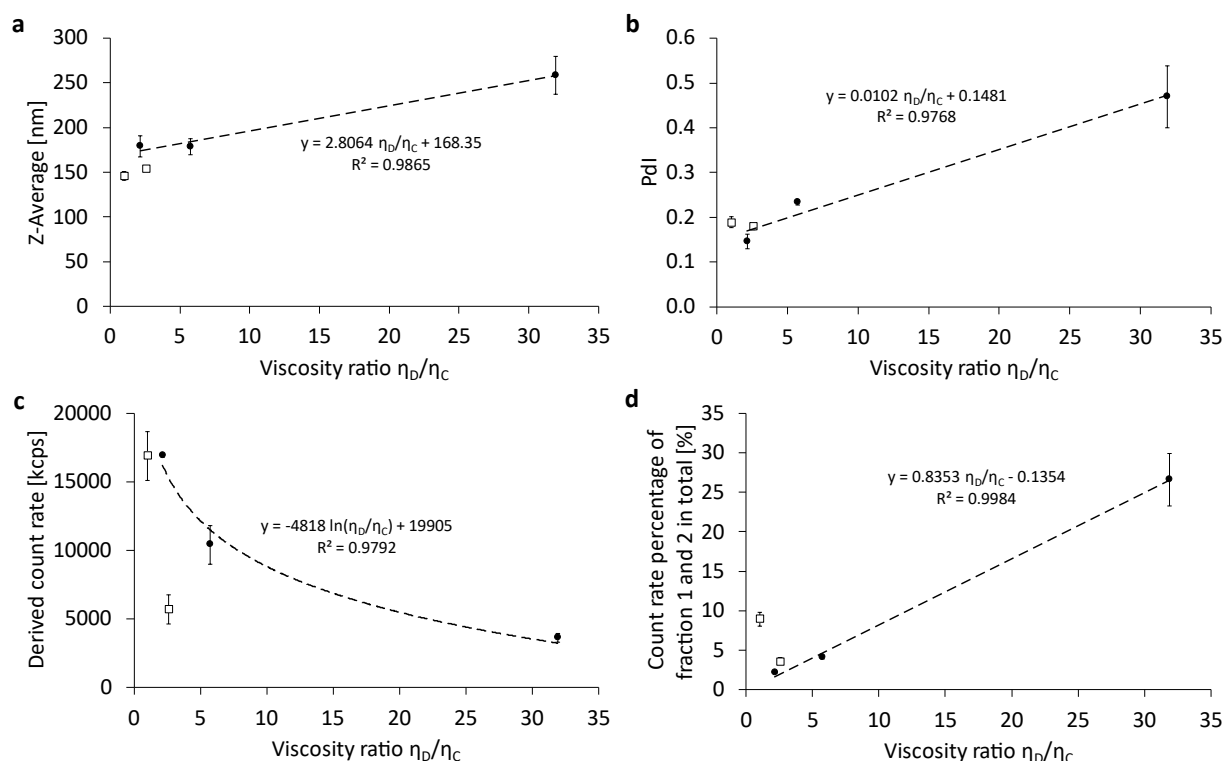


Figure 58: Comparison of different viscosity ratios of the dispersed phase to the continuous phase by variation of the perfluorocarbon, sub-classified as linear (\square) and cyclic (\bullet) perfluorocarbons (PFC) with all regressions shown corresponding only to the cyclic PFC. The continuous phase consisted of water with a dynamic viscosity of 0.89 mPa·s at 25 °C (a) The Z-Average (Z-Ave) after 6 cycles at 1,000 bar without fractionation using a sucrose gradient (b) the corresponding polydispersity index (Pdl), (c) the corresponding derived count rate (DCR) of the PFC/W nanoemulsion and (d) the count rate percentages of fraction 1 and 2 after fractionation using a sucrose gradient. The dots represent the mean \pm SD, $n = 3$.

For the Z-averaged particle size (Figure 58a), the polydispersity index Pdl (Figure 58b) and the count rate percentage of remaining liposomes (Figure 58d), a linear correlation of the respective parameter with increasing viscosity of the cyclic perfluorocarbons is shown. Only the derived count rate of the PFC/W nanoemulsion before separation in the sucrose gradient shows a logarithmically decreasing correlation between the DCR with increasing viscosity of the cyclic perfluorocarbons. As can be seen, the linear PFCs deviate from the correlations for cyclic perfluorocarbons. Minor deviations occur for the Z-Ave (Figure 58a) and Pdl (Figure 58b), but larger deviations are visible for the derived count rate (Figure 58c) and count rate percentage of non-transformed liposomes (Fig-

ure 58d). The dependency of emulsification on the viscosity ratio of dispersed and continuous phases was studied for various practical applications in the last decades (Briceño et al., 2001; Fournier et al., 2009; Hohl et al., 2023; Lewerentz et al., 2023; Pandolfe, 1981; Qian and McClements, 2011). However, most studies focus on emulsion droplets in the micrometer range except for Qian & McClements 2011. Moreover, none of the prior studies applies phospholipids as emulsifiers, but their properties are decisive as Qian & McClements prove by a comparison of β -lactoglobulin and sodium dodecyl sulfate (SDS) with the former having no size increase with increasing viscosity ratio, while the latter increases with a power law exponent of 0.2271 (Qian and McClements, 2011). Comparing our data with those by Qian & McClements (Qian and McClements, 2011) concerning the increase of the Z-averaged droplet size, we find a linear correlation. In absolute numbers, our minimum and maximum viscosity ratios η_D/η_C (1.0 vs. 31.9) in Figure 58a differ in their respective Z-Ave between $179 \text{ nm} \pm 12 \text{ nm}$ and $259 \text{ nm} \pm 21 \text{ nm}$, thus showing a relative size increase of 44 %. For the same viscosity ratios η_D/η_C (1.0 vs. 31.9), the increase in Z-Ave would have been 219 % for SDS as an emulsifier according to the assessment shown by Qian & McClements (Qian and McClements, 2011). This comparison shows that the emulsifying properties of dispersed phases follow 2 mechanisms:

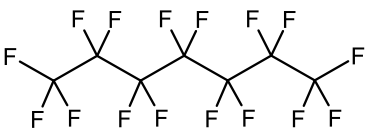
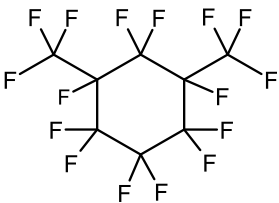
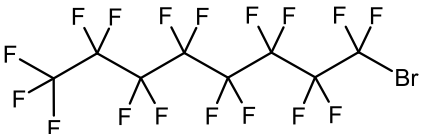
1. The molecular weight of the emulsifier dictates if the mean droplet sizes show a dependency on the viscosity ratio of dispersed and continuous phases η_D/η_C . β -Lactoglobulin (M_w : 19.9 kDa) shows no significant size difference with varying η_D/η_C , egg phospholipid E80 with 40 mol% cholesterol (averaged M_w : 617 Da) has a mild dependency while SDS (M_w : 288 Da) has a stronger dependency in the same viscosity ratio range.
2. In case the emulsifier allows droplet size differences depending on the viscosity ratio, higher η_D/η_C produces larger average droplet sizes.

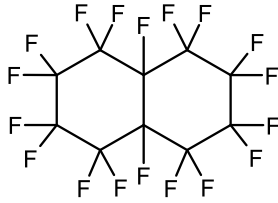
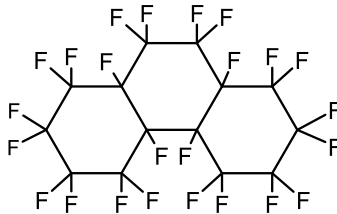
This comparison shows that the mechanical properties of both the emulsifier and the bulk phases' viscosities influence high-pressure emulsification. The influence of the emulsifier has higher priority, as the example of β -lactoglobulin shows, indicating that overcoming the mechanical resistance of the emulsifying mono- or multilayer is the main key for successful droplet size minimization. Ruptures of emulsifying layers obviously lead to direct droplet break-up irrespective of the resistance of a high-viscosity dispersed

phase. In contrast, emulsifiers of very low surface viscosities and elasticities are dominated by the bulk viscosity of the dispersed phase. Summarizing, it can be noted that the averaged particle sizes of emulsification by phospholipids are affected by the viscosity ratio η_D/η_C leading to a mild increase in size with growing viscosity of the dispersed phase.

A similar effect also occurs for the Pdl due to the increase in viscosity for cyclic PFCs of higher molar weight. The DCR is strongly affected by the increase in the viscosity ratio η_D/η_C of the cyclic PFCs. Moreover, linear PFCs seem to have an even stronger dependency on the viscosity ratio, but this effect could also be specific to perfluorooctoyl bromide and would need additional linear PFCs to be confirmed. The count rate percentage of persistent liposomal bilayers not transformed into emulsifiers is also strongly dependent on the viscosity ratio η_D/η_C . Here, linear PFCs also show different characteristics where the properties of perfluorooctoyl bromide cannot be differentiated from those of the cyclic PFCs.

Table 19: Overview of various physicochemical properties of the perfluorocarbons used, such as boiling point, density and viscosity, as well as the corresponding structural formula.

Name	Boiling Point [°C]	Density ρ at 25 °C [g/mL]	Dynamic Viscosity η at 25 °C [mPa·s]	Structure
Perfluoroheptane	82	1.72	0.9	
Perfluoro-1,3-dimethylcyclohexane	102	1.83	1.9	
Perfluorooctoyl bromide	141 – 143	1.93	2.3	

Perfluorodecalin	142	1.94	5.1	
Perfluoroperhydrophenanthrene	215	2.03	28.4	

5.3 Conclusion

Our investigations allow several generalizations and conclusions to be made. In the case of the cholesterol content added to the natural blend of egg phosphatidylcholine (E80), an increase in droplet size ($Z\text{-Ave}$) can be observed with increasing cholesterol content $x_{chol} > 10$ mol%. A general statement can also be made concerning the lipid concentration c_L , as an optimum was found at 5 mM. In combination with the dispersed phase volume fraction V_D used, it results in an optimum ratio of c_L / V_D of 2 mM per 1 % (v/v). By calculation of the mean area per molecule, we show that emulsification is only in a monolayer conformation for $c_L / V_D = 1$ mM / 1 % (v/v) but forms inhomogeneous or homogeneous multilayers for $c_L / V_D \geq 2$ mM / 1 % (v/v). This ratio and the conclusions about monolayer vs. triple layers forming at the PFC/water interfaces were also confirmed in our studies on the dispersed phase volume fraction. For the dispersed volume V_D , it can generally be stated that an increasing V_D leads to an increase in particle size without influencing the Pdl and the DCR. By calculation of the mean area per molecule and comparison to literature we show that emulsification is only in a monolayer conformation for $c_L / V_D = 1$ mM / 1 % (v/v) but forms an inhomogeneous mixture of mono and triple layers or homogeneous triple layers for $c_L / V_D \geq 2$ mM / 1 % (v/v). Concerning the selection of the specific phospholipid composition as an emulsifier, the following conclusions can be made for the fatty acid chain lengths: DPPC consisting of the two saturated fatty acids with 16 carbons without double bonds (16:0; 16:0) generates the smallest nanoemulsion droplets compared to DMPC (14:0; 14:0) and DSPC (18:0; 18:0) and

moreover has a significantly increased DCR. These effects can be correlated to the transition temperature which for DMPC allows re-coalescence of newly formed nanodroplets under processing temperatures ($> 25\text{ }^{\circ}\text{C}$) but remaining below DPPC main transition ($41\text{ }^{\circ}\text{C}$). Durable mechanical break-up and droplet atomization is therefore optimized for fatty acids closely below their main transition temperature. Concerning phospholipid head groups, the following mechanisms can be observed: increasing ζ -potential and increasing molecular surface area of the phospholipid in a bilayer result in droplet size decreases and elevated derived count rates (DCR). Concerning the emulsification efficiency, phospholipid head groups can be divided into two subgroups Zwitterionic phospholipids are significantly less effective in emulsification compared to anionic phospholipids. When considering the viscosity of the dispersed phase η_D , normalized by the viscosity of the continuous phase η_C , a generalized statement can be made. For the particle size, the Pdl and also the proportion of remaining liposomes as a measure of emulsification efficiency, there is a linear correlation with increasing viscosity ratio η_D/η_C . Comparing the emulsification properties of phospholipids with other amphiphiles in the literature (Qian and McClements, 2011), it can be shown that the emulsifier's molecular weight is decisive for a hierarchical combination of emulsification mechanisms. High molecular weight (M_w) emulsifiers are not dependent on η_D/η_C , while smaller molecular weight compounds like phospholipids show a mild increase with growing η_D/η_C . In contrast, low molecular detergents like sodium dodecyl sulfate exhibit a stronger dependency on η_D/η_C . These examples show that overcoming the mechanical resistance of the emulsifier is the main key to successful droplet size minimization. Ruptures of emulsifying interfacial layers obviously lead to direct droplet break-up irrespective of the resistance of a high-viscosity droplet. Thus, the lower the surface viscosities and elasticities of an emulsifier, the more is break-up of droplets governed by the bulk viscosity of the dispersed phase. Finally, it should be noted that the correlations found for different chemical species of perfluorocarbons only apply to cyclic perfluorocarbons while linear PFCs do not always follow these correlations.

Chapter 6

Liposomal Surface Modifications for Targeting Aspects

6.1 Succinimide- and Glucose- Modifications for Elevated Uptake³

In this subchapter, the influence of different liposomal surface modifications on the cellular uptake of liposomes in endothelial or glioma cells is investigated. Figure 59a shows the structure of the different distal ends of DSPE-PEG5k, while Figure 59b shows a schematic representation of the liposomal composition listed in Table 20.

Table 20: Composition of the liposomal formulations.

Sample nomenclature	mPEG	NHS	GLU	APG
Components	Molar ratio [%]			
DPPC	54.9	49.9	49.9	49.9
Cholesterol	40	40	40	40
DSPE-PEG2k	5	5	5	5
DSPE-PEG5k-NHS	-	5		-
DSPE-PEG5k-GLU	-	-	5	-
DSPE-PEG5k-APG	-	-		5
DiD	0.1	0.1	0.1	0.1

³ Content of this section is published in the *Biomedicines* Journal and adapted for this thesis: L. Lubitz, M. Haffner, H. Rieger, G. Leneweit, „Elevated cellular uptake of succinimide- and glucose-modified liposomes for blood-brain barrier transfer and glioblastoma therapy“; doi: 10.3390/biomedicines12092135.

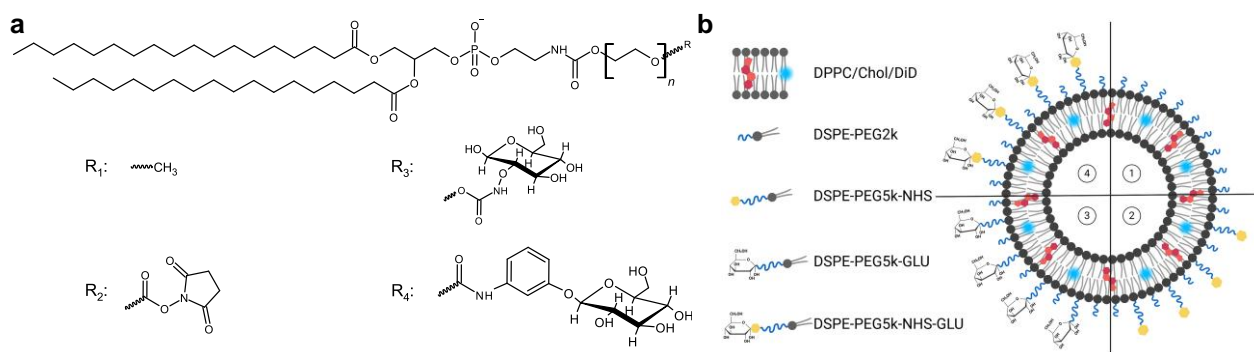


Figure 59: Schematic overview of structures, different liposomal formulations and the reaction scheme of the conjugation. (a) Displays the chemical structures of the liposomal components, (b) illustrates a schematic overview of the four liposomal formulations and (c) shows the conjugation reaction of the succinimidyl-modified phospholipid with the 4-Aminophenyl-β-D-glucopyranoside (APG).

6.1.1 Characterization and Stability of Liposomes

The results of the size and size distribution characterization (Z-Average and Pdl) of the liposomes are summarized in Table 21. All liposomal formulations showed a Z-Average (Z-Ave) of around 100 nm. In addition, all liposomes had a very small size distribution, which can be seen from the low Pdl values < 0.1, except for GLU with a Pdl of 0.159 ± 0.032 .

Table 21: Summary of particle size, polydispersity index and the Zeta potential of the tested liposomal formulations. Values are given as mean \pm SD, n = 3.

Liposomes	Z-Average [nm]	Pdl	Zeta potential [mV]
mPEG	108.5 ± 2.1	0.065 ± 0.028	-3.1 ± 0.3
NHS	104.6 ± 2.3	0.070 ± 0.030	-4.5 ± 4.5
GLU	106.2 ± 1.6	0.159 ± 0.032	-5.4 ± 1.6
APG	106.2 ± 2.3	0.047 ± 0.030	-5.1 ± 1.9

The stability of the liposomal formulations was investigated for four weeks while stored at 4 °C under light-protected conditions. Figure 60a shows the evolution of size over 4 weeks, please note that the y-axis only shows a size range of 100 – 115 nm. Linear regressions of the size evolution of the four liposomal formulations were analyzed by Student's t-test, please see Figure A 4.1. Only NHS liposomes are shown to have a significant size increase. All other formulations showed non-significant fluctuations in particle size over 4 weeks.

The polydispersity index (Pdl) served as a further characteristic for assessing liposomal stability. As presented in Figure 60b, NHS, APG and mPEG showed a similar increase in polydispersity, whereby the increase of the Pdl for NHS and APG are significant. The individual graphs of the trend analysis for the Z-Ave (Figure A 4.11) and the Pdl (Figure A 4.2) can be found in the Appendix A4.

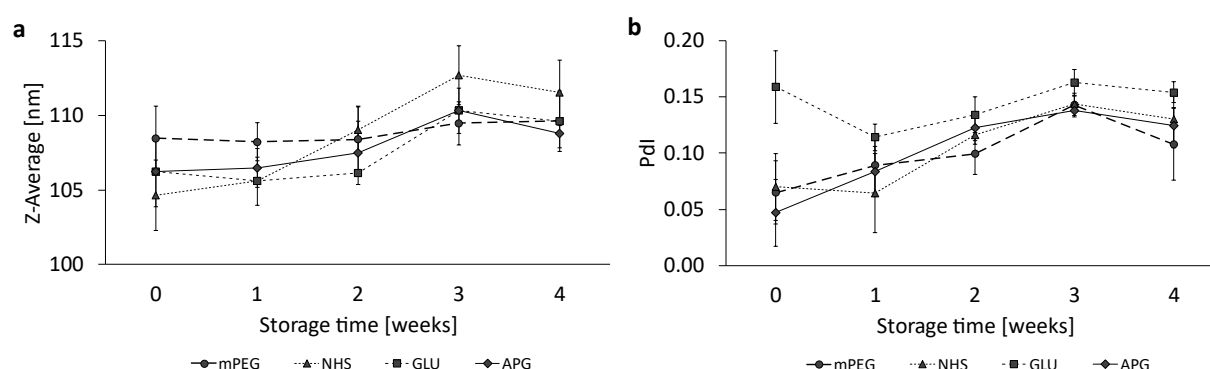


Figure 60: Liposomal stability over a storage period of 4 weeks at 4 °C. Representation of (a) the Z-Average and (b) the Pdl. The dots represent the mean \pm SD, $n = 3$.

The glucose concentrations of the functionalized formulations GLU and APG were determined using the Glucose Hexokinase Assay Kit. The GLU liposomes had a glucose concentration of $0.279 \text{ mg/mL} \pm 0.009 \text{ mg/mL}$ and APG had a glucose concentration of $0.154 \text{ mg/mL} \pm 0.010 \text{ mg/mL}$. Employing the determined cholesterol concentrations, the conjugation efficiency and the molar percentage of the APG post-conjugate as well as the molar percentage of the incorporated DSPE-PEG5k-GLU pre-conjugate were calculated. The conjugation efficiency for APG is 81.40 %, the recalculated molar percentage is 5.85 % while the molar percentage of the glucose pre-conjugate is 10.91 mol%.

6.1.2 Expression Levels of GLUT1 in Endothelial and Cancer Cells under Different Glucose Concentrations

Figure 3 shows the expression of the glucose 1 transporter (GLUT1) in murine bEnd.3 brain endothelial cells (Figure 61a) and human U-87 MG glioblastoma cells (Figure 61b) at different glucose concentrations in the culture medium. Expression was determined by staining of the transporter using the dye-coupled antibody EPR3915 and subsequent flow cytometric analysis.

As shown in Figure 61a, the bEnd.3 cells show the highest expression of GLUT1 at 0 g/L or 1 g/L glucose in the medium with no significant difference. The GLUT1 expression is however significantly lower when cultivated under high glucose conditions with 4.5 g/L. In contrast, human U-87MG glioblastoma cells showed the lowest expression when cultured with low or high glucose conditions in the cell culture medium with no significant difference. Cells cultured under glucose deprivation showed the highest expression.

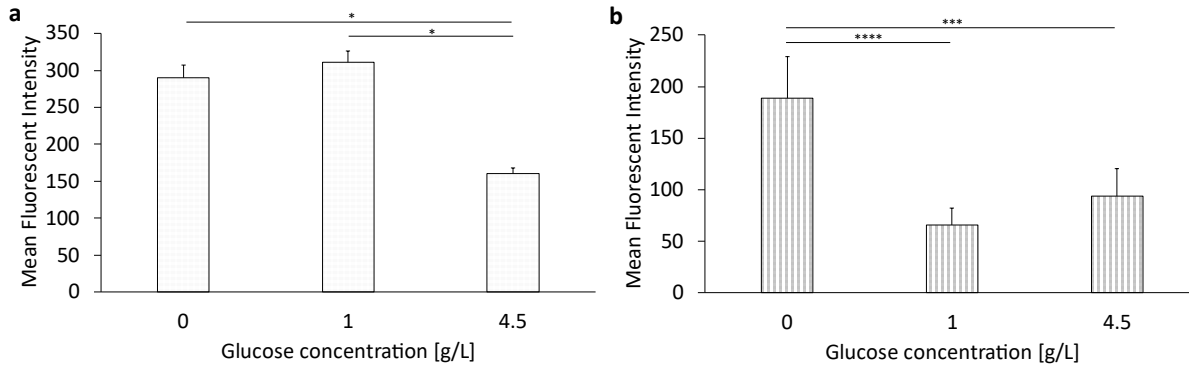


Figure 61: Expression levels of GLUT1 in bEnd.3 cells and U-87 MG cells after culturing with different glucose concentrations in media. (a) Representation of target expression in bEnd.3 cells and (b) U-87 MG cells. The bars represent the mean \pm SD. Statistical analysis: two-way ANOVA followed by Tukey's multiple comparison test. * $p < 0.05$, ** $p < 0.01$, *** $p < 0.001$, **** $p < 0.0001$; $n = 3$.

6.1.3 Cellular Uptake of Succinimide- or Glucose-modified Liposomes in Endothelial Cells

To investigate the ability of liposomes or 2-NBDG as a positive control concerning their internalization in murine bEnd.3 brain endothelial cells under complete deprivation of glucose (0 g/L), the cells were incubated with increasing liposomal concentrations. Figures 62a and 62b show the liposomal uptake at 1 h or 3 h. Figure 62c represents the cellular liposomal saturation and Figure 62d shows the saturation half-time considering an exponential convergence to a saturation maximum according to Ashraf (2020) (Eq. 14):

$$I(t) = S \left(1 - \exp \left(-\frac{t}{k} \right) \right) \text{ with } k = t_{1/2} \ln(2) \quad \text{Eq. 14}$$

Both values, S and $t_{1/2}$, were determined employing a coordinate transformation ($x \rightarrow -x$; $y \rightarrow -y$) and subsequent iterative approximation of the cellular liposomal saturation S

by an exponential fit, approaching a coefficient of variation $r^2 = 1$. The supplementary graphs for the various liposomal formulations can be found in Figure A 4.3 in the Appendix A4. Figure A 4.3g contains exemplarily the cellular liposomal saturation S and the cellular saturation half-time $t_{1/2}$ as red lines.

As can be seen in Figure 62a and 62b, the measurement data of cellular uptake at 1 h and 3 h displayed as bar plots provide the impression of complex relationships of significant or insignificant differences. These are noted by the interconnecting lines with stars for the different levels of significance. At liposomal concentrations of 100 μM and 500 μM , mPEG and GLU liposomes show low uptake while NHS and APG liposomes exhibit significantly higher cellular uptake.

The uptake of mPEG liposomes remains low at the highest liposomal concentration of 1,000 μM (Figure 62b). In contrast, GLU and NHS liposomes have a more pronounced increase in cellular uptake with increasing liposomal concentration, while APG liposomes increase much less at this high concentration.

Cellular uptakes of the four liposomal samples can however only be compared and understood mechanistically by observing the exponential evolutions converging to their specific saturation limits S at different speeds, characterized by the saturation half-times $t_{1/2}$ as shown in Figures 62c and d. NHS liposomes have the highest cellular saturations S for all incubation concentrations c which are doubled when c is increased from 100 μM to 500 μM and show a threefold increase in S upon a 10-fold increase in c from 100 μM to 1,000 μM . The cellular saturation S of APG liposomes increases parallel to that of NHS liposomes, but saturation for APG is at around 67 % of that for NHS at all c . The saturation half-time $t_{1/2}$ of APG liposomes is apparently very small, leading to the fact that cellular uptake is almost complete at 1 h and 3 h, leading to the fact that the exponential regressions cannot be fitted very precisely with $r^2 < 1$. In such cases we use the MFI data at 3 h as a close approximation to S , indicated in Figures 62c and 62d by faded symbols and interconnecting lines.

In contrast to the parallel increases of NHS and APG liposomes, GLU liposomes show very low cellular saturations S at both 100 μM and 500 μM being only about 30 % of those of NHS liposomes. Surprisingly, S increases strongly for the highest c of 1,000 μM so that both GLU liposomes have an S almost as high as NHS liposomes. Different characteristics can be found for mPEG liposomes which can only be fitted with an $r^2 < 1$. Therefore, the fluorescence intensity at 3 h is used as S , showing extremely low cellular

saturations of only 22 %, 13 % and 11 % of the saturation for NHS for increasing concentrations from 100 μM to 500 μM and 1,000 μM , respectively. Thus, increasing c has only a very minor effect on S for mPEG which is only increased by 38 % when c is increased 10-fold from 100 μM to 1,000 μM .

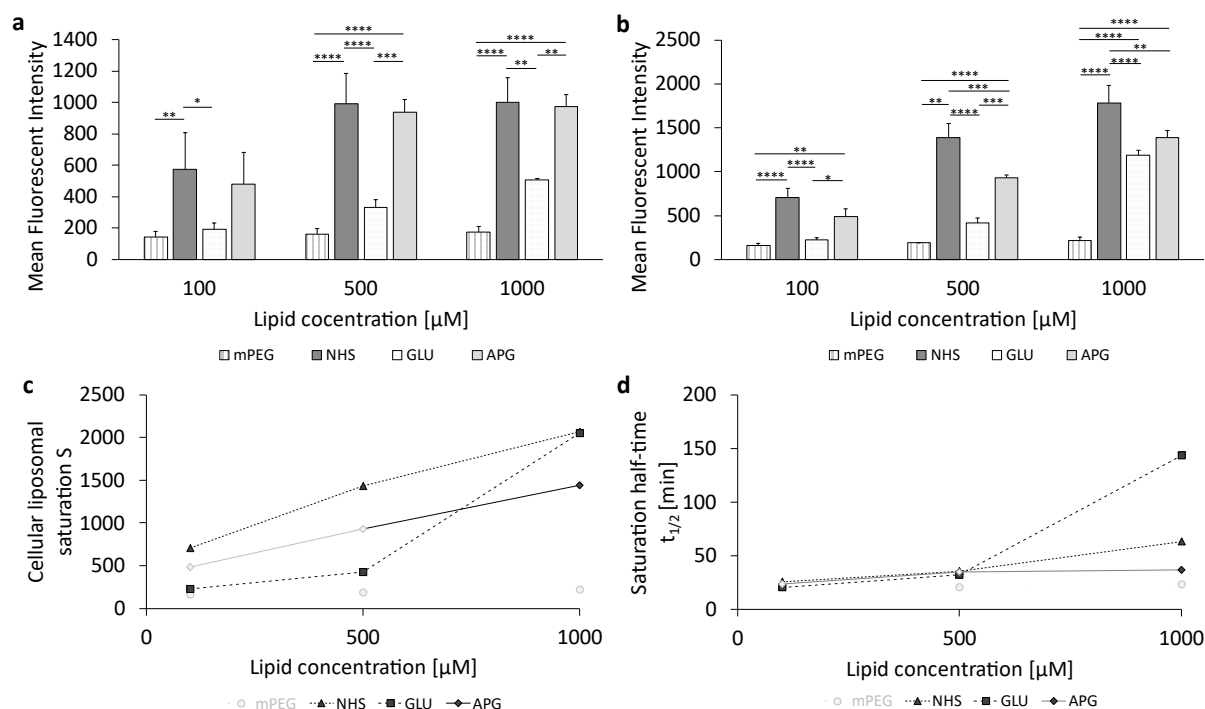


Figure 62: Uptake of glucose-modified liposomes in bEnd.3 cells under complete glucose deprivation conditions. (a) Liposomal uptake in bEnd.3 cells after 1 h and (b) 3 h of treatment. The bars represent the mean \pm SD. Statistical analysis: two-way ANOVA followed by Tukey's multiple comparison test. * $p < 0.05$, ** $p < 0.01$, *** $p < 0.001$, **** $p < 0.0001$; $n = 3$. (c) Cellular liposomal saturation and (d) the corresponding saturation half-time $t_{1/2}$ calculated according to eq. (1). In those cases where the exponential regression only produced $r^2 < 1$, the mean fluorescence intensity (MFI) at 3 h is used as an approximation to the cellular saturation S and these data are shown in faint grey. The data points in faint gray in (d) are calculated using approximate values for the exponential fit.

Figure 62d shows the saturation half-times $t_{1/2}$ for the four liposomal samples. Since the exponential regressions for mPEG are unprecise ($r^2 < 1$), the results are not sufficiently quantifiable but indicate short half-times for all concentrations. Surprisingly, the half-times of all three other samples NHS, GLU and APG are uniform for the lower concentrations 100 μM and 500 μM but diversify for 1,000 μM . Here, APG liposomes are fastest in reaching the saturation half-time, followed by NHS, with GLU being slowest in reaching the saturation half-time, needing almost 4 times longer to reach $t_{1/2}$.

For the cellular uptake of 2-NBDG as a positive control, shown in the supplementary Figure A 4.5. The uptake of 2-NBDG was found to be both time- and concentration-dependent.

6.1.4 Cellular Uptake of Succinimide- or Glucose-modified Liposomes in Glioblastoma Cells

Cellular uptake of different liposomal formulations under complete glucose deprivation was studied also for the human glioblastoma cell line U-87 MG at three different lipid concentrations (100 μ M, 500 μ M and 1,000 μ M) for 2 incubation periods (1 h and 3 h). The results are shown in Figure 63a and 63b. Figures 63c and 63d are similar to Figures 62c and 62d, representing the cellular liposomal saturation S and the saturation half-time $t_{1/2}$ with the corresponding Figure A 4.4.

Contrary to the murine endothelial bEnd.3 cells, human U-87 MG glioblastoma cells show almost uniform cellular uptake. At the lowest concentration of 100 μ M at 1 h, cellular uptake of mPEG liposomes is not yet significantly lower than all other three liposomal coatings (NHS, GLU, and APG) – this only occurs for higher concentrations and longer incubation. Although GLU liposomes have lower MFI at 100 μ M and 500 μ M, this subtle distinction is not significant and vanishes for the highest concentration.

The mechanisms behind these raw data are disclosed by the saturations of cellular uptake and their respective half times as shown in Figures 63c and 63d. As can be seen, the saturations are almost identical for the three surface coatings: NHS, GLU and APG; only mPEG liposomes have substantially lower saturations. The uniformity of the 3 coatings (NHS, GLU, APG) regarding their cellular saturation is contrasted by a strong diversification regarding their half times for the lower concentrations of 100 μ M and 500 μ M as shown in Figure 63d. Clearly, GLU is slowest in cellular uptake (at 500 μ M, not determinable for 100 μ M) and APG is fastest while NHS and mPEG are in between these extremes. Surprisingly, all 4 liposomal coatings produce almost identical half-times at the highest concentration of 1,000 μ M. In total, the human glioblastoma cell line U-87 MG has quite distinct characteristics regarding cellular uptake of PEGylated liposomal with differences in the distal polymer ends: while saturation is identical for all liposomal coatings except for mPEG, the saturation half-times are clearly diversified at low and intermediate concentrations but unify at the highest concentration.

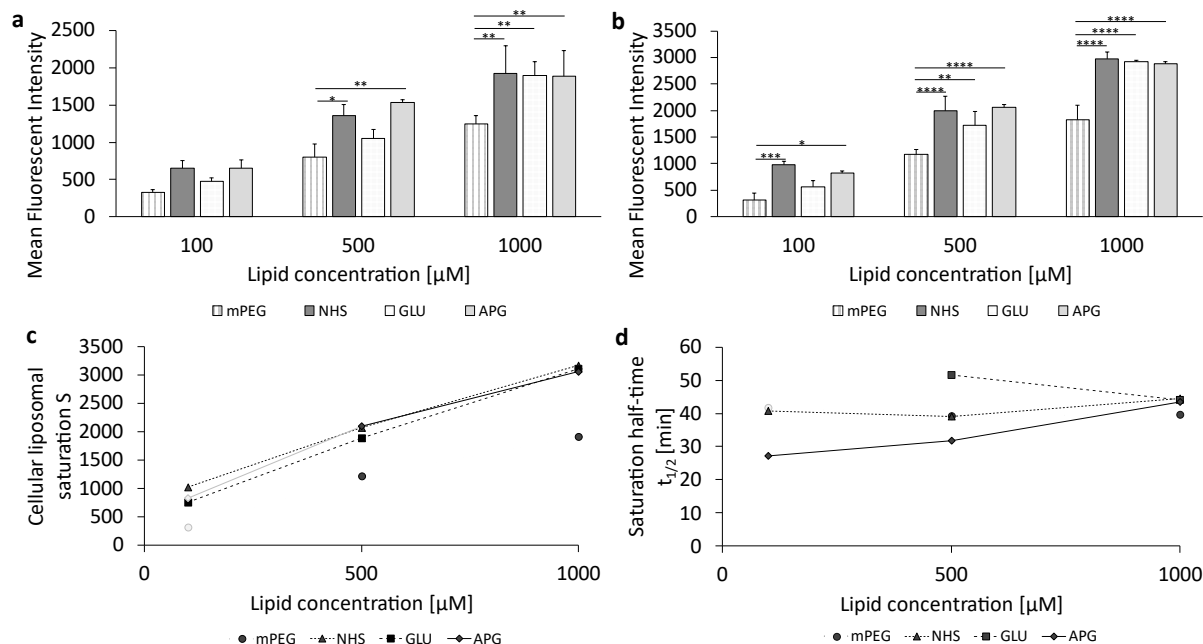


Figure 63: Cellular uptake of glucose-modified liposomes for U-87 MG cells under starving conditions (0 mg/ml glucose in cell medium). (a) Liposomal uptake in U-87 MG cells after 1 h and (b) 3 h of treatment. The bars represent the mean \pm SD. Statistical analysis: two-way ANOVA followed by Tukey's multiple comparison test. * $p < 0.05$, ** $p < 0.01$, *** $p < 0.001$, **** $p < 0.0001$; $n = 3$. (c) Cellular liposomal saturation S vs. lipid concentration as calculated according to eq. (1). (d) Saturation half-time $t_{1/2}$ according to eq. (1) vs. lipid concentration. In those cases where the exponential regression only produced $r^2 < 1$, the mean fluorescence intensity (MFI) at 3 h is used as an approximation to the cellular saturation S , but these data are shown in faint grey. The saturation half-time value for GLU liposomes at 100 μM was discarded due to the insufficient accuracy of the regression.

6.1.5 Expression Levels of 5-HT₇ in Endothelial and Cancer Cells Under Normal Cultivation Conditions

To evaluate the expression of the 5-HT₇ receptor, its staining was performed analogously to GLUT1, using a labeled antibody, the phycoerythrin (PE)-coupled 5-HT₇ antibody AA 405-433, as described in Chapter 3.2.3.2. Cellular staining of the receptor was performed under normal glucose conditions of 4.5 g/L glucose in the culture medium. Comparison of treated cells stained with antibody versus unstained cells showed significant expression of the 5-HT₇ receptor in both bEnd.3 cells (MFI 3631.50 ± 586.90) and U-87 MG cells (MFI 5910.40 ± 486.70).

6.1.6 Cellular Viability After Treatment with the Liposomal Formulations

To assess the cytotoxic effect of the basic liposomal formulations and the functionalized formulation without encapsulated cytotoxic active pharmaceutical ingredient (API), a cell viability assay was performed as described in Chapter 3.2.3.4. The data are shown in Figure 64 and 65 for the bEnd.3 cells and the U-87 MG respectively, with subgraphs a to d showing the four liposomal formulations tested at the three concentrations (100 μ M, 500 μ M and 1,000 μ M).

The bEnd.3 cells (Figure 64) showed a reduction in viability to around 70 % after 3 h of incubation of the cells with liposomes at the highest concentration of 1,000 μ M, except the GLU liposomes (Figure 64c), where the viability was reduced to 62.62 % \pm 7.91 %.

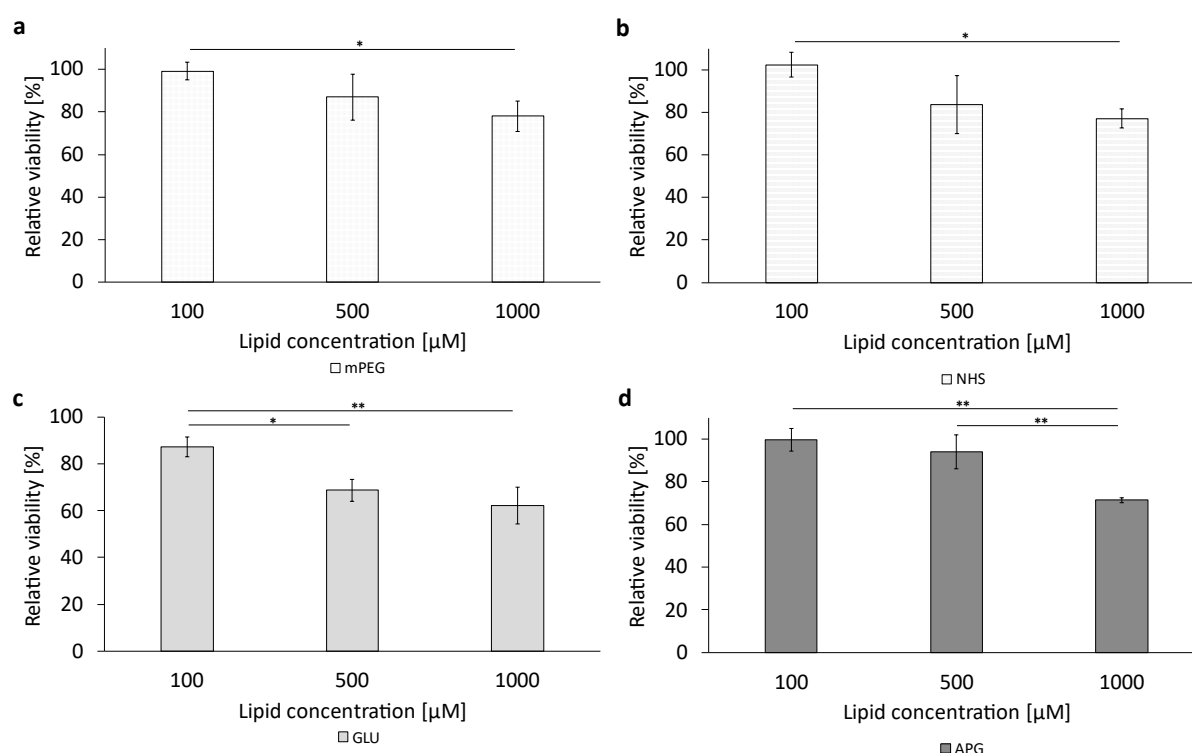


Figure 64: Liposomal cytotoxicity on bEnd.3 cells using alamarBlue™ HS reagent. Representation of all different tested formulations: (a) to (d). The bars represent the mean \pm SD. Statistical analysis: one-way ANOVA followed by Tukey's multiple comparison test. * p < 0.05, ** p < 0.01, *** p < 0.001, **** p < 0.0001; n = 3.

The U-87 MG cells showed a stronger reduction in viability at the highest concentration tested compared to the bEnd.3 cells. Viability decreased to around 60 % for all formulations except for the mPEG liposomes (Figure 65a) with a viability of 42.42 ± 5.26 when incubated with 1000 μM for 3 h.

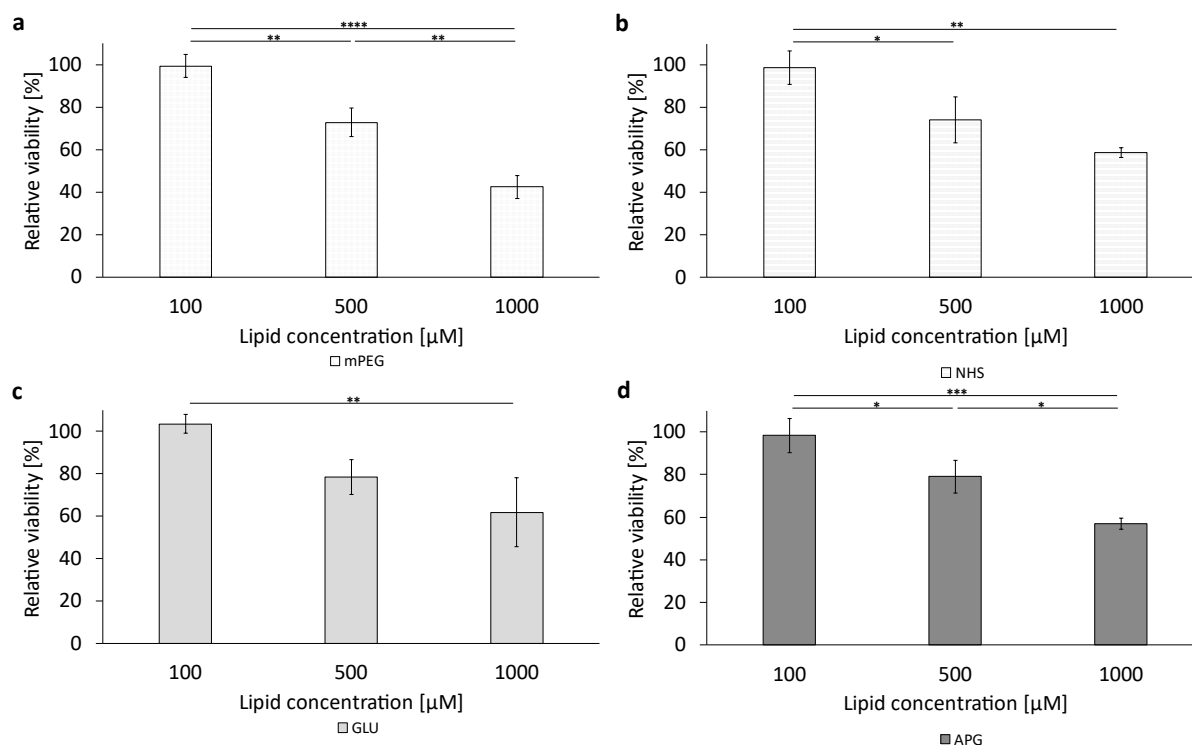


Figure 65: Liposomal cytotoxicity on U-87 MG cells using alamarBlue™ HS reagent. Representation of all different tested formulations: (a) mPEG; (b) NHS; (c) GLU; (d) APG. The bars represent the mean \pm SD. Statistical analysis: one-way ANOVA followed by a Tukey multiple comparison test. * $p < 0.05$, ** $p < 0.01$, *** $p < 0.001$, **** $p < 0.0001$; $n = 3$.

6.1.7 Discussion and Conclusion

Glucose as a ligand has attracted great interest concerning various carrier systems aiming for active targeting, as the glucose transporter is mainly expressed in the endothelial cells of the CNS (Patching, 2017). This is consistent with the results in Figure 61, which shows that GLUT1 expression is generally higher in bEnd.3 endothelial cells compared to expression in human glioblastoma cells U-87 MG. The staining of GLUT1 was performed to determine whether hypoglycemic conditions promote the expression of GLUT1 in bEnd.3 and U-87 MG cells, as described by Simpson et al. 1999, among others (Simpson et al., 1999). The results in Figure 61 show a significant upregulation of GLUT1 under hypoglycemic conditions with complete glucose deprivation (0 g/L glucose) in the

medium. bEnd.3 cells are more sensitive to changes in the glucose concentration in the medium. Already 1 g/L glucose in the medium causes a significant upregulation of GLUT1 compared to its expression at 4.5 g/L while U-87 MG cells do not express more GLUT1 when glucose is reduced from 4.5 to 1.0 g/L. One possible reason for the less sensitive reaction of the tumor cells U-87 MG is the fact that tumor cells have an adapted metabolism. Thus, mitochondria in tumor cells can use lactate as fuel for biochemical reactions to enable cell growth (Chen et al., 2016; Keenan and Chi, 2015).

GLUT1 is present on both the luminal and abluminal membranes of BCECs (Anraku et al., 2017) so glucose deprivation can increase the localization of GLUT1 at the luminal plasma membrane by up to 50 % (Simpson et al., 1999). Thus, GLUT1 moves from the cell interior to the plasma surface depending on the glucose demand in the brain. Generally, endothelial cells have very high glycolytic rates, similar to many cancer cells (Fitzgerald et al., 2018). Nevertheless, the higher liposomal uptake in U-87 MG cells (Figure 63) compared to liposomal uptake in endothelial cells bEnd.3 (Figure 62) indicates that liposomal uptake is not merely triggered by environmental glucose concentration but also by cell-specific metabolic rates.

There is not only a higher uptake of liposomes in the tumor cell line U-87 MG than in the endothelial cells bEnd.3 which is in contrast to the GLUT1 cell surface concentration, but also a fundamentally different uptake behavior between the two cell lines. For example, the endothelial cells bEnd.3 differentiate liposomes concerning the cellular uptake according to their surfaces, as the cellular saturations at low and medium concentrations are very different between the individual liposomal formulations (Figure 62c). The most important finding of this study is that the succinimide residue (NHS) proves to have a much higher liposomal uptake saturation than APG and GLU-coated liposomes, which makes it a very promising and so far largely unexplored candidate for BBB transfer and brain cancer therapies.

Succinimides are widely studied due to their extensive pharmacological applications. Recent studies showed potential applications of succinimide structural analogs as a serotonin 5-hydroxytryptamine receptor ligand (Zhao et al., 2021). However, it should be noted that to date there are no publications on the use of succinimides as ligands of drug delivery systems. The 5-HT₇ receptor is highly expressed in the CNS (Quintero-Villegas 2022), which was also demonstrated in our staining experiments. Binding of succinimide to the 5-HT₇ receptor leads to clathrin-mediated endocytosis (Redpath and Deo, 2022).

The expression of the 5-HT₇ receptor in the U-87 MG cells is increased compared to the bEnd.3 cells, which is shown by the mean fluorescent intensities of around 4,000 and 6,000, respectively. Despite the higher expression of the 5-HT₇ receptor, uptake of NHS liposomes in U-87 cells is not favored over the other modified liposomes. The 5-HT₇ receptor is one of many subtypes of serotonin receptors, so cellular uptake can also occur through other receptor subtypes. Since most 5-hydroxytryptamine receptors are also G-protein coupled receptors, it is of interest for future studies to investigate further details in the uptake mechanism of NHS liposomes by uptake inhibition assays.

In contrast to the uptake in bEnd.3 cells, there is almost no difference in cellular saturation between liposomes with different distal ends of the PEG5k chain in the U-87 MG cells (Figure 63c). When looking at the saturation half-time, it can be seen that the “speed of uptake” in bEnd.3 cells is uniform at low concentrations and starts to differentiate at high lipid concentrations (Figure 62d) whereas in U-87 MG cells it is the opposite. For tumor cells such as the U-87 MG cells, the rate of liposomal uptake differs greatly at low and medium lipid concentrations, but nearly of the same speed for all liposomal formulations at the highest lipid concentration (Figure 63d). The uniformity of the liposomal uptake saturation for all three ligands NHS, GLU, and APG makes it very likely that uptake in U-87 MG cells is not very strongly affected by ligand-specific transporters. This aspect needs to be explored in more detail to find clear proof on liposomal uptake mechanisms in glioblastoma cells.

It has to be assumed that the GLUT1 and 5-HT₇ only serve as a recognition pattern for the liposomes, whereas uptake of liposomes is achieved by other endocytotic mechanisms. This assumption is obvious, as e.g. GLUT1 has a cavitation volume (exofacial occluded) of 4,385 Å³ (Lloyd et al., 2017) whereas a liposome of 110 nm has a volume of roughly 700×10⁶ Å³. Jiang et al. 2014 showed that both caveolae-mediated and clathrin-mediated endocytosis are involved in the cellular uptake of D-Glucose-decorated PEG-PTMC co-polymeric nanoparticles by glioma cells (Jiang et al., 2014). This example demonstrates that only the endocytosis mechanisms can lead to liposomal intracellular uptake.

In general, mPEG liposomes show the lowest intracellular uptake regardless of the cell line or incubation time. This is in line with our previous study (Mellinger et al., 2023), where we were able to show intracellular uptake of mPEG liposomes as an energy-dependent process, as the uptake nearly dropped to zero when incubation is performed at

4 °C. In addition, the intracellular uptake of liposomes in our current study is confirmed by the increasing cytotoxicity with increasing liposomal uptake interfering with the intracellular reducing activity as an indicator of their viability.

GLUT1 binds glucose molecules primarily through weak interactions such as hydrogen bonds and hydrophobic effects (Lodish, 2000). Therefore, the binding of a single glucose molecule is not strong enough to retain the nanocarrier in the blood flow of the organism. To achieve a strong retention of nanocarriers on the BCECs by GLUT1 binding, multivalent interactions by a high surface density of glucose molecules on the liposomal surface are preferable (Mammen et al., 1998; Underhill and Toole, 1980). Qin et al. 2010 were able to prove the hypothesis that a higher surface density of glucose on the liposomal surface causes a higher cellular uptake (Qin et al., 2010). They showed that a liposomal formulation with almost 33 mol% of a cholesterol-glucose conjugate led to the highest cellular uptake.

In our study, we achieved increased uptake with glucose-modified liposomes having 5.85 mol% glucose on the surface of APG liposomes and 10.91 mol% on GLU liposomes. For both compositions of the liposomes, it was intended to include 5 mol% glucose. For this aim, liposomes were produced based on an assumed molecular weight of an approx. 5 kDa PEG-chain + 745 Da (DSPE). After fabrication of the liposomes, glucose analytics in comparison to the cholesterol analytics showed the mentioned excess glucose contents of 5.9 mol% and 10.9 mol%, respectively. We therefore have to conclude that the difference is due to an inaccurate specification of the glucose-conjugating PEG-DSPE anchors' molecular weights by the manufacturer. This inaccuracy is caused by the polydisperse PEG chain length of DSPE-PEG5k-GLU or DSPE-PEG5k-NHS.

Despite the very high glucose content of the GLU liposomes, APG liposomes showed higher uptake in bEnd.3 cells at low and medium concentrations despite the lower glucose molar percentage. This could probably be the result of two counteracting factors: 1) the unconjugated succinimide residues, as the conjugation efficiency is at around 80 %. The free NHS groups with a surface density of approx. 1.5 mol% might cause the higher uptake of APG liposomes despite the higher glucose surface concentration of the GLU liposomes and 2) the conjugation position for the covalent binding of 4-aminophenyl- β -D-glucopyranoside which occurs at the C-1 position. According to Barnett et al. 1973, covalent binding via the C-6 position of the glucose is preferable, as this preserves the ability to bind to GLUT1 (Barnett et al., 1973). The interaction of glucose with GLUT1

is essentially based on the hydroxyl groups in positions C-1, C-3 and C-4. In our study, the APG liposomes increased cellular uptake despite conjugation via the C-1 position. This might be the result of the unconjugated succinimide residues which overcompensate the disadvantage of the APG liposomes in their ligand function with the GLUT1 receptor, at least in the low and medium liposome concentration range (100 μ M and 500 μ M). However, at the highest concentration of 1,000 μ M, GLU liposomes are superior to APG liposomes which indicates that not only NHS residues contribute to the selective cellular uptake in bEnd.3 cells, but also glucose moieties.

In conclusion, essential differences exist in the uptake speed and saturation of liposomal formulations which are both cell-specific and specific to the surface coatings of nanoparticles. Liposomes containing a coating of 5 mol% of mPEG clearly have the lowest cellular uptake saturation. At the same time, these particles have the strongest impact on cellular viability measured by their reducing activity which goes down to 78 % and 42 %, respectively for bEnd.3 and U-87 MG cells incubated with 1,000 μ M lipid for 3 h, compared to their viabilities without liposomal uptake. In this comparison, liposomal uptake saturation is 7.8 times higher the glioblastoma cells than in the endothelial cells. For all other liposomal coatings, viability is not lower than 57 % even though uptake saturation is for NHS, GLU and APG liposomes is 60 % higher than for mPEG liposomes, proving the much higher tolerability of these surface coatings for cell viability, along with much higher uptake saturations. These findings may also provide new aspects to the frequently discussed PEG dilemma.

For practical applications, liposomal concentrations in the endothelium or tumor micro-environment will be much lower and clearly without impact on viability. For future clinical use in targeting brain tumors, it is most relevant that at a lipid concentration of 100 μ M, succinimide-coated liposomes achieve 3.2 and 4.2 times higher cellular uptake in endothelial cells than the glucose coatings GLU and APG, respectively. We, therefore, expect a great potential for future clinical perspectives in exploring and developing the potential of succinimide or serotonin-derived ligands in their interactions with the serotonin receptor family to enhance the BBB transfer of targeted therapies.

6.2 Surface Modifications with ApoE3 and c(RGD)⁴

In this subchapter, the influence of different liposomal surface modifications on the cellular uptake of liposomes in endothelial or glioma cells is investigated. Figure 66a shows the structure of the different distal ends of DSPE-PEG5k, while Figure 66b shows a schematic representation of the liposomal composition listed in Table 22.

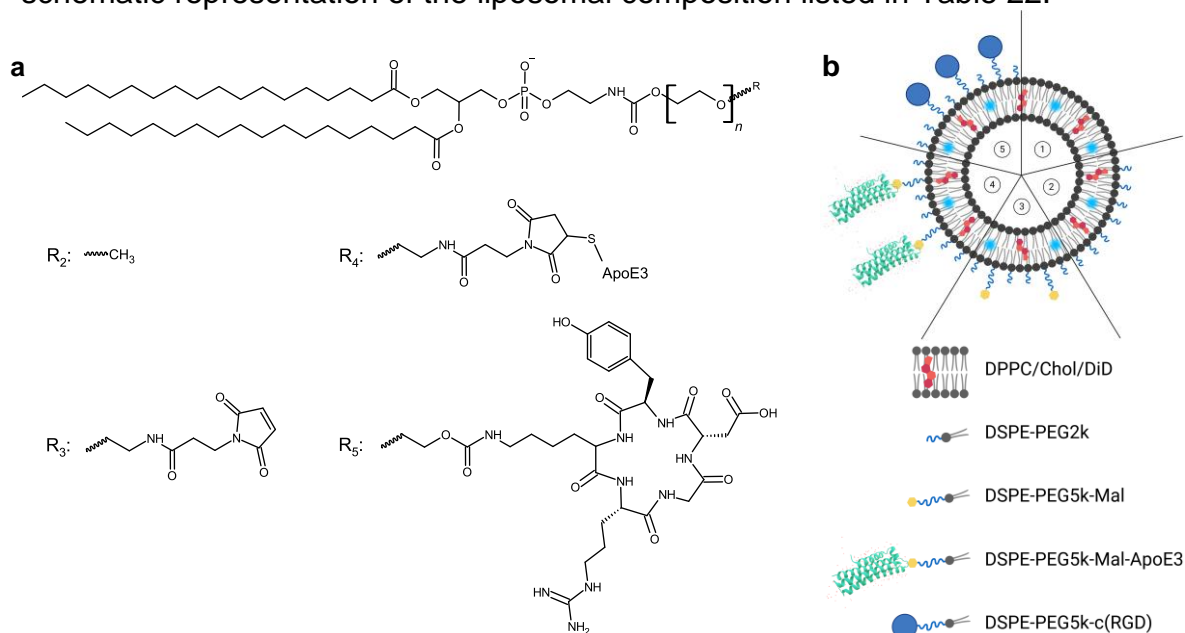


Figure 66: Schematic overview of structures, different liposomal formulations and the tertiary protein structures. (a) Displays different distal ends (R2 to R5) of the DSPE-PEG5k in liposomal formulations 2 to 5 and (b) illustrates a schematic overview of the 5 liposomal formulations.

Table 22: Composition of liposomal formulations.

Sample nomenclature	Control	mPEG	Mal	ApoE3	c(RGD)
Components	Molar ratio [%]				
DPPC	59.9	54.9	54.8	54.8	49.9
Cholesterol	40	40	40	40	40
DSPE-PEG2k	-	5	5	5	5
DSPE-PEG5k-Mal	-	-	0.1	-	-
DSPE-PEG5k-Mal-ApoE3	-	-	-	0.1	-
DSPE-PEG5k-c(RGDyk)	-	-	-	-	5
DiD	0.1	0.1	0.1	0.1	0.1

⁴ Content of this section is published in the *Pharmaceutics* Journal and adapted for this thesis: L. Lubitz, M. Haffner, H. Rieger, G. Leneweit, "Increased cellular uptake of ApoE3- or c(RGD)-modified liposomes for glioblastoma therapy depending on the target cells"; doi: 10.3390/pharmaceutics16091112.

6.2.1 Characterization and Stability of Liposomes

The results of the characterization of size (Z-Average) and polydispersity index (Pdl) of the liposomes are summarized in Table 23. All liposomal formulations showed a Z-Average (Z-Ave) of < 130 nm and a low Pdl value < 0.2. In addition, all liposomes exhibited a monomodal size distribution.

Table 23: Composition, particle size (Z-Average) and polydispersity index of the tested liposomal formulations.

Liposomes	Z-Average [nm]	Pdl
Control	110.8 ± 2.0	0.106 ± 0.020
mPEG	108.5 ± 1.9	0.065 ± 0.028
Mal	103.8 ± 0.7	0.136 ± 0.014
ApoE3	125.1 ± 1.1	0.195 ± 0.012
c(RGD)	99.6 ± 2.3	0.143 ± 0.037

The stability of the liposomal formulation was investigated for four weeks of storage at 4 °C under light-protected conditions. The results in Figure 67a show no significant changes in the liposomal size over time. The polydispersity index (Pdl) served as a further characteristic for assessing liposomal stability. As shown in Figure 67b, the fluctuations in the polydispersity index do not show a significant trend for all formulations over a period of 4 weeks. Linear regressions of the size and Pdl evolution of the 4 liposomal formulations were analyzed by Student's t-test. The individual graphs of the trend analysis for the Z-Ave (Figure A 5.1) and the Pdl (Figure A 5.2), can be found in the Appendix A5.

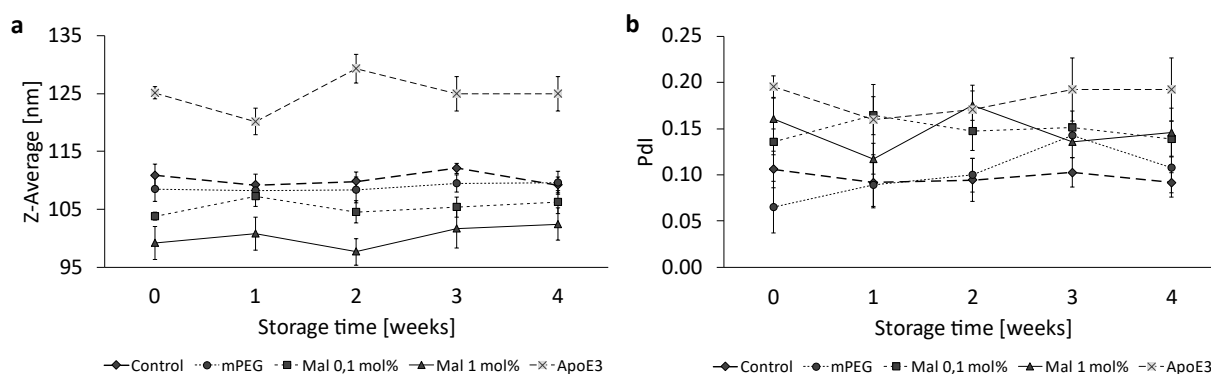


Figure 67: Liposomal stability over a storage period of 4 weeks at 4 °C. Representation of (a) the Z-Average and (b) the Pdl. The bars represent the mean \pm SD, $n = 3$.

To estimate the conjugation efficiency more precisely, the apolipoprotein E3 concentration on the liposomal surface was determined using the Human ApoE ELISA^{BASIC} Kit. Based on the determined concentration of $2.39 \pm 0.38 \mu\text{g/mL}$ the molar amount of ApoE3 n_{ApoE3} was calculated and correlated with half of the molar amount of DSPE-PEG5k-Mal n_{Mal} as the distribution of this lipid anchor is assumed to be spread evenly on the inner and outer bilayer leaflet for symmetrical liposomes. The amount of DSPE-PEG5k-Mal n_{Mal} is calculated via the cholesterol concentration of the final sterile filtrated liposomes. Since $n_{\text{ApoE3}} / n_{\text{Mal}} = 0.129$, this result documents a conjugation efficiency of 12.9 %. The increase of the liposomal size of the liposomes by more than 20 nm (Mal liposomes have a Z-Ave of $103.8 \pm 0.7 \text{ nm}$ while ApoE3 liposomes $125.1 \pm 1.1 \text{ nm}$) can be seen as additional confirmation of the successful conjugation of ApoE3 to the liposomal surface. The determination of the thiol groups directly after the reaction of the protein with Traut's reagent and after the final sterile filtration of the liposomes showed a reduction of the thiol groups by almost 90 %. Conversely, this corresponds to a percentage of 10 % remaining thiol groups. This indicates two aspects: 1) a successful conjugation of ApoE3 to the liposomal surface and an effective purification of the liposomes by dialysis and 2) free thiol groups on already covalently bound ApoE3 on the liposomal surface since the binding of ApoE3 to the liposome presumably occurs via several thiol groups. Therefore, the approach for thiolation and subsequent conjugation should be examined in more detail. The ApoE3 sequence contains a total of 13 lysines, of which most likely only 4 are relevant for thiolation using Traut's reagent due to their localization on the outside of the protein. In addition, the maximum number of ApoE3 molecules per liposome can be estimated by forming the ratio of the surface area of a spherical liposome A_{Liposome} and the total cylindrical protein surface area A_{ApoE3} . The result is that at maximum 9 ApoE3

molecules can be bound on the liposomal surface. This theoretical value is compared to the measured value of ApoE3 concentration determined by ELISA. To do so, the number of ApoE3 molecules per milliliter N_{ApoE3} is related to the number of liposomes per unit volume $N_{Liposomes}$ from the measured total lipid concentration. As a result, it is found that ~ 1 ApoE3 molecule is bound per liposome.

6.2.2 Expression Levels of LRP1 and Integrin α_v in Endothelial and Cancer Cells

Figure 68 presents the expression levels of the low-density lipoprotein receptor-related protein 1 (LRP1) and the integrin α_v receptor in the endothelial cell line bEnd.3 as well as in the two glioma cell lines U-87 MG and F98. The determination was carried out as described in Chapter 3.2.3.2.

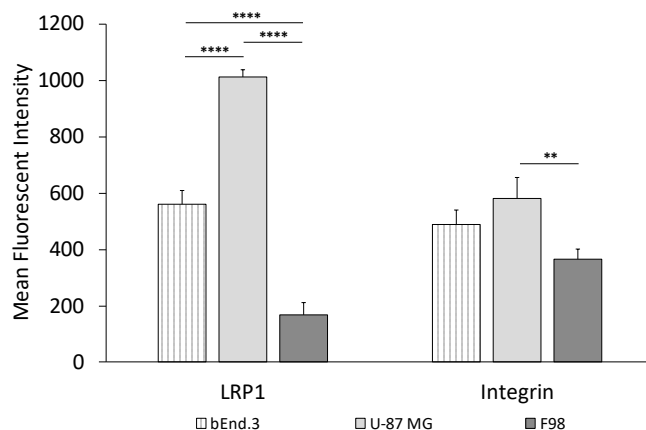


Figure 68: Expression levels of LRP1 and integrin receptor in cancer cells (U-87 MG and F98) and endothelial cells (bEnd.3). The bars represent the mean \pm SD. Statistical analysis: one-way ANOVA followed by Tukey's multiple comparison test. * $p < 0.05$, ** $p < 0.01$, *** $p < 0.001$, **** $p < 0.0001$; $n = 3$.

As can be seen in Figure 68, the expression of both receptors is highest for the U-87 MG glioma cells. In case of the LRP1 receptor, the expression is significant in U-87 MG cells compared to the rat glioma cell line F98 or the endothelial cells bEnd.3. Considering the integrin α_v receptor, there was only a significantly higher expression for the U-87 MG cells when comparing both tumor cell lines. No significant difference between the human glioma cells (U-87 MG) and the endothelial cells bEnd.3 could be detected.

As can be seen in Figure 68, the expression of both receptors is highest for the U-87 MG glioma cells. In case of the LRP1 receptor, the expression is significant in U-87 MG cells compared to the rat glioma cell line F98 or the endothelial cells bEnd.3. Considering the integrin α_v receptor, there was only a significantly higher expression for the U-87 MG cells when comparing both tumor cell lines. No significant difference between the human glioma cells (U-87 MG) and the endothelial cells bEnd.3 could be detected. Concerning LRP1, it is reported to be highly expressed in neurons (Andersen and Willnow, 2006) and its localization on the abluminal endothelial cell membrane (Deane et al., 2003), makes it an advantageous target. Furthermore, LRP1 is associated with the pathobiology of glioblastoma as indicated by an increased expression in neoplastic glioblastoma cells (Maletínská et al., 2000; Shruti et al., 2022; Yamamoto et al., 1998, 1997). Maletinska et al. 2000 were able to show that the LRP1 receptor is differentially expressed in 7 different human glial cells, with expression in the U-87 MG cells being among the three highest (Maletínská et al., 2000). Our results presented in Figure 68 are in line with Maletinska et al. 2000 (Maletínská et al., 2000; Taylor and Zahid, 2020), as the LRP1 is expressed twice as high in U-87 MG cells compared to bEnd.3 cells. When comparing the 2 different glioma cell lines U-87 MG and F98, the LRP1 expression is nearly 6-times increased in the human glioma cell line U-87 MG compared to the rat F98 cells as we show in Figure 68.

On the other hand, so-called cell-penetrating peptides (CPPs) such as the cyclic RGD as ligand for the integrin α_v receptor attracted more and more attention over the past decades as the first CPP was identified more than 25 years ago (Taylor and Zahid, 2020). The integrin $\alpha_v\beta_3$ receptor is overexpressed in tumor and angiogenic endothelial cells (Danhier et al., 2012b) and is correlated with poorer glioblastoma prognosis (Ducassou et al., 2013) which is in accordance with our results presented in Figure 68. There is no significant difference in the expression of the receptor between the glioma U-87 MG cells and the endothelial bEnd.3 cells, but when comparing the expression between both tumoral cell lines a significant difference can be found. The integrin α_v receptor is expressed 1,6-fold higher in human U-87 MG cells than in rat F98 cells.

6.2.3 Cellular Uptake of ApoE3-Modified Liposomes

The cellular uptake of liposomes modified with apolipoprotein E3 in bEnd.3 endothelial cells was studied according to Chapter 3.2.3.3. Uptake quantified by MFI of the ApoE3-modified liposomes is either compared to the MFI of PEGylated liposomes (Figure 69a) or the MFI of Maleimide-functionalized liposomes (Figure 69b). It was found that ApoE3-modification of the liposomal surface could increase the cellular uptake compared to PEGylated liposomes (Figure 69a) up to 2.3-fold when cells were incubated with 100 μ M for 1 h. Increasing lipid concentration resulted in a decrease of uptake of ApoE3-modified liposomes, while an increase in incubation time to 3 h led to an increase of liposomal uptake up to 4.7-fold.

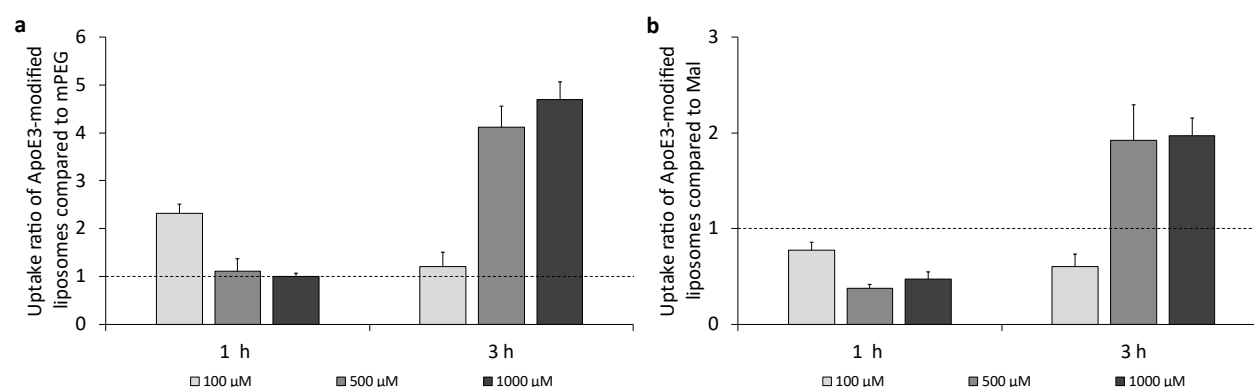


Figure 69: Uptake ratio of ApoE3-modified liposomes in bEnd.3 cells. (a) Liposomal uptake ratio of ApoE3-modified liposomes compared to mPEG liposomes in bEnd.3 cells after 1 h and 3 h of and (b) liposomal uptake factor of ApoE3-modified liposomes compared to Mal liposomes in bEnd.3 cells after 1 h and 3 h of incubation; $n = 3$.

When comparing the uptake of ApoE3-modified liposomes to Mal (precursor) liposomes, there was no increased uptake at 1 h of incubation as the ratio remains below 1.0. Only for medium and high lipid concentrations (500 μ M and 1,000 μ M) at 3 h of incubation resulted in a 2-fold increase in cellular uptake of ApoE3-modified liposomes.

The following Figure 70 shows the concentration- and time-dependent uptake of the 4 liposomal formulations in the human glioblastoma cell line U-87 MG. The investigation of cellular uptake after 1 h of incubation showed that ApoE3-modified liposomes are always taken up most efficiently and this is consistently significant compared to PEGylated liposomes. There was no significant difference in cellular uptake between the

control liposomes, PEGylated liposomes and the maleimide anchor liposomes at 100 μM or 1,000 μM .

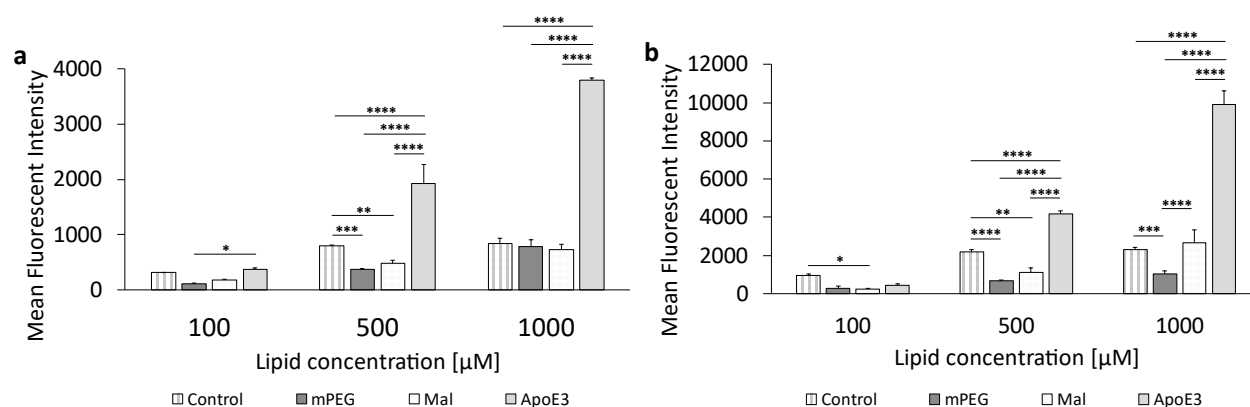


Figure 70: Uptake of ApoE3-modified liposomes in U-87 MG cells. (a) Liposomal uptake in U-87 MG cells after 1 h of incubation and (b) 3 h of incubation. The bars represent the mean \pm SD. Statistical analysis: two-way ANOVA followed by a Tukey's multiple comparison test. * $p < 0.05$, ** $p < 0.01$, *** $p < 0.001$, **** $p < 0.0001$; $n = 3$.

An increase in incubation time from 1 h to 3 h (Figure 70b) led to a general increased uptake for all liposomal formulations, and a similar trend of steadily increasing cellular uptake with increasing concentration was observed for the ApoE3-modified liposomes. It was also shown once again that PEGylated liposomes are taken up more poorly, in the case of 500 μM and also 1,000 μM the uptake is significantly reduced compared to the control liposomes.

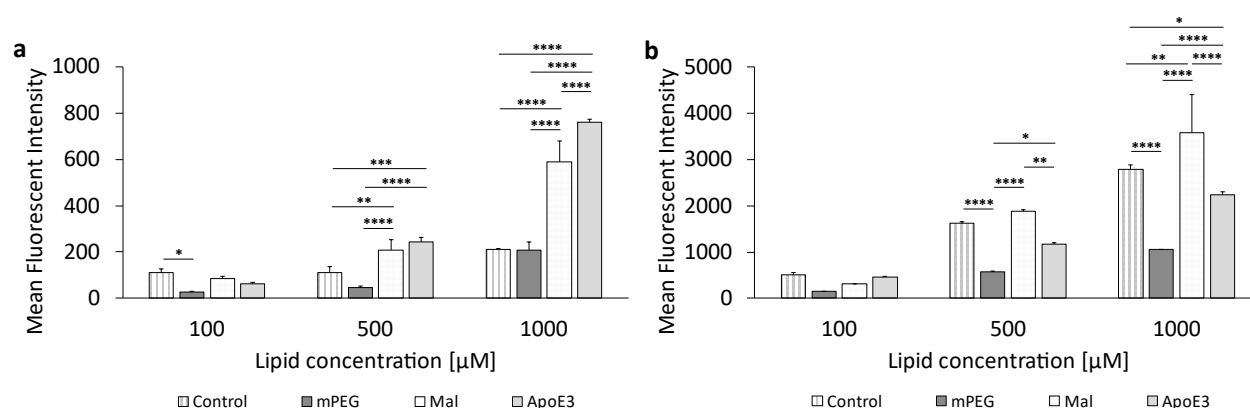


Figure 71: Uptake of ApoE3-modified liposomes in F98 cells. (a) Liposomal uptake in F98 after 1 h of incubation and (b) 3 h of incubation. The bars represent the mean \pm SD. Statistical analysis: two-way ANOVA followed by a Tukey's multiple comparison test. * $p < 0.05$, ** $p < 0.01$, *** $p < 0.001$, **** $p < 0.0001$; $n = 3$.

The rat-derived glioblastoma cell line F98 was used as a further tumor cell line to evaluate cellular uptake. The results are shown in Figure 71. It was shown that the ApoE3-modified liposomes are only taken up significantly higher at the highest concentration of 1,000 μM after 1 h of incubation compared to the maleimide-anchor liposomes. A significantly higher uptake compared to PEGylated liposomes was already shown at 500 μM .

In the case of the F98 cells, an extension of the incubation time (Figure 6b) did not lead to a comparable result to the 1 h of incubation. On the one hand, there was an almost linear increase in the cellular uptake of the control liposomes. Furthermore, a significant reduction in the cellular uptake of PEGylated liposomes was again observed above a tested liposomal concentration of 500 μM . However, a 3 h incubation showed that above a concentration of 500 μM the maleimide-anchor liposomes were significantly higher taken up compared to the ApoE3-modified liposomes.

When cellular uptake is compared with the expression of the receptor, a correlation can be found. This can be seen, for example, when comparing the uptake after 1 h (Figure 70a) at 100 μM . In this case, the uptake of the ApoE-3-modified liposomes at 100 μM in U-87 MG cells is increased 6-fold compared to F98 cells. Even with increasing lipid concentrations to 500 μM or 1,000 μM , the uptake in the U-87 MG cells remains at roughly 6-fold higher compared to F98 cells.

For a more precise comparison between those two cell lines, Figure 72a represents the cellular liposomal saturation S and the saturation half-time $t_{1/2}$ (Figure 72b). Figure A 5.7a contains exemplarily the cellular liposomal saturation S and the cellular saturation half-time $t_{1/2}$ as red lines. Supplementary graphs for the ApoE3-modified liposomes are included in Figure A 5.6.

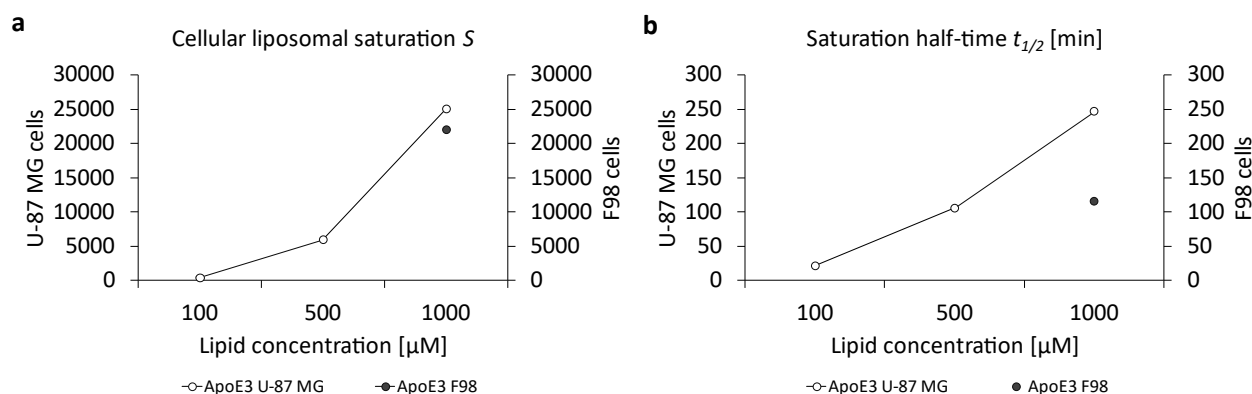


Figure 72: Calculation of (a) the cellular liposomal saturation S and (b) the saturation half-time $t_{1/2}$ vs. lipid concentration of ApoE3-modified liposomes in U-87 MG and F98 cells according to eq. (1). In those cases where the exponential regression is only possible with a coefficient of variation $r^2 < 1$, the data points were discarded due to insufficient accuracy.

There are almost identical saturation values (Figure 72a) for both cell lines of $\sim 25,000$ for U-87 MG cells and $\sim 22,000$ for F98 cells, but enormous differences if the saturation half-time is considered as an indicator of the "speed of uptake" in Figure 72b. Uptake of the ApoE3-modified liposomes occurs in U-87 cells at more than twice the speed of F98 cells. This contrast of very similar saturations despite large differences in uptake speed measured at 1 h or 3 h can be explained by a cell biological effect: continuous endocytosis via the LRP1 receptor leads to a depletion of LRP1 at the plasma membrane. However, LRP1 is intracellularly recycled through different pathways and starts to re-appear on the plasma membrane surface around 90 min after internalization (Donoso et al., 2009; Marzolo et al., 2003; Van Kerkhof et al., 2005). Additionally, the de novo biosynthesis takes more than 4 h and therefore also contributes to the continuous uptake of ApoE3-modified liposomes via the LRP1 receptor. In general, our results are in accordance with what is demonstrated by others: ApoE3-modified formulation showed an increased uptake in endothelial cells or higher penetration in co-culture models (Dal Magro et al., 2017; Ismail et al., 2022; Topal et al., 2021; Wagner et al., 2012).

6.2.4 Cellular Uptake of c(RGD)-Modified Liposomes

In addition to the apolipoprotein E3 as a possible ligand for the LRP1 receptor, the cyclic tripeptide c(RGD) on the liposomal surface was investigated as a ligand for the integrin α_v receptor. The experiments to determine the cellular uptake in the endothelial cell line bEnd.3 as well as the two tumoral cell lines U-87 MG and F98 were also carried out according to Chapter 3.2.3.3. Figure 72 summarizes the results after 1 h and 3 h of incubation of the bEnd.3 cells with the 3 different liposomal formulations.

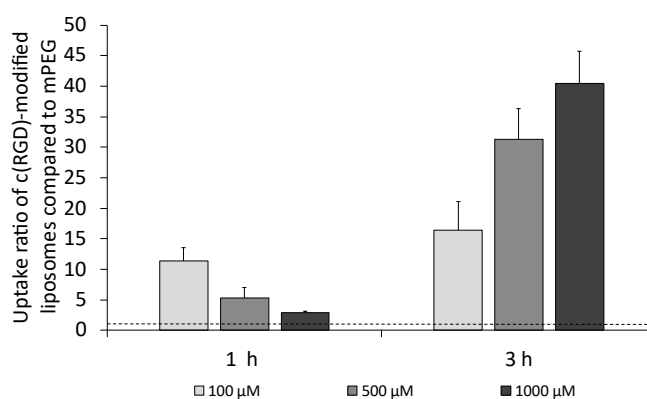


Figure 73: Uptake ratio of c(RGD)-modified liposomes in bEnd.3 cells compared to mPEG liposomes in bEnd.3 cells after 1 h and 3 h of incubation; $n = 3$.

In general, it was found that c(RGD)-modification of the liposomal surface resulted in an enormous increase in cellular uptake as the uptake factor comparing the uptake with PEGylated liposomes is above 1.0 in all cases (concentrations and duration of incubation). Considering the results obtained after 1 h of incubation, there was a decrease in the uptake ratio of c(RGD)-modified liposomes when compared to mPEG liposomes for an increase in the tested lipid concentration. Contrary to this, there was an increase in the uptake ratio with increasing lipid concentration for 3 h of incubation. A 3 h incubation of the bEnd.3 cells (Figure 72) showed a 16.4-fold up to 40.5-fold increase with increasing concentration.

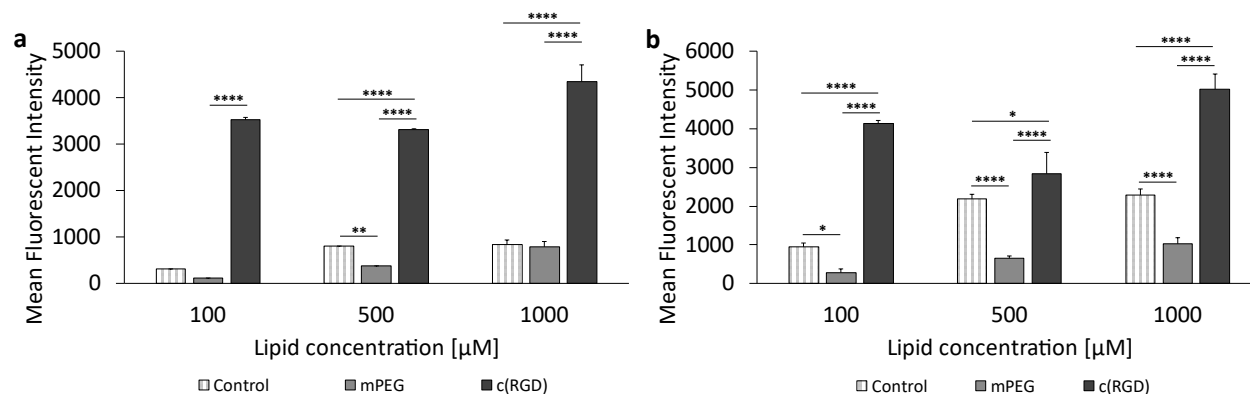


Figure 74: Uptake of c(RGD)-modified liposomes in U-87 MG cells. (a) Liposomal uptake in U-87 MG cells after 1 h of incubation and (b) 3 h of incubation. The bars represent the mean values with the standard deviation as error bars. Statistical analysis: two-way ANOVA followed by a Tukey's multiple comparison test. * $p < 0.05$, ** $p < 0.01$, *** $p < 0.001$, **** $p < 0.0001$; $n = 3$.

Figure 73 presents the results of liposomal uptake in U-87 MG cells. Except for 500 μM , there was no significant difference between the uptake of the control liposomes and the PEGylated liposomes when incubated for 1 h (Figure 73a). In comparison, there were significant differences between the cellular uptake of the control liposomes compared to the PEGylated liposomes when incubated for 3 h at all concentrations (Figure 73b). The c(RGD) modified liposomes had significantly the highest cellular uptake at all three concentrations, both at 1 h and 3 h incubation. However, there was no concentration-dependent increase in uptake.

The cellular uptake of c(RGD) modified liposomes was also assessed in rat F98 GBM cells. The results are given in Figure 74. For the c(RGD) liposomes, 1 h incubation (Figure 74a) showed an almost linear increase in cellular uptake with increasing concentration. In the case of 500 μM and also 1,000 μM , the uptake of the c(RGD) modified liposomes is significantly higher than the uptake of the control liposomes and mPEG liposomes. The uptake of the control liposomes and the PEGylated liposomes did not differ significantly at any of the concentrations tested during a 1 h incubation.

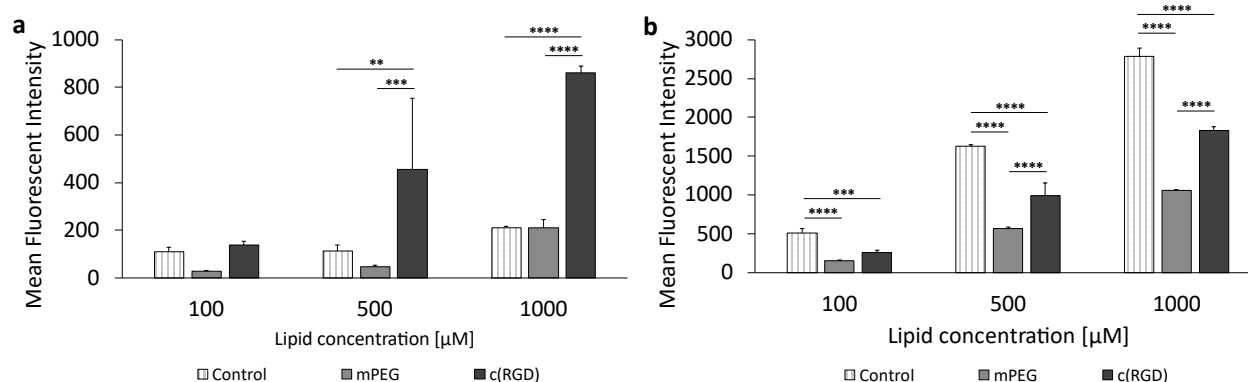


Figure 75: Uptake of c(RGD)-modified liposomes in F98 cells. (a) Liposomal uptake in F98 cells after 1 h of incubation and (b) 3 h of incubation. The bars represent the mean values with the standard deviation as error bars. Statistical analysis: two-way ANOVA followed by a Tukey's multiple comparison test. * $p < 0.05$, ** $p < 0.01$, *** $p < 0.001$, **** $p < 0.0001$; $n = 3$.

In contrast to the 1 h incubation, all three liposomal formulations showed a concentration-dependent increase in cellular uptake with prolonged incubation time (Figure 74b). The control liposomes were significantly taken up highest at all three liposomal concentrations tested.

In the case of the c(RGD)-modified liposomes, no comparatively precise correlation can be found between the expression of the target and the cellular uptake of the liposomes as with the ApoE3-modified liposomes, since the uptake behavior of c(RGD)-modified liposomes in both tumoral cell lines is fundamentally different. The F98 cells show both time- and concentration-dependent uptake, whereas the U-87 cells appear to have reached a kind of "maximum" even at the lowest lipid concentration and incubation over 1 h, as uptake could not be increased either by increasing lipid concentration or by increasing the incubation time. One possible reason for this could be the comparatively high cytotoxicity of the formulation on the U-87 MG cells, as the relative viability was reduced to as low as 51.7 % at highest lipid concentrations of 1,000 μM . This might be due to the fact that c(RGD) occupies the integrin receptors on the cell surface and inhibits integrin-mediated cell adhesion, leading to cell detachment and even apoptosis (Desgrosellier and Cheresh, 2010; Hersel et al., 2003). A closer look at the results of the uptake can also be obtained by the cellular saturation (Figure 76a) and the saturation half-time (Figure 76b). Supplementary graphs for c(RGD)-modified liposomes are included in Figure A 5.7. The saturation values for c(RGD)-modified liposomes in U-87 MG cells is 1.95-fold higher compared to F98 cells, whereas the uptake rate in the F98 cells is 5-fold

higher compared to the U-87 cells. Chen et al. 2012 already showed a 2.5-fold increased uptake of RGD-modified liposomes when compared to PEGylated liposomes (Chen et al., 2012). Dou et al. 2018 showed, that the cellular uptake of c(RGD)-modified liposomes correlated with the receptor expression as they compared the uptake in high-expression human glioma U-87 MG cells and low-expression human myelogenous leukemia K562 cells (Dou et al., 2018).

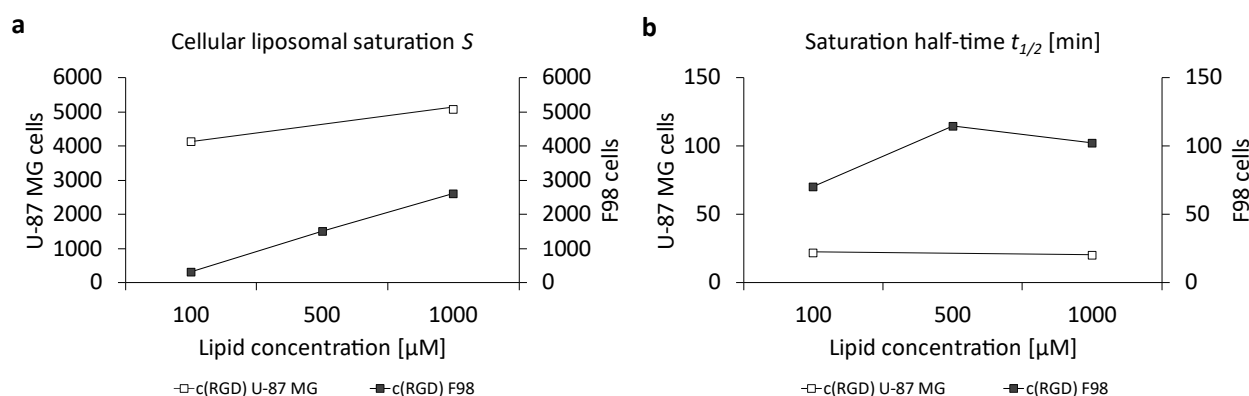


Figure 76: Representation of the (a) cellular liposomal saturation S and (b) saturation half-time $t_{1/2}$ vs. lipid concentration of c(RGD)-modified liposomes in U-87 MG and F98 cells as calculated according to eq. (1). In those cases where the exponential regression only produced $r^2 < 1$, the data points were discarded due to insufficient accuracy.

The cytotoxicity of all liposomal formulations in the 3 concentrations 100 μM , 500 μM and also 1,000 μM was determined for all three cell lines in order to be able to assess the basic toxicity of the liposomes without encapsulated active substance. The results can be found in Figure A 5.3 to A 5.5 in the Appendix A5. In the case of bEnd.3 cells, comparable cell viabilities were observed for all liposomal formulations at 1,000 μM , except for c(RGD)-modified liposomes where cell viability was reduced to below 50 %. In the case of U-87 MG glioma cells, all formulations exerted a higher cytotoxicity, whereby this was most pronounced with mPEG liposomes. Cell viability was reduced to almost 40 % at 1000 μM . For the F98 cells, the results are comparable to the bEnd.3 cells, as here too the c(RGD)-modified liposomes caused the highest reduction in cell viability. In general, ApoE3-modified liposomes showed the lowest cytotoxicity for all tested cell lines. This could be due to an increased ATP concentration and thus increased energy potential in the cells due to the presence of ApoE3, as already shown by (Chin et al., 2014) in mice and transgenic cells.

6.2.5 Conclusion

In this study, a targeted drug delivery system with either ApoE3 or c(RGD) on the surface was successfully constructed for glioblastoma therapy and showed promising in vitro data regarding the possibility of elevated cellular uptake. Our results indicate that the selection of a ligand is less dependent on its chemical species (peptide or protein) than on the target structure (cell type). Thus, the ApoE3-modification of liposomes is a favorable strategy for tumor cell targeting but it might be also a good ligand candidate for BBB passaging, as the uptake is increased in endothelial cells at higher lipid concentrations. As these high lipid concentrations are non-therapeutic for in vivo, it will be of interest to increase the ApoE3-surface density on the liposomes for an increased uptake even at lower lipid concentrations. Contrary, liposomes modified with the cyclic RGD peptide showed a stronger increase in the uptake in endothelial cells. In most cases, surface modifications with either ApoE3 or c(RGD) showed a time- and concentration-dependent manner of uptake for all cell lines, except for U-87 MG cells. In the case of the human glioma cells, a saturation of uptake could be seen. To answer the question of whether a correlation of liposomal cellular uptake with the expression of the receptor can be correlated, an affirmative response is only possible for ApoE3-modified liposomes. For the uptake of either ApoE3- or c(RGD)-modified liposomes, there are enormous differences in the cellular uptake between two different glioma cell lines of different origin. However, it is important to add that the uptake of the ApoE3-modified liposomes results in a comparable saturation of F98 cells and U-87 MG cells despite lower expression of LRP1 in F98 cells and a significantly slower uptake rate. Our current studies do not allow an absolute statement as to whether the liposomes are completely transcytosed in the endothelial cells. Therefore, it is of interest to evaluate the BBB passage using a transwell model. Investigating the liposomal uptake in different glioma cells of the same species (e.g. patient-derived) as well as an investigation on the liposomal uptake in non-targeted cells can complement the data.

Chapter 7

Conclusions and Outlook

7.1 Conclusions

With regard to a comprehensive conclusion for the present work, the following questions will be raised and answered:

- (1) *How do the process pressure and the number of cycles influence the break-up of liposomes and emulsion droplets in a PFC/W nanoemulsion?*

A higher input of energy, either through increased homogenization pressure or an increased number of processing cycles, is not always beneficial or effective, as this can lead to so-called "over-processing" and the associated increased coalescence of droplets. The choice of pressure also depends on the species of the particles to be comminuted - PFC droplets can only be broken up efficiently below 750 bar. In contrast, liposomes are reduced in size at a constant rate over the entire pressure range from 250 bar to 2,000 bar. For the Microfluidizer® LV1 as a representative of the high-pressure homogenizers, two turbulence changes within the pressure range are to be noted as a characteristic due to the channel geometry, whereby only the turbulence change between 750 bar and 1000 bar affects the break-up of the particles. In general, a strong reduction in particle size was observed in laminar flows due to the higher shear rate caused by the particle distribution in the channel. As a recommendation, 750 bar for 15 cycles could be used as the optimum setting for high-pressure homogenization.

(2) *How do the emulsifying properties of phospholipids in PFC/W nanoemulsions change when the formulation is varied? Can an optimal formulation of a PFC/W nanoemulsion be composed?*

The following aspects have to be considered for an optimized formulation of a PFC/W nanoemulsion:

- i. An optimum ratio of the lipid concentration to the volume fraction of the disperse phase is 2 mM / 1 % (v/v), with the phospholipids forming a monolayer around the PFC droplet. Other ratios result in inhomogeneous distributions or the formation of multilayers.
- ii. The selection of the fatty acid chain length of the phospholipid as an emulsifier should be made taking into account the phase transition temperature of the phospholipid due to the heat development during processing on the homogenizer. A phase transition temperature that is too low results in a high rate of droplet recoalescence, whereas a phase transition temperature that is too high results in poor disruption of the vesicles.
- iii. High emulsification efficiencies, i.e. exclusion of liposomal bilayers and subsequent accumulation of the emulsifier molecules as a monolayer around a PFC droplet, are particularly evident with phospholipids with anionic head groups. Small particle sizes can be achieved for head groups with a high Zeta potential and a high surface area of the phospholipid in bilayers. DPPG can be mentioned as an example of such a phospholipid.
- iv. A low viscosity ratio between the two emulsion phases should be preferred. The ratio can be adjusted, for example, by varying the perfluorocarbon as the disperse phase.

(3) *Liposomal surface coatings: A question of whether a small molecule, peptide or protein?*

It is less a question of the type of ligand than of the target cell intended for increased uptake. Glucose as a small molecule showed preferential uptake in tumor cells under glucose deprivation, whereas c(RGD) as an example of a CPP is preferentially taken up by endothelial cells. Liposomes whose surface is modified with apolipoprotein E3 are preferentially taken up in tumor cells, but also in high concentrations in endothelial cells. It should also be noted that the expression of the corresponding

target structure usually correlates with the liposomal cellular uptake, but this is not universally valid. The uptake of modified liposomes can also differ enormously between two cell lines at a certain point in time, but with the same saturation as a result of different saturation half-times.

7.2 Outlook

On the one hand, this study provides a deeper understanding of the flow processes during high-pressure homogenization and their influence on the PFC/W nanoemulsion. On the other hand, various formulation parameters are examined in depth concerning their influence on the emulsifying properties of phospholipids. The combination of both aspects and the continuation of this by using the optimized emulsion to produce asymmetric liposomes should be the focus of future experiments. Ideally, the production should take place directly with the inclusion of an active ingredient for encapsulation so that the potential of asymmetric liposomes can be fully exploited.

With regard to surface modifications for targeted therapy, the following further investigations are conceivable:

- i. An elucidation of the uptake mechanisms of the respective surface-modified liposomes with the aid of uptake inhibition studies.
- ii. The assessment of the passage of the targeted liposomes through the BBB or BBTB in a 2D transwell model or a 3D model including a tumor spheroid or by using organ-on-a-chip models.
- iii. Investigations concerning the intracellular trafficking of the liposomes, whereby fluorescence microscopy can be used to localize the recorded structures.
- iv. Experiments to assess endosomal escape, as cellular uptake and intracellular release of the encapsulated drug are equally relevant for a high therapeutic effect.

References

- Abbas, A.K., Lichtman, A.H., Pillai, S., 2021. Cellular and Molecular Immunology E-Book: Cellular and Molecular Immunology 10th Edition E-Book. Elsevier Health Sciences.
- Abbott, N.J., Patabendige, A.A.K., Dolman, D.E.M., Yusof, S.R., Begley, D.J., 2010. Structure and function of the blood-brain barrier. *Neurobiol Dis* 37, 13–25. <https://doi.org/10.1016/j.nbd.2009.07.030>
- Abbott, N.J., Rönnbäck, L., Hansson, E., 2006. Astrocyte–endothelial interactions at the blood–brain barrier. *Nat Rev Neurosci* 7, 41–53. <https://doi.org/10.1038/nrn1824>
- Adan, A., Alizada, G., Kiraz, Y., Baran, Y., Nalbant, A., 2017. Flow cytometry: basic principles and applications. *Crit Rev Biotechnol* 37, 163–167. <https://doi.org/10.3109/07388551.2015.1128876>
- Adler, A., Fritsch, M., Fromell, K., Leneweit, G., Ekdahl, K.N., Nilsson, B., Teramura, Y., 2023. Regulation of the innate immune system by fragmented heparin-conjugated lipids on lipid bilayered membranes in vitro. *J Mater Chem B* 11, 11121–11134. <https://doi.org/10.1039/d3tb01721d>
- Adler, A., Inoue, Y., Ekdahl, K.N., Baba, T., Ishihara, K., Nilsson, B., Teramura, Y., 2022. Effect of liposome surface modification with water-soluble phospholipid polymer chain-conjugated lipids on interaction with human plasma proteins. *J Mater Chem B* 10, 2512–2522. <https://doi.org/10.1039/d1tb01485d>

- Adler, A., Inoue, Y., Sato, Y., Ishihara, K., Ekdahl, K.N., Nilsson, B., Teramura, Y., 2021. Synthesis of poly(2-methacryloyloxyethyl phosphorylcholine)-conjugated lipids and their characterization and surface properties of modified liposomes for protein interactions. *Biomater Sci* 9, 5854–5867. <https://doi.org/10.1039/d1bm00570g>
- Alam, M.I., Beg, S., Samad, A., Baboota, S., Kohli, K., Ali, J., Ahuja, A., Akbar, M., 2010. Strategy for effective brain drug delivery. *Eur J Pharm Sci* 40, 385–403. <https://doi.org/10.1016/j.ejps.2010.05.003>
- Allen, T.M., Cullis, P.R., 2004. Drug delivery systems: entering the mainstream. *Science* 303, 1818–22. <https://doi.org/10.1126/science.1095833>
- Allen, T.M., Mumbengegwi, D.R., Charrois, G.J.R., 2005. Anti-CD19-targeted liposomal doxorubicin improves the therapeutic efficacy in murine B-cell lymphoma and ameliorates the toxicity of liposomes with varying drug release rates. *Clin Cancer Res* 11, 3567–73. <https://doi.org/10.1158/1078-0432.CCR-04-2517>
- Alonso, J.M., Garcia-Fuentes, M., 2014. Nano-Oncologicals, *Advances in Delivery Science and Technology*. Springer International Publishing, Cham. <https://doi.org/10.1007/978-3-319-08084-0>
- Amarandi, R.-M., Ibanescu, A., Carasevici, E., Marin, L., Dragoi, B., 2022. Liposomal-Based Formulations: A Path from Basic Research to Temozolomide Delivery Inside Glioblastoma Tissue. *Pharmaceutics* 14, 308. <https://doi.org/10.3390/pharmaceutics14020308>
- Andersen, O.M., Willnow, T.E., 2006. Lipoprotein receptors in Alzheimer's disease. *Trends Neurosci* 29, 687-694. <https://doi.org/10.1016/j.tins.2006.09.002>
- Andersson, J., Ekdahl, K.N., Larsson, R., Nilsson, U.R., Nilsson, B., 2002. C3 Adsorbed to a Polymer Surface Can Form an Initiating Alternative Pathway Convertase. *The Journal of Immunology* 168, 5786–5791. <https://doi.org/10.4049/jimmunol.168.11.5786>

- Anraku, Y., Kuwahara, H., Fukusato, Y., Mizoguchi, A., Ishii, T., Nitta, K., Matsumoto, Y., Toh, K., Miyata, K., Uchida, S., Nishina, K., Osada, K., Itaka, K., Nishiyama, N., Mizusawa, H., Yamasoba, T., Yokota, T., Kataoka, K., 2017. Glycaemic control boosts glucosylated nanocarrier crossing the BBB into the brain. *Nat Commun* 8, 1001. <https://doi.org/10.1038/s41467-017-00952-3>
- Asawa, K., Ishihara, K., Ekdahl, K.N., Nilsson, B., Teramura, Y., 2021. Cell Surface Functionalization with Heparin-Conjugated Lipid to Suppress Blood Activation. *Adv Funct Mater* 31. <https://doi.org/10.1002/adfm.202008167>
- Bangham, A.D., Standish, M.M., Watkins, J.C., 1965. Diffusion of univalent ions across the lamellae of swollen phospholipids. *J Mol Biol* 13, 238–52. [https://doi.org/10.1016/s0022-2836\(65\)80093-6](https://doi.org/10.1016/s0022-2836(65)80093-6)
- Barenholz, Y., 2001. Liposome application: problems and prospects. *Curr Opin Colloid Interface Sci* 6, 66–77. [https://doi.org/10.1016/S1359-0294\(00\)00090-X](https://doi.org/10.1016/S1359-0294(00)00090-X)
- Barenholz, Y., Thompson, T.E., 1999. Sphingomyelin: biophysical aspects. *Chem Phys Lipids* 102, 29–34. [https://doi.org/10.1016/s0009-3084\(99\)00072-9](https://doi.org/10.1016/s0009-3084(99)00072-9)
- Barnett, J.E., Holman, G.D., Munday, K.A., 1973. Structural requirements for binding to the sugar-transport system of the human erythrocyte. *Biochem J* 131, 211–21. <https://doi.org/10.1042/bj1310211>
- Belykh, E., Shaffer, K. V., Lin, C., Byvaltsev, V.A., Preul, M.C., Chen, L., 2020. Blood-Brain Barrier, Blood-Brain Tumor Barrier, and Fluorescence-Guided Neurosurgical Oncology: Delivering Optical Labels to Brain Tumors. *Front Oncol*. <https://doi.org/10.3389/fonc.2020.00739>
- Berends, E.T.M., Gorham, R.D., Ruyken, M., Soppe, J.A., Orhan, H., Aerts, P.C., de Haas, C.J.C., Gros, P., Rooijackers, S.H.M., 2015. Molecular insights into the surface-specific arrangement of complement C5 convertase enzymes. *BMC Biol* 13, 93. <https://doi.org/10.1186/s12915-015-0203-8>

- Bergquist, P.L., Hardiman, E.M., Ferrari, B.C., Winsley, T., 2009. Applications of flow cytometry in environmental microbiology and biotechnology. *Extremophiles* 13, 389–401. <https://doi.org/10.1007/s00792-009-0236-4>
- Bernacki, J., Dobrowolska, A., Nierwińska, K., Małecki, A., 2008. Physiology and pharmacological role of the blood-brain barrier. *Pharmacol Rep* 60, 600–22. PMID: 19066407
- Bexborn, F., Andersson, P.O., Chen, H., Nilsson, B., Ekdahl, K.N., 2008. The tick-over theory revisited: formation and regulation of the soluble alternative complement C3 convertase (C3(H₂O)Bb). *Mol Immunol* 45, 2370–9. <https://doi.org/10.1016/j.molimm.2007.11.003>
- Bibette, J., Calderon, F.L., Poulin, P., 1999. Emulsions: basic principles. *Reports on Progress in Physics* 62, 969–1033. <https://doi.org/10.1088/0034-4885/62/6/203>
- BMBF Krebsforschung, 2020. URL <https://www.bmbf.de/bmbf/shareddocs/kurzmeldungen/de/krebsforschung.html> (accessed 4.8.24).
- Boucher, P., Herz, J., 2011. Signaling through LRP1: Protection from atherosclerosis and beyond. *Biochem Pharmacol* 81, 1–5. <https://doi.org/10.1016/j.bcp.2010.09.018>
- Bozzuto, G., Molinari, A., 2015. Liposomes as nanomedical devices. *Int J Nanomedicine* 10, 975–99. <https://doi.org/10.2147/IJN.S68861>
- Bray, F., Laversanne, M., Sung, H., Ferlay, J., Siegel, R.L., Soerjomataram, I., Jemal, A., 2024. Global cancer statistics 2022: GLOBOCAN estimates of incidence and mortality worldwide for 36 cancers in 185 countries. *CA Cancer J Clin* 74, 229–263. <https://doi.org/10.3322/caac.21834>
- Briceño, M., Salager, J.L., Bertrand, J., 2001. Influence of Dispersed Phase Content and Viscosity on the Mixing of Concentrated Oil-in-Water Emulsions in the Transition

-
- Flow Regime. *Chemical Engineering Research and Design* 79, 943–948.
<https://doi.org/10.1205/02638760152721794>
- Briuglia, M.-L., Rotella, C., McFarlane, A., Lamprou, D.A., 2015. Influence of cholesterol on liposome stability and on in vitro drug release. *Drug Deliv Transl Res* 5, 231–42.
<https://doi.org/10.1007/s13346-015-0220-8>
- Bruinsmann, F.A., Richter Vaz, G., de Cristo Soares Alves, A., Aguirre, T., Raffin Pohlmann, A., Stanisçuaski Guterres, S., Sonvico, F., 2019. Nasal Drug Delivery of Anticancer Drugs for the Treatment of Glioblastoma: Preclinical and Clinical Trials. *Molecules* 24. <https://doi.org/10.3390/molecules24234312>
- Bruno, E., Quattrocchi, G., Nicoletti, A., Le Pira, F., Maci, T., Mostile, G., Andreoli, V., Quattrone, A., Zappia, M., 2010. Lack of interaction between LRP1 and A2M polymorphisms for the risk of Alzheimer disease. *Neurosci Lett* 482, 112–116.
<https://doi.org/10.1016/j.neulet.2010.07.012>
- Bulbake, U., Doppalapudi, S., Kommineni, N., Khan, W., 2017. Liposomal Formulations in Clinical Use: An Updated Review. *Pharmaceutics* 9. <https://doi.org/10.3390/pharmaceutics9020012>
- Çağdaş, M., Sezer, A.D., Bucak, S., 2014. Liposomes as Potential Drug Carrier Systems for Drug Delivery, in: *Application of Nanotechnology in Drug Delivery*. InTech.
<https://doi.org/10.5772/58459>
- Cavaillon, J.-M., Sansonetti, P., Goldman, M., 2019. 100th Anniversary of Jules Bordet's Nobel Prize: Tribute to a Founding Father of Immunology. *Front Immunol* 10, 2114.
<https://doi.org/10.3389/fimmu.2019.02114>
- Chang, W., Pu-Zhen, G., Si-Chao, T., Chao, X., 2012. Effect of aspect ratio on the laminar-to-turbulent transition in rectangular channel. *Ann Nucl Energy* 46, 90–96.
<https://doi.org/10.1016/j.anucene.2012.03.018>

- Chapman, D., 1975. Phase transitions and fluidity characteristics of lipids and cell membranes. *Q Rev Biophys* 8, 185–235. <https://doi.org/10.1017/s0033583500001797>
- Chen, I.Y., Chen, Y.M., Liaw, J.S., Wang, C.C., 2007. Two-phase frictional pressure drop in small rectangular channels. *Exp Therm Fluid Sci* 32, 60–66. <https://doi.org/10.1016/j.expthermflusci.2007.01.005>
- Chen, J., Cheng, D., Li, J., Wang, Y., Guo, J., Chen, Z., Cai, B., Yang, T., 2013. Influence of lipid composition on the phase transition temperature of liposomes composed of both DPPC and HSPC. *Drug Dev Ind Pharm* 39, 197–204. <https://doi.org/10.3109/03639045.2012.668912>
- Chen, Y.-J., Mahieu, N.G., Huang, X., Singh, M., Crawford, P.A., Johnson, S.L., Gross, R.W., Schaefer, J., Patti, G.J., 2016. Lactate metabolism is associated with mammalian mitochondria. *Nat Chem Biol* 12, 937–943. <https://doi.org/10.1038/nchembio.2172>
- Chen, Z., Deng, J., Zhao, Y., Tao, T., 2012. Cyclic RGD peptide-modified liposomal drug delivery system: Enhanced cellular uptake in vitro and improved pharmacokinetics in rats. *Int J Nanomedicine* 7, 3803–3811. <https://doi.org/10.2147/IJN.S33541>
- Chin, D., Hagl, S., Hoehn, A., Huebbe, P., Pallauf, K., Grune, T., Frank, J., Eckert, G.P., Rimbach, G., 2014. Adenosine triphosphate concentrations are higher in the brain of APOE3- compared to APOE4-targeted replacement mice and can be modulated by curcumin. *Genes Nutr* 9. <https://doi.org/10.1007/s12263-014-0397-3>
- Chung, K., Ullah, I., Kim, N., Lim, J., Shin, J., Lee, S.C., Jeon, S., Kim, S.H., Kumar, P., Lee, S.-K., 2020. Intranasal delivery of cancer-targeting doxorubicin-loaded PLGA nanoparticles arrests glioblastoma growth. *J Drug Target* 28, 617–626. <https://doi.org/10.1080/1061186X.2019.1706095>
- Cornell, B.A., Fletcher, G.C., Middlehurst, J., Separovic, F., 1982. The lower limit to the size of small sonicated phospholipid vesicles. *Biochim Biophys Acta* 690, 15–9. [https://doi.org/10.1016/0005-2736\(82\)90233-4](https://doi.org/10.1016/0005-2736(82)90233-4)

- Cullis, P.R., de Kruijff, B., 1979. Lipid polymorphism and the functional roles of lipids in biological membranes. *Biochim Biophys Acta* 559, 399–420. [https://doi.org/10.1016/0304-4157\(79\)90012-1](https://doi.org/10.1016/0304-4157(79)90012-1)
- Cytiva, 2020. Principle SEC, Cytiva. URL <https://cdn.cytivalifesciences.com/api-public/content/digi-11639-pdf> (accessed 8.8.24).
- Dai, T., Jiang, K., Lu, W., 2018. Liposomes and lipid disks traverse the BBB and BBTB as intact forms as revealed by two-step Förster resonance energy transfer imaging. *Acta Pharm Sin B* 8, 261–271. <https://doi.org/10.1016/j.apsb.2018.01.004>
- Dal Magro, R., Ornaghi, F., Cambianica, I., Beretta, S., Re, F., Musicanti, C., Rigolio, R., Donzelli, E., Canta, A., Ballarini, E., Cavaletti, G., Gasco, P., Sancini, G., 2017. ApoE-modified solid lipid nanoparticles: A feasible strategy to cross the blood-brain barrier. *Journal of Controlled Release* 249, 103–110. <https://doi.org/10.1016/j.jconrel.2017.01.039>
- Danhier, F., Breton, A. Le, Préat, V., 2012a. RGD-based strategies to target alpha(v) beta(3) integrin in cancer therapy and diagnosis. *Mol Pharm* 9, 2961–2973. <https://doi.org/10.1021/mp3002733>
- Danhier, F., Feron, O., Préat, V., 2010. To exploit the tumor microenvironment: Passive and active tumor targeting of nanocarriers for anti-cancer drug delivery. *J Control Release* 148, 135–46. <https://doi.org/10.1016/j.jconrel.2010.08.027>
- Danhier, F., Pourcelle, V., Marchand-Brynaert, J., Jérôme, C., Feron, O., Préat, V., 2012b. Targeting of tumor endothelium by RGD-grafted PLGA-nanoparticles, in: *Methods in Enzymology*. Academic Press Inc., pp. 157–175. <https://doi.org/10.1016/B978-0-12-391860-4.00008-2>
- Davies, J.E., 1957. A quantitative kinetic theory of emulsion type. I. Physical chemistry of emulsifying, in: *Proceedings of 2nd International Congress Surface Activity*, Butterworths, London. pp. 426–438, Corpus ID: 37394087.

- Deane, R., Du Yan, S., Subramanyam, R.K., LaRue, B., Jovanovic, S., Hogg, E., Welch, D., Manness, L., Lin, C., Yu, J., Zhu, H., Ghiso, J., Frangione, B., Stern, A., Schmidt, A.M., Armstrong, D.L., Arnold, B., Liliensiek, B., Nawroth, P., Hofman, F., Kindy, M., Stern, D., Zlokovic, B., 2003. RAGE mediates amyloid- β peptide transport across the blood-brain barrier and accumulation in brain. *Nat Med* 9, 907–913. <https://doi.org/10.1038/nm890>
- Deane, R., Wu, Z., Sagare, A., Davis, J., Du Yan, S., Hamm, K., Xu, F., Parisi, M., LaRue, B., Hu, H.W., Spijkers, P., Guo, H., Song, X., Lenting, P.J., Van Nostrand, W.E., Zlokovic, B. V., 2004a. LRP/Amyloid β -Peptide Interaction Mediates Differential Brain Efflux of A β Isoforms. *Neuron* 43, 333–344. <https://doi.org/10.1016/j.neuron.2004.07.017>
- Deane, R., Wu, Z., Zlokovic, B. V., 2004b. RAGE (Yin) Versus LRP (Yang) Balance Regulates Alzheimer Amyloid β -Peptide Clearance Through Transport Across the Blood–Brain Barrier. *Stroke* 35, 2628–2631. <https://doi.org/10.1161/01.STR.0000143452.85382.d1>
- Demeule, M., Currie, J., Bertrand, Y., Ché, C., Nguyen, T., Régina, A., Gabathuler, R., Castaigne, J., Béliveau, R., 2008. Involvement of the low-density lipoprotein receptor-related protein in the transcytosis of the brain delivery vector Angiopep-2. *J Neurochem* 106, 1534–1544. <https://doi.org/10.1111/j.1471-4159.2008.05492.x>
- Derksen, J.T., Morselt, H.W., Scherphof, G.L., 1988. Uptake and processing of immunoglobulin-coated liposomes by subpopulations of rat liver macrophages. *Biochim Biophys Acta* 971, 127–36. [https://doi.org/10.1016/0167-4889\(88\)90184-x](https://doi.org/10.1016/0167-4889(88)90184-x)
- Descamps, L., Dehouck, M.P., Torpier, G., Cecchelli, R., 1996. Receptor-mediated transcytosis of transferrin through blood-brain barrier endothelial cells. *Am J Physiol* 270, H1149–58. <https://doi.org/10.1152/ajpheart.1996.270.4.H1149>
- Desgrosellier, J.S., Cheresh, D.A., 2010. Integrins in cancer: biological implications and therapeutic opportunities. *Nat Rev Cancer* 10, 9–22. <https://doi.org/10.1038/nrc2748>

- Desrumaux, A., Marcand, J., 2002. Formation of sunflower oil emulsions stabilized by whey proteins with high-pressure homogenization (up to 350 MPa): effect of pressure on emulsion characteristics. *Int J Food Sci Technol* 37, 263–269. <https://doi.org/10.1046/j.1365-2621.2002.00565.x>
- Diez, B.D., Statkevich, P., Zhu, Y., Abutarif, M.A., Xuan, F., Kantesaria, B., Cutler, D., Cantillon, M., Schwarz, M., Pallotta, M.G., Ottaviano, F.H., 2010. Evaluation of the exposure equivalence of oral versus intravenous temozolomide. *Cancer Chemother Pharmacol* 65, 727–34. <https://doi.org/10.1007/s00280-009-1078-6>
- Dinh, H.-H.-Q., Santanach-Carreras, E., Schmitt, V., Lequeux, F., 2020. Coalescence in concentrated emulsions: theoretical predictions and comparison with experimental bottle test behaviour. *Soft Matter* 16, 10301–10309. <https://doi.org/10.1039/d0sm01459a>
- Döbereiner, H.G., Käs, J., Noppl, D., Sprenger, I., Sackmann, E., 1993. Budding and fission of vesicles. *Biophys J* 65, 1396–403. [https://doi.org/10.1016/S0006-3495\(93\)81203-7](https://doi.org/10.1016/S0006-3495(93)81203-7)
- Donoso, M., Cancino, J., Lee, J., Van Kerkhof, P., Retamal, C., Bu, G., Gonzalez, A., Cáceres, A., Marzolo, M.-P., 2009. Polarized Traffic of LRP1 Involves AP1B and SNX17 Operating on Y-dependent Sorting Motifs in Different Pathways. *Mol Biol Cell* 20, 481–497. <https://doi.org/10.1091/mbc.E08>
- Dou, X., Nomoto, T., Takemoto, H., Matsui, M., Tomoda, K., Nishiyama, N., 2018. Effect of multiple cyclic RGD peptides on tumor accumulation and intratumoral distribution of IRDye 700DX-conjugated polymers. *Sci Rep* 8. <https://doi.org/10.1038/s41598-018-26593-0>
- Drescher, S., van Hoogevest, P., 2020. The Phospholipid Research Center: Current Research in Phospholipids and Their Use in Drug Delivery. *Pharmaceutics* 12, 1235. <https://doi.org/10.3390/pharmaceutics12121235>

- Drioli, E., Giorno, L., 2016. Encyclopedia of Membranes, Encyclopedia of Membranes. Springer Berlin Heidelberg, Berlin, Heidelberg. <https://doi.org/10.1007/978-3-662-44324-8>
- Dropcho, E.J., 2011. The Neurologic Side Effects of Chemotherapeutic Agents. *CONTINUUM: Lifelong Learning in Neurology* 17, 95–112. <https://doi.org/10.1212/01.CON.0000394676.67372.87>
- Ducassou, A., Uro-Coste, E., Verrelle, P., Filleron, T., Benouaich-Amiel, A., Lubrano, V., Sol, J.C., Delisle, M.B., Favre, G., Ken, S., Laprie, A., De Porre, P., Toulas, C., Poublanc, M., Cohen-Jonathan Moyal, E., 2013. $\alpha\beta 3$ Integrin and Fibroblast growth factor receptor 1 (FGFR1): Prognostic factors in a phase I-II clinical trial associating continuous administration of Tipifarnib with radiotherapy for patients with newly diagnosed glioblastoma. *Eur J Cancer* 49, 2161–2169. <https://doi.org/10.1016/j.ejca.2013.02.033>
- Duffy, K.R., Pardridge, W.M., Rosenfeld, R.G., 1988. Human blood-brain barrier insulin-like growth factor receptor. *Metabolism* 37, 136–140. [https://doi.org/10.1016/S0026-0495\(98\)90007-5](https://doi.org/10.1016/S0026-0495(98)90007-5)
- Dunkelberger, J.R., Song, W.-C., 2010. Complement and its role in innate and adaptive immune responses. *Cell Res* 20, 34–50. <https://doi.org/10.1038/cr.2009.139>
- Eze, M.O., 1991. Phase transitions in phospholipid bilayers: Lateral phase separations play vital roles in biomembranes. *Biochem Educ* 19, 204–208. [https://doi.org/10.1016/0307-4412\(91\)90103-F](https://doi.org/10.1016/0307-4412(91)90103-F)
- Fabian, D., Guillermo Prieto Eibl, M. del P., Alnahhas, I., Sebastian, N., Giglio, P., Puduvalli, V., Gonzalez, J., Palmer, J.D., 2019. Treatment of Glioblastoma (GBM) with the Addition of Tumor-Treating Fields (TTF): A Review. *Cancers (Basel)* 11, 174. <https://doi.org/10.3390/cancers11020174>
- Faithfull, N.S., Weers, J.G., 1998. Perfluorocarbon compounds. *Vox Sang* 74 Suppl 2, 243–8. <https://doi.org/10.1111/j.1423-0410.1998.tb05426.x>

- Fan, Y., Zhang, Q., 2013. Development of liposomal formulations: From concept to clinical investigations. *Asian J Pharm Sci* 8, 81–87. <https://doi.org/10.1016/j.ajps.2013.07.010>
- Fearon, D.T., Austen, K.F., 1975. Properdin: binding to C3b and stabilization of the C3b-dependent C3 convertase. *J Exp Med* 142, 856–63. <https://doi.org/10.1084/jem.142.4.856>
- Fitzgerald, G., Soro-Arnaiz, I., De Bock, K., 2018. The Warburg Effect in Endothelial Cells and its Potential as an Anti-angiogenic Target in Cancer. *Front Cell Dev Biol* 6. <https://doi.org/10.3389/fcell.2018.00100>
- Floury, J., Legrand, J., Desrumaux, A., 2004. Analysis of a new type of high pressure homogeniser. Part B. study of droplet break-up and recoalescence phenomena. *Chem Eng Sci* 59, 1285–1294. <https://doi.org/10.1016/j.ces.2003.11.025>
- Fornari, W., Kazerooni, H.T., Hussong, J., Brandt, L., 2018. Suspensions of finite-size neutrally buoyant spheres in turbulent duct flow. *J Fluid Mech* 851, 148–186. <https://doi.org/10.1017/jfm.2018.490>
- Fournier, C.-O., Fradette, L., Tanguy, P.A., 2009. Effect of dispersed phase viscosity on solid-stabilized emulsions. *Chemical Engineering Research and Design* 87, 499–506. <https://doi.org/10.1016/j.cherd.2008.11.008>
- Gabizon, A., Shiota, R., Papahadjopoulos, D., 1989. Pharmacokinetics and tissue distribution of doxorubicin encapsulated in stable liposomes with long circulation times. *J Natl Cancer Inst* 81, 1484–8. <https://doi.org/10.1093/jnci/81.19.1484>
- Garred, P., Genster, N., Pilely, K., Bayarri-Olmos, R., Rosbjerg, A., Ma, Y.J., Skjoedt, M.-O., 2016. A journey through the lectin pathway of complement-MBL and beyond. *Immunol Rev* 274, 74–97. <https://doi.org/10.1111/imr.12468>

- Ghosh, S., Ray, A., Pramanik, N., 2020. Self-assembly of surfactants: An overview on general aspects of amphiphiles. *Biophys Chem* 265, 106429. <https://doi.org/10.1016/j.bpc.2020.106429>
- Gogate, P.R., Kabadi, A.M., 2009. A review of applications of cavitation in biochemical engineering/biotechnology. *Biochem Eng J* 44, 60–72. <https://doi.org/10.1016/j.bej.2008.10.006>
- Gregoriadis, G., Leathwood, P.D., Ryman, B.E., 1971. Enzyme entrapment in liposomes. *FEBS Lett* 14, 95–99. [https://doi.org/10.1016/0014-5793\(71\)80109-6](https://doi.org/10.1016/0014-5793(71)80109-6)
- Gregoriadis, G., Ryman, B.E., 1972a. Fate of protein-containing liposomes injected into rats. An approach to the treatment of storage diseases. *Eur J Biochem* 24, 485–91. <https://doi.org/10.1111/j.1432-1033.1972.tb19710.x>
- Gregoriadis, G., Ryman, B.E., 1972b. Lysosomal localization of -fructofuranosidase-containing liposomes injected into rats. *Biochem J* 129, 123–33. <https://doi.org/10.1042/bj1290123>
- Griffin, W.C., 1949. Classification of surface-active agents by “HLB”. *J Soc Cosmet Chem* 1, 311-324
- Griffin, W.C., 1954. Calculation of HLB values of non-ionic surfactants. *J Soc Cosmet Chem* 5, 249-56
- Groothuis, D.R., 2000. The blood-brain and blood-tumor barriers: A review of strategies for increasing drug delivery. *Neuro Oncol* 2, 45–59. <https://doi.org/10.1093/neuroonc/2.1.45>
- Gupta, A., Eral, H.B., Hatton, T.A., Doyle, P.S., 2016. Controlling and predicting droplet size of nanoemulsions: scaling relations with experimental validation. *Soft Matter* 12, 1452–1458. <https://doi.org/10.1039/C5SM02051D>

- Hajal, C., Le Roi, B., Kamm, R.D., Maoz, B.M., 2021. Biology and Models of the Blood-Brain Barrier. *Annu Rev Biomed Eng.* 2021, 359-384 <https://doi.org/10.1146/annurev-bioeng-082120>
- Hanif, F., Muzaffar, K., Perveen, K., Malhi, S.M., Simjee, S.U., 2017. Glioblastoma Multiforme: A Review of its Epidemiology and Pathogenesis through Clinical Presentation and Treatment. *Asian Pac J Cancer Prev* 18, 3–9. <https://doi.org/10.22034/APJCP.2017.18.1.3>
- Hardee, M.E., Zagzag, D., 2012. Mechanisms of glioma-associated neovascularization. *Am J Path* 181, 1126-41. <https://doi.org/10.1016/j.ajpath.2012.06.030>
- Haynes, D.H., 1992. Phospholipid-coated microcrystals: injectable formulations of water-insoluble drugs, US5091187A.
- He, H., Lu, Y., Qi, J., Zhu, Q., Chen, Z., Wu, W., 2019. Adapting liposomes for oral drug delivery. *Acta Pharm Sin B* 9, 36–48. <https://doi.org/10.1016/j.apsb.2018.06.005>
- Hersel, U., Dahmen, C., Kessler, H., 2003. RGD modified polymers: Biomaterials for stimulated cell adhesion and beyond. *Biomaterials* 24, 4385–4415. [https://doi.org/10.1016/S0142-9612\(03\)00343-0](https://doi.org/10.1016/S0142-9612(03)00343-0)
- Hersh, A.M., Alomari, S., Tyler, B.M., 2022. Crossing the Blood-Brain Barrier: Advances in Nanoparticle Technology for Drug Delivery in Neuro-Oncology. *Int J Mol Sci* 23, 4153. <https://doi.org/10.3390/ijms23084153>
- Hesse, M., Meier, H., Zeeh, B., 2005. Spektroskopische Methoden in der organischen Chemie, Thieme electronic book library. Thieme. <https://doi:10.1055/b-002-46985>
- Hoang Thi, T.T., Pilkington, E.H., Nguyen, D.H., Lee, J.S., Park, K.D., Truong, N.P., 2020. The Importance of Poly(ethylene glycol) Alternatives for Overcoming PEG Immunogenicity in Drug Delivery and Bioconjugation. *Polymers (Basel)* 12, 298. <https://doi.org/10.3390/polym12020298>

- Hohl, L., Röhl, S., Kraume, M., 2023. Drop Size Distributions as a Function of Dispersed Phase Viscosity: Experiments and Modeling. *Chem Eng Technol* 46, 1260–1270. <https://doi.org/10.1002/ceat.202200589>
- Hu, Y.-T., Ting, Y., Hu, J.-Y., Hsieh, S.-C., 2017. Techniques and methods to study functional characteristics of emulsion systems. *J Food Drug Anal* 25, 16–26. <https://doi.org/10.1016/j.jfda.2016.10.021>
- Huber-Lang, M., Ekdahl, K.N., Wiegner, R., Fromell, K., Nilsson, B., 2018. Auxiliary activation of the complement system and its importance for the pathophysiology of clinical conditions. *Semin Immunopathol* 40, 87-102. <https://doi.org/10.1007/s00281-017-0646-9>
- Ismail, M., Yang, W., Li, Y., Chai, T., Zhang, D., Du, Q., Muhammad, P., Hanif, S., Zheng, M., Shi, B., 2022. Targeted liposomes for combined delivery of artesunate and temozolomide to resistant glioblastoma. *Biomaterials* 287. <https://doi.org/10.1016/j.biomaterials.2022.121608>
- IUPAC, 2014. , in: *The IUPAC Compendium of Chemical Terminology*. International Union of Pure and Applied Chemistry (IUPAC), Research Triangle Park, NC. <https://doi.org/10.1351/goldbook.C01395>
- Jaegers, J., Haferkamp, S., Arnolds, O., Moog, D., Wrobeln, A., Nocke, F., Cantore, M., Pütz, S., Hartwig, A., Franzkoch, R., Psathaki, O.E., Jastrow, H., Schauerte, C., Stoll, R., Kirsch, M., Ferenz, K.B., 2022. Deciphering the Emulsification Process to Create an Albumin-Perfluorocarbon-(o/w) Nanoemulsion with High Shelf Life and Bioresistivity. *Langmuir* 38, 10351–10361. <https://doi.org/10.1021/acs.langmuir.1c03388>
- Jafari, S.M., Assadpoor, E., He, Y., Bhandari, B., 2008. Re-coalescence of emulsion droplets during high-energy emulsification. *Food Hydrocoll* 22, 1191–1202. <https://doi.org/10.1016/j.foodhyd.2007.09.006>

- Jafari, S.M., He, Y., Bhandari, B., 2007a. Production of sub-micron emulsions by ultrasound and microfluidization techniques. *J Food Eng* 82, 478–488. <https://doi.org/10.1016/j.jfoodeng.2007.03.007>
- Jafari, S.M., He, Y., Bhandari, B., 2007b. Optimization of nano-emulsions production by microfluidization. *European Food Research and Technology* 225, 733–741. <https://doi.org/10.1007/s00217-006-0476-9>
- Jafari, S.M., He, Y., Bhandari, B., 2007c. Effectiveness of encapsulating biopolymers to produce sub-micron emulsions by high energy emulsification techniques. *Food Research International* 40, 862–873. <https://doi.org/10.1016/j.foodres.2007.02.002>
- Janjic, J.M., Ahrens, E.T., 2009. Fluorine-containing nanoemulsions for MRI cell tracking. *Wiley Interdiscip Rev Nanomed Nanobiotechnol* 1, 492–501. <https://doi.org/10.1002/wnan.35>
- Jiang, X., Xin, H., Ren, Q., Gu, J., Zhu, L., Du, F., Feng, C., Xie, Y., Sha, X., Fang, X., 2014. Nanoparticles of 2-deoxy-D-glucose functionalized poly(ethylene glycol)-copoly(trimethylene carbonate) for dual-targeted drug delivery in glioma treatment. *Biomaterials* 35, 518–29. <https://doi.org/10.1016/j.biomaterials.2013.09.094>
- Jo, J., Schiff, D., Purow, B., 2012. Angiogenic inhibition in high-grade gliomas: Past, present and future. *Expert Rev Neurother* 12, 733–747. <https://doi.org/10.1586/ern.12.53>
- Johnson, U., Ohlsson, K., Olsson, I., 1976. Effects of granulocyte neutral proteases on complement components. *Scand J Immunol* 5, 421–6. <https://doi.org/10.1111/j.1365-3083.1976.tb00296.x>
- Juliano, R.L., Stamp, D., 1978. Pharmacokinetics of liposome-encapsulated anti-tumor drugs. Studies with vinblastine, actinomycin D, cytosine arabinoside, and daunomycin. *Biochem Pharmacol* 27, 21–7. [https://doi.org/10.1016/0006-2952\(78\)90252-6](https://doi.org/10.1016/0006-2952(78)90252-6)

- Kadry, H., Noorani, B., Cucullo, L., 2020. A blood-brain barrier overview on structure, function, impairment, and biomarkers of integrity. *Fluids Barriers CNS* 17, 69. <https://doi.org/10.1186/s12987-020-00230-3>
- Kaewbumrung, M., Plengsa-Ard, C., 2024. Relaminarization of jet impingement on a flat plate using separation-induced transition correction turbulence modeling preliminarily applied in archeological applications. *Heliyon* 10, e26040. <https://doi.org/10.1016/j.heliyon.2024.e26040>
- Karbstein, H., Schubert, H., 1995. Developments in the continuous mechanical production of oil-in-water macro-emulsions. *Chemical Engineering and Processing: Process Intensification* 34, 205–211. [https://doi.org/10.1016/0255-2701\(94\)04005-2](https://doi.org/10.1016/0255-2701(94)04005-2)
- Karthik, P., Ezhilarasi, P.N., Anandharamakrishnan, C., 2017. Challenges associated in stability of food grade nanoemulsions. *Crit Rev Food Sci Nutr* 57, 1435–1450. <https://doi.org/10.1080/10408398.2015.1006767>
- Kazerooni, H.T., Fornari, W., Hussong, J., Brandt, L., 2017. Inertial migration in dilute and semidilute suspensions of rigid particles in laminar square duct flow. *Phys Rev Fluids* 2, 084301. <https://doi.org/10.1103/PhysRevFluids.2.084301>
- Keenan, M.M., Chi, J.-T., 2015. Alternative fuels for cancer cells. *Cancer J* 21, 49–55. <https://doi.org/10.1097/PPO.0000000000000104>
- Keipert, P.E., 2006. OxygentTM, a Perfluorochemical-Based Oxygen Therapeutic for Surgical Patients, in: *Blood Substitutes*. Elsevier, pp. 312–323. <https://doi.org/10.1016/B978-012759760-7/50037-8>
- Kesarwani, P., Prabhu, A., Kant, S., Chinnaiyan, P., 2019. Metabolic remodeling contributes towards an immune-suppressive phenotype in glioblastoma. *Cancer Immunol Immunother* 68, 1107–1120. <https://doi.org/10.1007/s00262-019-02347-3>

- Khalfallah, A., 2024. Structure and Applications of Surfactants, in: *Surfactants - Fundamental Concepts and Emerging Perspectives*. IntechOpen. <https://doi.org/10.5772/intechopen.111401>
- Kirby, C., Clarke, J., Gregoriadis, G., 1980. Effect of the cholesterol content of small unilamellar liposomes on their stability in vivo and in vitro. *Biochem J* 186, 591–8. <https://doi.org/10.1042/bj1860591>
- Klapper, Y., Vrânceanu, M., Ishitsuka, Y., Evans, D., Scheider, D., Nienhaus, G.U., Leneweit, G., 2013. Surface energy of phospholipid bilayers and the correlation to their hydration. *J Colloid Interface Sci* 390, 267–74. <https://doi.org/10.1016/j.jcis.2012.09.027>
- Klein, E., Ciobanu, M., Klein, J., Machi, V., Leborgne, C., Vandamme, T., Frisch, B., Pons, F., Kichler, A., Zuber, G., Lebeau, L., 2010. “HFP” fluorinated cationic lipids for enhanced lipoplex stability and gene delivery. *Bioconjug Chem* 21, 360–71. <https://doi.org/10.1021/bc900469z>
- Kleinschmidt, J.H., Tamm, L.K., 2002. Structural Transitions in Short-Chain Lipid Assemblies Studied by ³¹P-NMR Spectroscopy. *Biophys J* 83, 994–1003. [https://doi.org/10.1016/S0006-3495\(02\)75225-9](https://doi.org/10.1016/S0006-3495(02)75225-9)
- Köhler, K., Schuchmann, H., 2012. *Emulgiertechnik: Grundlagen, Verfahren und Anwendungen*. Behr's Verlag.
- Kojima, H., Fujimiya, M., Matsumura, K., Nakahara, T., Hara, M., Chan, L., 2004. Extra-pancreatic insulin-producing cells in multiple organs in diabetes. *Proceedings of the National Academy of Sciences* 101, 2458–2463. <https://doi.org/10.1073/pnas.0308690100>
- Kolb, G., Viardot, K., Wagner, G., Ulrich, J., 2001. Evaluation of a New High-Pressure Dispersion Unit (HPN) for Emulsification. *Chem Eng Technol* 24, 293–296. [https://doi.org/10.1002/1521-4125\(200103\)24:3<293::AID-CEAT293>3.0.CO;2-0](https://doi.org/10.1002/1521-4125(200103)24:3<293::AID-CEAT293>3.0.CO;2-0)

- Kolb, H.C., Finn, M.G., Sharpless, K.B., 2001. Click-Chemie: diverse chemische Funktionalität mit einer Handvoll guter Reaktionen. *Angewandte Chemie* 113, 2056–2075. [https://doi.org/10.1002/1521-3757\(20010601\)113:11<2056::AID-ANGE2056>3.0.CO;2-W](https://doi.org/10.1002/1521-3757(20010601)113:11<2056::AID-ANGE2056>3.0.CO;2-W)
- Krafft, M.P., Riess, J.G., 2009. Chemistry, Physical Chemistry, and Uses of Molecular Fluorocarbon–Hydrocarbon Diblocks, Triblocks, and Related Compounds—Unique “Apolar” Components for Self-Assembled Colloid and Interface Engineering. *Chem Rev* 109, 1714–1792. <https://doi.org/10.1021/cr800260k>
- Lachmann, P.J., Halbwachs, L., 1975. The influence of C3b inactivator (KAF) concentration on the ability of serum to support complement activation. *Clin Exp Immunol* 21, 109–14. PMID: 52423
- Lachmann, P.J., Nicol, P., 1973. Reaction mechanism of the alternative pathway of complement fixation. *Lancet* 1, 465–7. [https://doi.org/10.1016/s0140-6736\(73\)91886-2](https://doi.org/10.1016/s0140-6736(73)91886-2)
- Lajoie, J.M., Shusta, E. V, 2015. Targeting receptor-mediated transport for delivery of biologics across the blood-brain barrier. *Annu Rev Pharmacol Toxicol* 55, 613–31. <https://doi.org/10.1146/annurev-pharmtox-010814-124852>
- Lasic, D.D., 1993. *Liposomes: From Physics to Applications*. Elsevier.
- Lassman, A.B., Joanta-Gomez, A.E., Pan, P.C., Wick, W., 2020. Current usage of tumor treating fields for glioblastoma. *Neurooncol Adv* 2. <https://doi.org/10.1093/no-ajnl/vdaa069>
- Lebelt, A., Dzieciół, J., Guzińska-Ustymowicz, K., Lemancewicz, D., Zimnoch, L., Czykier, E., 2008. Angiogenesis in gliomas. *Folia Histochem Cytobiol* 46, 69–72. <https://doi.org/10.2478/v10042-008-0009-4>
- Lee, J.Y., Spicer, A.P., 2000. Hyaluronan: a multifunctional, megaDalton, stealth molecule. *Curr Opin Cell Biol* 12, 581–6. [https://doi.org/10.1016/s0955-0674\(00\)00135-6](https://doi.org/10.1016/s0955-0674(00)00135-6)

- Lewerentz, F., Pappas, K., Bergenståhl, B., Håkansson, A., 2023. The effect of disperse phase viscosity in the emulsification of a semi-dairy beverage—combining emulsification experiments and numerical single drop breakup simulations. *Food and Bioproducts Processing* 138, 103–115. <https://doi.org/10.1016/j.fbp.2023.01.008>
- Lillis, A.P., Van Duyn, L.B., Murphy-Ullrich, J.E., Strickland, D.K., 2008. LDL Receptor-Related Protein 1: Unique Tissue-Specific Functions Revealed by Selective Gene Knockout Studies. *Physiol Rev* 88, 887–918. <https://doi.org/10.1152/physrev.00033.2007>
- Liu, P., Chen, G., Zhang, J., 2022. A Review of Liposomes as a Drug Delivery System: Current Status of Approved Products, Regulatory Environments, and Future Perspectives. *Molecules* 27. <https://doi.org/10.3390/molecules27041372>
- Lloyd, K.P., Ojelabi, O.A., De Zutter, J.K., Carruthers, A., 2017. Reconciling contradictory findings: Glucose transporter 1 (GLUT1) functions as an oligomer of allosteric, alternating access transporters. *J Biol Chem* 292, 21035–21046. <https://doi.org/10.1074/jbc.M117.815589>
- Lodish, H.F., 2000. *Molecular cell biology*. W.H. Freeman.
- Louis, D.N., Perry, A., Wesseling, P., Brat, D.J., Cree, I.A., Figarella-Branger, D., Hawkins, C., Ng, H.K., Pfister, S.M., Reifenberger, G., Soffietti, R., von Deimling, A., Ellison, D.W., 2021. The 2021 WHO Classification of Tumors of the Central Nervous System: a summary. *Neuro Oncol* 23, 1231–1251. <https://doi.org/10.1093/neuroonc/noab106>
- Lowe, K.C., 2006. Fluosol®: The First Commercial Injectable Perfluorocarbon Oxygen Carrier, in: *Blood Substitutes*. Elsevier, pp. 276–287. <https://doi.org/10.1016/B978-012759760-7/50034-2>

- Lubitz, L.J., Rieger, H., Leneweit, G., 2024a. Laminar and turbulent flow effects in high-pressure homogenization of liposomes and perfluorocarbon nanoemulsions. *Sci Rep* 14, 27856. <https://doi.org/10.1038/s41598-024-78550-9>
- Lubitz, L.J., Rieger, H., Leneweit, G.L., 2024b. Emulsifying mechanisms of phospholipids in high-pressure homogenization of perfluorocarbon nanoemulsions. *Soft Matter*. <https://doi.org/10.1039/d4sm00828f>
- Lubitz, L.J., Haffner, M.P., Rieger, H., Leneweit, G., 2024c. Elevated Cellular Uptake of Succinimide- and Glucose-Modified Liposomes for Blood–Brain Barrier Transfer and Glioblastoma Therapy. *Biomedicines* 12, 2135. <https://doi.org/10.3390/biomedicines12092135>
- Lubitz, L.J., Haffner, M.P., Rieger, H., Leneweit, G., 2024d. Increased Cellular Uptake of ApoE3- or c(RGD)-Modified Liposomes for Glioblastoma Therapy Depending on the Target Cells. *Pharmaceutics* 16, 1112. <https://doi.org/10.3390/pharmaceutics16091112>
- Maeda, H., Bharate, G.Y., Daruwalla, J., 2009. Polymeric drugs for efficient tumor-targeted drug delivery based on EPR-effect. *Eur J Pharm Biopharm* 71, 409–19. <https://doi.org/10.1016/j.ejpb.2008.11.010>
- Maeda, H., Sawa, T., Konno, T., 2001. Mechanism of tumor-targeted delivery of macromolecular drugs, including the EPR effect in solid tumor and clinical overview of the prototype polymeric drug SMANCS. *J Control Release* 74, 47–61. [https://doi.org/10.1016/s0168-3659\(01\)00309-1](https://doi.org/10.1016/s0168-3659(01)00309-1)
- Maletínská, L., Blakely, E.A., Bjornstad, K.A., Deen, D.F., Knoff, L.J., Forte, T.M., 2000. Human glioblastoma cell lines: levels of low-density lipoprotein receptor and low-density lipoprotein receptor-related protein. *Cancer Res* 60, 2300–3. PMID: 10786698

- Malvern Panalytical, 2013. User Manual ZetaSizer Nano. URL <https://www.chem.uci.edu/~dmitryf/manuals/Malvern%20Zetasizer%20ZS%20DLS%20user%20manual.pdf> (accessed 8.8.24).
- Mammen, M., Choi, S.-K., Whitesides, G.M., 1998. Polyvalent Interactions in Biological Systems: Implications for Design and Use of Multivalent Ligands and Inhibitors. *Angew Chem Int Ed Engl* 37, 2754–2794. [https://doi.org/10.1002/\(SICI\)1521-3773\(19981102\)37:20<2754::AID-ANIE2754>3.0.CO;2-3](https://doi.org/10.1002/(SICI)1521-3773(19981102)37:20<2754::AID-ANIE2754>3.0.CO;2-3)
- Mao, H., Lockyer, P., Li, L., Ballantyne, C.M., Patterson, C., Xie, L., Pi, X., 2017. Endothelial LRP1 regulates metabolic responses by acting as a co-activator of PPAR γ . *Nat Commun* 8, 14960. <https://doi.org/10.1038/ncomms14960>
- Marie, P., Perrier-Cornet, J.M., Gervais, P., 2002. Influence of major parameters in emulsification mechanisms using a high-pressure jet. *J Food Eng* 53, 43–51. [https://doi.org/10.1016/S0260-8774\(01\)00138-8](https://doi.org/10.1016/S0260-8774(01)00138-8)
- Marzolo, M.P., Yuseff, M.I., Retamal, C., Donoso, M., Ezquer, F., Farfán, P., Li, Y., Bu, G., 2003. Differential distribution of low-density lipoprotein-receptor-related protein (LRP) and megalin in polarized epithelial cells is determined by their cytoplasmic domains. *Traffic* 4, 273–288. <https://doi.org/10.1034/j.1600-0854.2003.00081.x>
- Mason, T.G., Wilking, J.N., Meleson, K., Chang, C.B., Graves, S.M., 2006. Nanoemulsions: formation, structure, and physical properties. *Journal of Physics: Condensed Matter* 18, R635–R666. <https://doi.org/10.1088/0953-8984/18/41/R01>
- Matsumura, Y., Maeda, H., 1986. A new concept for macromolecular therapeutics in cancer chemotherapy: mechanism of tumoritropic accumulation of proteins and the antitumor agent smancs. *Cancer Res* 46, 6387–92. PMID: 2946403
- Matsuoka, K., 2003. Micellization of fluorinated amphiphiles. *Curr Opin Colloid Interface Sci* 8, 227–235. [https://doi.org/10.1016/S1359-0294\(03\)00056-6](https://doi.org/10.1016/S1359-0294(03)00056-6)

- Mayer, L.D., Cullis, P.R., Bally, M.B., 1998. Designing therapeutically optimized liposomal anticancer delivery systems: Lessons from conventional liposomes, in: *Medical Applications of Liposomes*. Elsevier, pp. 231–257. <https://doi.org/10.1016/B978-044482917-7/50014-4>
- McClements, David J, Jafari, S.M., 2018. Chapter 1 - General Aspects of Nanoemulsions and Their Formulation, in: Jafari, S.M., McClements, David Julian (Eds.), *Nanoemulsions*. Academic Press, pp. 3–20. <https://doi.org/https://doi.org/10.1016/B978-0-12-811838-2.00001-1>
- McElhaney, R.N., 1976. The biological significance of alterations in the fatty acid composition of microbial membrane lipids in response to changes in environmental temperature, in: *Extreme Environments*. Elsevier, pp. 255–281. <https://doi.org/10.1016/B978-0-12-337850-7.50020-5>
- McEwen, B.S., Reagan, L.P., 2004. Glucose transporter expression in the central nervous system: relationship to synaptic function. *Eur J Pharmacol* 490, 13–24. <https://doi.org/10.1016/j.ejphar.2004.02.041>
- McNamara, M.G., Mason, W.P., 2012. Antiangiogenic therapies in glioblastoma multiforme. *Expert Rev Anticancer Ther* 12, 643–654. <https://doi.org/10.1586/era.12.35>
- Mellinger, A., Lubitz, L.J., Gazaille, C., Leneweit, G., Bastiat, G., Lépinoux-Chambaud, C., Eyer, J., 2023. The use of liposomes functionalized with the NFL-TBS.40–63 peptide as a targeting agent to cross the in vitro blood–brain barrier and target glioblastoma cells. *Int J Pharm* 646. <https://doi.org/10.1016/j.ijpharm.2023.123421>
- Merle, N.S., Church, S.E., Fremeaux-Bacchi, V., Roumenina, L.T., 2015. Complement system part I - molecular mechanisms of activation and regulation. *Front Immunol* 6. <https://doi.org/10.3389/fimmu.2015.00262>
- Mishra, S., Lin, Z., Pang, S., Zhang, Y., Bhatt, P., Chen, S., 2021. Biosurfactant is a powerful tool for the bioremediation of heavy metals from contaminated soils. *J Hazard Mater* 418, 126253. <https://doi.org/10.1016/j.jhazmat.2021.126253>

- Mitchell, M.J., Billingsley, M.M., Haley, R.M., Wechsler, M.E., Peppas, N.A., Langer, R., 2021. Engineering precision nanoparticles for drug delivery. *Nat Rev Drug Discov* 20, 101–124. <https://doi.org/10.1038/s41573-020-0090-8>
- Mohan, S., Narsimhan, G., 1997. Coalescence of Protein-Stabilized Emulsions in a High-Pressure Homogenizer. *J Colloid Interface Sci* 192, 1–15. <https://doi.org/10.1006/jcis.1997.5012>
- Mozafari, M.R., 2005. Liposomes: an overview of manufacturing techniques. *Cell Mol Biol Lett* 10, 711–9. PMID: 16341279
- Muller, P.Y., Milton, M.N., 2012. The determination and interpretation of the therapeutic index in drug development. *Nat Rev Drug Discov* 11, 751–61. <https://doi.org/10.1038/nrd3801>
- Murphy, K., Weaver, C., 2018. *Janeway Immunologie*. Springer Verlag. <https://doi.org/10.1007/978-3-662-56004-4>
- Needham, D., Nunn, R.S., 1990. Elastic deformation and failure of lipid bilayer membranes containing cholesterol. *Biophys J* 58, 997–1009. [https://doi.org/10.1016/S0006-3495\(90\)82444-9](https://doi.org/10.1016/S0006-3495(90)82444-9)
- Nesargikar, P.N., Spiller, B., Chavez, R., 2012. The complement system: history, pathways, cascade and inhibitors. *Eur J Microbiol Immunol (Bp)* 2, 103–11. <https://doi.org/10.1556/EuJMI.2.2012.2.2>
- Neumaier, F., Zlatopolskiy, B.D., Neumaier, B., 2021. Drug Penetration into the Central Nervous System: Pharmacokinetic Concepts and In Vitro Model Systems. *Pharmaceutics* 13. <https://doi.org/10.3390/pharmaceutics13101542>
- Ng, N., Powell, C.A., 2021. Targeting the Complement Cascade in the Pathophysiology of COVID-19 Disease. *J Clin Med* 10. <https://doi.org/10.3390/jcm10102188>

- Nicol, P.A., Lachmann, P.J., 1973. The alternate pathway of complement activation. The role of C3 and its inactivator (KAF). *Immunology* 24, 259–75. PMID: 4632688
- Nilsson, B., Ekdahl, K.N., Mollnes, T.E., Lambris, J.D., 2007. The role of complement in biomaterial-induced inflammation. *Mol Immunol* 44, 82–94. <https://doi.org/10.1016/j.molimm.2006.06.020>
- Nonaka, M., 2014. Evolution of the complement system. *Subcell Biochem* 80, 31–43. https://doi.org/10.1007/978-94-017-8881-6_3
- Obermeier, B., Daneman, R., Ransohoff, R.M., 2013. Development, maintenance and disruption of the blood-brain barrier. *Nat Med* 19, 1584–96. <https://doi.org/10.1038/nm.3407>
- Ohgaki, H., Dessen, P., Jourde, B., Horstmann, S., Nishikawa, T., Di Patre, P.-L., Burkhard, C., Schüler, D., Probst-Hensch, N.M., Maiorka, P.C., Baeza, N., Pisani, P., Yonekawa, Y., Yasargil, M.G., Lütolf, U.M., Kleihues, P., 2004. Genetic pathways to glioblastoma: a population-based study. *Cancer Res* 64, 6892–9. <https://doi.org/10.1158/0008-5472.CAN-04-1337>
- Oliva, C.R., Nozell, S.E., Diers, A., McClugage, S.G., Sarkaria, J.N., Markert, J.M., Darley-Usmar, V.M., Bailey, S.M., Gillespie, G.Y., Landar, A., Griguer, C.E., 2010. Acquisition of temozolomide chemoresistance in gliomas leads to remodeling of mitochondrial electron transport chain. *J Biol Chem* 285, 39759–67. <https://doi.org/10.1074/jbc.M110.147504>
- Oller-Salvia, B., Sánchez-Navarro, M., Giralt, E., Teixidó, M., 2016. Blood-brain barrier shuttle peptides: an emerging paradigm for brain delivery. *Chem Soc Rev* 45, 4690–707. <https://doi.org/10.1039/c6cs00076b>
- Olson, D.W., White, C.H., Richter, R.L., 2004. Effect of Pressure and Fat Content on Particle Sizes in Microfluidized Milk. *J Dairy Sci* 87, 3217–3223. [https://doi.org/10.3168/jds.S0022-0302\(04\)73457-8](https://doi.org/10.3168/jds.S0022-0302(04)73457-8)

- Ostrom, Q.T., Price, M., Neff, C., Cioffi, G., Waite, K.A., Kruchko, C., Barnholtz-Sloan, J.S., 2022. CBTRUS Statistical Report: Primary Brain and Other Central Nervous System Tumors Diagnosed in the United States in 2015–2019. *Neuro Oncol* 24, V1–V95. <https://doi.org/10.1093/neuonc/noac202>
- Pandolfe, W.D., 1981. Effect of dispersed and continuous phase viscosity on droplet size of emulsions generated by homogenization. *J Dispers Sci Technol* 2, 459–474. <https://doi.org/10.1080/01932698108943924>
- Pangburn, M.K., 2023. Initiation of the alternative pathway of complement and the history of “tickover.” *Immunol Rev.* <https://doi.org/10.1111/imr.13130>
- Pangburn, M.K., Müller-Eberhard, H.J., 1980. Relation of putative thioester bond in C3 to activation of the alternative pathway and the binding of C3b to biological targets of complement. *J Exp Med* 152, 1102–14. <https://doi.org/10.1084/jem.152.4.1102>
- Pangburn, M.K., Rawal, N., 2002. Structure and function of complement C5 convertase enzymes. *Biochem Soc Trans* 30, 1006–10. <https://doi.org/10.1042/bst0301006>
- Pangburn, M.K., Schreiber, R.D., Müller-Eberhard, H.J., 1981. Formation of the initial C3 convertase of the alternative complement pathway. Acquisition of C3b-like activities by spontaneous hydrolysis of the putative thioester in native C3. *J Exp Med* 154, 856–67. <https://doi.org/10.1084/jem.154.3.856>
- Papahadjopoulos, D., Watkins, J.C., 1967. Phospholipid model membranes. II. Permeability properties of hydrated liquid crystals. *Biochim Biophys Acta* 135, 639–52. [https://doi.org/10.1016/0005-2736\(67\)90095-8](https://doi.org/10.1016/0005-2736(67)90095-8)
- Pardridge, W.M., 2017. Delivery of Biologics Across the Blood–Brain Barrier with Molecular Trojan Horse Technology. *BioDrugs* 31, 503–519. <https://doi.org/10.1007/s40259-017-0248-z>
- Pardridge, W.M., 2005. Molecular Biology of the Blood–Brain Barrier. *Mol Biotechnol* 30, 057–070. <https://doi.org/10.1385/MB:30:1:057>

- Patching, S.G., 2017. Glucose Transporters at the Blood-Brain Barrier: Function, Regulation and Gateways for Drug Delivery. *Mol Neurobiol* 54, 1046–1077. <https://doi.org/10.1007/s12035-015-9672-6>
- Pautot, S., Frisken, B.J., Weitz, D.A., 2003. Engineering asymmetric vesicles. *Proceedings of the National Academy of Sciences* 100, 10718–10721. <https://doi.org/10.1073/pnas.1931005100>
- Perrier-Cornet, J.M., Marie, P., Gervais, P., 2005. Comparison of emulsification efficiency of protein-stabilized oil-in-water emulsions using jet, high pressure and colloid mill homogenization. *J Food Eng* 66, 211–217. <https://doi.org/10.1016/j.jfoodeng.2004.03.008>
- Pflanzner, T., Janko, M.C., André-Dohmen, B., Reuss, S., Weggen, S., Roebroek, A.J.M., Kuhlmann, C.R.W., Pietrzik, C.U., 2011. LRP1 mediates bidirectional transcytosis of amyloid- β across the blood-brain barrier. *Neurobiol Aging* 32, 2323.e1-2323.e11. <https://doi.org/10.1016/j.neurobiolaging.2010.05.025>
- Pierschbacher, M.D., Ruoslahti, E., 1984. Cell attachment activity of fibronectin can be duplicated by small synthetic fragments of the molecule. *Nature* 309, 30–33. <https://doi.org/10.1038/309030a0>
- Pillemer, L., Blum, L., Lepow, I.H., Ross, O.A., Todd, E.W., Wardlaw, A.C., 1954. The Properdin System and Immunity: I. Demonstration and Isolation of a New Serum Protein, Properdin, and Its Role in Immune Phenomena. *Science* (1979) 120, 279–285. <https://doi.org/10.1126/science.120.3112.279>
- Plenderleith, I.H., 1990. Treating the treatment: toxicity of cancer chemotherapy. *Can Fam Physician* 36, 1827–30. PMID: 21234006
- Pulgar, V.M., 2019. Transcytosis to Cross the Blood Brain Barrier, New Advancements and Challenges. *Front Neurosci* 12. <https://doi.org/10.3389/fnins.2018.01019>

- Qian, C., McClements, D.J., 2011. Formation of nanoemulsions stabilized by model food-grade emulsifiers using high-pressure homogenization: Factors affecting particle size. *Food Hydrocoll* 25, 1000–1008. <https://doi.org/10.1016/j.foodhyd.2010.09.017>
- Qin, Y., Fan, W., Chen, H., Yao, N., Tang, W., Tang, J., Yuan, W., Kuai, R., Zhang, Z., Wu, Y., He, Q., 2010. In vitro and in vivo investigation of glucose-mediated brain-targeting liposomes. *J Drug Target* 18, 536–549. <https://doi.org/10.3109/10611861003587235>
- Rabe, E., Bauersachs, R.M., Pannier, F., List, S.M., 2019. Venenerkrankungen der Beine. URL: https://www.rki.de/DE/Content/Gesundheitsmonitoring/Gesundheitsberichterstattung/GBEDownloadsT/venen.pdf?__blob=publicationFile (accessed 8.8.24).
- Raemdonck, K., Braeckmans, K., Demeester, J., De Smedt, S.C., 2014. Merging the best of both worlds: hybrid lipid-enveloped matrix nanocomposites in drug delivery. *Chem. Soc. Rev.* 43, 444–472. <https://doi.org/10.1039/C3CS60299K>
- Rahman, A., Carmichael, D., Harris, M., Roh, J.K., 1986. Comparative pharmacokinetics of free doxorubicin and doxorubicin entrapped in cardiolipin liposomes. *Cancer Res* 46, 2295–9. PMID: 3697976
- Ravera, F., Dziza, K., Santini, E., Cristofolini, L., Liggieri, L., 2021. Emulsification and emulsion stability: The role of the interfacial properties. *Adv Colloid Interface Sci* 288, 102344. <https://doi.org/10.1016/j.cis.2020.102344>
- Rawicz, W., Olbrich, K.C., McIntosh, T., Needham, D., Evans, E., 2000. Effect of chain length and unsaturation on elasticity of lipid bilayers. *Biophys J* 79, 328–39. [https://doi.org/10.1016/S0006-3495\(00\)76295-3](https://doi.org/10.1016/S0006-3495(00)76295-3)
- Redpath, G., Deo, N., 2022. Serotonin: an overlooked regulator of endocytosis and endosomal sorting? *Biol Open* 11. <https://doi.org/10.1242/bio.059057>

- Ricklin, D., Hajishengallis, G., Yang, K., Lambris, J.D., 2010. Complement: a key system for immune surveillance and homeostasis. *Nat Immunol* 11, 785–97. <https://doi.org/10.1038/ni.1923>
- Riedl, J., 2006. Partikelgrößenbestimmung über Lichtstreuung. URL: BIOCHEMIE - Josef Riedl - Regensburg (accessed 4.8.24)
- Riess, J.G., 2009. Highly fluorinated amphiphilic molecules and self-assemblies with biomedical potential. *Curr Opin Colloid Interface Sci* 14, 294–304. <https://doi.org/10.1016/j.cocis.2009.05.008>
- Riess, J.G., 2001. Oxygen carriers (“blood substitutes”)--raison d’etre, chemistry, and some physiology. *Chem Rev* 101, 2797–920. <https://doi.org/10.1021/cr970143c>
- Riess, J.G., Krafft, M.P., 1998. Fluorinated materials for in vivo oxygen transport (blood substitutes), diagnosis and drug delivery. *Biomaterials* 19, 1529–1539. [https://doi.org/10.1016/S0142-9612\(98\)00071-4](https://doi.org/10.1016/S0142-9612(98)00071-4)
- Ronckers, C., Spix, C., Trübenbach, C., Katalinic, A., Christ, M., Cicero, A., Folkerts, J., Hansmann, J., Kranzhöfer, K., Kunz, B., Manegold, K., Meyer zum Büschenfelde, U., Penzkofer, A., Vollmer, G., Weg-Remers, S., Barnes, B., Buttmann-Schweiger, N., Dahm, S., Franke, M., Schönfeld, I., Kraywinkel, K., Wienecke, A., 2023. Krebs in Deutschland für 2019/2020. URL: RKI – Krebs in Deutschland – 2019/2020 (krebsdaten.de) (accessed 4.8.24)
- Rosen, M.J., 2004. *Surfactants and Interfacial Phenomena*. Wiley. <https://doi.org/10.1002/0471670561>
- Saallah, S., Lenggono, I.W., 2018. Nanoparticles Carrying Biological Molecules: Recent Advances and Applications. *KONA Powder and Particle Journal* 35, 89–111. <https://doi.org/10.14356/kona.2018015>

- Sahu, A., Lambris, J.D., 2001. Structure and biology of complement protein C3, a connecting link between innate and acquired immunity. *Immunol Rev* 180, 35–48. <https://doi.org/10.1034/j.1600-065x.2001.1800103.x>
- Saka, R., Sathe, P., Khan, W., 2019. Brain local delivery strategy, in: *Brain Targeted Drug Delivery System*. Elsevier, pp. 241–286. <https://doi.org/10.1016/B978-0-12-814001-7.00011-1>
- Samad, A., Sultana, Y., Aqil, M., 2007. Liposomal Drug Delivery Systems: An Update Review. *Curr Drug Deliv* 4, 297–305. <https://doi.org/10.2174/156720107782151269>
- Sano, M., Tamai, K., 2016. A universal transition to turbulence in channel flow. *Nat Phys* 12, 249–253. <https://doi.org/10.1038/nphys3659>
- Scartazzini, R., Luisi, P.L., 1988. Organogels from lecithins. *J Phys Chem* 92, 829–833. <https://doi.org/10.1021/j100314a047>
- Schubert, H., Armbruster, H., 1989. Prinzipien der Herstellung und Stabilität von Emulsionen. *Chemie Ingenieur Technik* 61, 701–711. <https://doi.org/10.1002/cite.330610906>
- Schuchmann, H.P., Danner, T., 2004. Emulgieren: Mehr als nur Zerkleinern. *Chemie Ingenieur Technik* 76, 364–375. <https://doi.org/10.1002/cite.200406163>
- Schultz, S., Wagner, G., Urban, K., Ulrich, J., 2004. High-Pressure Homogenization as a Process for Emulsion Formation. *Chem Eng Technol* 27, 361–368. <https://doi.org/10.1002/ceat.200406111>
- Schweizer, T., Kubach, H., Koch, T., 2021. Investigations to characterize the interactions of light radiation, engine operating media and fluorescence tracers for the use of qualitative light-induced fluorescence in engine systems. *Automotive and Engine Technology* 6, 275–287. <https://doi.org/10.1007/s41104-021-00092-3>

- Sheikh, A., Alhakamy, N.A., Md, S., Kesharwani, P., 2021. Recent Progress of RGD Modified Liposomes as Multistage Rocket Against Cancer. *Front Pharmacol* 12, 803304. <https://doi.org/10.3389/fphar.2021.803304>
- Shruti, N. R., Behera, M.M., Naik, S.K., Das, S.K., Gopan, S., Ghosh, A., Sahu, R.N., Patra, S., Purkait, S., 2022. Elevated expression of cholesterol transporter LRP-1 is crucially implicated in the pathobiology of glioblastoma. *Front Neurol* 13, 1003730. <https://doi.org/10.3389/fneur.2022.1003730>
- Simpson, I.A., Appel, N.M., Hokari, M., Oki, J., Holman, G.D., Maher, F., Koehler-Stec, E.M., Vannucci, S.J., Smith, Q.R., 1999. Blood-brain barrier glucose transporter: effects of hypo- and hyperglycemia revisited. *J Neurochem* 72, 238–47. <https://doi.org/10.1046/j.1471-4159.1999.0720238.x>
- Soroceanu, L., Murase, R., Limbad, C., Singer, E., Allison, J., Adrados, I., Kawamura, R., Pakdel, A., Fukuyo, Y., Nguyen, D., Khan, S., Arauz, R., Yount, G.L., Moore, D.H., Desprez, P.-Y., McAllister, S.D., 2013. Id-1 is a key transcriptional regulator of glioblastoma aggressiveness and a novel therapeutic target. *Cancer Res* 73, 1559–69. <https://doi.org/10.1158/0008-5472.CAN-12-1943>
- Spahn, D.R., 1999. Blood substitutes. Artificial oxygen carriers: perfluorocarbon emulsions. *Crit Care* 3, R93-7. <https://doi.org/10.1186/cc364>
- Spuch, C., Ortolano, S., Navarro, C., 2012. LRP-1 and LRP-2 receptors function in the membrane neuron. Trafficking mechanisms and proteolytic processing in Alzheimer's disease. *Front Physiol* 3. <https://doi.org/10.3389/fphys.2012.00269>
- Stetefeld, J., McKenna, S.A., Patel, T.R., 2016. Dynamic light scattering: a practical guide and applications in biomedical sciences. *Biophys Rev* 8, 409-427. <https://doi.org/10.1007/s12551-016-0218-6>
- Stupp, R., Mason, W.P., van den Bent, M.J., Weller, M., Fisher, B., Taphoorn, M.J.B., Belanger, K., Brandes, A.A., Marosi, C., Bogdahn, U., Curschmann, J., Janzer,

- R.C., Ludwin, S.K., Gorlia, T., Allgeier, A., Lacombe, D., Cairncross, J.G., Eisenhauer, E., Mirimanoff, R.O., European Organisation for Research and Treatment of Cancer Brain Tumor and Radiotherapy Groups, National Cancer Institute of Canada Clinical Trials Group, 2005. Radiotherapy plus concomitant and adjuvant temozolomide for glioblastoma. *N Engl J Med* 352, 987–96. <https://doi.org/10.1056/NEJMoa043330>
- Sweeney, M.D., Zhao, Z., Montagne, A., Nelson, A.R., Zlokovic, B. V., 2019. Blood-Brain Barrier: From Physiology to Disease and Back. *Physiol Rev* 99, 21–78. <https://doi.org/10.1152/physrev.00050.2017>
- Tadros, T.F., 2013. Emulsion Formation, Stability, and Rheology, in: *Emulsion Formation and Stability*. Wiley, pp. 1–75. <https://doi.org/10.1002/9783527647941.ch1>
- Taylor, R.E., Zahid, M., 2020. Cell penetrating peptides, novel vectors for gene therapy. *Pharmaceutics* 12. <https://doi.org/10.3390/pharmaceutics12030225>
- Tehrani-Bagha, A., Holmberg, K., 2013. Solubilization of Hydrophobic Dyes in Surfactant Solutions. *Materials* 6, 580–608. <https://doi.org/10.3390/ma6020580>
- Tesch, S., Schubert, H., 2002. Influence of increasing viscosity of the aqueous phase on the short-term stability of protein stabilized emulsions. *J Food Eng* 52, 305–312. [https://doi.org/10.1016/S0260-8774\(01\)00120-0](https://doi.org/10.1016/S0260-8774(01)00120-0)
- Thrombose bei Krebs: Risiko zu wenig bekannt | DKFZ - Krebsinformationsdienst, 2023. URL <https://www.krebsinformationsdienst.de/aktuelles/detail/thrombose-bei-krebs-risiko-zu-wenig-bekannt> (accessed 8.8.24).
- Tikhonov, A.M., 2020. Nonspecular X-Ray Scattering from a Planar Phospholipid Multilayer. *Journal of Experimental and Theoretical Physics* 131, 714–722. <https://doi.org/10.1134/S1063776120100088>
- Tirotta, I., Dichiarante, V., Pigliacelli, C., Cavallo, G., Terraneo, G., Bombelli, F.B., Metrangolo, P., Resnati, G., 2015. (19)F magnetic resonance imaging (MRI): from

design of materials to clinical applications. *Chem Rev* 115, 1106–29. <https://doi.org/10.1021/cr500286d>

Tirri, L.J., Ayengar, N.K.N., Lipton, L.C., Chatterjie, N., Brockerhoff, H., 1978. Studies on the hydrogen belts of membranes: III. Glycerol permeability of dihydrosphingomyelin-cholesterol membranes. *Lipids* 13, 267–269. <https://doi.org/10.1007/BF02533668>

Topal, G.R., Mészáros, M., Porkoláb, G., Szecskó, A., Polgár, T.F., Siklós, L., Deli, M.A., Veszelka, S., Bozkir, A., 2021. ApoE-targeting increases the transfer of solid lipid nanoparticles with donepezil cargo across a culture model of the blood–brain barrier. *Pharmaceutics* 13, 1–19. <https://doi.org/10.3390/pharmaceutics13010038>

Torchilin, V.P., 2010. Passive and active drug targeting: drug delivery to tumors as an example. *Handb Exp Pharmacol* 197, 3–53. https://doi.org/10.1007/978-3-642-00477-3_1

Träuble, H., Grell, E., 1971. Carriers and specificity in membranes. IV. Model vesicles and membranes. The formation of asymmetrical spherical lecithin vesicles. *Neurosci Res Program Bull* 9, 373–80. PMID: 5164655

Trost, A., Lange, S., Schroedl, F., Bruckner, D., Motloch, K.A., Bogner, B., Kaser-Eichberger, A., Strohmaier, C., Runge, C., Aigner, L., Rivera, F.J., Reitsamer, H.A., 2016. Brain and Retinal Pericytes: Origin, Function and Role. *Front Cell Neurosci* 10. <https://doi.org/10.3389/fncel.2016.00020>

Uchida, Y., Ohtsuki, S., Katsukura, Y., Ikeda, C., Suzuki, T., Kamiie, J., Terasaki, T., 2011. Quantitative targeted absolute proteomics of human blood–brain barrier transporters and receptors. *J Neurochem* 117, 333–345. <https://doi.org/10.1111/j.1471-4159.2011.07208.x>

Underhill, C.B., Toole, B.P., 1980. Physical characteristics of hyaluronate binding to the surface of simian virus 40-transformed 3T3 cells. *J Biol Chem* 255, 4544–9. PMID: 6246078

- Urbańska, K., Sokołowska, J., Szmidt, M., Sysa, P., 2014. Review Glioblastoma multi-forme – an overview. *Współczesna Onkologia* 5, 307–312. <https://doi.org/10.5114/wo.2014.40559>
- Ushikubo, F.Y., Cunha, R.L., 2014. Stability mechanisms of liquid water-in-oil emulsions. *Food Hydrocoll* 34, 145–153. <https://doi.org/10.1016/j.foodhyd.2012.11.016>
- van der Flier, A., Sonnenberg, A., 2001. Function and interactions of integrins. *Cell Tissue Res* 305, 285–298. <https://doi.org/10.1007/s004410100417>
- Van Kerkhof, P., Lee, J., McCormick, L., Tetrault, E., Lu, W., Schoenfish, M., Oorschot, V., Strous, G.J., Klumperman, J., Bu, G., 2005. Sorting nexin 17 facilitates LRP recycling in the early endosome. *EMBO Journal* 24, 2851–2861. <https://doi.org/10.1038/sj.emboj.7600756>
- Vierling, P., Santaella, C., Greiner, J., 2001. Highly fluorinated amphiphiles as drug and gene carrier and delivery systems. *J Fluor Chem* 107, 337–354. [https://doi.org/10.1016/S0022-1139\(00\)00378-X](https://doi.org/10.1016/S0022-1139(00)00378-X)
- Virchow, R., 1865. Die krankhaften Geschwülste; dreissig Vorlesungen: gehalten während des Wintersemesters 1862-1863 an der Universität zu Berlin, Hirschwald.
- Vollmar, A., Zündorf, I., Dingermann, T., 2012. Immunologie Grundlagen und Wirkstoffe. BiblioScout. <https://doi.org/10.52778/9783804731172>
- Vorob'ev, S.I., 2009. First- and second-generation perfluorocarbon emulsions. *Pharm Chem J* 43, 209–218. <https://doi.org/10.1007/s11094-009-0268-1>
- Wagner, S., Zensi, A., Wien, S.L., Tschickardt, S.E., Maier, W., Vogel, T., Worek, F., Pietrzik, C.U., Kreuter, J., von Briesen, H., 2012. Uptake mechanism of ApoE-modified nanoparticles on brain capillary endothelial cells as a blood-brain barrier model. *PLoS One* 7. <https://doi.org/10.1371/journal.pone.0032568>

- Wakimoto, H., Mohapatra, G., Kanai, R., Curry, W.T., Yip, S., Nitta, M., Patel, A.P., Barnard, Z.R., Stemmer-Rachamimov, A.O., Louis, D.N., Martuza, R.L., Rabkin, S.D., 2012. Maintenance of primary tumor phenotype and genotype in glioblastoma stem cells. *Neuro Oncol* 14, 132–44. <https://doi.org/10.1093/neuonc/nor195>
- Walport, M.J., 2001. Complement. First of two parts. *N Engl J Med* 344, 1058–66. <https://doi.org/10.1056/NEJM200104053441406>
- Wang, L.-H., Wu, D.-C., Xu, H.-X., You, Y.-Z., 2016. High DNA-Binding Affinity and Gene-Transfection Efficacy of Bio reducible Cationic Nanomicelles with a Fluorinated Core. *Angew Chem Int Ed Engl* 55, 755–9. <https://doi.org/10.1002/anie.201508695>
- Wang, M., Liu, H., Li, L., Cheng, Y., 2014. A fluorinated dendrimer achieves excellent gene transfection efficacy at extremely low nitrogen to phosphorus ratios. *Nat Commun* 5, 3053. <https://doi.org/10.1038/ncomms4053>
- Wang, Q., Qin, X., Fang, J., Sun, X., 2021. Nanomedicines for the treatment of rheumatoid arthritis: State of art and potential therapeutic strategies. *Acta Pharm Sin B* 11, 1158–1174. <https://doi.org/10.1016/j.apsb.2021.03.013>
- Weers, J.G., 1993. A physicochemical evaluation of perfluorochemicals for oxygen transport applications. *J Fluor Chem* 64, 73–93. [https://doi.org/10.1016/S0022-1139\(00\)80064-0](https://doi.org/10.1016/S0022-1139(00)80064-0)
- WHO Global Cancer Observatory, 2022. URL https://gco.iarc.fr/today/en/dataviz/tables?mode=population&group_populations=0 (accessed 8.8.24).
- Wick, W., 2021. Gliome Entwicklungsstufe: S2k Leitlinien für Diagnostik und Therapie in der Neurologie. URL: [030-099l_S2k_Gliome_2021-07-verlaengert.pdf](https://www.awmf.org/uploads/tx_awmf/030-099l_S2k_Gliome_2021-07-verlaengert.pdf) (awmf.org) (accessed 4.8.24)
- Wirthmueller, U., Dewald, B., Thelen, M., Schäfer, M.K., Stover, C., Whaley, K., North, J., Eggleton, P., Reid, K.B., Schwaebler, W.J., 1997. Properdin, a positive regulator

- of complement activation, is released from secondary granules of stimulated peripheral blood neutrophils. *The Journal of Immunology* 158, 4444–4451. <https://doi.org/10.4049/jimmunol.158.9.4444>
- Wong, A.D., Ye, M., Levy, A.F., Rothstein, J.D., Bergles, D.E., Searson, P.C., 2013. The blood-brain barrier: an engineering perspective. *Front Neuroeng* 6. <https://doi.org/10.3389/fneng.2013.00007>
- Wu, C.-H., Liu, I.-J., Lu, R.-M., Wu, H.-C., 2016. Advancement and applications of peptide phage display technology in biomedical science. *J Biomed Sci* 23, 8. <https://doi.org/10.1186/s12929-016-0223-x>
- Xiao, Q., Rubien, J.D., Wang, Z., Reed, E.H., Hammer, D.A., Sahoo, D., Heiney, P.A., Yadavalli, S.S., Goulian, M., Wilner, S.E., Baumgart, T., Vinogradov, S.A., Klein, M.L., Percec, V., 2016. Self-Sorting and Coassembly of Fluorinated, Hydrogenated, and Hybrid Janus Dendrimers into Dendrimersomes. *J Am Chem Soc* 138, 12655–12663. <https://doi.org/10.1021/jacs.6b08069>
- Xu, L., Nirwane, A., Yao, Y., 2019. Basement membrane and blood-brain barrier. *Stroke Vasc Neurol* 4, 78–82. <https://doi.org/10.1136/svn-2018-000198>
- Yamamoto, M., Ikeda, K., Ohshima, K., Tsugu, H., Kimura, H., Tomonaga, M., 1998. Expression and cellular localization of low-density lipoprotein receptor-related protein/alpha 2-macroglobulin receptor in human glioblastoma in vivo. *Brain Tumor Pathol* 15, 23–30. <https://doi.org/10.1007/BF02482097>
- Yamamoto, M., Ikeda, K., Ohshima, K., Tsugu, H., Kimura, H., Tomonaga, M., 1997. Increased expression of low density lipoprotein receptor-related protein/alpha2-macroglobulin receptor in human malignant astrocytomas. *Cancer Res* 57, 2799–805. PMID: 9205092
- Yang, R., Zhang, X., Li, F., Ding, L., Li, B., Sun, H., Gan, Y., 2013. Role of phospholipids and copolymers in enhancing stability and controlling degradation of intravenous

lipid emulsions. *Colloids Surf A Physicochem Eng Asp* 436, 434–442.
<https://doi.org/10.1016/j.colsurfa.2013.07.022>

Zalba, S., Ten Hagen, T.L.M., Burgui, C., Garrido, M.J., 2022. Stealth nanoparticles in oncology: Facing the PEG dilemma. *J Control Release* 351, 22–36.
<https://doi.org/10.1016/j.jconrel.2022.09.002>

Zhang, C.-X., Zhao, W.-Y., Liu, L., Ju, R.-J., Mu, L.-M., Zhao, Y., Zeng, F., Xie, H.-J., Yan, Y., Lu, W.-L., 2015. A nanostructure of functional targeting epirubicin liposomes dually modified with aminophenyl glucose and cyclic pentapeptide used for brain glioblastoma treatment. *Oncotarget* 6, 32681–700.
<https://doi.org/10.18632/oncotarget.5354>

Zhang, Z., Li, Xin, Yang, F., Chen, C., Liu, P., Ren, Y., Sun, P., Wang, Z., You, Y., Zeng, Y.-X., Li, Xinjian, 2021. DHHC9-mediated GLUT1 S-palmitoylation promotes glioblastoma glycolysis and tumorigenesis. *Nat Commun* 12, 5872.
<https://doi.org/10.1038/s41467-021-26180-4>

Zhao, J., Xu, L., Sun, J., Song, M., Wang, L., Yuan, S., Zhu, Y., Wan, Z., Larsson, S., Tsilidis, K., Dunlop, M., Campbell, H., Rudan, I., Song, P., Theodoratou, E., Ding, K., Li, X., 2023. Global trends in incidence, death, burden and risk factors of early-onset cancer from 1990 to 2019. *BMJ Oncology* 2, e000049.
<https://doi.org/10.1136/bmjonc-2023-000049>

Zhao, Z., Yue, J., Ji, X., Nian, M., Kang, K., Qiao, H., Zheng, X., 2021. Research progress in biological activities of succinimide derivatives. *Bioorg Chem* 108, 104557.
<https://doi.org/10.1016/j.bioorg.2020.104557>

Zhigaltsev, I. V., Belliveau, N., Hafez, I., Leung, A.K.K., Huft, J., Hansen, C., Cullis, P.R., 2012. Bottom-up design and synthesis of limit size lipid nanoparticle systems with aqueous and triglyceride cores using millisecond microfluidic mixing. *Langmuir* 28, 3633–3640. <https://doi.org/10.1021/la204833h>

Zülch, K.J., 1979. Histological Typing of Tumours of the Central Nervous System, International histological classification of tumours. World Health Organization.

Appendix

A1 Process Optimization of a PFC/W Nanoemulsion Based on Membrane Extrusion

Comparison of Pre-Emulsification Methods

Within this chapter, the PFC/W nanoemulsion was prepared by membrane extrusion as described in Chapter 3.2.1.2.1. In order to evaluate the pre-mixing methods, a PFC/W nanoemulsion containing 7.5 mM lipid as a combination of E80 and cholesterol in a molar ratio of 95:5 and 2.5 % (v/v) PPHP was first prepared with the sonotrode or with the Ultra-Turrax. After this, a 3-fold extrusion using a track-etched membrane with 80 nm pore sizes followed by a 3-fold extrusion utilizing a membrane with a pore size of 50 nm was done

Figure A 1.1 summarizes the results obtained by the sonotrode for pre-mixing. Figure A 1.1a displays a decreasing particle size as the extrusion process proceeds with a final particle size of < 150 nm. This can also be seen in the case of the polydispersity index (Pdl) in Figure 1b, which drops from the initial value of 0.4 to < 0.2. The derived count rate (DCR), as a relative measure of the number of particles, shows an increase until the 50 nm membrane is used for extrusion. Considering the count rate percentages of all fractions after separation using a sucrose gradient (Figure A 1.1d), almost a third of the droplets are found in fractions 1 and 2. Due to the preparation of the PFC/W nanoemulsion using a lipid stock suspension in which the lipids are present in the form of liposomal vesicles and the subsequent density-based separation of the emulsion, liposomes are predominantly present in the first two fractions (Figure A 2.16).

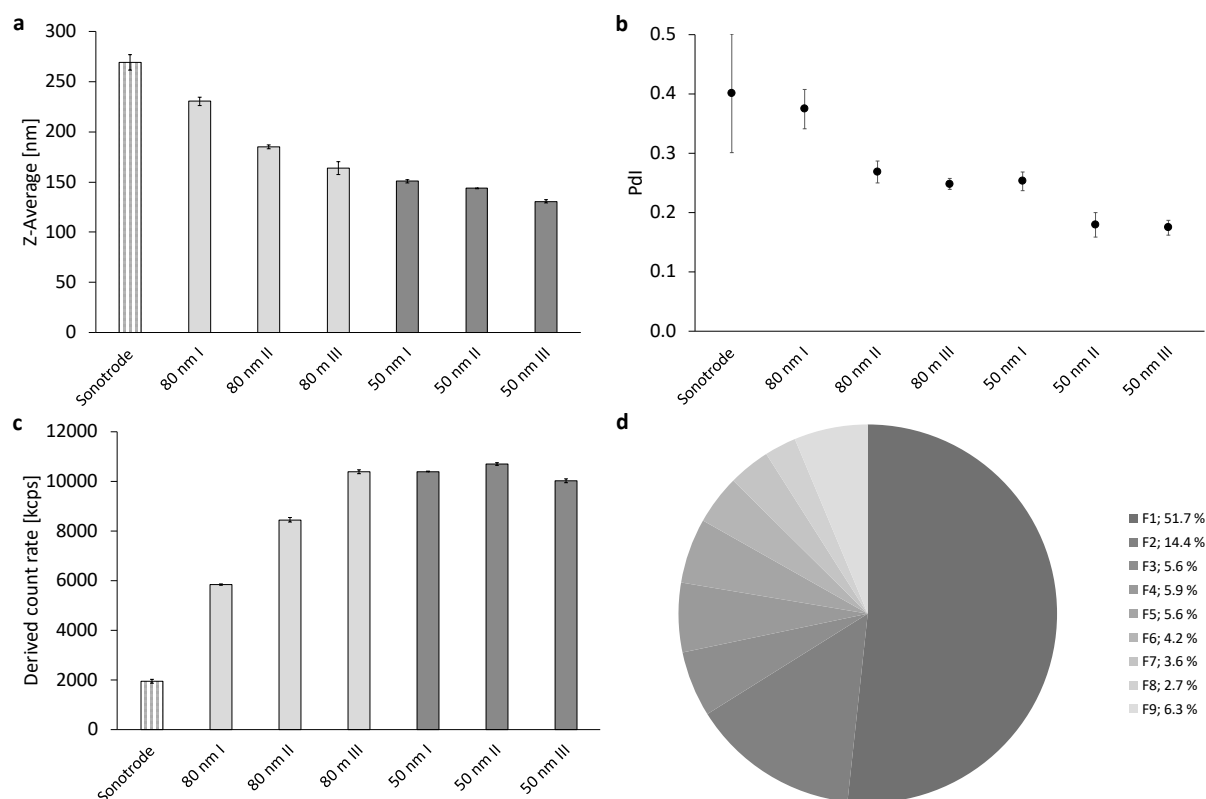


Figure A 1.1: Overview of the PFC/W nanoemulsion characteristics at all steps of the extrusion process after pre-mixing with the sonotrode. Representation of (a) the Z-Average, (b) the Pdl, (c) the DCR and (d) the count rate percentages of all fractions 1 to 9 after separation of the final nanoemulsion using a sucrose gradient. The bars or dots represent the mean \pm SD, $n = 3$.

Almost identical results were obtained for the extrusion process after pre-mixing with the Ultra-Turrax® (Figure A 1.2). Despite the significantly higher particle size (after pre-mixing > 400 nm (Figure A 1.2a) and the Pdl > 0.8 (Figure A 1.2b), the results after the extrusion process do not differentiate between the two pre-mixing methods. The proportion of remaining liposomes (Figure A 1.2d) is also around one-third. For many reasons, the Ultra-Turrax® is the more suitable emulsification method despite the high initial values with regard to Z-Ave and Pdl. The sonotrode is limited in its application to preparation sizes, and particles could get into the emulsion through the abrasion of the sonotrode tip. The simple and time-saving handling of the Ultra-Turrax® has to be mentioned as an additional advantage, which is why this method was chosen for pre-mixing.

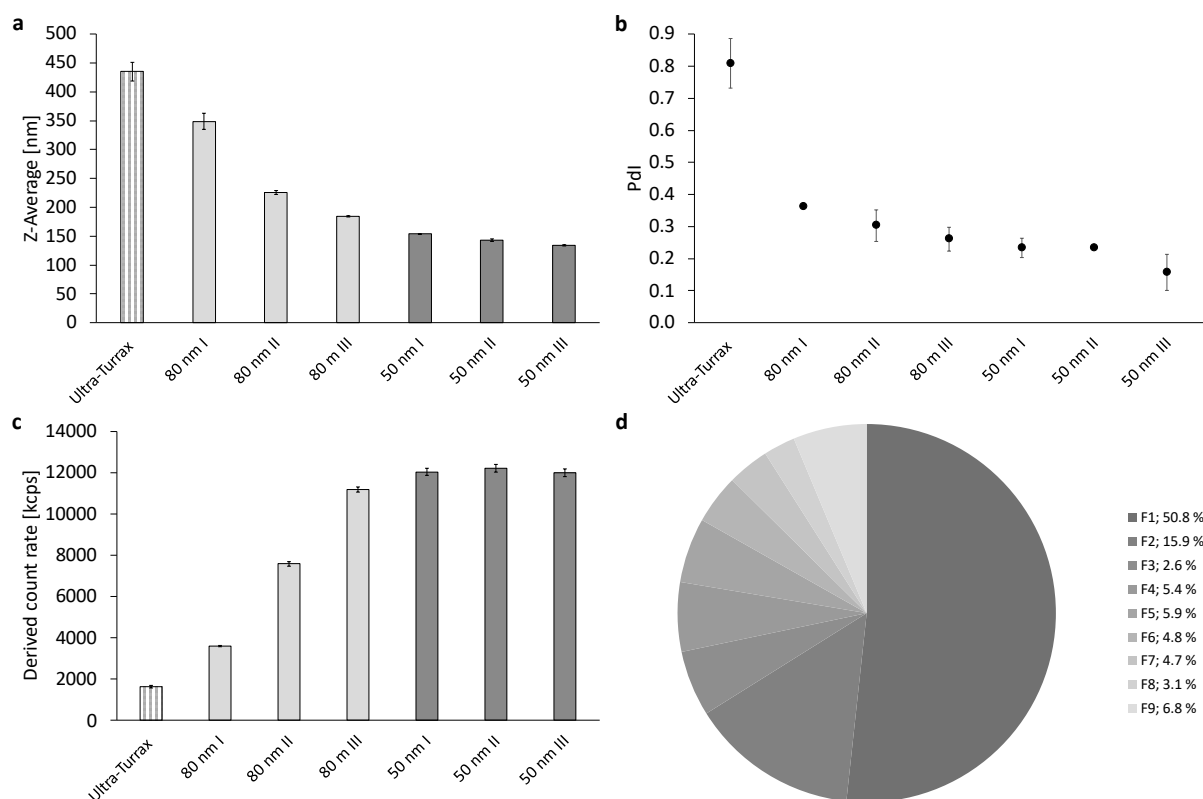


Figure A 1.2: Overview of the PFC/W nanoemulsion characteristics at all steps of the extrusion process after pre-mixing with the Ultra-Turrax®. Representation of (a) the Z-Average, (b) the Pdl, (c) the derived count rate (DCR) and (d) the count rate percentages of all fractions 1 to 9 after separation of the final nanoemulsion using a sucrose gradient. The bars or dots represent the mean \pm SD, $n = 3$.

Investigations on the Number of Membrane Passages

The following series of tests was carried out with the aim of the number of passages through different membrane pore sizes required. For this purpose, membranes with a pore diameter of 80 nm, 50 nm, 30 nm and 15 nm were tested (Table A 1.1). The individual results of the different membrane sizes and passages with regard to the Z-Ave, Pdl and DCR of the emulsion can be found in the supplementary figures (Figures S 1.1 – 1.4). Each particle size after a membrane passage was compared with the following one. For this purpose, a one-sided t-test for independent samples with a significance level of 5 % was carried out with the aim of determining the number of membrane passages from which there is no difference between the sizes.

The 80 nm membrane was tested first. The results indicate that the first 5 extrusions differ significantly (Figure S 1.1). From the 5th extrusion onwards, there is no significant

difference to the sixth extrusion, so that a number of 5 membrane passages was determined, where a Z-Ave of around 140 nm was achieved with the 80 nm membrane. In general, a Z-Ave of < 100 nm was aimed for with the 50 nm membrane. As soon as this value is reached, the significant difference of the next membrane passage is examined. With the 50 nm membrane, a Z-Ave of 98 nm was achieved with the 7th membrane passage; there is no significant difference to the next extrusion (Figure S 1.2).

For the 30 nm and 15 nm membrane (Figure S 1.3 and S 1.4), no further significant reduction in the Z-Ave compared to the results obtained with the 50 nm membrane was achieved. It has to be mentioned, that only a number of 10 membrane passages was tested, due to the tremendous increase of pressurization using Argon. A one-sided t-test is evaluated with the assumption that the size of the liposomes or oil droplets decreases. Contrary to the assumption, the mean values show that the Z-Ave increases in the first 4 extrusions when using the 15 nm membrane, so that the significant difference to be detected is not relevant. No size reduction was achieved with the 15 nm membrane.

Table A 1.1: Test setting for the determination of the membrane passages for the extrusion process of PFC/W nanoemulsion preparation.

Pore size	Membrane passages			
	Set 1	Set 2	Set 3	Set 4
80 nm	20 times	5 times	5 times	5 times
50 nm	-	20 times	7 times	7 times
30 nm	-	-	10 times	3 times
15 nm	-	-	-	10 times

Variation of Different Process Parameters for Optimization

A full-factorial experimental design was used to investigate the influence of the numbers of used membranes per pore size parameter, sonication of the extruder placed in a sonication bath and cooling on the extrusion process. An overview of the 8 different experimental setups can be found in Table A 1.2. For each experimental setup, the emulsion was extruded 5 times through an 80 nm membrane and then 7 times through a 50 nm membrane. Both after the 80 nm membrane and after the 50 nm membrane, the emulsion was measured using DLS and a separation using a sucrose gradient was carried

out. Figure A 1.3 summarizes the results obtained with the 80 nm membrane, whereas Figure A 1.4 represents the results obtained with the 50 nm membrane.

Table A 1.2: Test settings of process optimization. The number of membranes is expressed as 1 or 2, whereas the plus (+) represents with configuration with either sonication or cooling and the minus (-) represents the configuration without one of those parameters.

Test Nr.	Combinations							
	1	2	3	4	5	6	7	8
Membranes	1	2	1	1	2	2	1	2
Sonication	-	-	+	-	+	-	+	+
Cooling	-	-	-	+	-	+	+	+

The Z-Ave is on average smaller in the uncooled experiments (no. 1, 2, 3 and 5) than in the cooled experiments (no. 4, 6, 7, 8) (Figure A 1.3a). The experiments with two membranes (No. 2, 5, 6, 8) show a smaller Z-Ave, which is further reduced by sonication. The tests (No. 1, 3, 4, 7) with one membrane show on average a higher DCR than the tests with two membranes. With one membrane, higher DCR values are generated by sonication (Figure 3c). With two membranes, the DCR values are higher without sonication. The tests (No. 1, 3, 4, 7) with one membrane show on average a higher Pdl than the tests with two membranes (No. 2, 5, 6, 8) (Figure A 1.3b). In addition, the tests without sonication show a lower Pdl. The experiments with one membrane (No. 1, 3, 4, 7) show a lower proportion of remaining liposomes, whereby setup No. 1 with one membrane and without sonication and cooling shows the best results in this respect. Summarizing, Test number 2, based on 2 membranes but without sonication and cooling, obtained the best results.

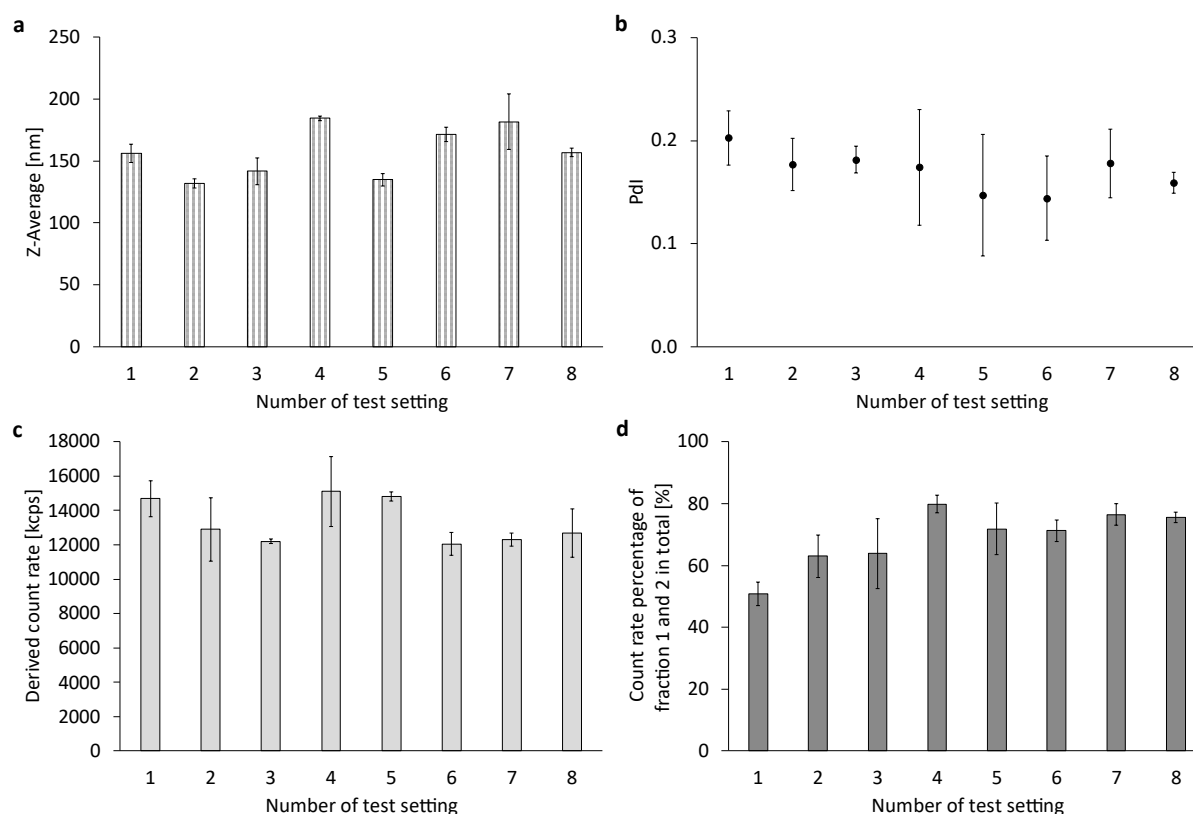


Figure A 1.3: Overview of the PFC/W nanoemulsion characteristics prepared by pre-mixing with the Ultra-Turrax® and 5-fold extrusion using an 80 nm membrane for all 8 different experimental setups. Representation of (a) the Z-Average, (b) the PDI, (c) the DCR and (d) the count rate percentages of fraction 1 and 2 in total. The bars or dots represent the mean \pm SD, $n = 3$.

The results of the different test settings after a further 7-fold extrusion using a 50 nm membrane (Figure A 1.4) are comparable to the results after the 80 nm membrane. There are only little differences concerning the DCR (Figure A 1.4c), where the minimum is at setup 2 instead of setup 3 (Figure A 1.3). In general, the Z-Ave was further decreased < 150 nm and the PDI was in all cases < 0.2 . Further processing of the nanoemulsion using a 50 nm membrane shows that the best results were also achieved with test number 2, in which two membranes were used on top of each other for extrusion.

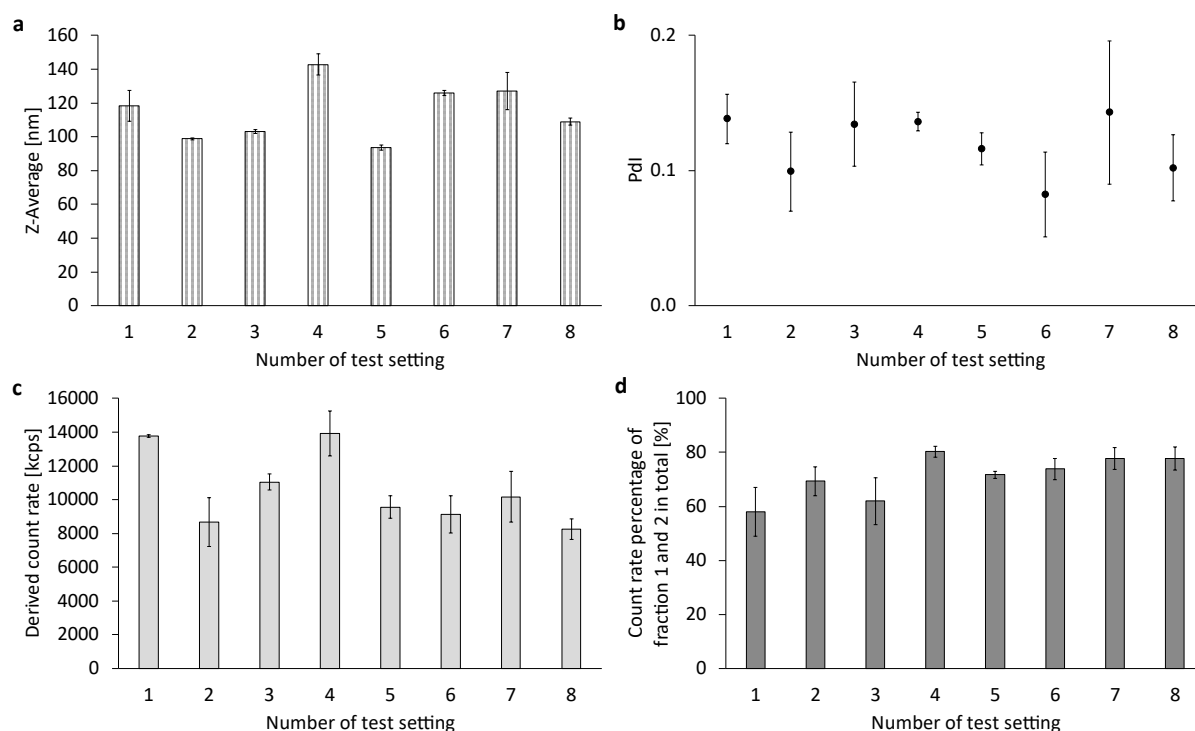


Figure A 1.4: Overview of the PFC/W nanoemulsion characteristics prepared by pre-mixing with the Ultra-Turrax® and 5-fold extrusion using a 50 nm membrane for all 8 different experimental setups. Representation of (a) the Z-Average, (b) the Pdl, (c) the DCR and (d) the count rate percentages of fractions 1 and 2 in total. The bars or dots represent the mean \pm SD, $n = 3$.

Evaluation of the Phospholipid Loss During Preparation

In order to estimate the loss of emulsifier during the preparation, a PFC/W nanoemulsion containing 5 mM lipid as a combination of DPPC, cholesterol and DSPE-PEG1k-Rhodamin B in a molar ratio of 69.9:30:0.1 and 2.5 % (v/v) PPHP was prepared by a 5-fold extrusion using a track-etched membrane with 80 nm pore sizes followed by a 7-fold extrusion using a membrane with a pore size of 50 nm. The results of the lipid quantification according to the Stewart Assay are displayed in Figure A 1.5.

The lipid concentrations were initially calculated using the theoretical intended concentrations such as 150 mM for the lipid stock suspension followed by a dilution step to 5 mM. Figure 5a displays a loss of the emulsifier of around 20 % over the manufacturing process. After separation of the final nanoemulsion using a sucrose gradient, the lipid concentration decreases from fraction 1 to 8 (Figure A 1.5b). The slight increase towards fraction 9 is presumably due to the manual fractionation and thus the carryover of lipids

to fraction 9. However, it should be noted that the lipid stock suspension, which was prepared with a total lipid concentration of 150 mM, only has a lipid concentration of $128.35 \text{ mM} \pm 0.99 \text{ mM}$ after resuspension. Taking this concentration into account, the corrected lipid concentrations were calculated over the manufacturing process (Figure A 1.5c and A 1.5d), resulting in an effective lipid loss of $11.60 \% \pm 5.45 \%$ during the extrusion process. The complementary DLS data as well as fluorescence intensities based on Rhodamin B can be found in the supplementary Figure S 1.5 and S 1.6.

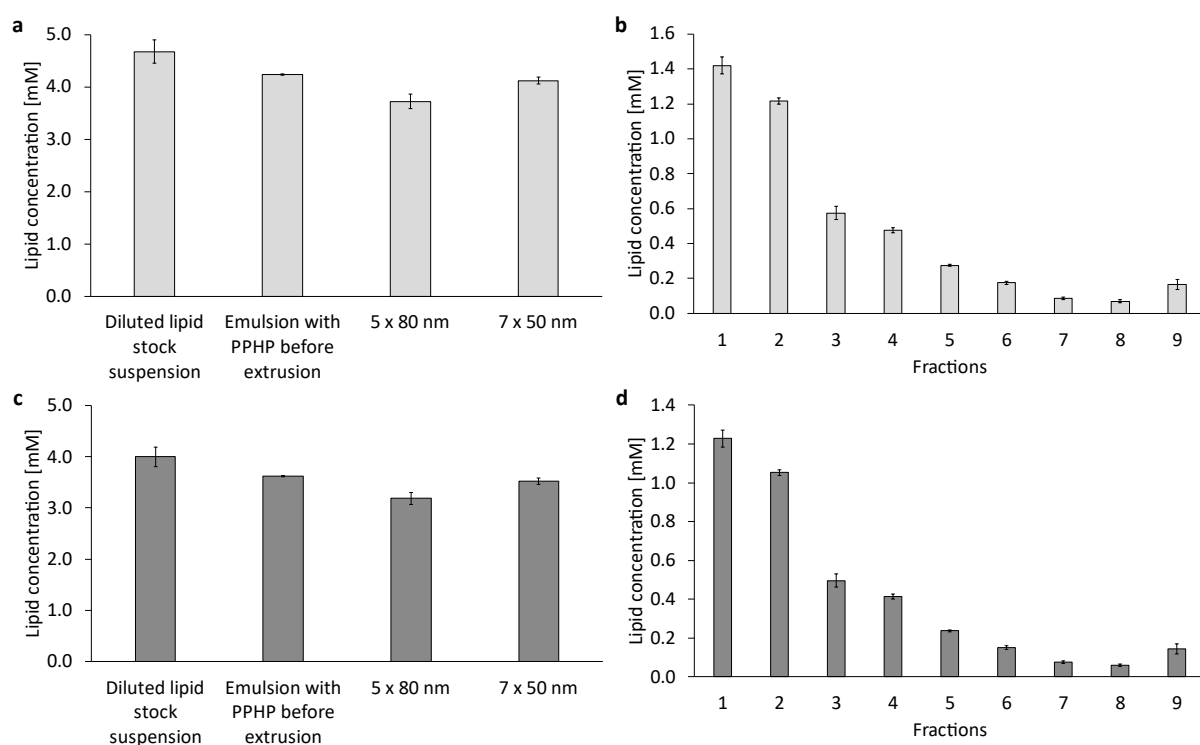


Figure A 1.5: Lipid loss during the PFC/W nanoemulsion preparation using membrane extrusion. Representation of the phospholipid concentrations according to the Stewart Assay at different steps of the emulsion preparation (a and c) and of all 9 fractions after separation using a sucrose gradient (b and d), whereas (a and b) are theoretically calculated and (c and d) are corrected to the determined concentration of the used lipid stock suspension. The bars represent the mean \pm SD, $n = 3$.

Supplementary Figures

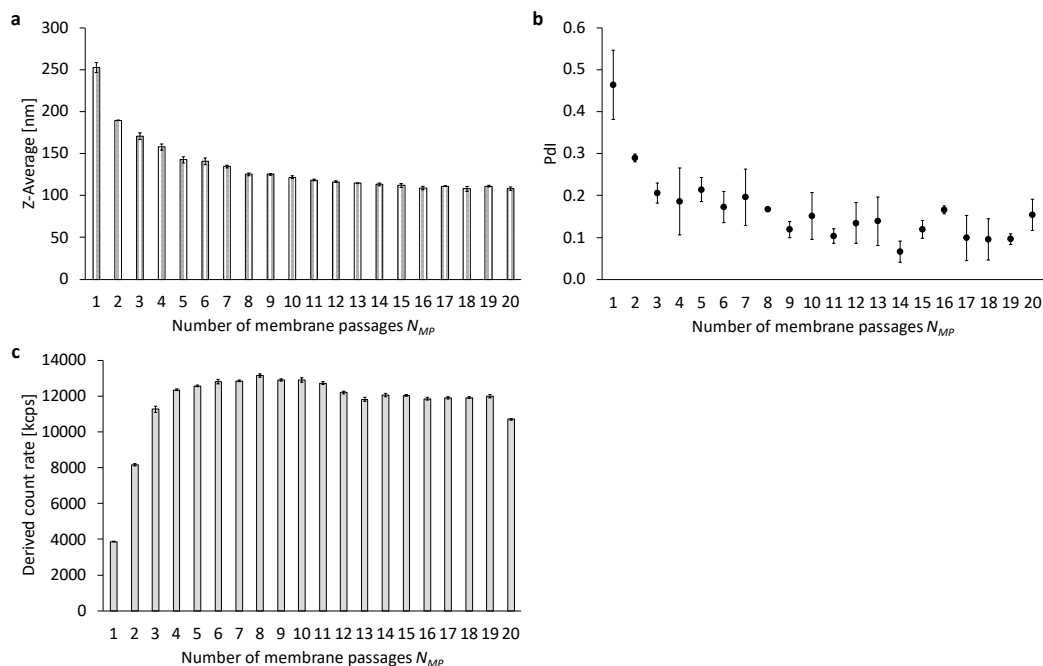


Figure S 1.1: Overview of the PFC/W nanoemulsion characteristics after each membrane passage through a 80 nm membrane. Representation of (a) the Z-Average, (b) the Pdl and (c) the DCR. The bars or dots represent the mean \pm SD, $n = 3$.

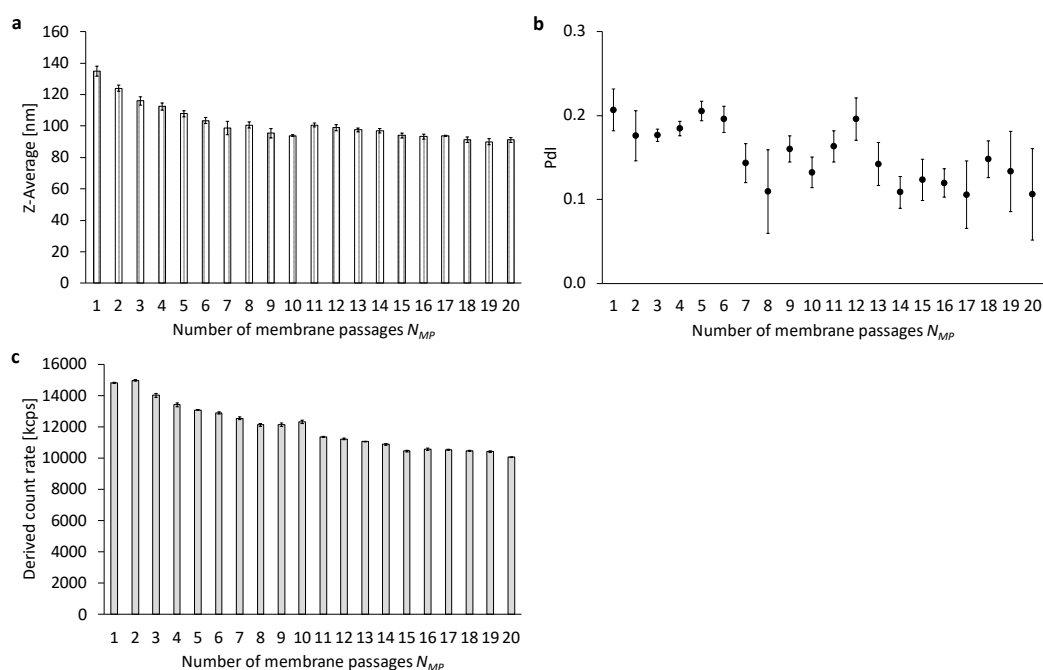


Figure S 1.2: Overview of the PFC/W nanoemulsion characteristics after each membrane passage through a 50 nm membrane. Representation of (a) the Z-Average, (b) the Pdl and (c) the DCR. The bars or dots represent the mean \pm SD, $n = 3$.

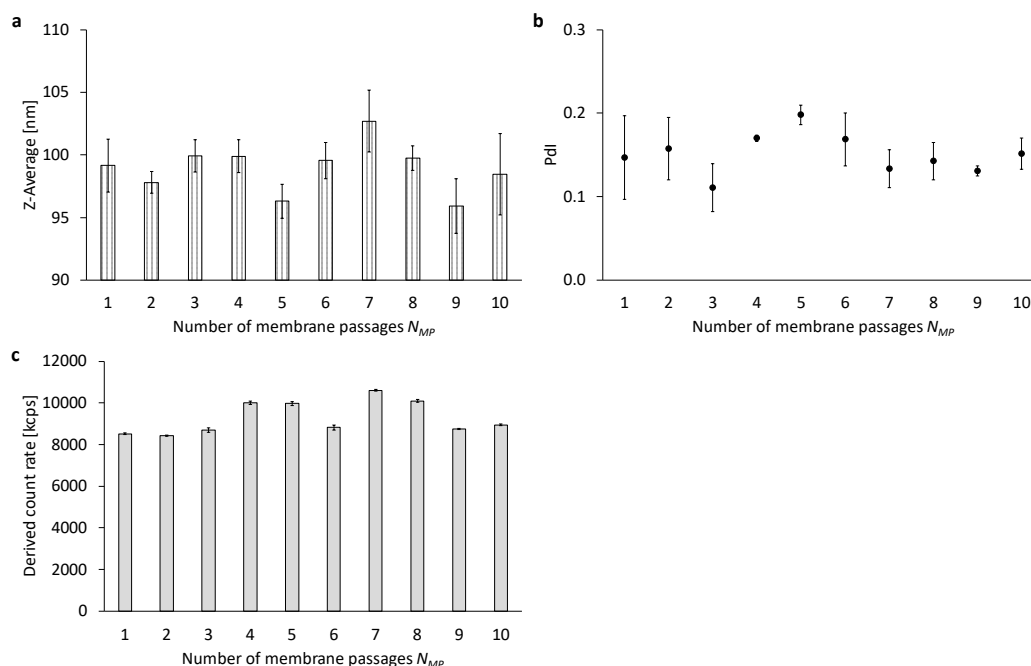


Figure S 1.3: Overview of the PFC/W nanoemulsion characteristics after each membrane passage through a 30 nm membrane. Representation of (a) the Z-Average in the range from 90 nm to 110 nm, (b) the Pdl and (c) the DCR. The bars or dots represent the mean \pm SD, $n = 3$.

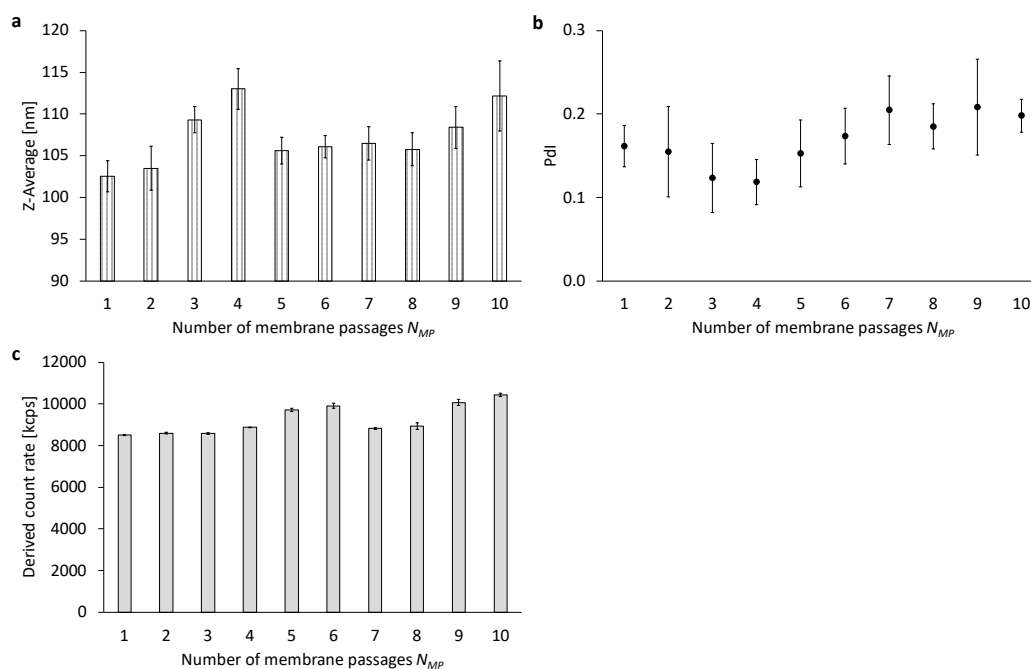


Figure S 1.4: Overview of the PFC/W nanoemulsion characteristics after each membrane passage through a 15 nm membrane. Representation of (a) the Z-Average in the range from 90 nm to 110 nm, (b) the Pdl and (c) the DCR. The bars or dots represent the mean \pm SD, $n = 3$.

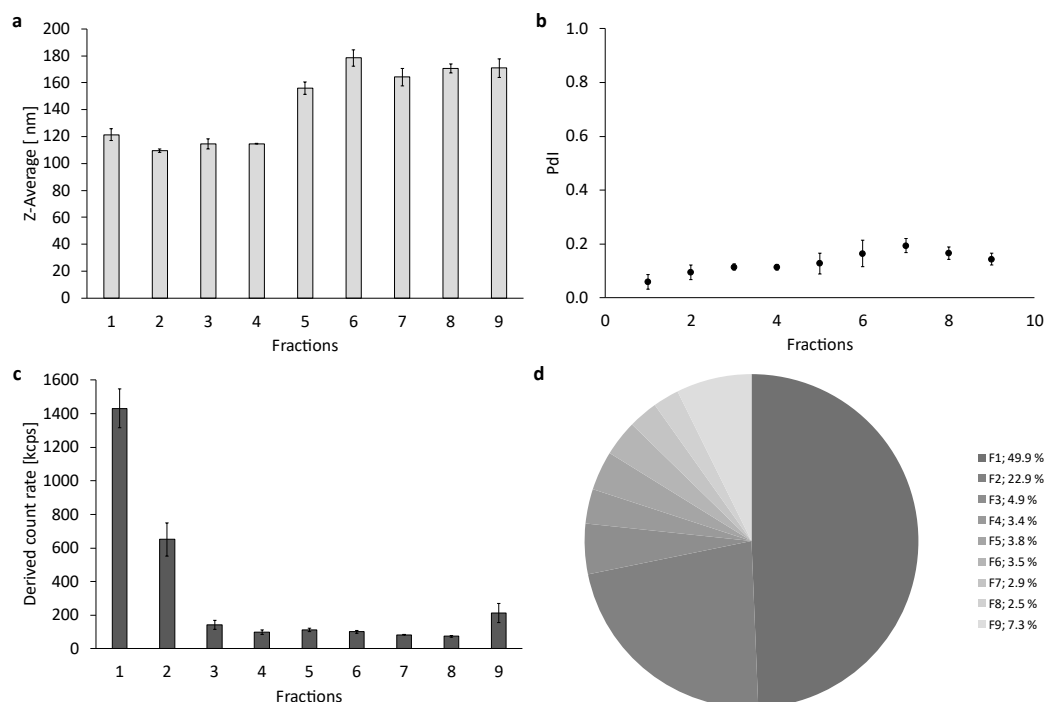


Figure S 1.5: Overview of the PFC/W nanoemulsion characteristics after the complete extrusion. Representation of (a) the Z-Average in the range from 90 nm to 110 nm, (b) the Pdl, (c) the DCR and (d) the count rate percentages of all fractions 1 to 9 after separation of the final nanoemulsion using a sucrose gradient. The bars or dots represent the mean \pm SD, $n = 3$.

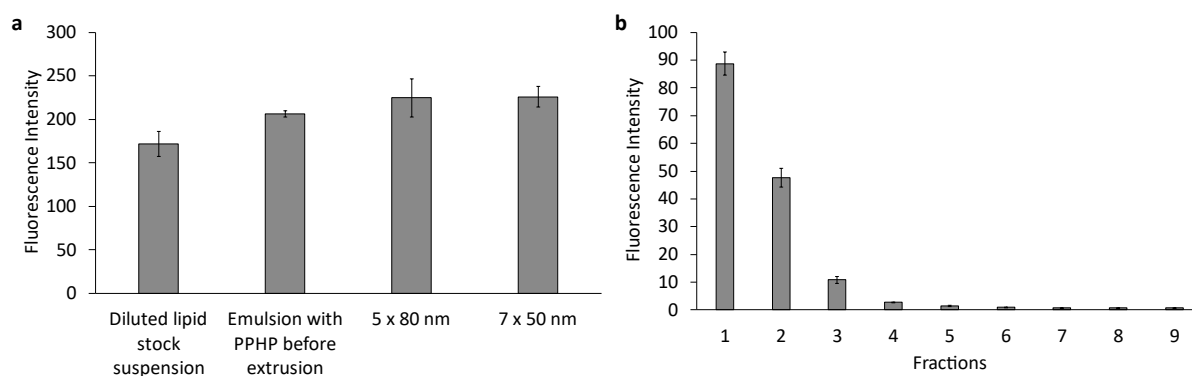


Figure S 1.6: Fluorescence intensities of a PFC/W nanoemulsion with incorporated DSPE-PEG1k-Rhodamin B at 0.1 mol%. Representation of the fluorescence intensities (a) at different steps of the nanoemulsion preparation and (b) of all 9 fractions after separation using a sucrose gradient. The bars represent the mean \pm SD, $n = 3$.

A2 Process Optimization of a PFC/W Nanoemulsion Based on High-Pressure Homogenization

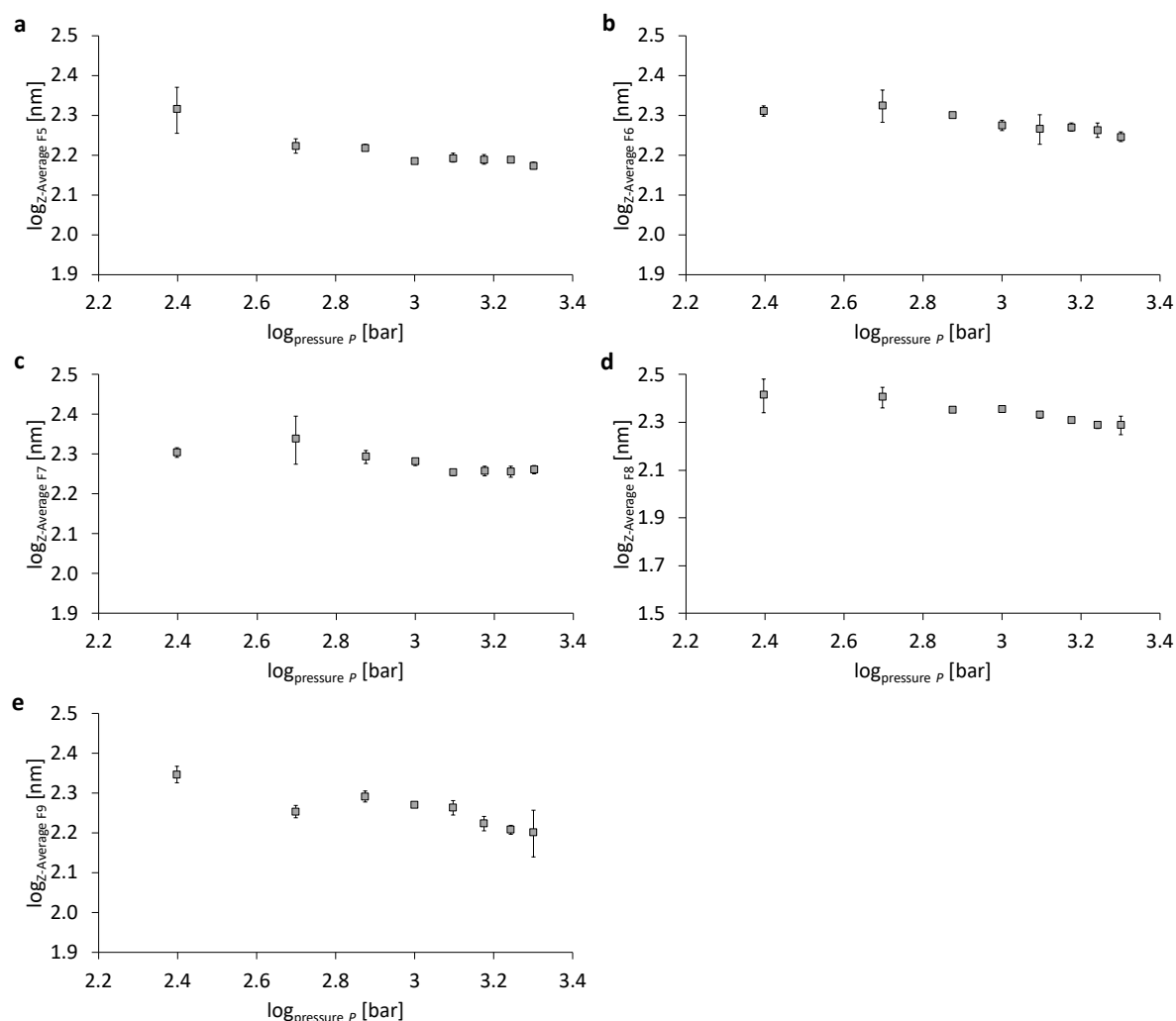


Figure A 2.1: Logarithmic representation of the pressure-dependent PFC-droplet size (Z-Average) of different fractions after separation using a sucrose gradient. Representation of logarithmic particle size of (a) fraction 5 (F5), (b) fraction 6 (F6), (c) fraction 7 (F7), (d) fraction 8 (F8) and (e) fraction 9 (F9). The grey squares represent the mean \pm SD, $n = 3$.

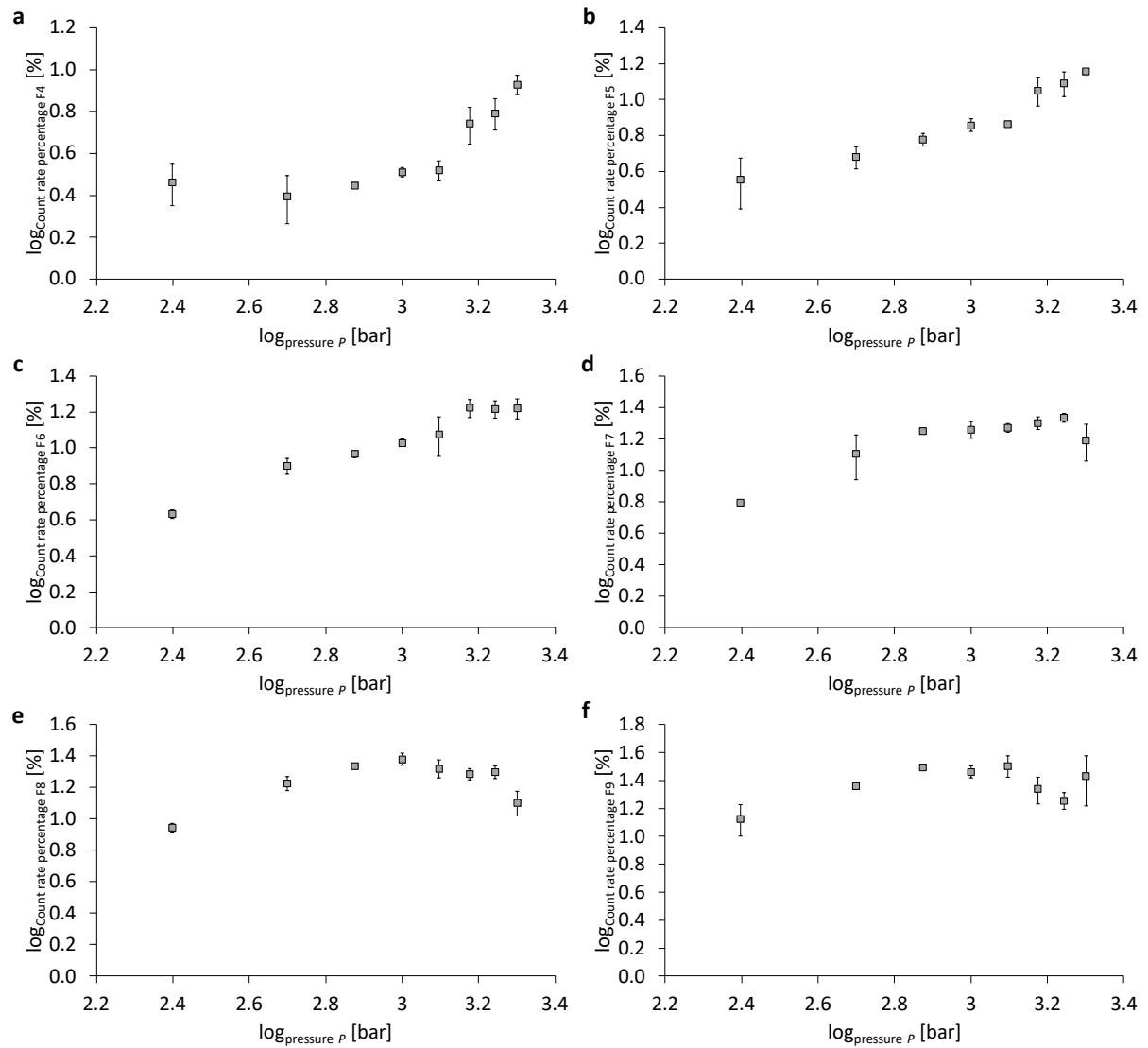


Figure A 2.2: Logarithmic representation of the pressure-dependent count rate percentage of different fractions after separation using a sucrose gradient. Representation of logarithmic count rate percentage of (a) fraction 4 (F4), (b) fraction 5 (F5), (c) fraction 6 (F6), (d) fraction 7 (F7), (e) fraction 8 (F8) and (f) fraction 9 (F9). The grey squares represent the mean \pm SD, $n = 3$.

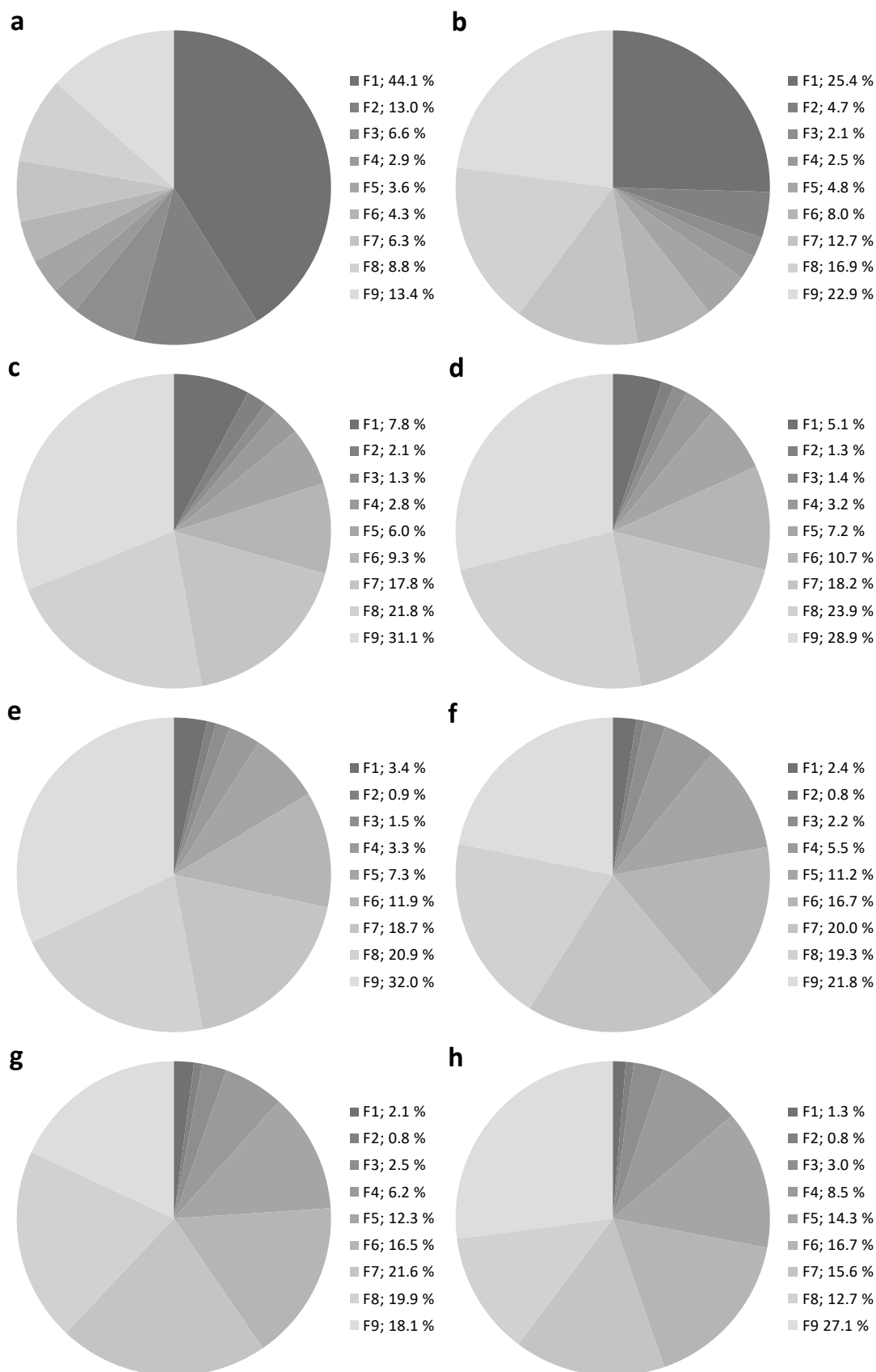


Figure A 2.3: Pressure-dependent count rate percentages of all fractions after separation using a sucrose gradient. Representation of the count rate percentages at (a) 250 bar, (b) 500 bar, (c) 750 bar, (d) 1,000 bar, (e) 1,250 bar, (f) 1,500 bar; (g) 1,750 bar and (h) 2,000 bar.

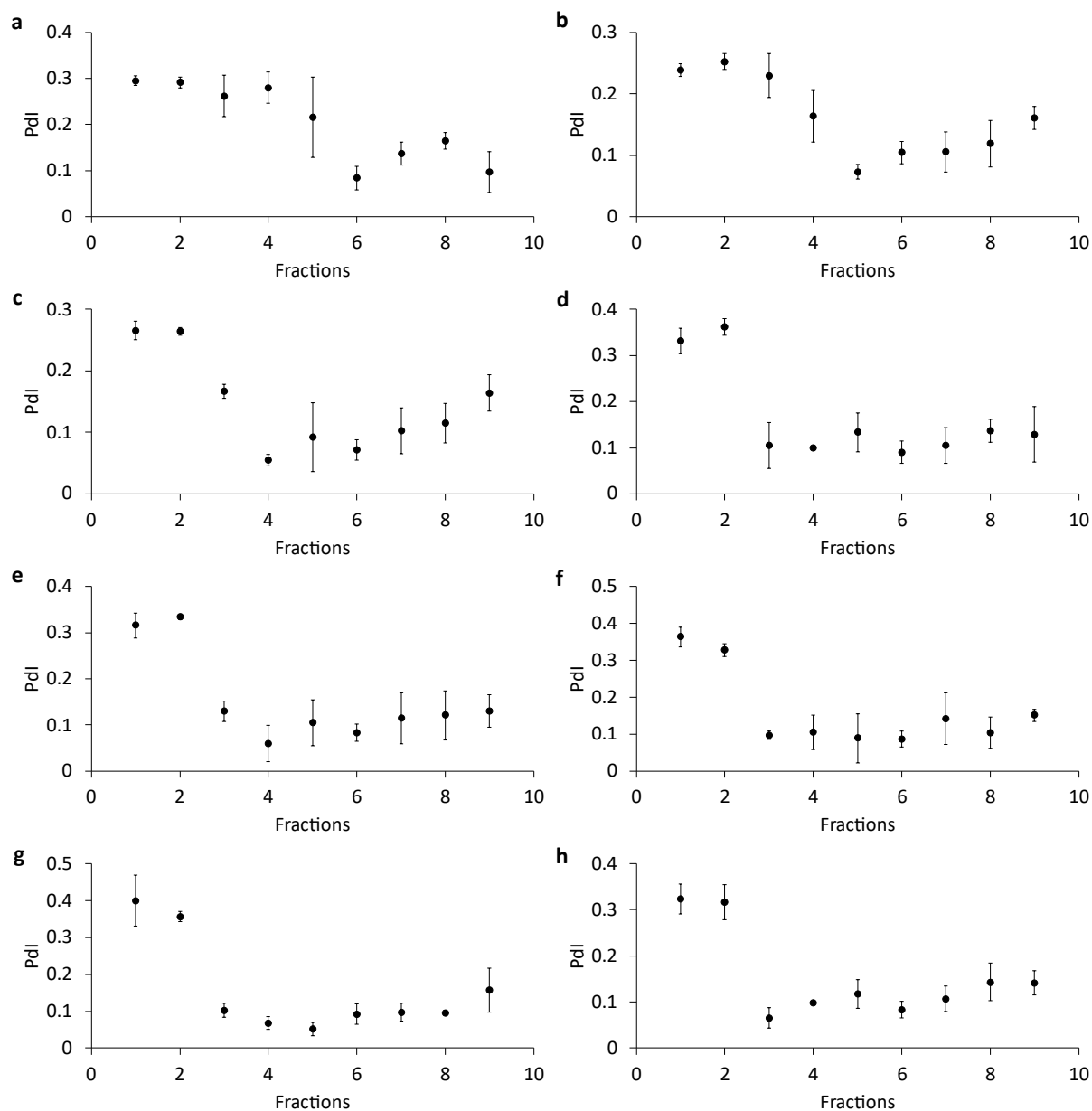


Figure A 2.4: Pressure-dependent particle distribution indices (PdI) of PFC/W nanoemulsions after separation using a sucrose gradient. Representation of the PdI in all fractions from F1 to F9 for a PFC/W nanoemulsion homogenized at (a) 250 bar, (b) 500 bar, (c) 750 bar, (d) 1,000 bar, (e) 1,250 bar, (f) 1,500 bar, (g) 1,750 bar and (h) 2,000 bar. The dots represent the mean \pm SD, $n = 3$.

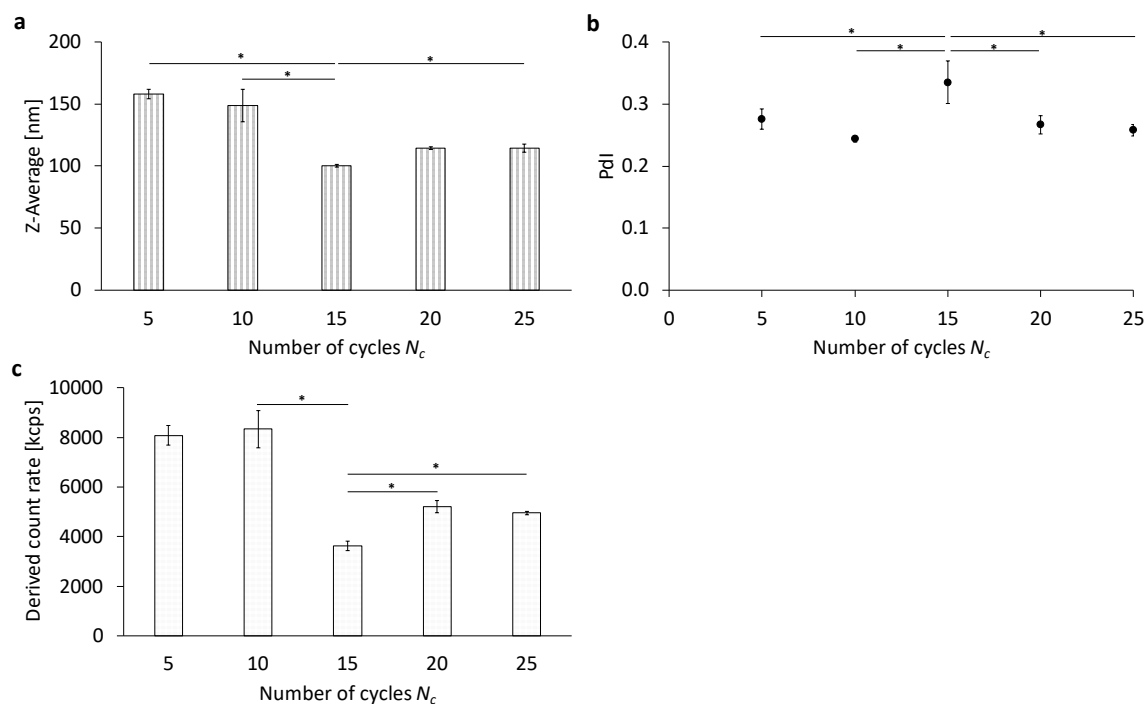


Figure A 2.5: Comparison of different numbers of homogenization cycles after 24 hours of storage at 4 °C. (a) The Z-Average (Z-Ave) (b) the polydispersity index (Pdl) and (c) the derived count rate (DCR) of the PFC/W nanoemulsion after 5, 10, 15, 20, or 25 cycles of homogenization at 1000 bar. The bars or dots represent the mean \pm SD, $n = 3$. A one-way ANOVA followed by a two-sample t-test assuming equal variances was performed at a significance level of $*p < 0.05$.

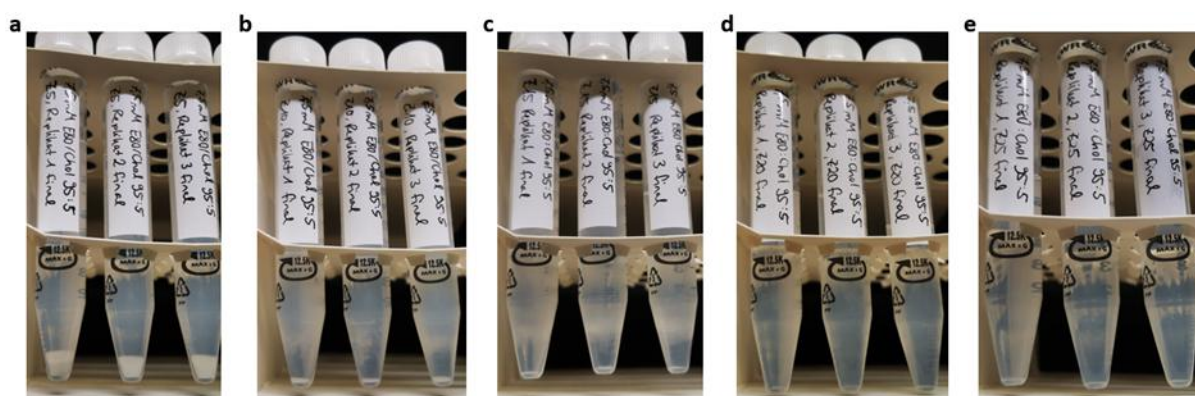


Figure A 2.6: Photos of the PFC/W nanoemulsions after different numbers of homogenization cycles after 24 h of storage time at 4°C. (a) Nanoemulsion after 5 cycles, (b) after 10 cycles, (c) after 15 cycles; (d) after 20 cycles and (e) after 25 cycles of homogenization.

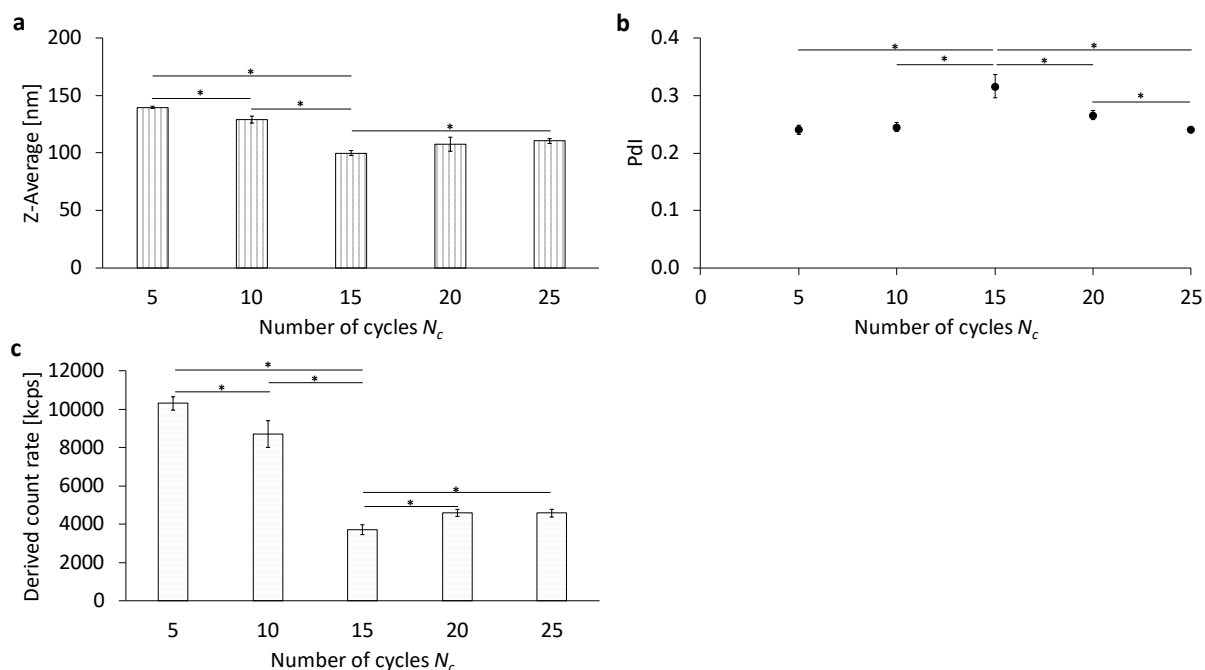


Figure A 2.7: Comparison of different numbers of homogenization cycles after 48 hours of storage at 4 °C. (a) The Z-Average (Z-Ave) (b) the polydispersity index (Pdl) and (c) the derived count rate (DCR) of the PFC/W nanoemulsion after 5, 10, 15, 20, or 25 cycles of homogenization at 1000 bar. The bars or dots represent the mean \pm SD, $n = 3$. A one-way ANOVA followed by a two-sample t-test assuming equal variances was performed at a significance level of $*p < 0.05$.

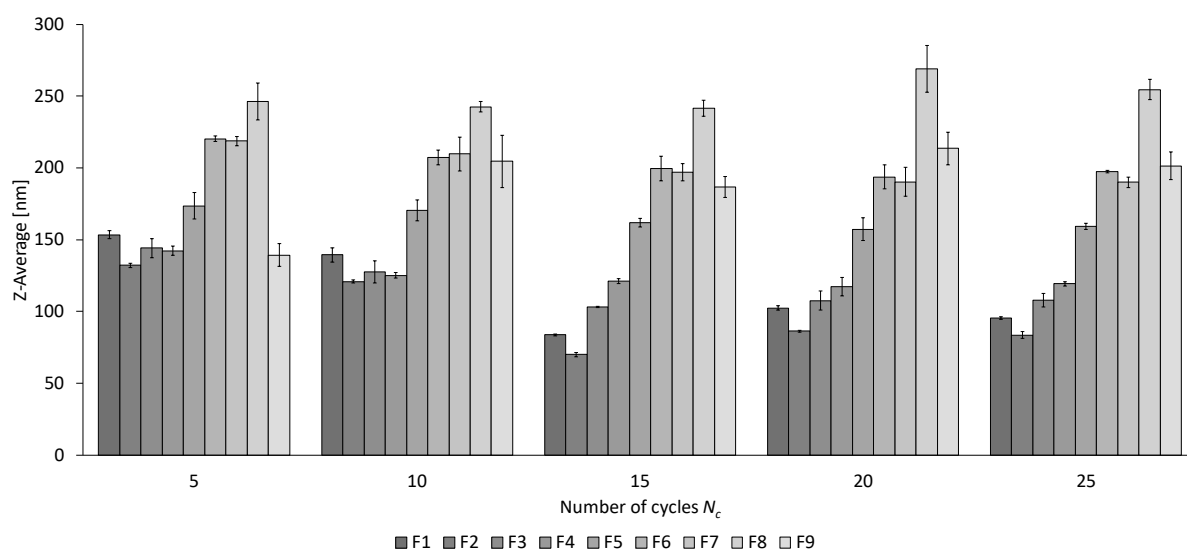


Figure A 2.8: Representation of cycle number-dependent particle sizes (Z-Average) of all fractions from F1 to F9 after separation using the sucrose gradient after 24 hours of storage at 4 °C. The bars represent the mean \pm SD, $n = 3$.

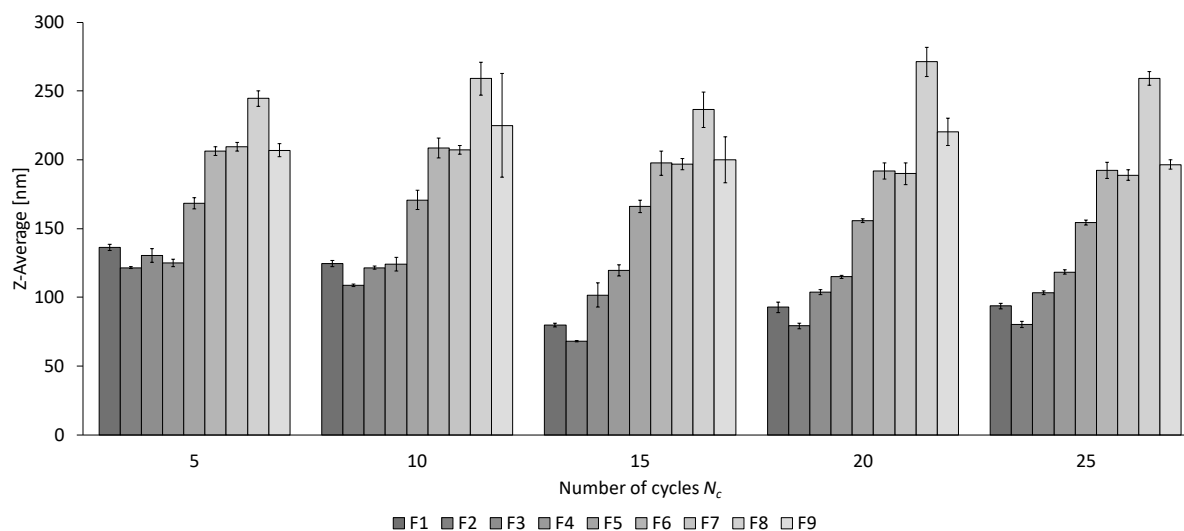


Figure A 2.6: Representation of cycle number-dependent particle sizes (Z-Average) of all fractions from F1 to F9 after separation using the sucrose gradient after 48 h of storage at 4 °C. The bars represent the mean \pm SD, $n = 3$.

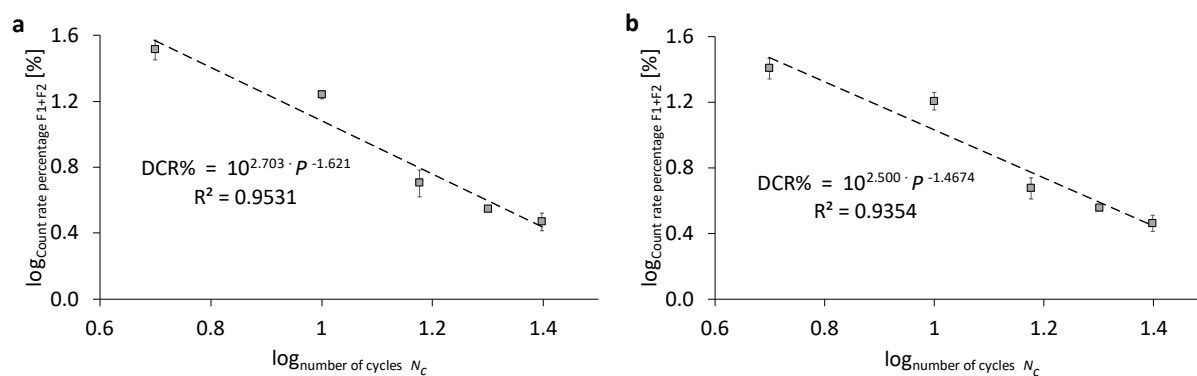


Figure A 2.10: Logarithmic representation of count rate percentages of fractions 1 and 2 in total (F1+F2) after separation using the sucrose gradient. Representation of count rate percentages of fraction 1 and 2 in total after (a) 24 h and (b) 48 h of storage at 4 °C. The grey squares represent the mean \pm SD, $n = 3$.

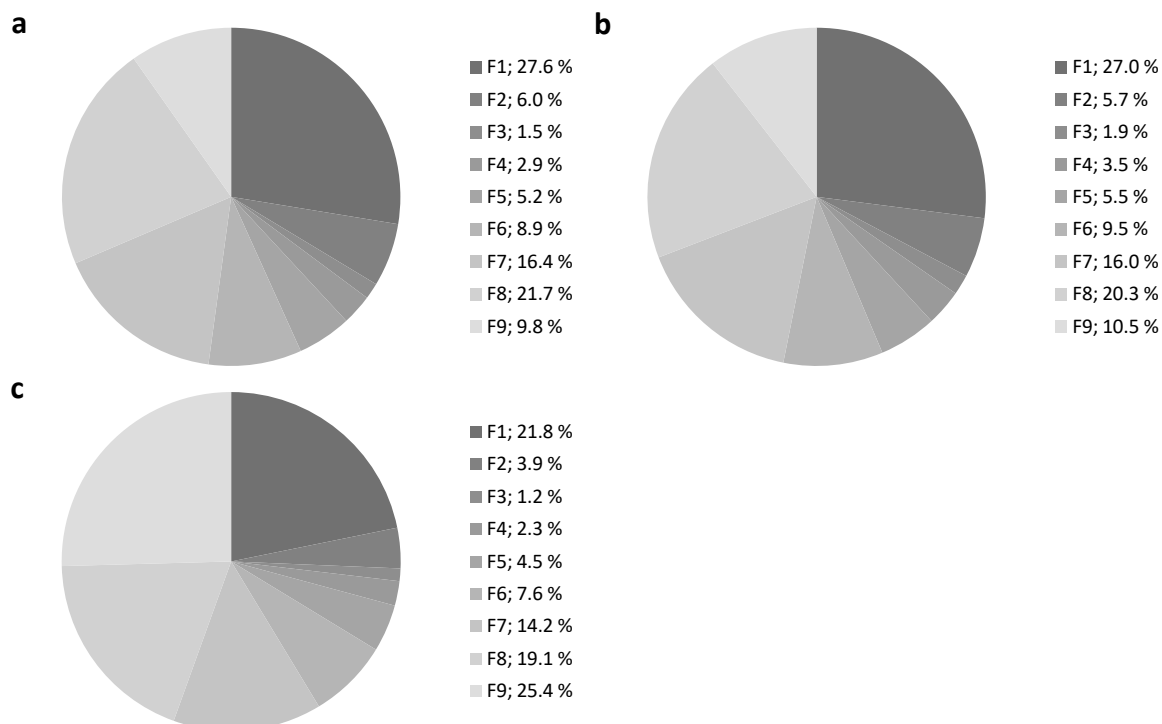


Figure A 2.7: DCR% of fractions 1 to 9 after separation of a PFC/W-nanoemulsion homogenized for 5 cycles using a sucrose gradient. (a) DCR% of a freshly prepared PFC/W-nanoemulsion, (b) after 24 hours of storage at 4 °C and (c) after 48 h of storage at 4 °C; n = 3.

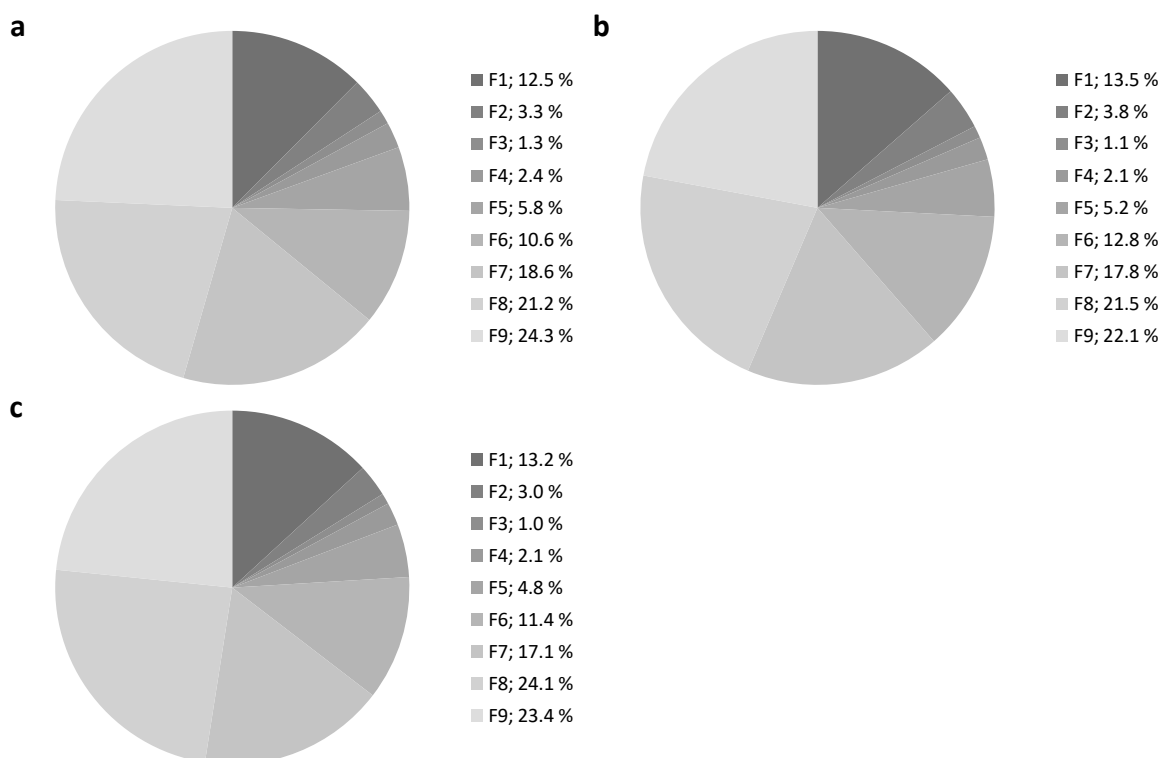


Figure A 2.8: DCR% of fractions 1 to 9 after separation of a PFC/W-nanoemulsion homogenized for 10 cycles using a sucrose gradient. (a) DCR% of a freshly prepared PFC/W nanoemulsion, (b) after 24 h of storage at 4 °C and (c) after 48 h of storage at 4 °C; n = 3.

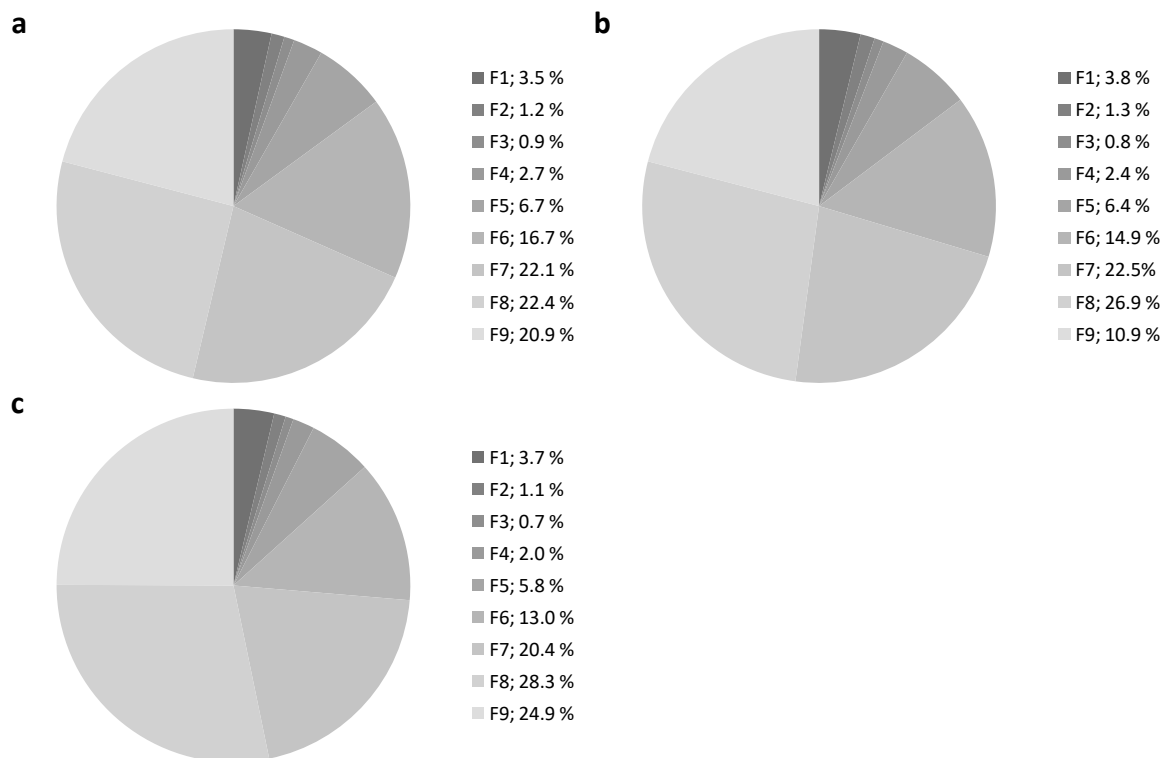


Figure A 2.9: DCR% of fractions 1 to 9 after separation of a PFC/W-nanoemulsion homogenized for 15 cycles using a sucrose gradient. (a) DCR% of a freshly prepared PFC/W nanoemulsion, (b) after 24 hours of storage at 4 °C and (c) after 48 h of storage at 4 °C; n = 3.

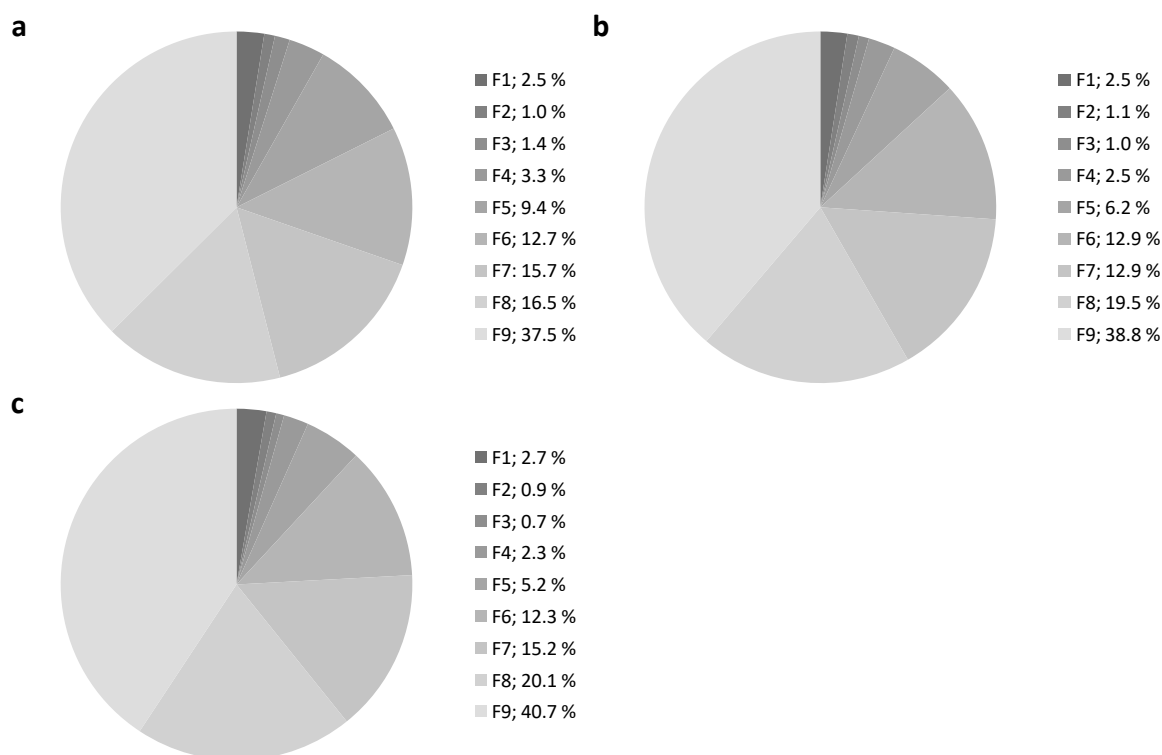


Figure A 2.10: DCR% of fractions 1 to 9 after separation of a PFC/W-nanoemulsion homogenized for 20 cycles using a sucrose gradient. (a) DCR% of a freshly prepared PFC/W nanoemulsion, (b) after 24 h of storage at 4 °C and (c) after 48 h of storage at 4 °C; n = 3.

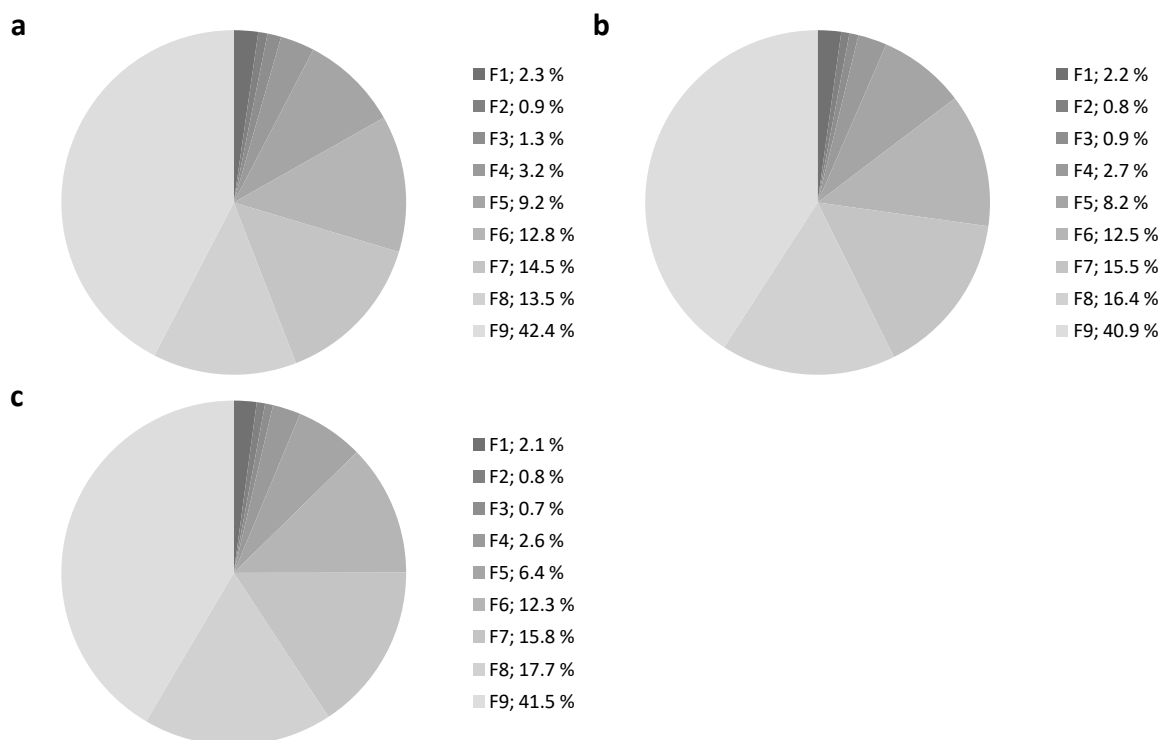


Figure A 2.15: DCR% of fractions 1 to 9 after separation of a PFC/W-nanoemulsion homogenized for 20 cycles using a sucrose gradient. (a) DCR% of a freshly prepared PFC/W nanoemulsion, (b) after 24 h of storage at 4 °C and (c) after 48 h of storage at 4 °C; n = 3.

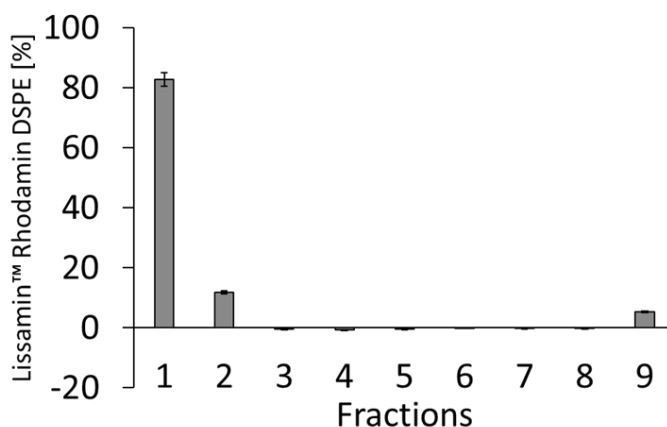


Figure A 2.16: Identification of fractions with fluorescently labeled liposomes containing 0.1 mol-% of Lissamine™ Rhodamine-DSPE without any perfluorocarbon emulsion. As can be seen, only the fractions F1 and F2 contain liposomes. Fluorescent dye in fraction F9 is a consequence of the aspiration technique by which the fractions are carefully pipetted, but the wall-wetting layer flowing down the centrifugation tube contaminated the final fraction F9.

A3 Formulation Optimization

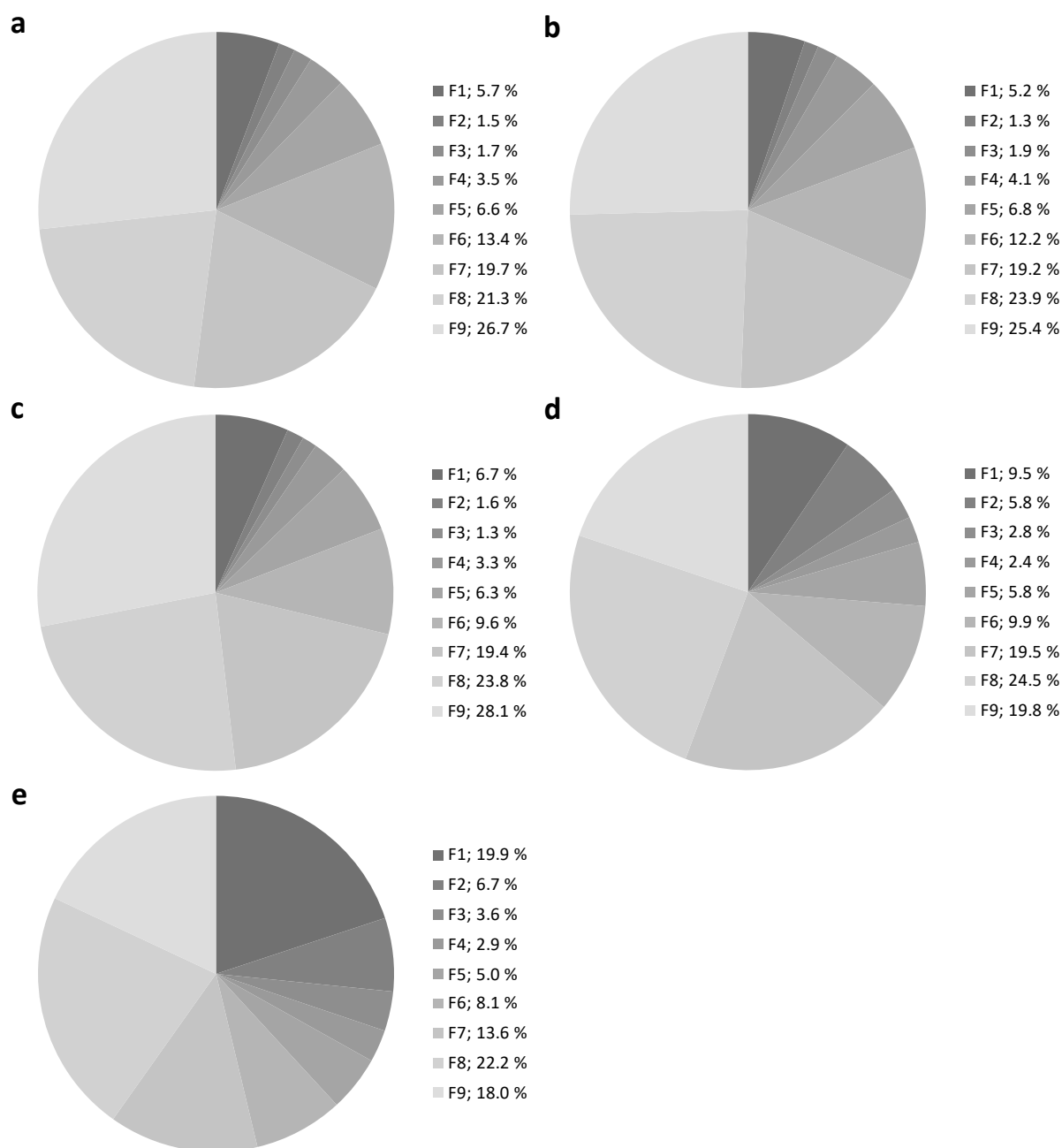


Figure A 3.1: Count rate percentages of all fractions after separation using a sucrose gradient in dependence on the cholesterol content x_{chol} . Representation of the count rate percentages at (a) 5 mol%, (b) 10 mol%, (c) 20 mol%, (d) 30 mol% and (e) 40 mol%.

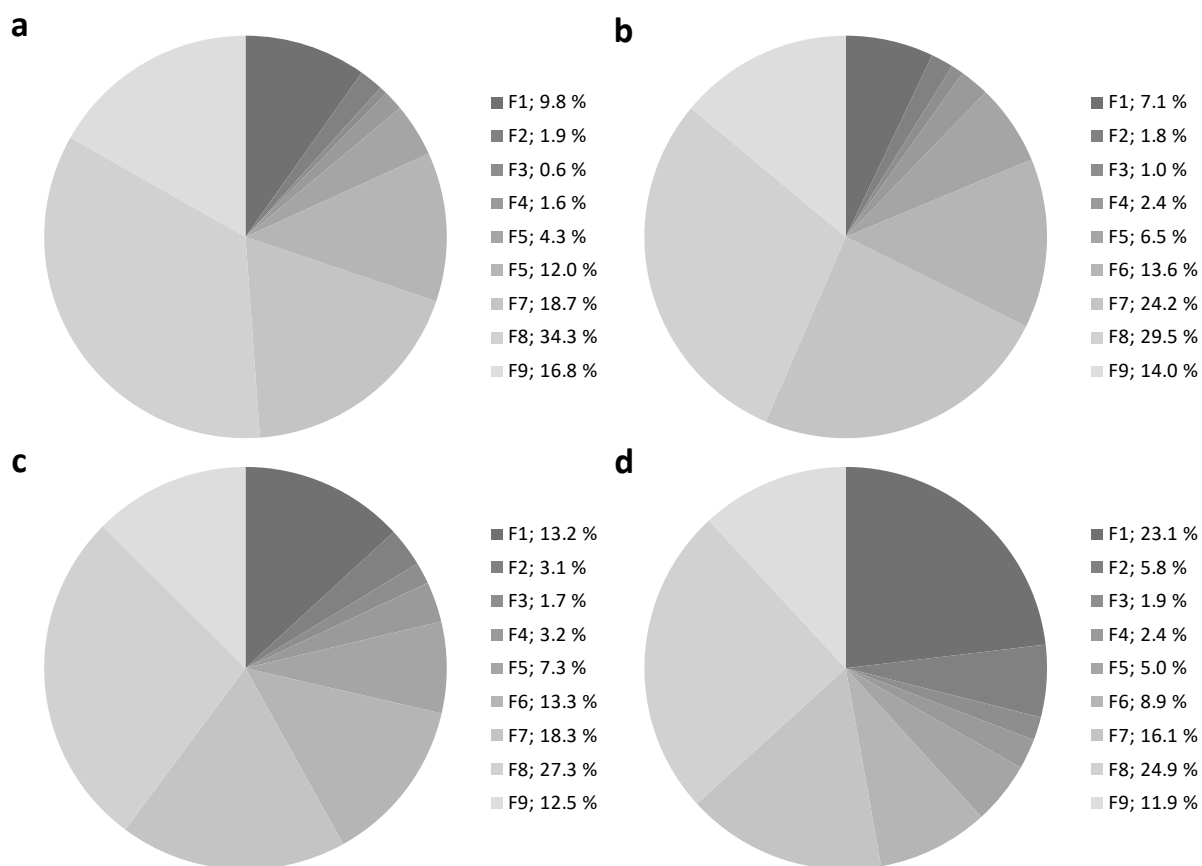


Figure A 3.2: Count rate percentages of all fractions after separation using a sucrose gradient dependent on the lipid concentration c_L . Representation of the count rate percentages at (a) 2.5 mM, (b) 5 mM, (c) 10 mM and (d) 15 mM.

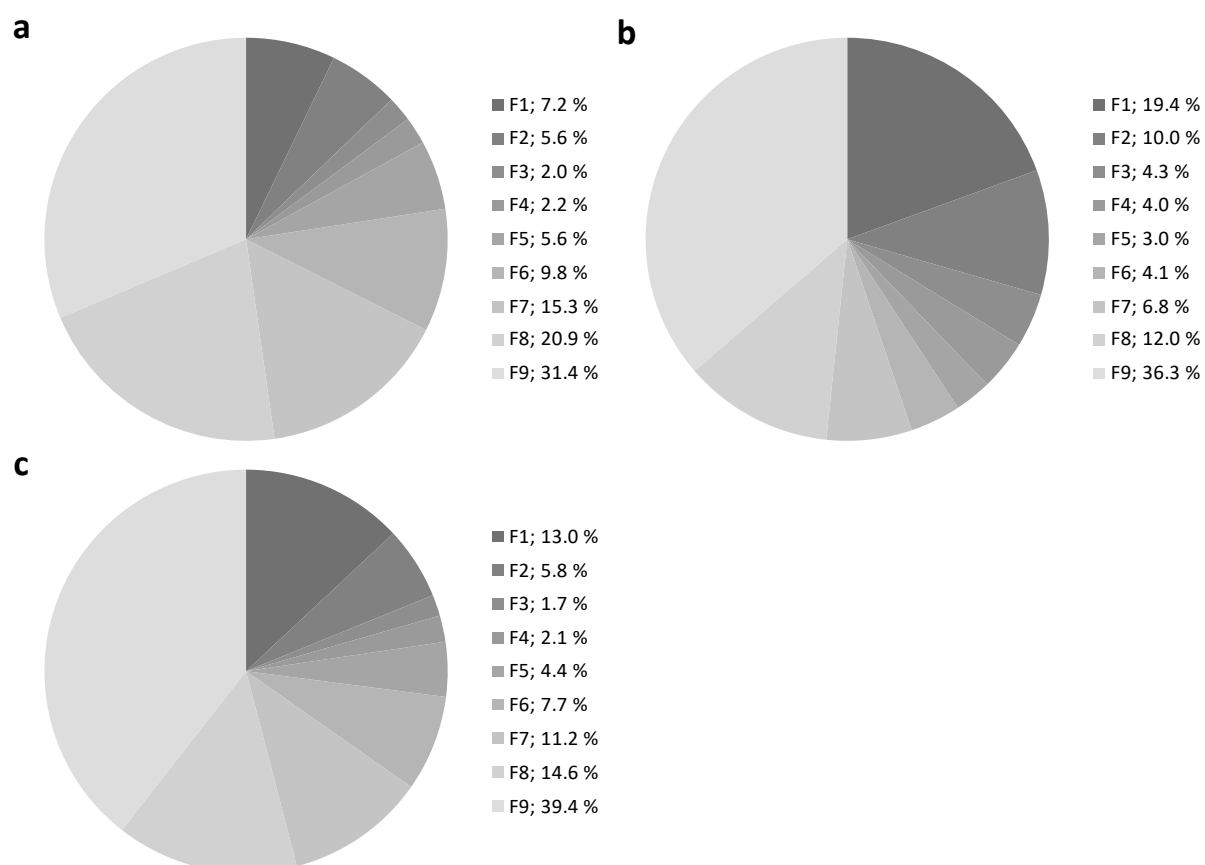


Figure A 3.3: Count rate percentages of all fractions after separation using a sucrose gradient dependent on the phospholipid chain length. Representation of the count rate percentages of (a) DMPC, (b) DPPC and (c) DSPC.

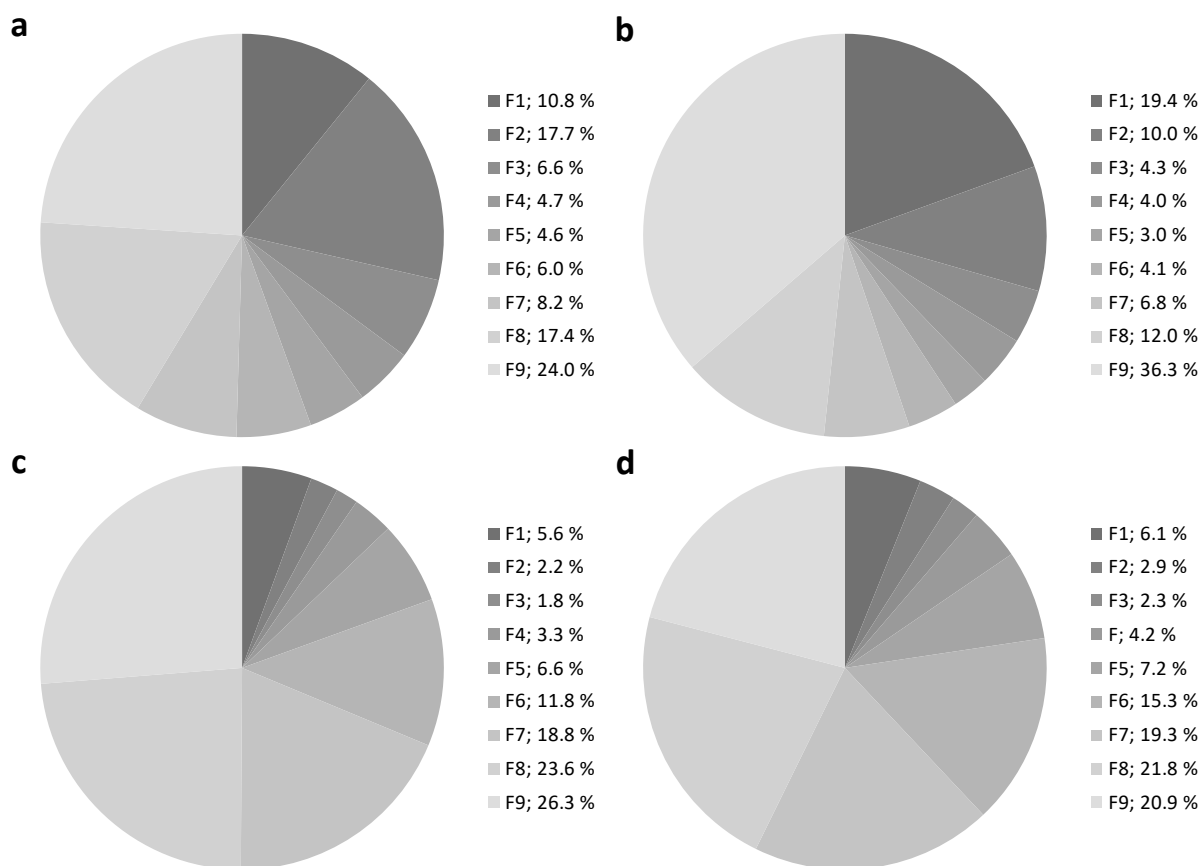


Figure A 3.4: Count rate percentages of all fractions after separation using a sucrose gradient dependent on the phospholipid head group. Representation of the count rate percentages of (a) DPPE, (b) DPPC, (c) DPPG and (d) DPPA.

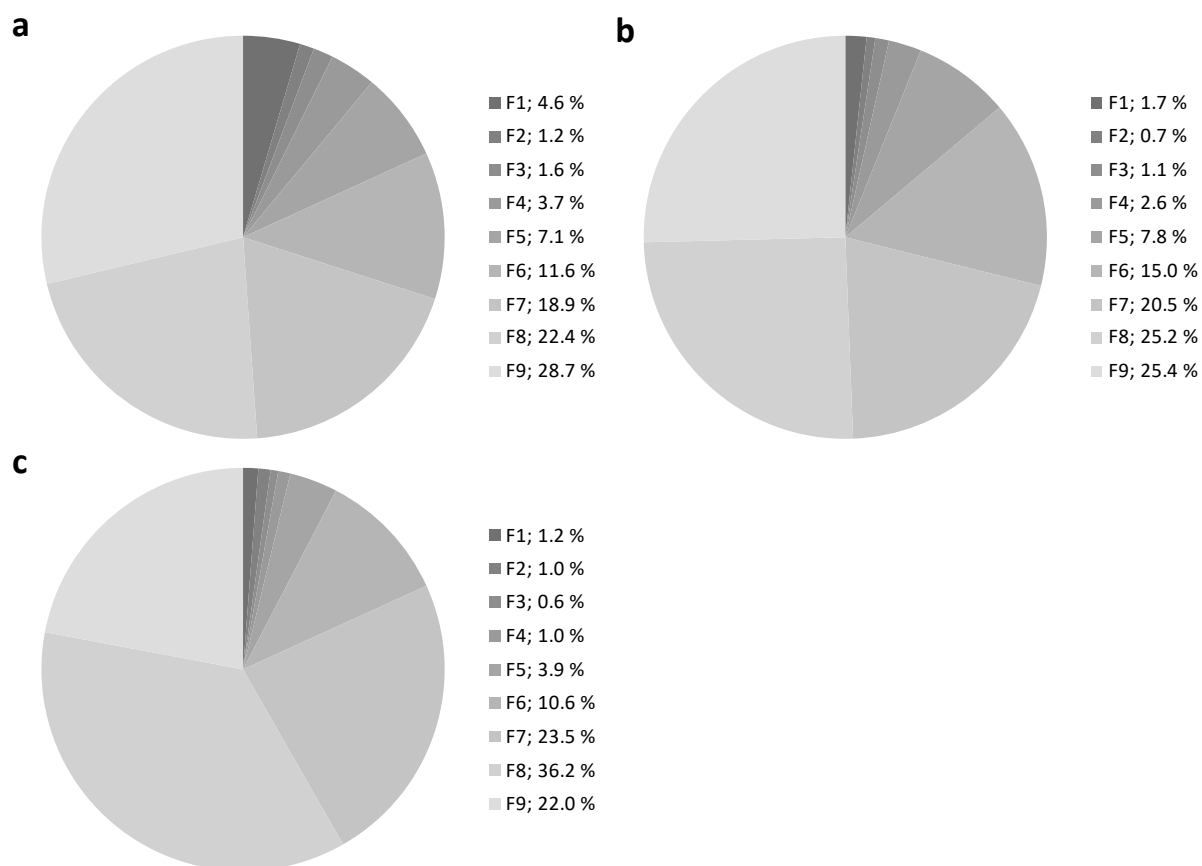


Figure A 3.5: Count rate percentages of all fractions after separation using a sucrose gradient dependent on the volume of the dispersed phase V_D . Representation of the count rate percentages of (a) 2.5 % (v/v), (b) 5 % (v/v) and (c) 10% (v/v).

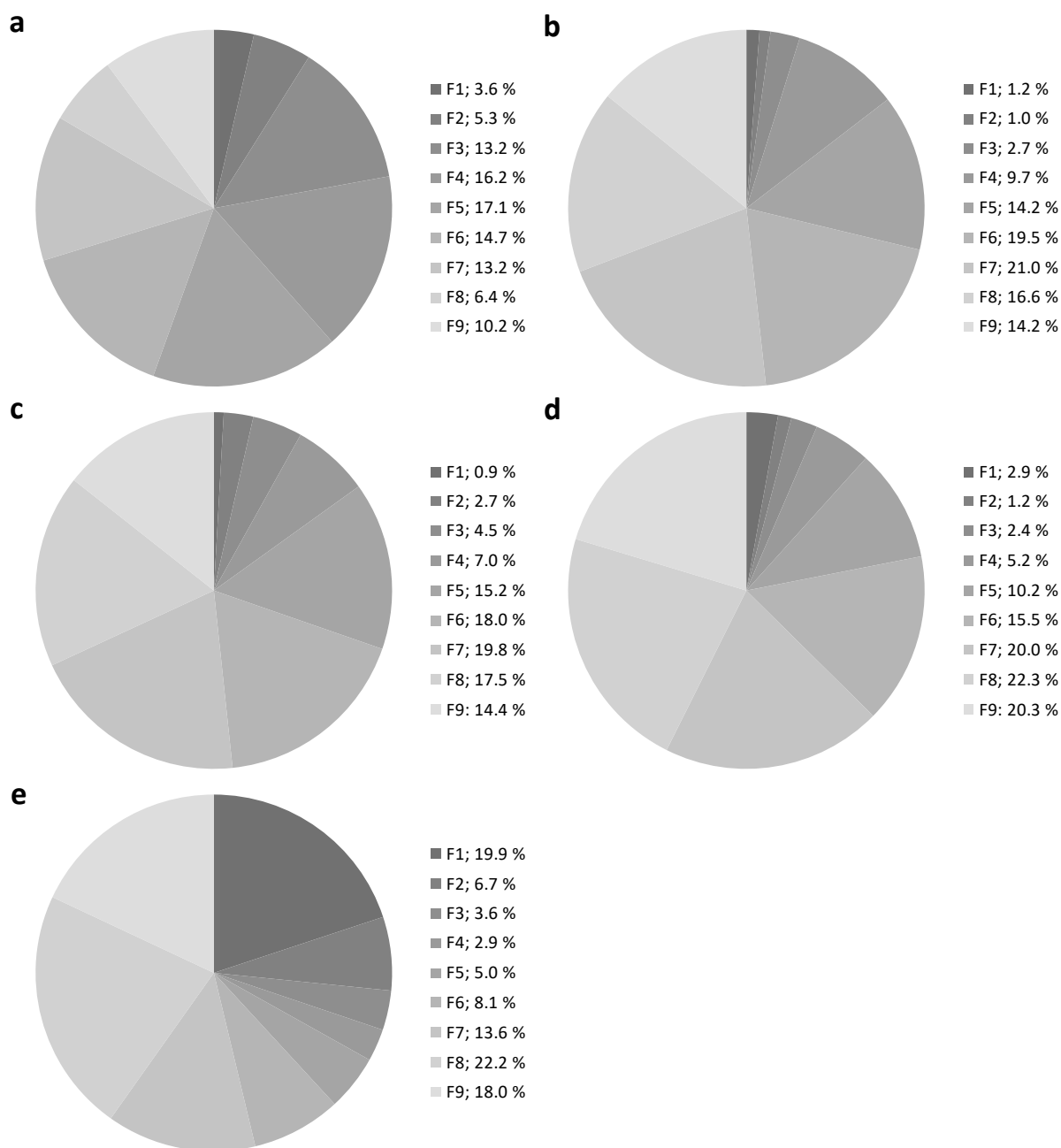


Figure A 3.6: Count rate percentages of all fractions after separation using a sucrose gradient dependent on the viscosity of the dispersed phase by variation of the PFC. Representation of the count rate percentages of (a) Perfluoroheptan (0.9 mPa·s), (b) Perfluoro-1,3-dimethylcyclohexane (1.9 mPa·s), (c) Perfluorooctylbromid (2.3 mPa·s), (d) Perfluorodecalin (5.1 mPa·s) and (e) Perfluoroperhydro-phenanthrene (28.4 mPa·s).

Table A 3.1: Calculation of the molecular surface area.

Step	Description	Equation
1	Volume of PFC in each fraction per mL [$\mu\text{L}/\text{mL}$]	$V_{PFC} [\mu\text{L}] = (1000 \cdot V_D [\% (v/v)]) \cdot \left(\frac{DCR\% F_X}{100}\right)$
2	Conversion to [m^3]	$V_{PFC} [\text{m}^3] = V_{PFC} [\mu\text{L}] \cdot 10^{-9}$
3	Volume of a PFC droplet in each fraction [nm^3]	$V_{droplet} [\text{nm}^3] = \frac{4}{3} \cdot \pi \cdot r_{F_X}^3$
4	Conversion to [m^3]	$V_{droplet} [\text{m}^3] = V_{droplet} [\text{nm}^3] \cdot 10^{-27}$
5	Surface area of a PFC droplet in each fraction [nm^2]	$A_{droplet} [\text{nm}^2] = 4 \cdot \pi \cdot r_{F_X}^2$
6	Conversion to [m^2]	$A_{droplet} [\text{m}^2] = A_{droplet} [\text{nm}^2] \cdot 10^{-18}$
7	Number of droplets in each fraction per mL [$1/\text{mL}$]	$n_{PFC} \left[\frac{1}{\text{mL}}\right] = \frac{V_{PFC} [\text{m}^3]}{V_{droplet} [\text{m}^3]}$
8	Surface area per mL of each fraction [nm^2/mL]	$A_{PFC} \left[\frac{\text{nm}^2}{\text{mL}}\right] = n_{PFC} \cdot A_{droplet} [\text{nm}^2]$
9	Conversion to [m^2/mL]	$A_{PFC} \left[\frac{\text{m}^2}{\text{mL}}\right] = A_{PFC} \left[\frac{\text{nm}^2}{\text{mL}}\right] \cdot 10^{-18}$
10	Number of lipid molecules per mL [$1/\text{mL}$]	$n_{PL} \left[\frac{1}{\text{mL}}\right] = c_{Lipid} \left[\frac{\text{mol}}{\text{mL}}\right] \cdot N_A \cdot RR_{PL}$
11	Corrected number of lipid molecules per mL	$n_{PLcorr} \left[\frac{1}{\text{mL}}\right] = n_{PL} \left[\frac{1}{\text{mL}}\right] \cdot (100 - (\sum DCR\%_{F1+F2}) \cdot 2)$
12	Molecular area [$\text{m}^2/\text{molecule}$]	$A_{molecule} \left[\frac{\text{m}^2}{\text{molecule}}\right] = \frac{\sum F3 \text{ to } F9 \text{ of } A_{PFC} \left[\frac{\text{m}^2}{\text{mL}}\right]}{n_{PLcorr} \left[\frac{1}{\text{mL}}\right]}$
13	Conversion to [$\text{\AA}^2/\text{molecule}$]	$A_{molecule} \left[\frac{\text{m}^2}{\text{molecule}}\right] = \frac{A_{molecule} \left[\frac{\text{m}^2}{\text{molecule}}\right]}{10^{-20}}$

RR = recovery rate of phospholipids

A4 Succinimide- and Glucose-Modified Liposomes

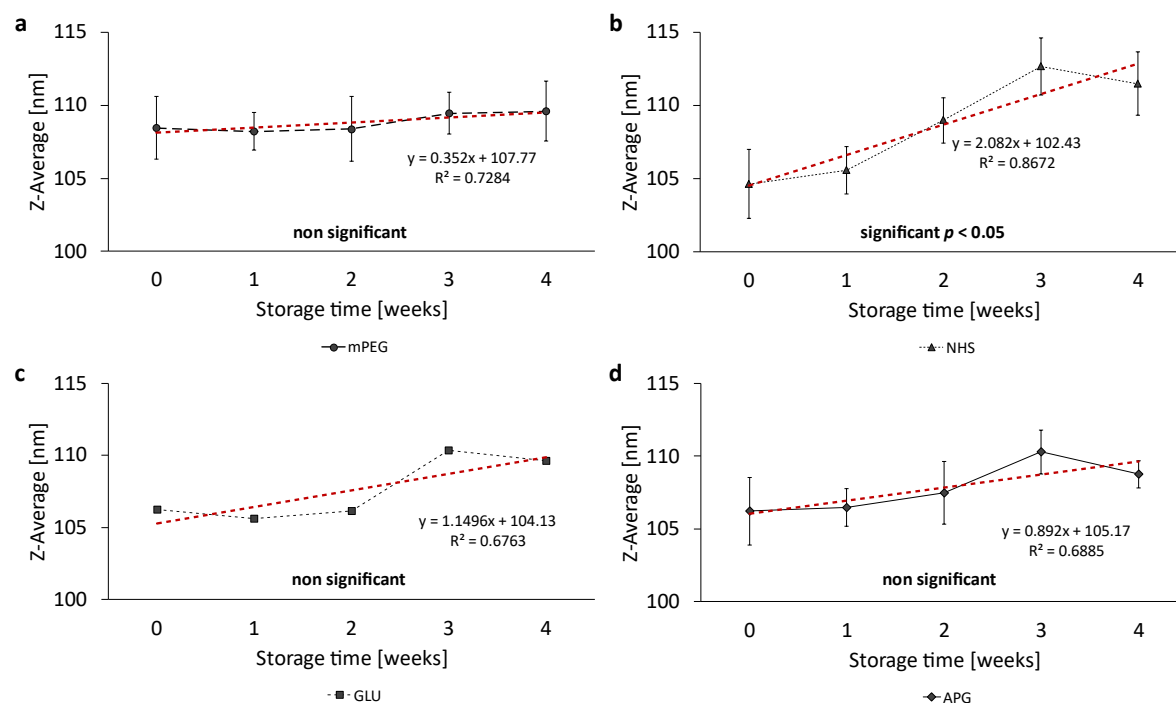


Figure A 4.1: Trend analysis of the Pdl of the liposomal formulations over a storage period of 4 weeks at 4 °C. Determination of significance of a linear regression using Student's t-test.

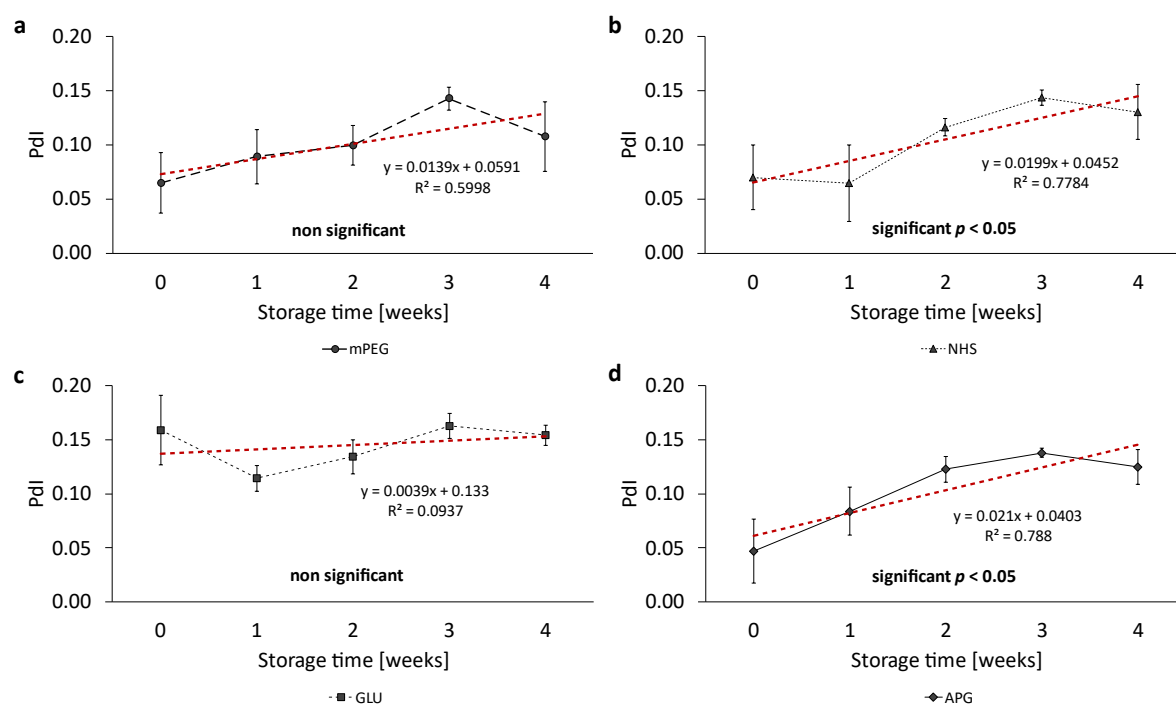


Figure A 4.2: Trend analysis of the Pdl of the liposomal formulations over a storage period of 4 weeks at 4 °C. Determination of significance of a linear regression using Student's t-test.

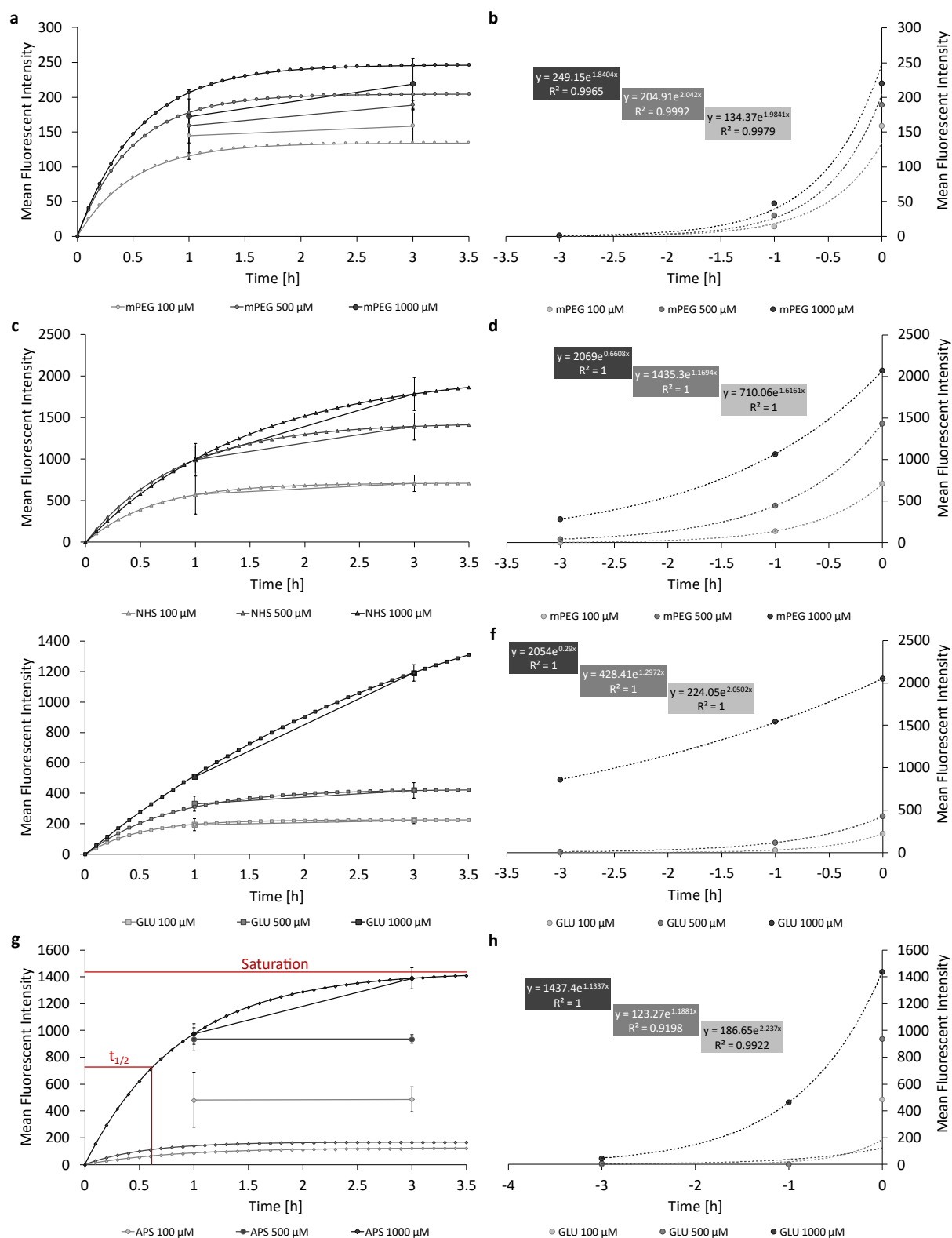


Figure A 4.3: Plot of the mean fluorescence intensities over time (a, c, e and g) and the corresponding exponential fits (b, d, f and h) for the cellular uptake of the different liposomal formulations into the bEnd.3 cells, where. (a and b) represent the data for the mPEG liposomes, (c and d) for the NHS liposomes, (e and f) for the GLU liposomes and (g and h) for the APG liposomes.

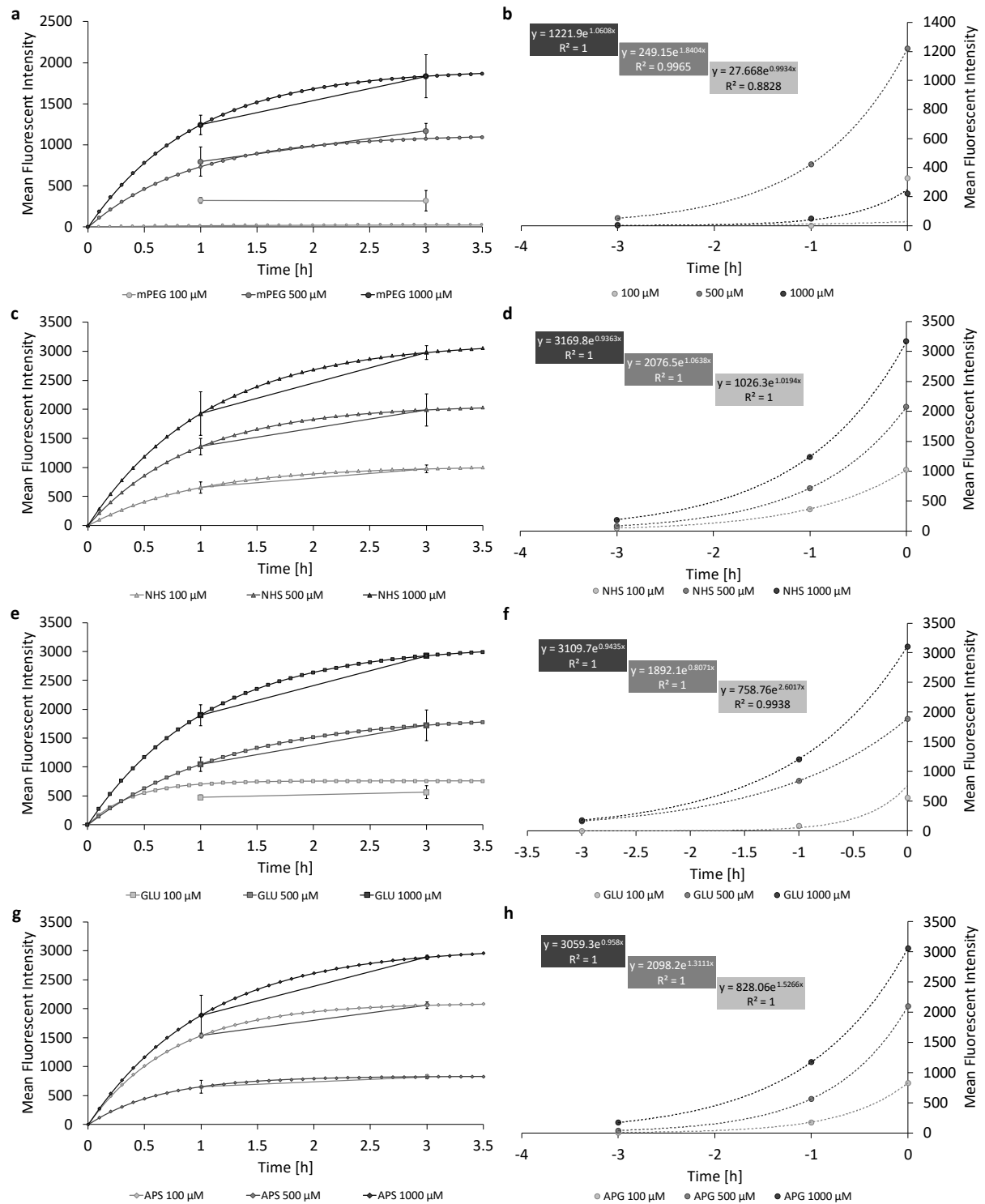


Figure A 4.4: Plot of the mean fluorescence intensities over time (a, c, e and g) and the corresponding exponential fits (b, d, f and h) for the cellular uptake of the different liposomal formulations into the U-87 MG cells, where. (a and b) represent the data for the mPEG liposomes, (c and d) for the NHS liposomes, (e and f) for the GLU liposomes and (g and h) for the APG liposomes.

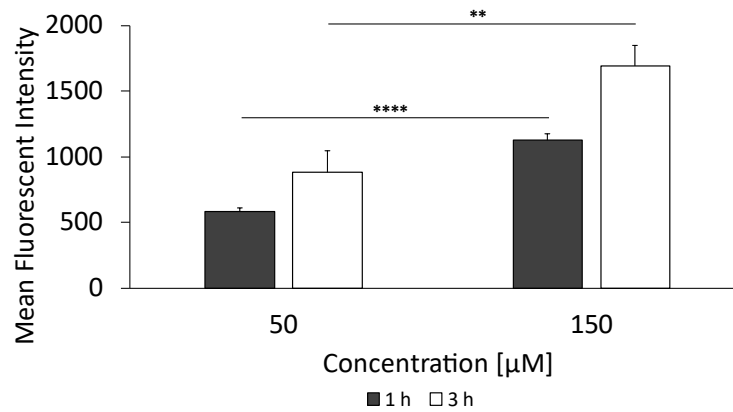


Figure A 4.5: Cellular uptake of 2-NBDG in bEnd.3 cells for two different times of incubation (1 h and 3 h). The bars represent the mean \pm SD, n = 3.

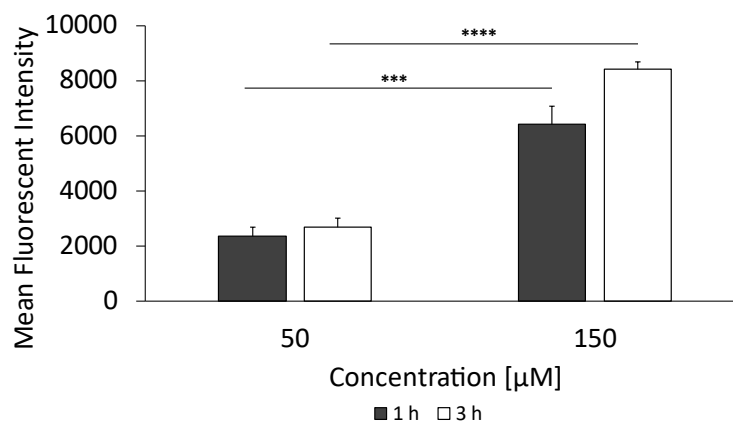


Figure A 4.6: Cellular uptake of 2-NBDG in U-87 MG cells for two different times of incubation (1 h and 3 h). The bars represent the mean \pm SD, n = 3.

A5 ApoE3- and c(RGD)-Modified Liposomes

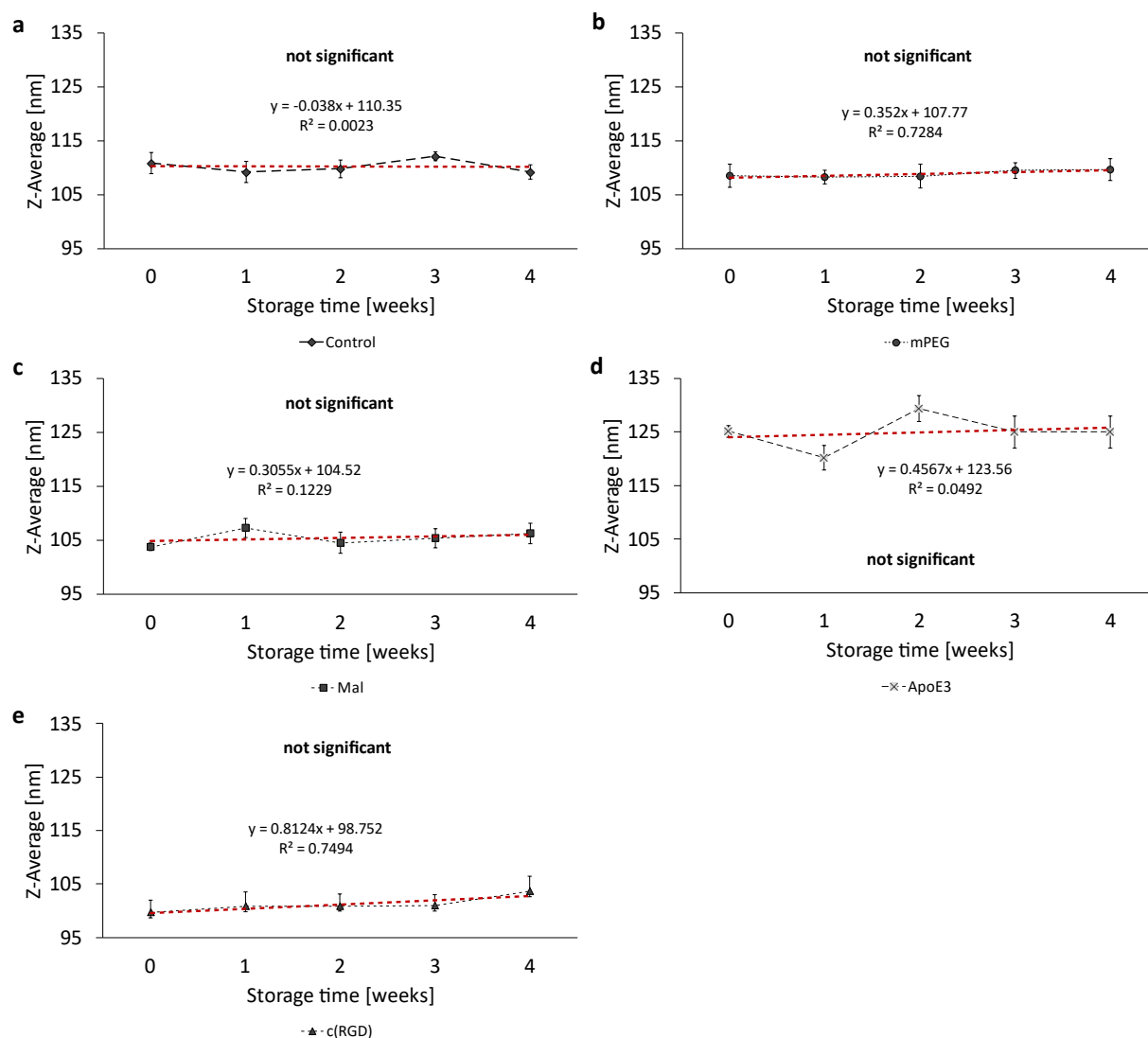


Figure A 5.1: Trend analysis of the Z-Average of the liposomal formulations over a storage period of 4 weeks at 4 °C. Determination of significance of a linear regression using Student's t-test.

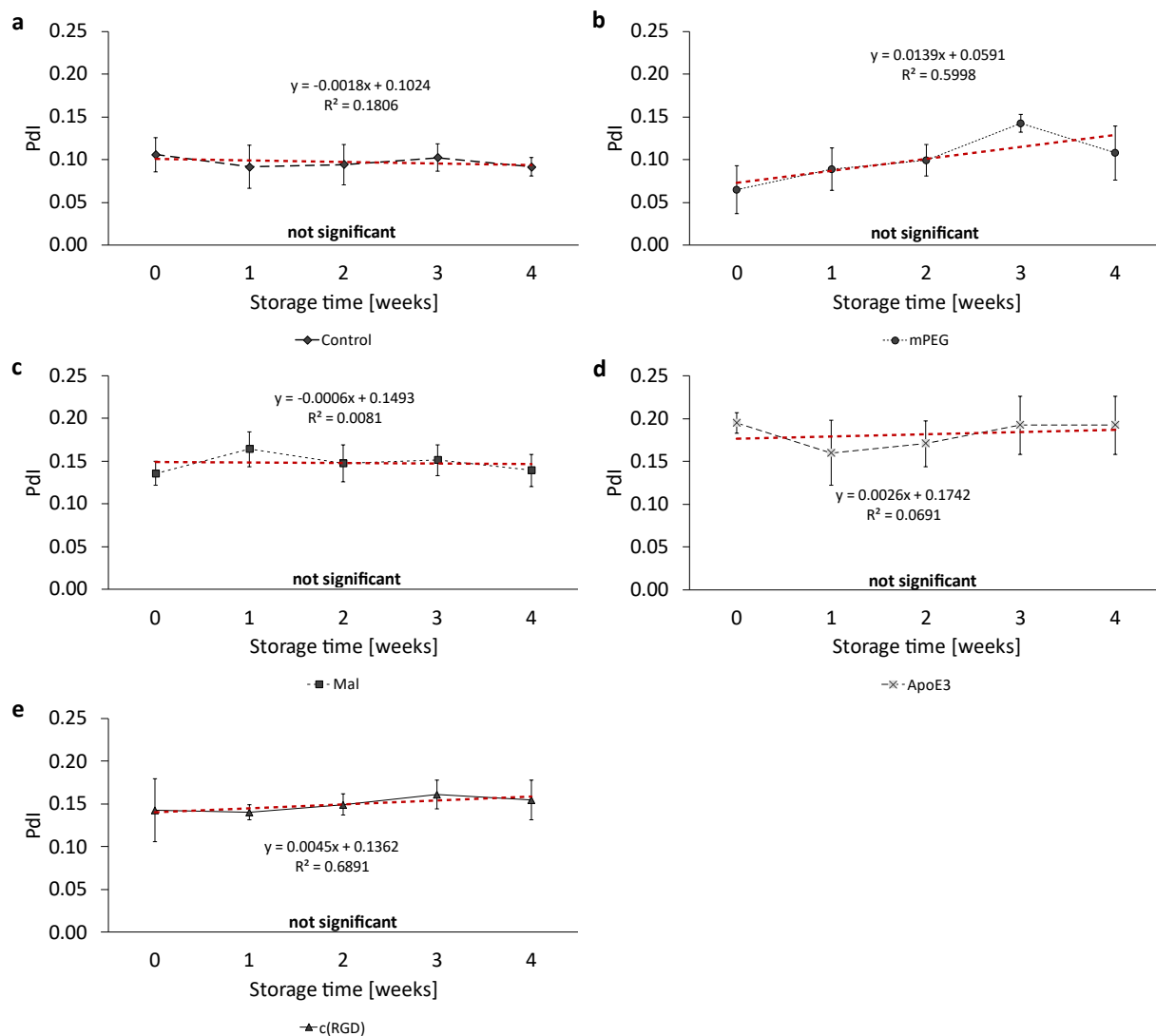


Figure A 5.2: Trend analysis of the Pdl of the liposomal formulations over a storage period of 4 weeks at 4 °C. Determination of significance of a linear regression using Student's t-test.

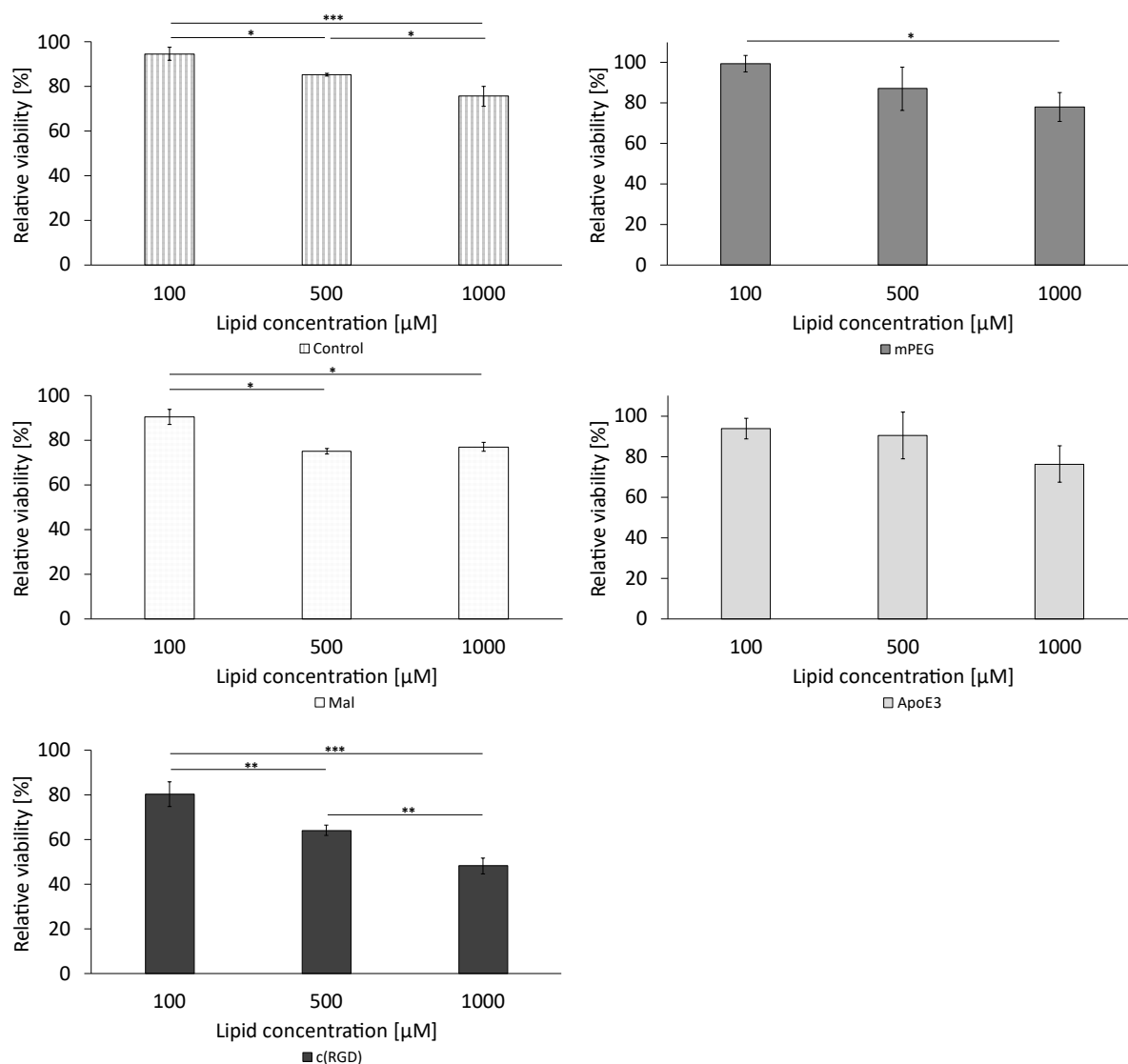


Figure A 5.3: Liposomal cytotoxicity on bEnd.3 cells using alamarBlue™ HS reagent. Representation of all different tested formulations (a) to (f). The bars represent the mean values with the standard deviation as error bars. Statistical analysis: one-way ANOVA followed by Tukey's multiple comparison test. * $p < 0.05$, ** $p < 0.01$, *** $p < 0.001$, **** $p < 0.0001$; $n = 3$.

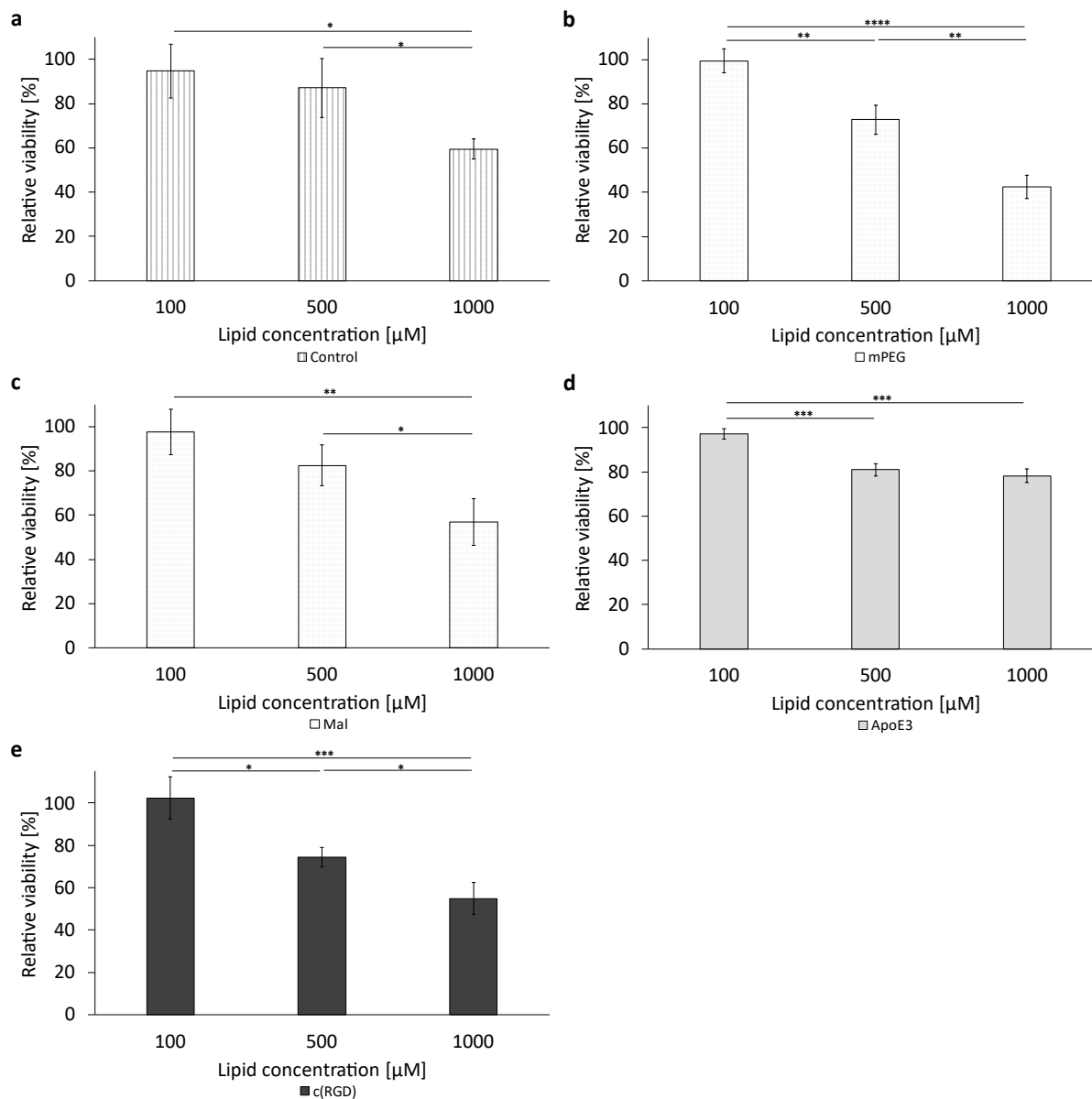


Figure A 5.4: Liposomal cytotoxicity on U-87 MG cells using alamarBlue™ HS reagent. Representation of all different tested formulations (a) to (f). The bars represent the mean values with the standard deviation as error bars. Statistical analysis: one-way ANOVA followed by Tukey's multiple comparison test. * $p < 0.05$, ** $p < 0.01$, *** $p < 0.001$, **** $p < 0.0001$; $n = 3$.

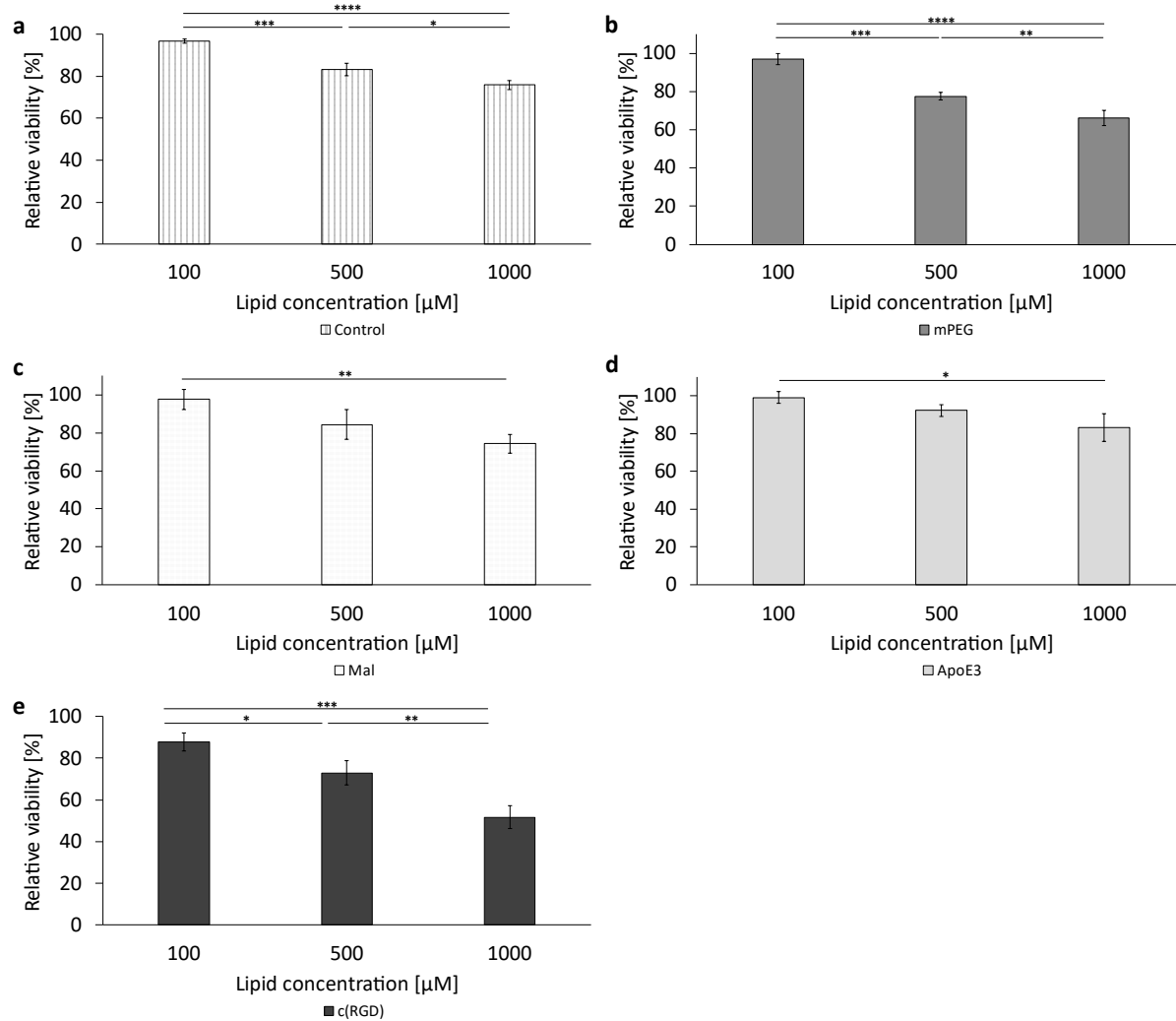


Figure A 5.5: Liposomal cytotoxicity on F98 cells using alamarBlue™ HS reagent. Representation of all different tested formulations (a) to (f). The bars represent the mean values with the standard deviation as error bars. Statistical analysis: one-way ANOVA followed by Tukey's multiple comparison test. * $p < 0.05$, ** $p < 0.01$, *** $p < 0.001$, **** $p < 0.0001$; $n = 3$.

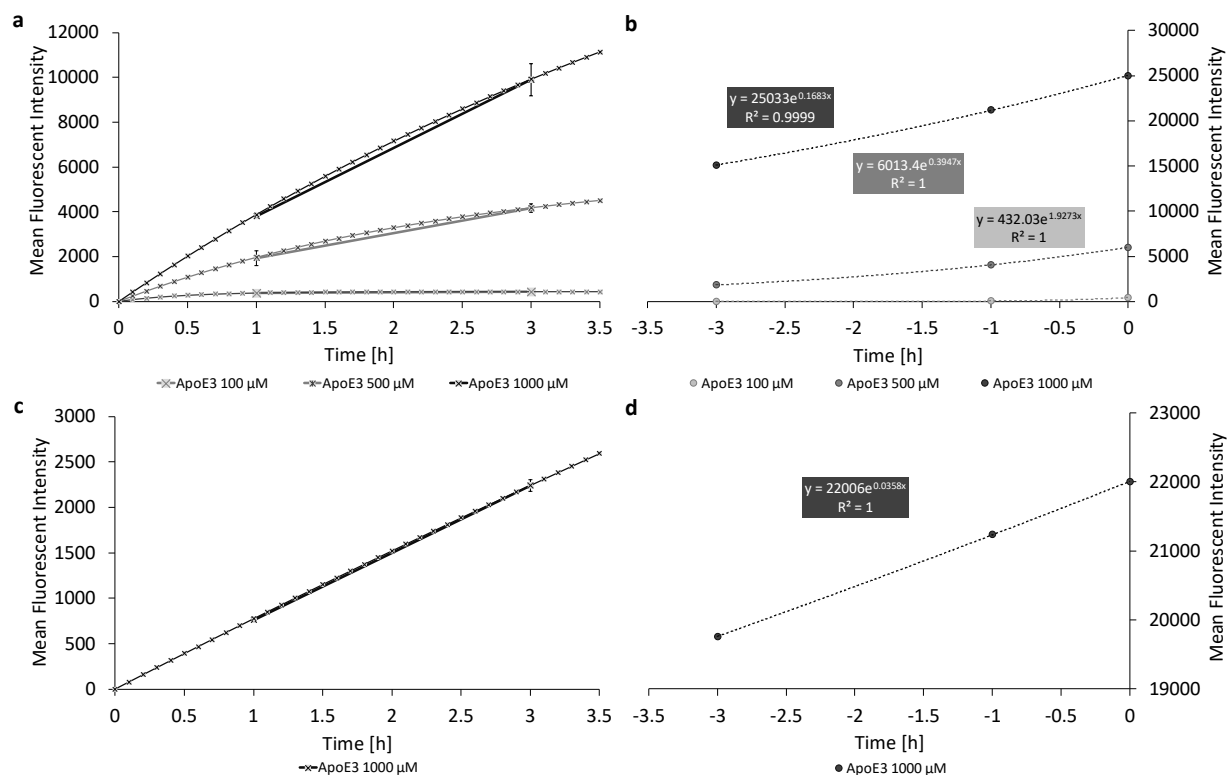


Figure A 5.6: Plot of the mean fluorescence intensities over time (a and c) and the corresponding exponential fits after a transformation of the coordinates ($x \rightarrow -x$; $y \rightarrow -y$) (b and d) for the cellular uptake of ApoE3-modified liposomes into the different glioblastoma cells, where, (a and b) represent the data for the U-87 MG cells and, (c and d) for the F98 cells.

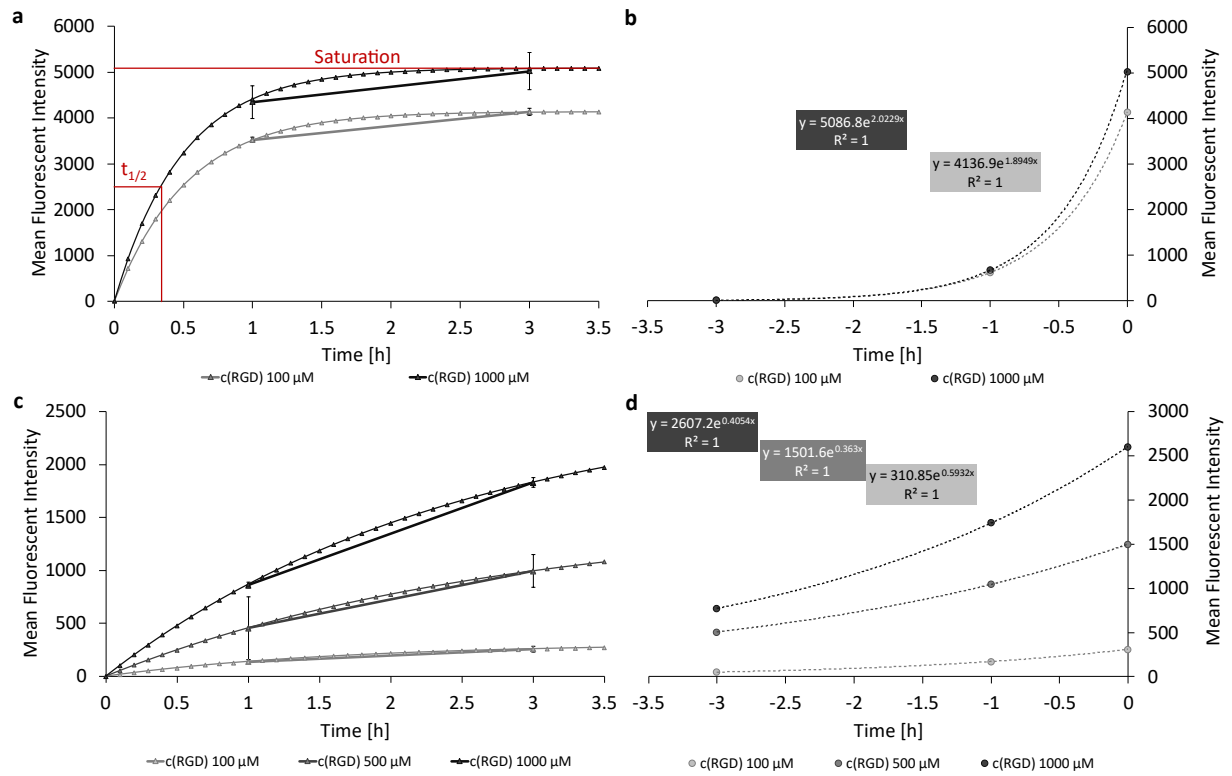


Figure A 5.7: Plot of the mean fluorescence intensities over time (a and c) and the corresponding exponential fits (b and d) for the cellular uptake of c(RGD)-modified liposomes into the different glioblastoma cells, where. (a and b) represent the data for the U-87 MG cells and, (c and d) for the F98 cells.

A6 Surface Modification using Heparin as an Alternative to PEG

Preparation and Analysis of Fractionated Fragmented Heparin

After acidic partial hydrolysis of unfragmented heparin (UFH), the UV/VIS spectra showed a considerable peak shift (Figure A 6.1a), as well as a distinct increase in absorbance at 260 nm (Figure A 6.1b) from 0.195 ± 0.001 of UFH to 1.937 ± 0.032 of fragmented heparin (fHep). The absorbance at 260 nm indicates the formation of an aldehyde group.

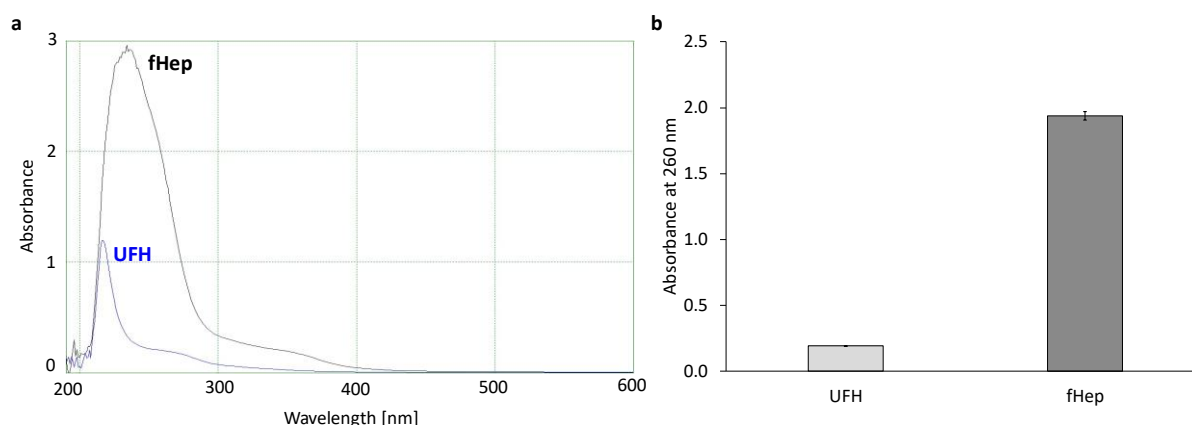


Figure A 6.1: UV/VIS characterization of acidic-fragmented heparin. Representation of (a) the UV/VIS spectra of unfragmented heparin (UFH) and fragmented heparin (fHep) and (b) bar plot of the absorbance at 260 nm of UFH and fHep. The bars represent the mean \pm SD, $n = 3$.

Size exclusion chromatography was performed to further separate the fHep according to molecular size. In the first step, separation was done using a Sephadex G25 column with a fractionation range of 100 Da to 5,000 Da. The individual fractions were measured photometrically at 232 nm, as the double bond at the non-reducing end of the uronic acid of heparin absorbs here.

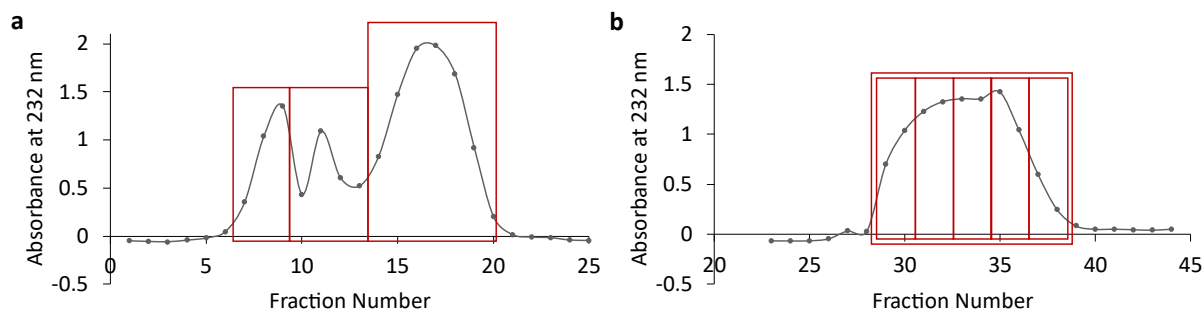


Figure A 6.2: Separation of fragmented heparin (fHep) using size exclusion chromatography. (a) Chromatogram of the separation of fHep using a Sephadex G25 fine column and (b) chromatogram of the separation of fHep fraction F14 – F20 using a Sephadex G50 fine column.

Figure A 6.2a shows three individual peaks that have already been washed off the column with PBS and are therefore above the separation range. The fractions outlined in red (F7 – F9, F10 – F13 and F14 – F20) were pooled and the latter was further separated using a Sephadex G50 column. The fractionation range here was 500 Da – 10000 Da. The chromatogram in Figure A 6.2b does not show a separation into several individual peaks, but the elution as a broadened overall peak over 10 individual fractions. The fractions outlined in red were combined and the buffer was exchanged to water by dialysis for further analysis (F29 + F30, F31 + F32, F33 + F34, F35 + F36, F37 + F38 and F29 – F38).

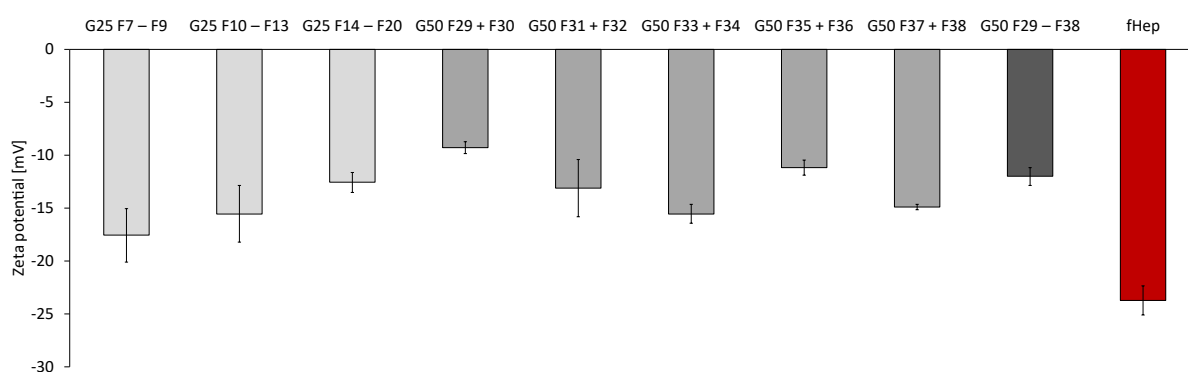


Figure A 6.3: Representation of the Zeta potential values of all separated fragmented heparin fractions compared to the fHep (red). The bars represent the mean \pm SD, $n = 3$.

Figure A 6.3 displays the Zeta potential (ZP) of all fractions after separation using the Sephadex G25 column (light gray), Sephadex G50 column (gray and dark gray) in comparison to the fHep before separation (red). The ZP significantly reduced from $-23.7 \text{ mV} \pm 1.4 \text{ mV}$ of the fHep to $-9.3 \text{ mV} \pm 0.6 \text{ mV}$ of the fraction G50 F29 + F30. The

average Zeta potential of the fractions is -14.0 mV. This corresponds to a reduction in the ZP of around 40 %.

Table A 6.1: Overview of the heparin activity of the different fragmented heparin fractions determined by the Factor Xa assay after separation by size exclusion chromatography, whereas LLOQ reflects the lower limit of quantification. The heparin activity is given as mean \pm SD, n = 3.

Fractions	Heparin Activity [IU/mL]
G25 F7 – F9	29.02 \pm 0.17
G25 F10 – F13	28.50 \pm 0.31
G25 F14 – F20	< LLOQ
G50 F29 + F30	< LLOQ
G50 F31 + F32	< LLOQ
G50 F33 + F34	< LLOQ
G50 F35 + F36	< LLOQ
G50 F37 + F38	< LLOQ
G50 F29 – F38	< LLOQ

As the ZP alone is not a valid indicator for the activity of the fractionated fragmented (ffHep), it was determined using a Factor Xa assay. The results in Table A 6.1 demonstrate that only the first two fractions of the Sephadex G25 column (F7 – F9 and F10 – F13) retain their heparin activity indicating that they contain a sufficient molecular weight and thus a characteristic pentasaccharide domain for binding antithrombin III. All other fractions showed no heparin activity and were below the detection limit of the assay.

Conjugation and Analysis of ffHep-Modified Liposomes

For the conjugation of the active heparin fractions F7 – F9 and F10 – F13, different anchors were integrated into the liposomal formulation of 5 mol% each. Therefore, the primary amine of the functionalized DSPE-PEG1k-NH₂ and the primary amines of the head groups of DPPE and DOPS served as anchors for the conjugation of ffHep via the aldehyde group (Figure 31, Chapter 3.2.2.2.3.3).

Conjugation was carried out by adding a 50-molar excess of a 6.4 M cyanoborohydride (CN) solution in PBS and subsequent incubation for one week. To terminate the reaction, a 20-molar excess of a 0.5 M succinic anhydride (SA) solution in 1,4-dioxane was added. To investigate the influence of both substances on plane liposomes without the purpose of conjugation, a stability study was carried out using dynamic light scattering (DLS). The results of the incubation of DPPC/cholesterol (60:40 mol%) liposomes with cyanoborohydride are shown in Figure S 6.1. Linear regressions of size development were analyzed using Student's t-test, showing an increasing trend for DCR over one week. This is possibly due to a slight aggregate formation. In contrast, neither the particle size (Z-Ave) nor the particle distribution index (Pdl) showed any trend. The results for the incubation with succinic anhydride in Figure S 6.3 are almost identical. There is also an increasing trend in the DCR over 24 h, but no trend concerning the Z-Ave and the Pdl.

Furthermore, the liposomes incubated with CN and SA were purified by dialysis and subsequently evaluated with regard to their cytotoxicity. The cytotoxicity of CN in PBS and SA in 1,4-dioxane itself was also investigated. The results can be found in the appendix in Figure S 6.2 and S 6.4. In both cases, there was no cytotoxicity of the treated liposomes after purification on the cells (Figure S 6.2a and S 6.4a)- However, the cytotoxicity of both substances can be observed in Figure S 6.2b and S 6.4b. CN already showed a reduction in relative cell viability to below 50 % from 5 mg/mL. In contrast, the viability of SA decreased below 60 % from a concentration of 4 mg/mL.

Table A 6.2 summarizes the most important physicochemical characteristics. The particle size of all liposomal formulations is below 150 nm and has a Pdl < 0.2. With the exception of the DPPE-containing liposomes, there is also an increase in size from the unconjugated (pure) liposomes to the liposomes conjugated with ffHep – either F7 – F9 or F10 – F13. The Zeta potential also shows an increase in more electronegative regions after conjugation.

Table A 6.2: Overview of the measurement data of unmodified and ffHep-modified liposomes using dynamic light scattering (DLS). Particle size (Z-Ave), particle size distribution (Pdl) and zeta potential as mean \pm SD, $n = 3$.

Liposomal anchor \pm ffHep fraction	Z-Average [nm]	Pdl	Zeta potential [mV]
NH ₂ pure	125.6 \pm 0.8	0.060 \pm 0.030	0.4 \pm 0.7
NH ₂ F7 – F9	142.6 \pm 4.8	0.178 \pm 0.017	-8.7 \pm 1.0
NH ₂ F10 – F13	141.8 \pm 3.4	0.202 \pm 0.025	-8.8 \pm 1.0
DPPE pure	123.8 \pm 1.9	0.160 \pm 0.021	-0.4 \pm 0.5
DPPE F7 – F9	102.6 \pm 0.7	0.077 \pm 0.046	-8.5 \pm 0.4
DPPE F10 – F13	103.6 \pm 0.5	0.092 \pm 0.013	-8.3 \pm 0.6
DOPS pure	106.1 \pm 1.2	0.108 \pm 0.031	-6.3 \pm 1.0
DOPS F7 – F9	119.1 \pm 0.6	0.083 \pm 0.031	-13.6 \pm 0.3
DOPS F10 – F13	121.7 \pm 2.2	0.096 \pm 0.013	-10.1 \pm 1.6

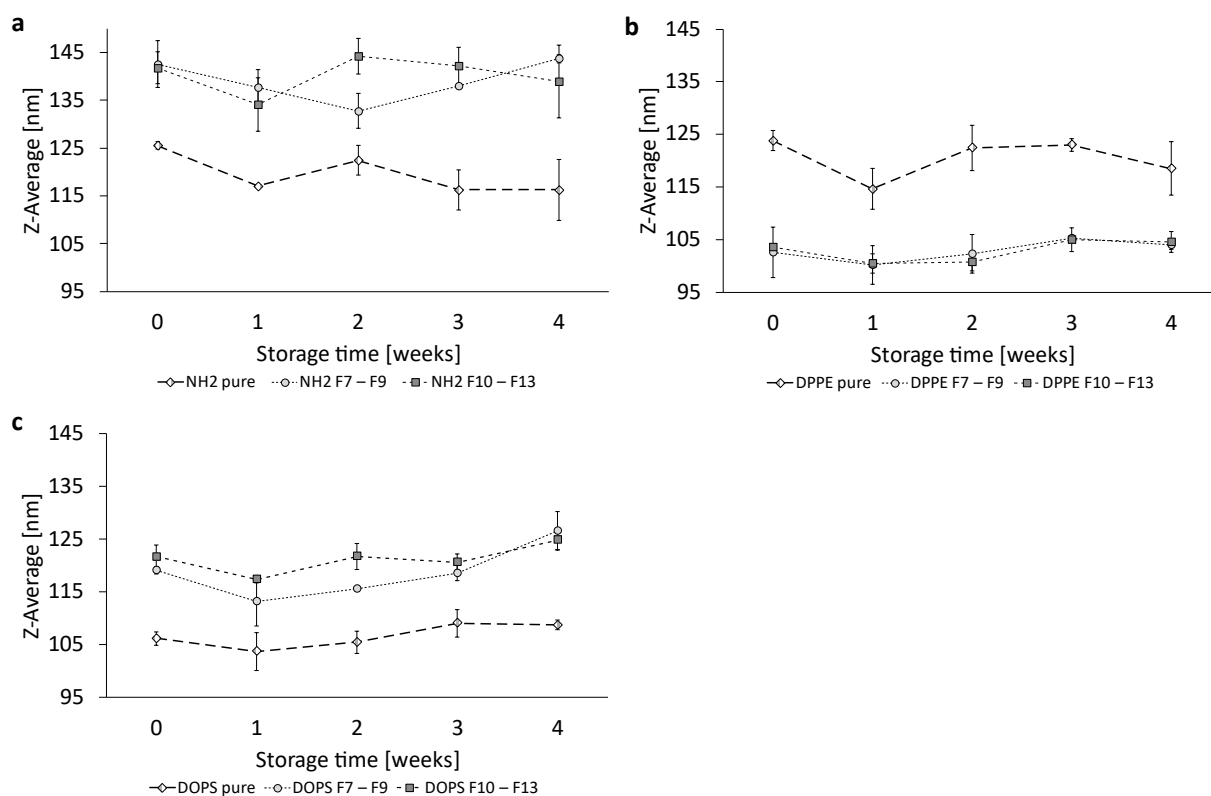


Figure A 6.4: Liposomal stability concerning the Z-Average over a storage period of 4 weeks at 4 °C. Representation of the storage stability of (a) NH₂-based liposomes, (b) DPPE-based liposomes and (c) DOPS-based liposomes. The dots represent the \pm SD, $n = 3$.

The stability of the liposomal formulations was investigated for 4 weeks when stored at 4 °C under light-protected conditions. Figure A 6.4 shows the development of the size over 4 weeks. It should be noted that the y-axis only shows a size range of 95 nm – 145 nm. None of the nine formulations investigated showed a significant increasing trend during the storage period. This is also the result for the Zeta potential (Figure A 6.6). Only the Pdl of the NH₂ F7 – F9 liposomes in Figure A 6.5b showed a significant increase. The linear regressions of the development concerning Z-Ave, Pdl and zeta potential of the 9 liposomal formulations were analyzed using Student's t-test (see Figure S 6.5 to S 6.7).

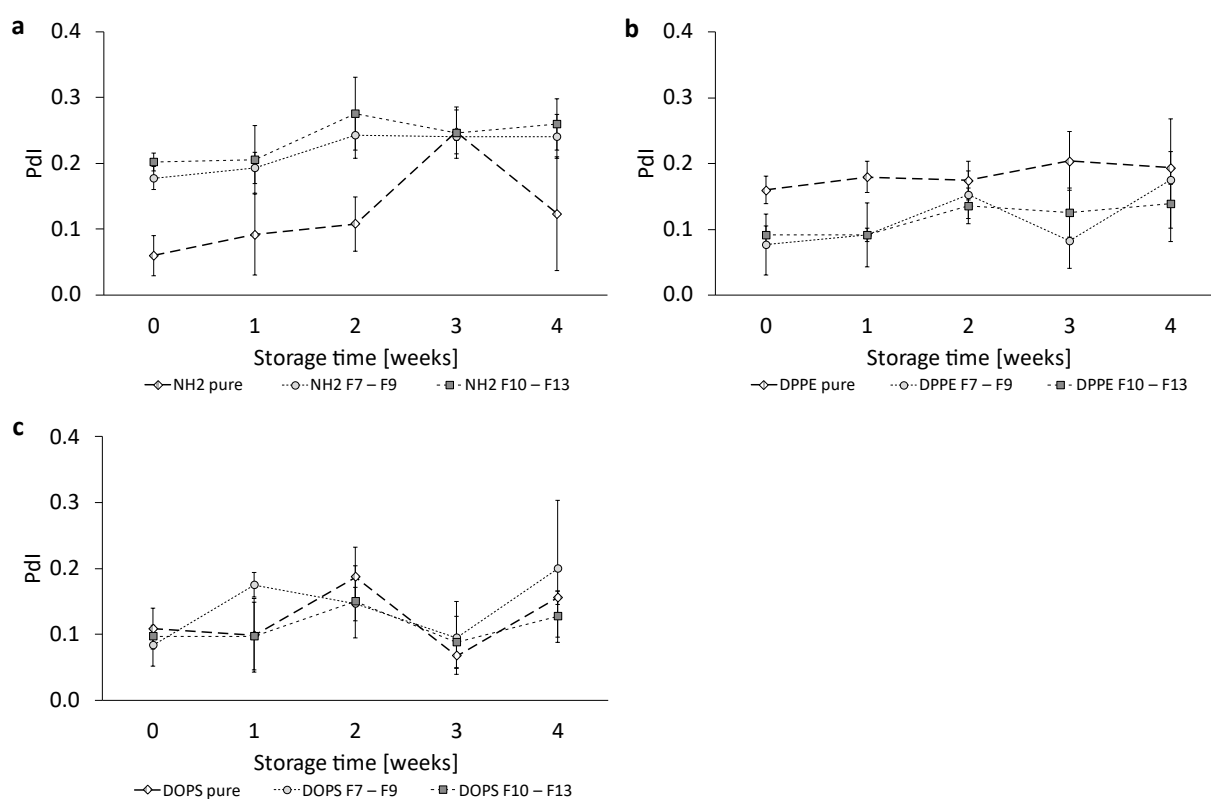


Figure A 6.5: Liposomal stability concerning the particle distribution index (Pdl) over a storage period of 4 weeks at 4 °C. Representation of the storage stability of (a) NH₂-based liposomes, (b) DPPE-based liposomes and (c) DOPS-based liposomes. The dots represent the mean \pm SD, n = 3.

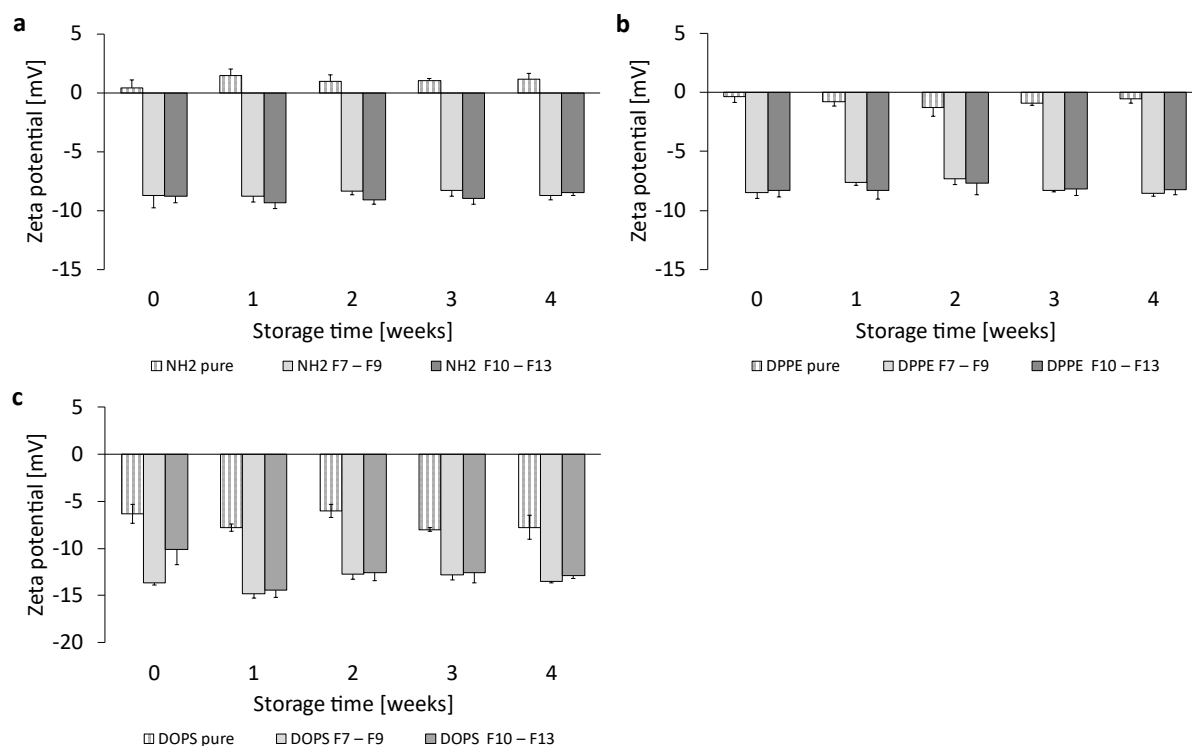


Figure A 6.6: Liposomal stability concerning the Zeta potential over a storage period of 4 weeks at 4 °C. Representation of the storage stability of (a) NH₂-based liposomes, (b) DPPE-based liposomes and (c) DOPS-based liposomes. The bars represent the mean \pm SD., n = 3.

The ffHep concentration on the liposomal surface was determined using the Alcian Blue Assay (Chapter 3.2.2.3.5.1) and can be seen in Figure A 6.7. Almost identical ffHep concentrations were found for the NH₂- and DOPS-containing liposomes. The ffHep concentrations were around 50 $\mu\text{g/mL}$. Both, the highest fHep concentration of 103.2 $\mu\text{g/mL} \pm 4.0 \mu\text{g/mL}$ and the lowest concentration of 25.6 $\mu\text{g/mL} \pm 2.3 \mu\text{g/mL}$ were found for the DPPE-containing liposomes.

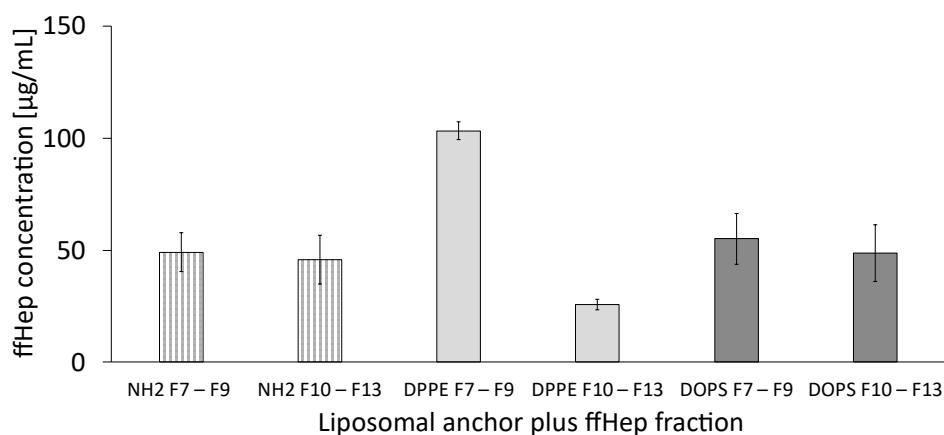


Figure A 6.7: Concentration of ffHep on the liposomal surface using Alcian Blue for quantification. The bars represent the mean \pm SD., $n = 3$.

Table A 6.3 summarizes the heparin activity of the 6 liposomal formulations with ffHep on the surface. It can be seen that a heparin activity can be maintained for all formulations, whereby the activity of the liposomes with F7 – F9 on the surface is always higher compared to the liposomes with F10 – F13. In general, however, there is a considerable reduction in heparin activity compared to the activity of the unconjugated fractions (Table A 6.1).

Table A 6.3: Overview of the heparin activity according to the Factor Xa Assay for the different types of liposomes with conjugated fragmented fractionated heparin on their surface. The values represent the mean \pm SD, $n = 3$.

Liposomal anchor + ffHep fraction	Heparin activity [IU/mL]
NH ₂ F7 – F9	7.58 \pm 0.20
NH ₂ F10 – F13	3.63 \pm 0.07
DPPE F7 – F9	4.47 \pm 0.65
DPPE F10 – F13	2.03 \pm 0.03
DOPS F7 – F9	5.15 \pm 2.92
DOPS F10 – F13	2.99 \pm 0.87

The conjugation efficiency was carried out using fluorescamine as a fluorescence labeling reagent for primary amines (Chapter 3.2.2.3.5.3) and is shown in Figure A 6.8. There were distinct differences between the individual liposomal anchors, but no significant differences between the two fHep fractions for any of the conjugation anchors. The highest conjugation efficiency was achieved for the liposomes with DSPE-PEG1k-NH₂ as the

conjugation anchor. The conjugation efficiency was $41.3 \% \pm 5.44 \%$ for NH_2 F7 – F9 and $43.5 \% \pm 4.99 \%$ for NH_2 F10 – F13. The lowest conjugation efficiency was found for the DPPE-containing liposomes with $15.2 \% \pm 4.65 \%$ and $10.5 \% \pm 3.04 \%$, respectively.

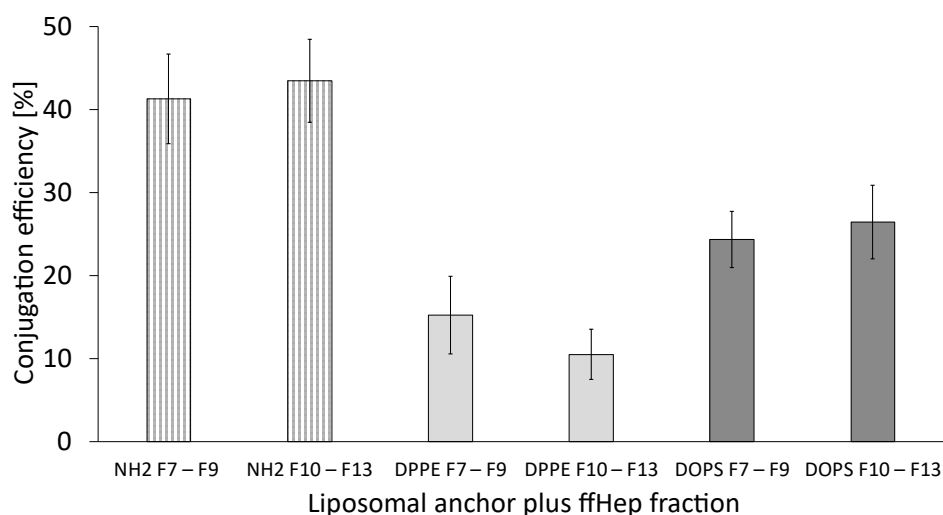


Figure A 6.8: Conjugation efficiency for the coupling of ffHep to the liposomal surface determined by fluorescamine assay for the different types of liposomes. The bars represent the mean \pm SD, $n = 3$.

Figure A 6.9 summarizes the results of the *Bacteroides Heparinase* I assay. The enzyme cleaves the glycosidic link between the individual hexosamines so that the cleaved oligosaccharides with unsaturated uronic acid residues can be analyzed photometrically at 232 nm. In general, it was shown that significantly longer incubation times to maximum absorption are required for the liposomes with the fHep fraction F10 – F13 (7 h and 8 h) compared to the liposomes with the fHep fraction F7 – F9 (4 h and 5 h).

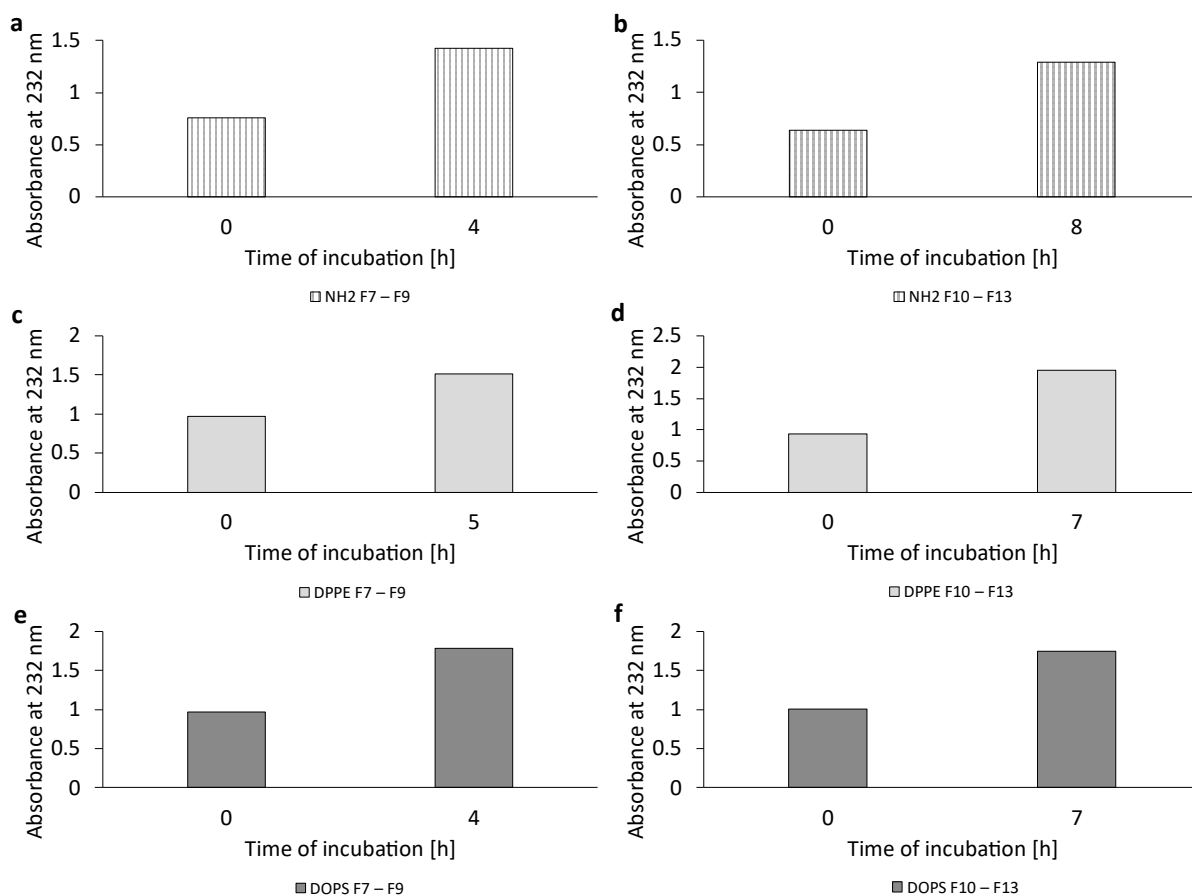


Figure A 6.9: Cleavage of fragmented fractionated heparin (ffHep) on the liposomal surface using *Bacteroides Heparinase I*. (a - f) Absorbance at 232 nm of the different liposomal anchors with conjugated ffHep fractions before the start of enzymatic cleavage (0 h) and at the time of maximum absorbance.

Ex vivo Analysis of ffHep-modified Liposome

For a preliminary evaluation of hemo- and immunocompatibility, human whole blood was incubated at 37 °C for 1 hour, analyzed for platelet count and then the plasma was isolated and analyzed for various complement factors by ELISA.

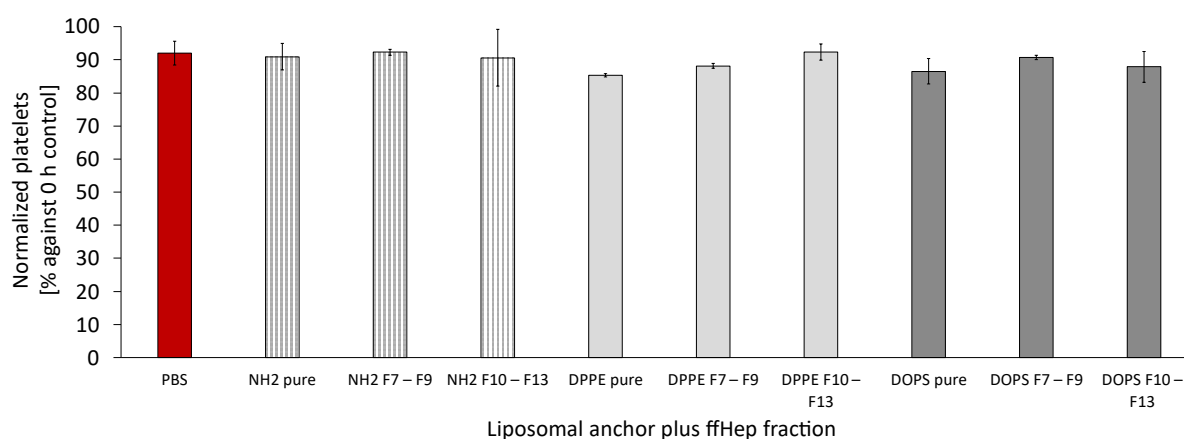


Figure A 6.10: Representation of the normalized platelet count after human whole blood incubation for 1 h with unmodified or ffHep-modified liposomes at 37 °C. The bars represent the mean \pm SD, n = 3.

Figure A 6.10 displays the platelet count normalized to the initial value after incubating the blood for 1 h. Incubation with PBS as a control led to a reduction of the platelet count to 92.02 % \pm 3.56 %. The highest reduction in platelet count was recorded when the blood was incubated with DPPE pure liposomes. Here the platelet count fell to 85.36 % \pm 0.44 % of the initial value.

The plasma tests for various complement factors using ELISA analysis are not shown as an average of the three donors due to strong inter-individual fluctuations, but rather individually in the sub-graphs a to c in Figures A 6.11 to A 6.13. The partially missing bars indicate that the data were not analyzable due to excessive pre-activation of the blood. Figure A 6.11 displays the normalized C3a plasma levels as this complement factor reflects the initial factor of the cascade. It can be seen that modification of the liposomes with ffHep led to an increase of the initial complement protein in most cases. The normalized plasma levels of C5b-9 (Figure A 6.12) – also referred to as terminal complex – showed in some cases a considerable reduction due to surface modification of the liposomes with heparin. For example, in the case of DPPE liposomes for both fHep

fractions for all 3 donors, but also in the case of NH₂ liposomes for donor 1 (Figure A 6.12 a). There is no apparent tendency with regard to normalized thrombin-antithrombin (TAT) plasma levels (Figure A 6.13). In some cases, the conjugation of ffHep to the liposomal surface causes an increase in TAT levels in plasma.

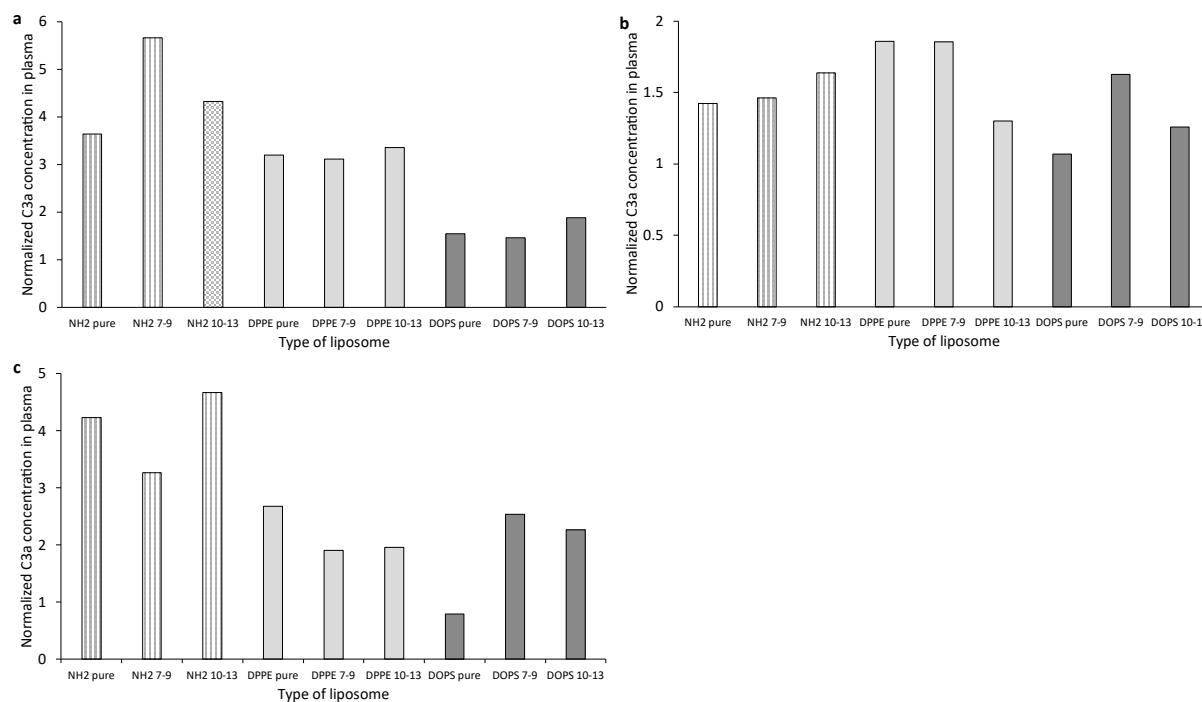


Figure A 6.11: Plasma levels of C3a normalized to PBS as control after 1 h of whole blood incubation at 37 °C with the different liposomal formulations where (a – c) represent donors 1, 2 and 3 respectively.

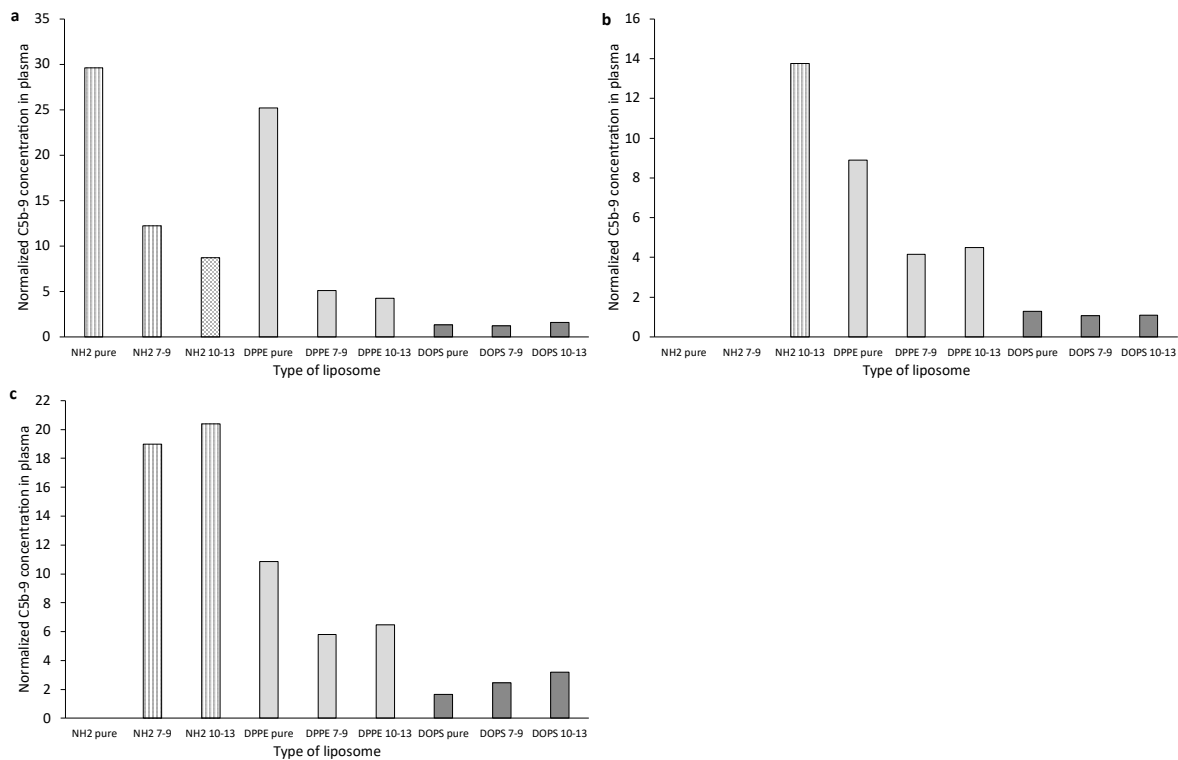


Figure A 6.12: Plasma levels of C5b-9 normalized to PBS as control after 1 h of whole blood incubation at 37 °C with the different liposomal formulations where (a – c) represent donors 1, 2 and 3 respectively.

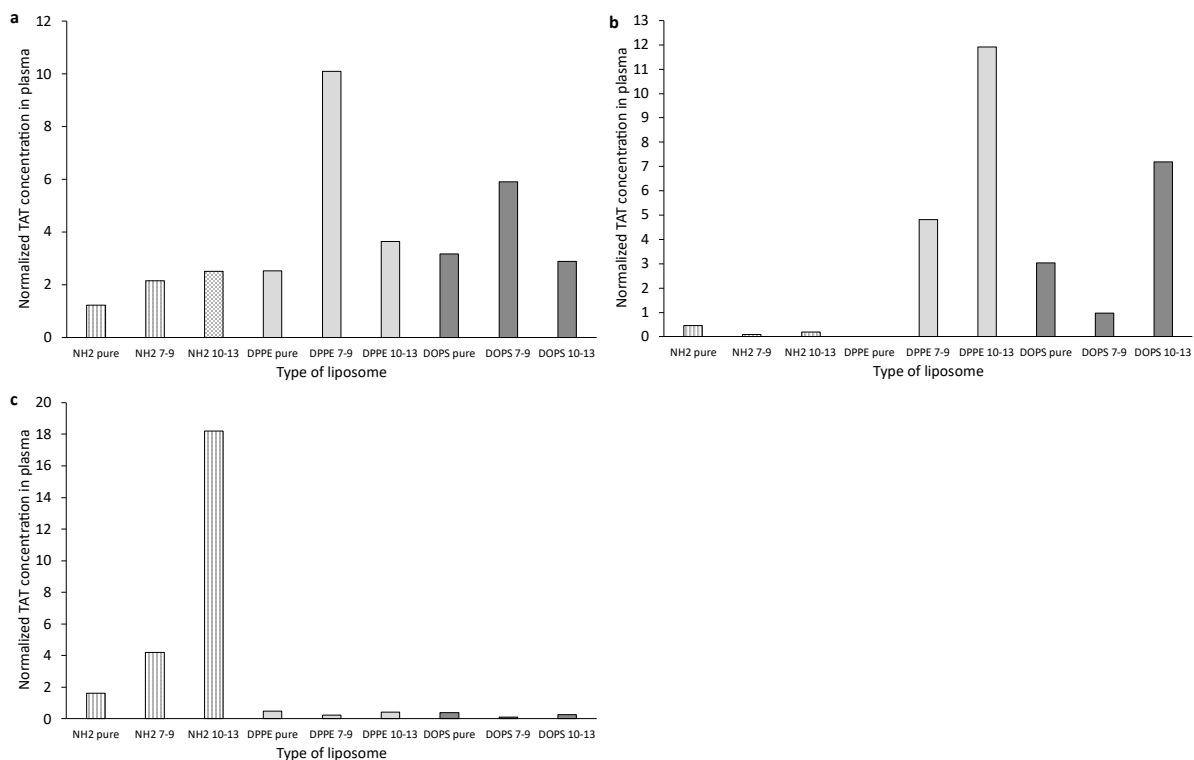


Figure A 6.13: Plasma levels of TAT normalized to PBS as control after 1 h of whole blood incubation at 37 °C with the different liposomal formulations where (a – c) represent donors 1, 2 and 3 respectively.

Supplementary Figures

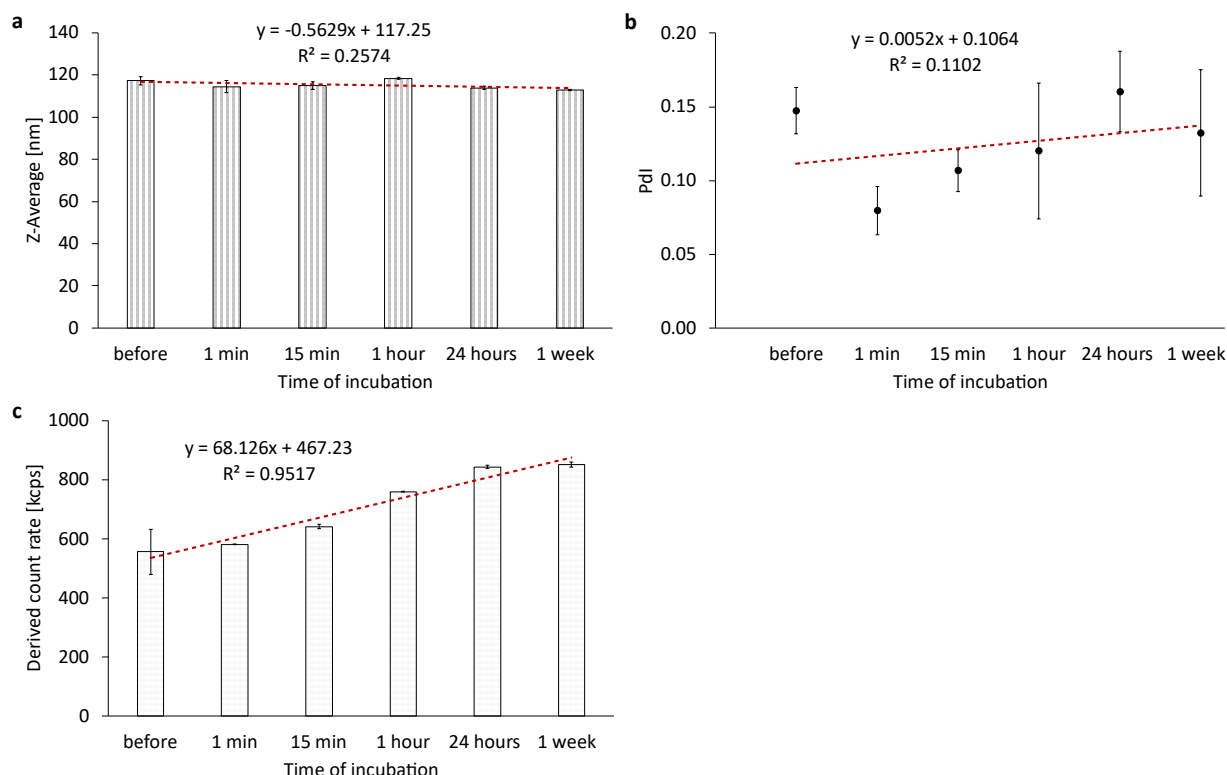


Figure S 6.1: Trend analysis of the (a) Z-Average, (b) the Pdl and (c) of the derived count rate (DCR) of liposomes treated with a 50-molar excess of cyanoborohydride (6.4 M in PBS). Determination of significance of a linear regression using Student's t-test.

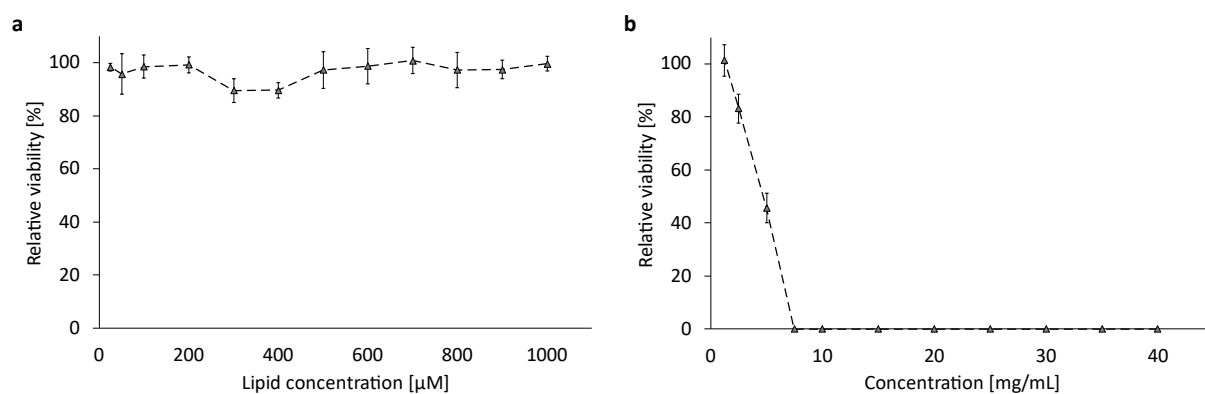


Figure S 6.2: Cytotoxicity evaluation on F98 cells using alamarBlue™ HS reagent. Representation of (a) the cytotoxicity of liposomes treated with a 50-molar excess of cyanoborohydride (6.4 M in PBS) for 1 week after dialysis and (b) the cytotoxicity of cyanoborohydride solution in PBS. The dots represent the mean values \pm SD, $n = 3$.

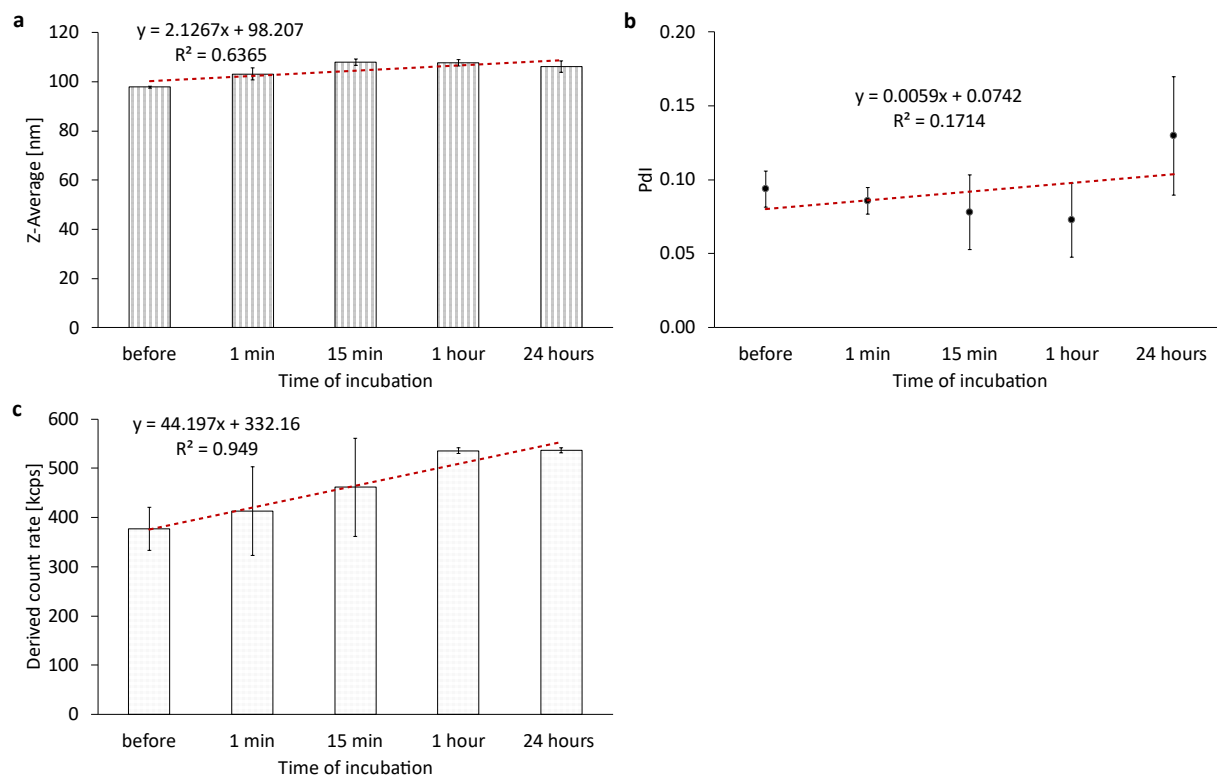


Figure S 6.3: Trend analysis of the (a) Z-Average, (b) the Pdl and (c) of the derived count rate (DCR) of liposomes treated with a 20-molar excess of succinic anhydride (1,4-Dioxan). Determination of significance of a linear regression using Student's t-test.

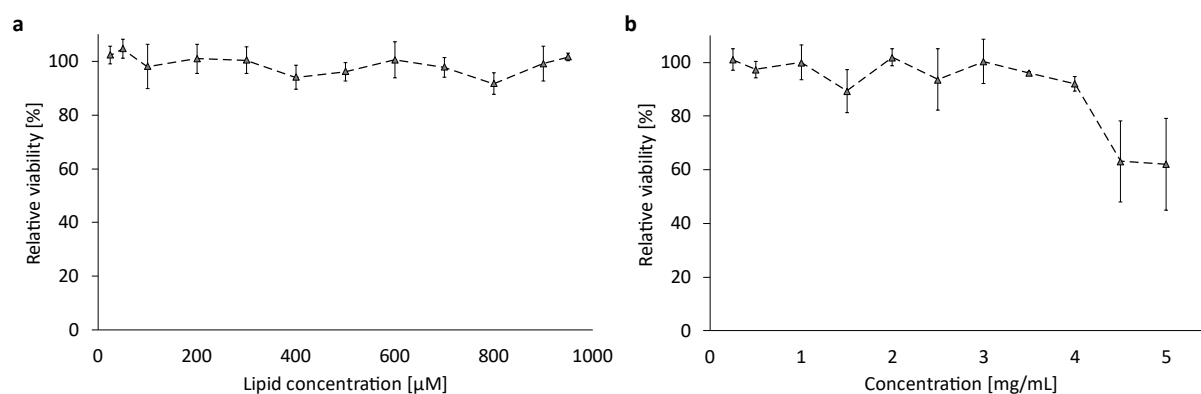


Figure S 6.4: Cytotoxicity evaluation succinic anhydride on F98 cells using alamarBlue™ HS reagent. Representation of (a) the cytotoxicity of liposomes treated with a 20-molar excess of succinic anhydride (0.5 M in 1,4-Dioxan) for 24 h after dialysis and (b) the cytotoxicity of succinic anhydride solution in 1,4-Dioxan. The dots represent the mean values \pm SD, $n = 3$.

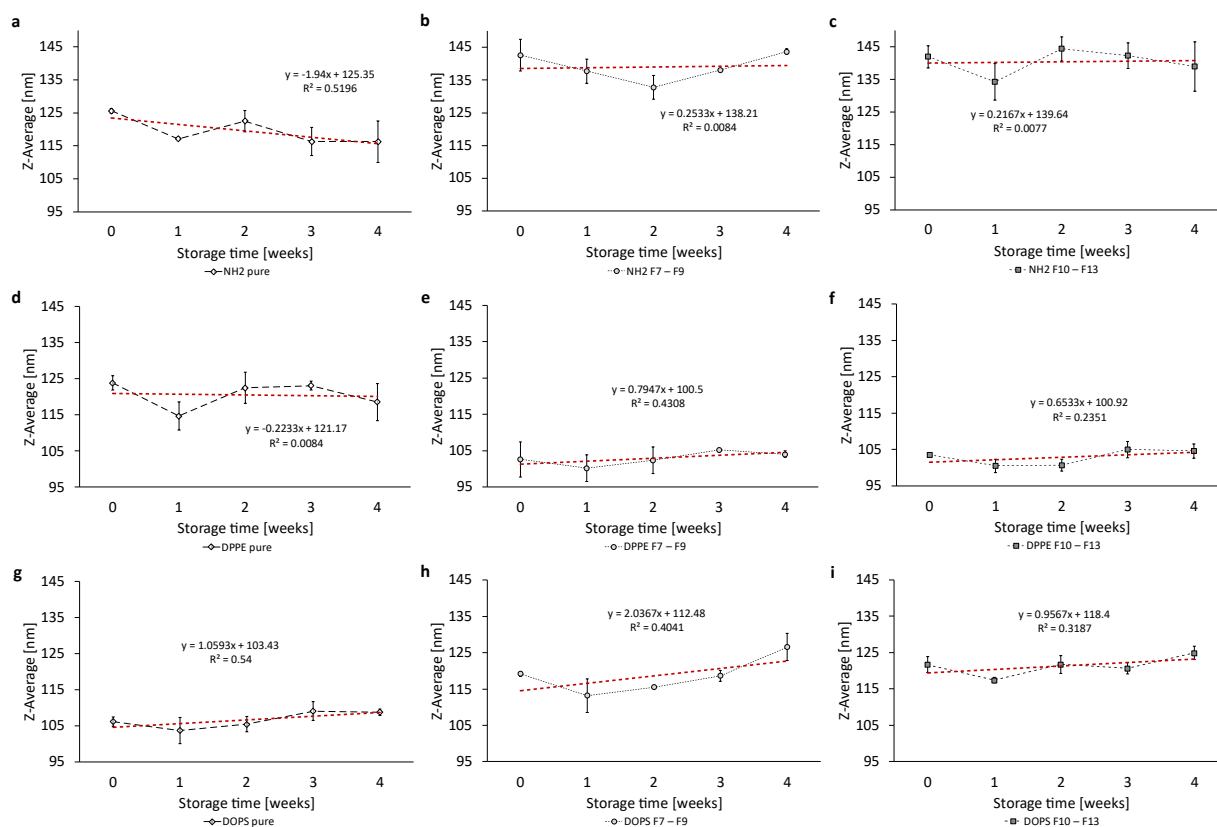


Figure S 6.5: Trend analysis of the Z-Ave of the liposomal formulations over a storage period of 4 weeks at 4 °C. Determination of significance of a linear regression using Student's t-test.

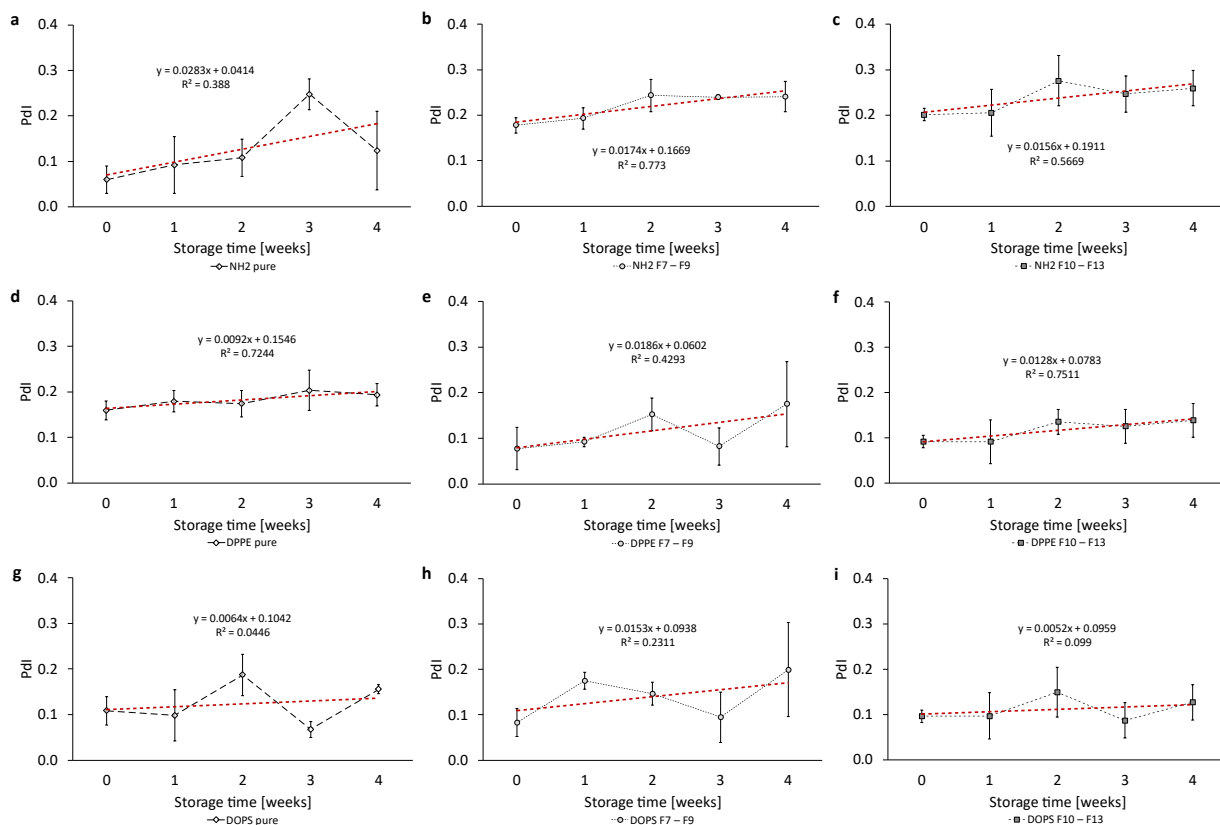


Figure S 6.6: Trend analysis of the Pdl of the liposomal formulations over a storage period of 4 weeks at 4 °C. Determination of significance of a linear regression using Student's t-test.

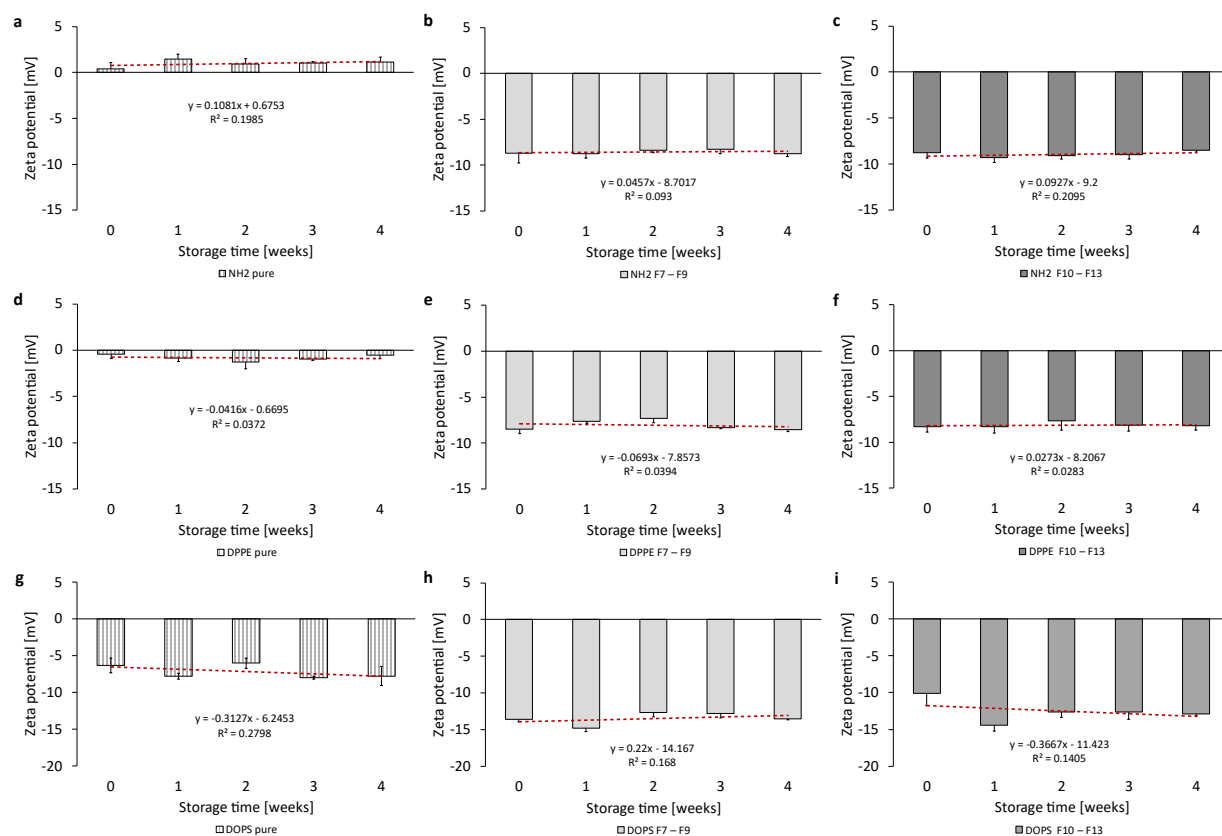


Figure S 6.7: Trend analysis of the Zeta potential of the liposomal formulations over a storage period of 4 weeks at 4 °C. Determination of significance of a linear regression using Student's t-test.

A7 Asymmetric Liposomes as Proof-of-Concept

Evaluation of Size, Polydispersity Index, Lipid Concentration and Stability

Asymmetric liposomes were prepared by centrifugation of 2 inverse nanoemulsions as described in Chapter 3.2.2.3.6. All characterized liposomes consisted of DPPC and cholesterol in a ratio of 70:30 mol% in their outer layer and a molar ratio of DMPC to cholesterol of 60:40 in the inner layer. The following Figure A 7.1 shows the particle size (Z-Ave) and particle size distribution (Pdl) for the liposomes without encapsulated dye at three different steps of the manufacturing process: 1) after centrifugation, 2) after extrusion and 3) after sterile filtration. After centrifugation, the liposomes had a size of 416.1 ± 4.2 nm and a Pdl of 0.762 ± 0.0398 . After extrusion or sterile filtration, the liposomes are less than half the size with 148.8 ± 1.1 nm and 149.1 ± 1.4 nm and a Pdl of 0.227 ± 0.047 and 0.0234 ± 0.0151 , respectively.

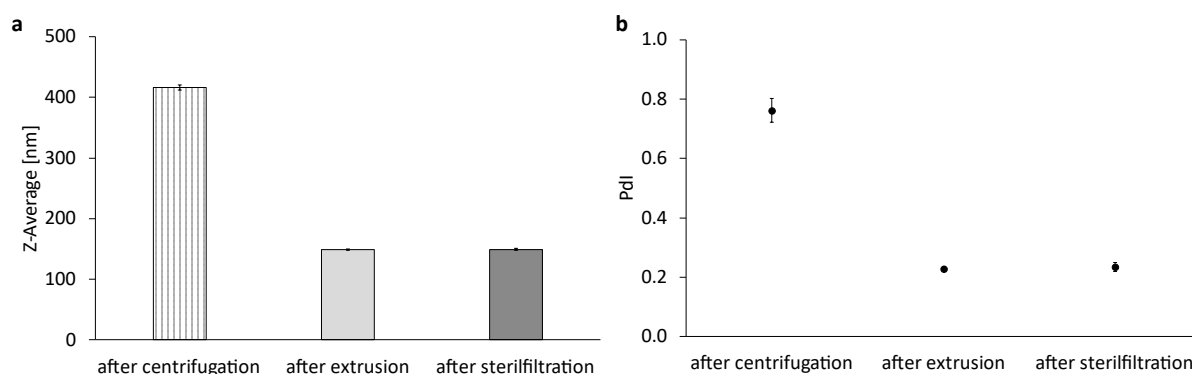


Figure A 7.1: Characterization of asymmetric liposomes without encapsulated dye at different steps of the manufacturing process using dynamic light scattering. Representation of (a) the Z-Average and (b) of the Pdl of asymmetric liposomes. The bars or dots represent the mean \pm SD, $n = 3$.

Figure A 7.2 represents the characterization of liposomes with encapsulated dye (fluoresceine sodium, FluNa) at the same steps of preparation. Both Z-Ave and Pdl show very similar results, compared to the liposomes without FluNa in Figure A 7.1. Thus, the encapsulation of FluNa does not result in any changes of liposomal characteristics, but rather in similar properties. Liposomes with encapsulated FluNa (Figure A 7.2) have a

Z-Ave of $362.1 \text{ nm} \pm 33.7 \text{ nm}$ and a Pdl of 0.548 ± 0.113 after centrifugation. They decrease in particle size to $172.5 \text{ nm} \pm 0.8 \text{ nm}$ and 0.281 ± 0.033 concerning the Pdl after extrusion, analogous to the liposomes without encapsulation of the dye.

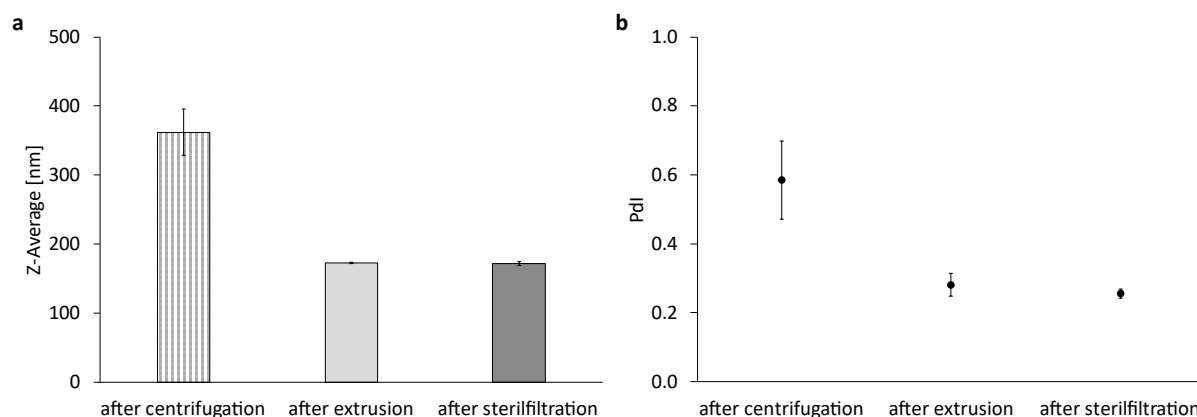


Figure A 7.2: Characterization of asymmetric liposomes with encapsulated FluNa at different steps of the manufacturing process using dynamic light scattering. Representation of (a) the Z-Average and (b) of the Pdl of asymmetric liposomes. The bars or dots represent the mean \pm SD, $n = 3$.

To assess the stability, liposomes were stored at 4°C for a period of 12 weeks and analyzed weekly using DLS. The results are shown in Figure A 7.3. Again, liposomes after centrifugation (Figure A 7.3a and A 7.3b), after extrusion (Figure A 7.3c and A 7.3d) and after sterile filtration (Figure A 7.3e and A 7.3f) were characterized. As presented in Figure A 7.3, no considerable differences of the Z-Ave can be detected over time.

The Pdl of centrifugated liposomes varies from 0.437 ± 0.209 to 0.897 ± 0.099 throughout storage and has the highest standard deviation, compared to the other liposomal samples. The Z-Ave stays around 350 nm for liposomes after centrifugation and at around 160 nm for liposomes after extrusion or sterile filtration. Figure A 7.3 clearly shows that the standard deviation of liposomes after centrifugation is much higher than after extrusion and sterile filtration. This can be observed for both characteristics, the Z-Ave and Pdl, assuming a wide particle size distribution which causes particle fusion over the storage time.

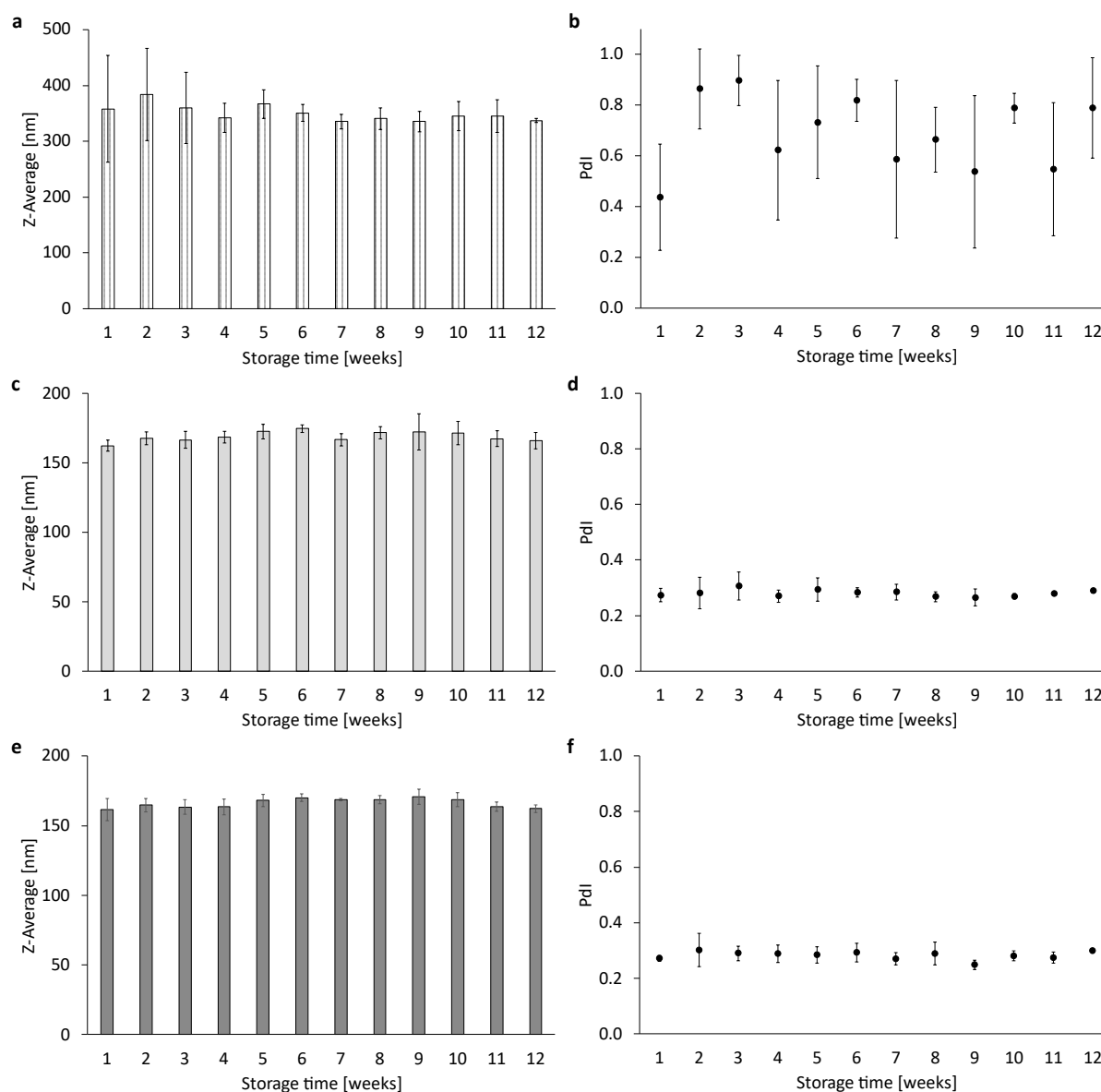


Figure A 7.3: Characterization of asymmetric liposomes over a 12-week storage period at 4 °C. Representation of the Z-Ave or Pdl for liposomes (a and b) after centrifugation, (c and d) after extrusion and (e and f) after sterile filtration. The bars or dots represent the mean \pm SD, $n = 3$.

Liposomes were characterized using the Stewart Assay, as described in Chapter 3.2.2.3.2.2, in order to determine the lipid concentration. The theoretical maximal lipid concentration is derived from the 5 mM PFC/W nanoemulsion and 1.5 % (v/v) of the 300 mM W/PFC emulsion and thus amounts to 9.5 mM. Figure A 7.4 represents the total lipid concentration for the asymmetric liposomes at the different steps of preparation – same as for the figures above. It can be seen that the lipid concentration varies between $7.63 \text{ mM} \pm 0.63 \text{ mM}$ and $8.64 \text{ mM} \pm 0.43 \text{ mM}$, whereas it is the highest in the liposomes after centrifugation assuming some loss of phospholipids during the process of extrusion.

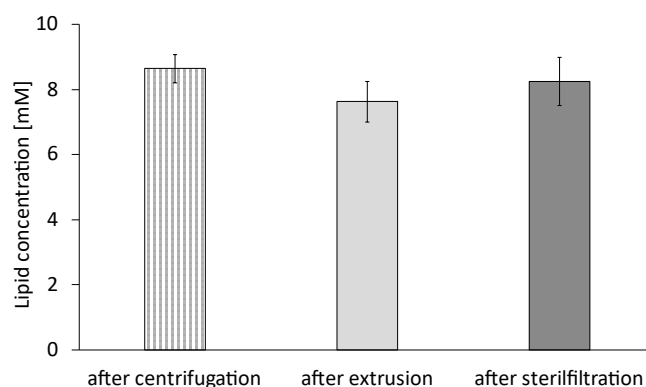


Figure A 7.4: Lipid concentration of asymmetric liposomes at different steps of the manufacturing process according to the StewartAssay. The bars represent the mean \pm SD, $n = 3$.

The lipid concentration of the asymmetric liposomes at different steps of preparation fluctuates within a range of 1 mM. As seen in Figure A 7.4, the lipid concentration of liposomes does not differ considerably after post-processing of the liposomes, as can be seen by the overlapping standard deviations.

Encapsulation Efficiency of Asymmetric Liposomes

The encapsulation efficiency (EE) was determined as described in Chapter 3.2.2.3.6.1. As the EE was determined based on UV/VIS spectroscopy, the absorbance spectra of all initial phases of the liposomes were measured beforehand. The initial phases include buffer, FluNa stock solution, and both nanoemulsions for liposome preparation. The spectra of the prepared liposomes with and without FluNa were measured as well, to ensure no interfering absorbance at 495 nm for FluNa quantification. Figure A 7.5a shows that all phases that contain FluNa expose a peak at 495 nm. The other phases do not reveal a peak at this characteristic wavelength, which demonstrates that the initial phases do not interfere with each other and that the method for encapsulation determination is valid. Additionally, the absorbance spectrum of PPHP was measured before and after centrifugation of the two inverse nanoemulsions. Figure A 7.5b reveals that PPHP after centrifugation of the liposomes exhibits the same spectrum as pure PPHP. No additional absorbance peaks are detected, which means that no lipids or FluNa-molecules remain in the PPHP and the transfer of PL from one phase to the other is complete.

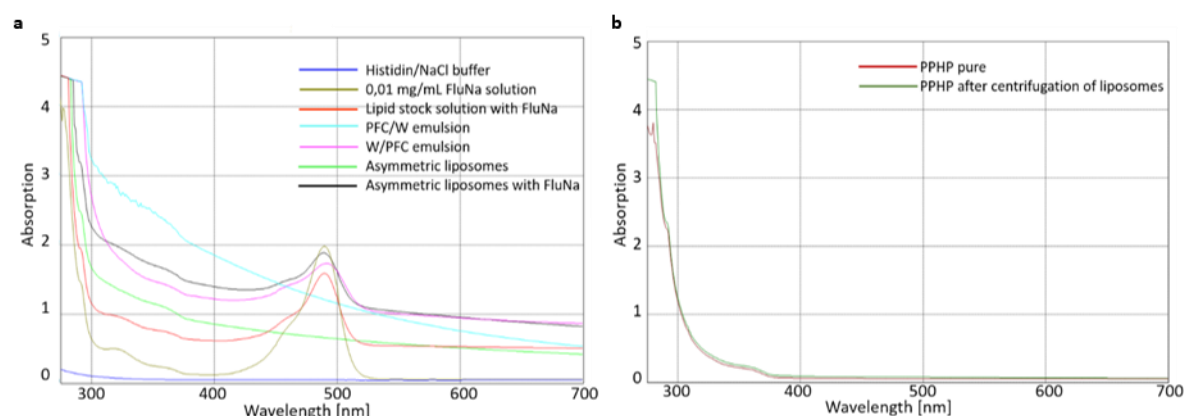


Figure A 7.5: Absorption spectra of (a) initial phases from liposome production and (b) absorption spectra of initial PPHP and PPHP after centrifugation of liposomes.

The EE of liposomes ranges from $22.3 \% \pm 3.1 \%$ to $29.3 \% \pm 3.5 \%$, as shown in Figure A 7.6a. No considerable difference can be seen between the liposomes at different steps of preparation. Figure A 7.6b displays the recovery rate (RR) of FluNa related to the initial concentration used, which varies between $70.1 \% \pm 3.7 \%$ and $89.1 \% \pm 5.3 \%$.

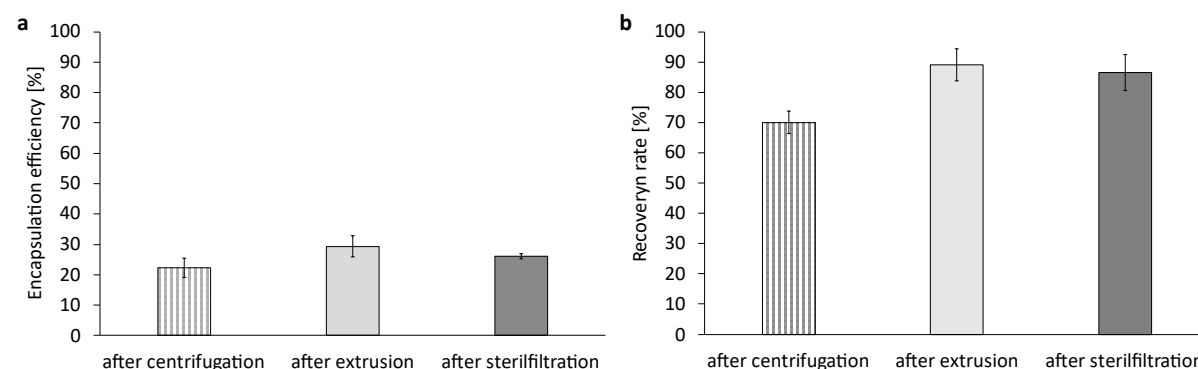


Figure A 7.6: Encapsulation efficiency of fluorescein sodium (FluNa) in asymmetric liposomes and recovery rate related to the initial FluNa concentration at different steps of preparation. The bars represent the mean \pm SD, $n = 3$.

Investigations on the Bilayer Asymmetry

The bilayer asymmetry was determined using the fluorescamine assay as described in Chapter 3.2.2.3.6.2. The fluorescence intensity was measured every 5 min over a period of 30 min after the reaction. The degree of bilayer asymmetry is shown in Figure A 7.7, whereas DOPS was integrated either into the PFC/W nanoemulsion for the outer layer (Figure A 7.7a) or in the W/PFC nanoemulsion for the inner layer (Figure A 7.7b).

For liposomes with DOPS in the PFC/W nanoemulsion (outer layer), the degree of asymmetry after 5 min is at $61.51 \% \pm 6.9 \%$ (Figure 6a). After 10 min an equilibrium is established and between 10 min and 30 min the asymmetry fluctuates between $51.09 \% \pm 0.8 \%$ and $52.69 \% \pm 1.2 \%$. Figure A 7.7b shows the degree of bilayer asymmetry of liposomes with 5 mol% DOPS incorporated in the W/PFC emulsion (inner layer). Within 15 min after incubation, an equilibrium at around 47 % is visible. The degree of asymmetry fluctuates between $45.15 \% \pm 3.6 \%$ and $48.25 \% \pm 5.2 \%$. After 20 min the asymmetry descends to $38.58 \% \pm 2.0 \%$, and a new equilibrium settles. The asymmetry of liposomes with DOPS in the outer layer and the first established equilibrium of liposomes with DOPS in the inner layer are both at around 50 %, where it has to be considered that the lipid stock suspension used for emulsification contains symmetrical liposomes.

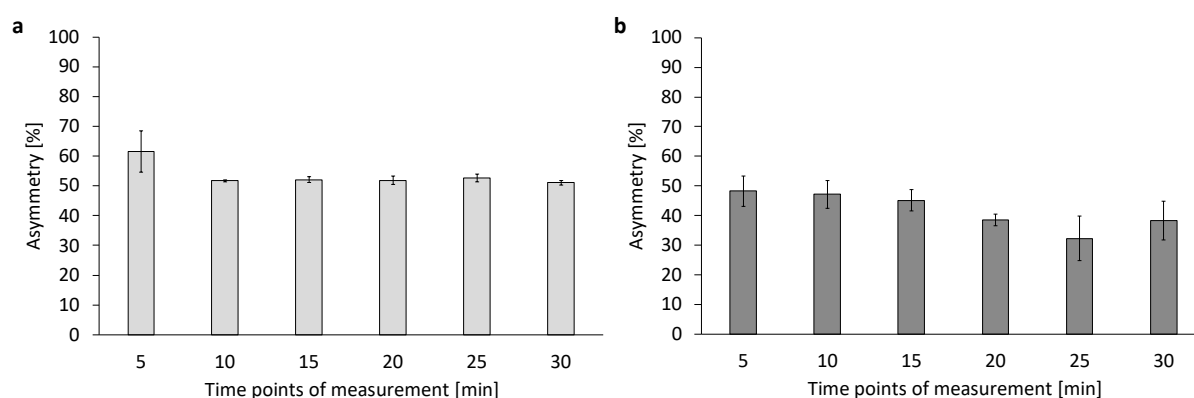


Figure A 7.7: Degree of bilayer asymmetry of liposomes whereas 5 mol% of DOPS was incorporated either in (a) the PFC/W nanoemulsion or (b) in the W/PFC emulsion. The measurement was conducted over a period of 30 min. The bars represent the mean \pm SD, $n = 3$.

A8 Calculations for Conjugation and Conjugation Efficiency

Glucose and 4-Aminophenyl-βD-glucopyranoside

Calculation for APG Conjugation to Liposomes

- lipid film with a molar concentration of 20 mM; 5 mL were used for conjugation; volume of the 10 mg/mL stock solution of DSPE-PEG5k-NHS: $V_{NHS} = 2.945 \text{ mL}$
 - therefore: $m_{NHS} = 29.45 \text{ mg}$ DSPE-PEG5k-NHS in 5 mL of liposomes
- calculation of the amount of DSPE-PEG5k-NHS

$$n_{NHS} = \frac{29.45 \cdot 10^{-3} \text{ g}}{5890 \frac{\text{g}}{\text{mol}}} = 5 \cdot 10^{-6} \text{ mol}$$

- calculation of the amount of material required for conjugation of 4-Aminophenyl-βD-glucopyranoside (APG) resulting in a 20% molar excess

$$n_{APG} = 5 \cdot 10^{-6} \text{ mol} \cdot 1.2 = 6 \cdot 10^{-6} \text{ mol}$$

$$m_{APG} = 6 \cdot 10^{-6} \text{ mol} \cdot 194.19 \frac{\text{g}}{\text{mol}} = 1.165 \cdot 10^{-3} \text{ g}$$

- APG-solution has a concentration of $c_m = 10 \text{ mg/mL}$

$$10 \text{ mg} = 1000 \mu\text{L}$$

$$1.165 \text{ mg} = x \rightarrow x = 116.5 \mu\text{L}$$

Calculation of the Conjugation Efficiency of APG

- dilution of 116.5 μL APG stock solution in 5,000 μL liposomal suspension results in a dilution factor of 1:44 and a resulting APG concentration of $c_m = 0.227 \frac{\text{mg}}{\text{mL}}$
- taking into account the 20% molar excess of APG, this results in the following concentration for APG

$$c_m = \frac{0.227 \frac{\text{mg}}{\text{mL}} \cdot 100}{120} = 0.1892 \frac{\text{mg}}{\text{mL}}$$

- APG concentration after conjugation, purification and sterile filtration $c_m = 0.154 \text{ mg/mL}$

- calculation of the conjugation efficiency:

$$\text{Conjugation efficiency [\%]} = \frac{0.154 \frac{\text{mg}}{\text{mL}} \cdot 100}{0.1892 \frac{\text{mg}}{\text{mL}}} = 81.40 \%$$

Calculation of the Molar Percentage [mol%] of GLU in Liposomes

- calculation of the molar concentration for GLU-liposomes based on the glucose concentration determined using the hexokinase kit $c_m = 0.279 \text{ mg/mL}$

$$c_n(\text{GLU}) = \frac{0.279 \frac{\text{g}}{\text{L}}}{180.156 \frac{\text{g}}{\text{mol}}} = 1.548 \cdot 10^{-3} \frac{\text{mol}}{\text{L}} = 1.548 \text{ mM}$$

- cholesterol concentration of the GLU-liposomes according LabAssay™ Cholesterol Kits $c_m = 2.195 \text{ mg/mL}$

$$c_n(\text{Chol}) = \frac{2.195 \frac{\text{g}}{\text{L}}}{365.654 \frac{\text{g}}{\text{mol}}} = 5.677 \cdot 10^{-3} \frac{\text{mol}}{\text{L}} = 5.677 \text{ mM}$$

- calculation of the mol% GLU using the assumption of 40 mol% cholesterol:

$$40 \text{ mol\%} = 5.677 \text{ mM}$$

$$y \text{ mol\%} = 1.548 \text{ mM} \rightarrow y = 10.91 \%$$

Calculation of the Molar Percentage [mol%] of APG in Liposomes

- calculation of the molar concentration for APG-liposomes based on the glucose concentration determined using the hexokinase kit $c_m = 0.154 \text{ mg/mL}$

$$c_n(\text{APG}) = \frac{0.154 \frac{\text{g}}{\text{L}}}{194.19 \frac{\text{g}}{\text{mol}}} = 7.93 \cdot 10^{-4} \frac{\text{mol}}{\text{L}} = 0.793 \text{ mM}$$

- cholesterol concentration of the GLU-liposomes according LabAssay™ Cholesterol Kits $c_m = 1.981 \text{ mg/mL}$

$$c_n(\text{chol}) = \frac{1.981 \frac{\text{g}}{\text{L}}}{365.654 \frac{\text{g}}{\text{mol}}} = 5.42 \cdot 10^{-3} \frac{\text{mol}}{\text{L}} = 5.42 \text{ mM}$$

- calculation of the mol% APG using the assumption of 40 mol% cholesterol:

$$40 \text{ mol\%} = 5.677 \text{ mM}$$

$$z \text{ mol\%} = 0.793 \text{ mM} \rightarrow z = 5.85 \%$$

Apolipoprotein E3

Thiolation of ApoE3 using Traut's Reagent

- an aliquot of ApoE3 has a volume of $V_{ApoE3} = 0.0237 \text{ mL}$ with a concentration of $c_m = 1.99 \text{ mg/mL}$

- calculation of the mass of ApoE3 in an aliquot:

$$1.99 \text{ mg} = 1000 \mu\text{L}$$

$$x = 125 \mu\text{L} \rightarrow x = 0.24875 \text{ mg}$$

- calculation of the amount of ApoE3 in an aliquot

$$n_{ApoE3} = \frac{0.24875 \cdot 10^{-3} \text{ g}}{34,400 \frac{\text{g}}{\text{mol}}} = 7.23 \cdot 10^{-9} \text{ mol} \hat{=} 7.23 \text{ nmol}$$

- calculation of the required amount and mass of Traut's reagent (2-Iminothiolan) using 50-fold molar excess

$$n_{Traut's} = n_{ApoE3} \cdot 50 = 3.616 \cdot 10^{-7} \text{ mol}$$

$$m_{Traut's} = 3.616 \cdot 10^{-7} \text{ mol} \cdot 137.63 \frac{\text{g}}{\text{mol}} = 4.98 \cdot 10^{-5} \text{ g} \hat{=} 49.8 \mu\text{g}$$

- Traut's stock solution has a concentration of $c_m = 50 \text{ mg/mL}$ in 5 mM EDTA-solution

$$50,000 \mu\text{g} = 1000 \text{ mL}$$

$$49.8 \mu\text{g} = x \rightarrow x = 0.996 \mu\text{L}$$

Calculation for ApoE3 Conjugation to Liposomes

- lipid film with a molar concentration of 20 mM; 2 mL were used for conjugation; volume of the 10 mg/mL stock solution of DSPE-PEG5k-Mal: $V_{Mal} = 0.0237 \text{ mL}$

- therefore: $m_{Mal} = 0.237 \text{ mg}$ DSPE-PEG5k-NHS in 5 mL of liposomes

$$0.237 \text{ mg} = 150 \%$$

$$x \text{ mg} = 100 \% \rightarrow x = 0.158 \text{ mg}$$

- ApoE3-solution has a concentration of $c_m = 1.99 \text{ mg/mL}$

$$1.99 \text{ mg} = 1000 \mu\text{L}$$

$$0.158 \text{ mg} = y \rightarrow y = 79.4 \mu\text{L}$$

- addition of TCEP as 10-fold molar excess:

$$n_{ApoE3} = \frac{0.158 \cdot 10^{-3} \text{ g}}{34,400 \frac{\text{g}}{\text{mol}}} = 4.59 \cdot 10^{-9} \text{ mol}$$

$$n_{TCEP} = n_{ApoE3} \cdot 10 = 4.59 \cdot 10^{-8} \text{ mol}$$

$$m_{TCEP} = 4.59 \cdot 10^{-8} \text{ mol} \cdot 286.65 \frac{\text{g}}{\text{mol}} = 1.32 \cdot 10^{-5} \text{ g} \hat{=} 13.2 \mu\text{g}$$

- TCEP-solution has a concentration of $c_m = 5 \text{ mg/mL}$

$$5000 \mu\text{g} = 1000 \mu\text{L}$$

$$13.2 \mu\text{g} = z \rightarrow z = 2.64 \mu\text{L}$$

Calculation of the conjugation efficiency of ApoE3

- calculation of the amount of ApoE3 in 1 mL according to the concentration determined by ELISA $c_m = 2.39 \mu\text{g/mL}$

$$n_{ApoE3} = \frac{0.00239 \cdot 10^{-3} \text{ g}}{34\,400 \frac{\text{g}}{\text{mol}}} = 6.95 \cdot 10^{-11} \text{ mol}$$

- calculation of the substance concentration of cholesterol according to the mass concentration of $c_m = 1.576 \text{ mg/mL}$

$$c_{n_{chol}} = \frac{1.576 \frac{\text{g}}{\text{L}}}{365.654 \frac{\text{g}}{\text{mol}}} = 4.31 \cdot 10^{-3} \frac{\text{mol}}{\text{L}}$$

- Correlation of the cholesterol concentration to the DSPE-PEG5k-Mal concentration

$$4.31 \cdot 10^{-3} \frac{\text{mol}}{\text{L}} = 40 \text{ mol}\%$$

$$x \frac{\text{mol}}{\text{L}} = 0.1 \text{ mol}\% \rightarrow x = c_{n_{Mal}} = 1.0775 \cdot 10^{-5} \frac{\text{mol}}{\text{L}}$$

- as the distribution in symmetrical liposomes has to be assumed as 50:50, the Mal-concentration has to be halved

$$c_{n_{Mal}} = \frac{1.0775 \cdot 10^{-5} \frac{\text{mol}}{\text{L}}}{2} = 5.3875 \cdot 10^{-6} \frac{\text{mol}}{\text{L}}$$

- calculation of the amount of maleimide in 1 mL:

$$n_{Mal} = 5.3875 \cdot 10^{-6} \frac{\text{mol}}{\text{L}} \cdot 1 \cdot 10^{-3} \text{ L} = 5.3875 \cdot 10^{-9} \text{ mol}$$

- calculation of the conjugation efficiency:

$$5.3875 \cdot 10^{-9} \text{ mol} = 100 \text{ mol}\%$$

$$6.95 \cdot 10^{-11} \text{ mol} = y \% \rightarrow y = 12.9 \%$$

Theoretical Calculation of ApoE3 Molecules per Liposome

- Apolipoprotein E3 is a cylindric protein
 - Protein volume according to the Peptide Property Calculator $\rightarrow V_{ApoE3} = 43\,744\text{ \AA}^3 \cong 43.744\text{ nm}^3$
- calculation of the protein volume using the following equation: $V = \pi \cdot r^2 \cdot h$
 - whereas h according to the PDB (Protein Data Base) as distance between Arg 175 (167) and Glu 212 (204) $\rightarrow h = 66.4\text{ \AA} \cong 6.64\text{ nm}$

$$r = \sqrt{\frac{43.744\text{ nm}^3}{\pi \cdot 6.64\text{ nm}}} = 1.45\text{ nm}$$

$$A = 2 \cdot \pi \cdot r \cdot (r + h) = 2 \cdot \pi \cdot 1.45\text{ nm} \cdot (1.45\text{ nm} + 6.64\text{ nm}) = 73.70\text{ nm}^2$$

- liposome as a spherical particle with $\varnothing\ 110\text{ nm}$ ($r = 55\text{ nm}$)

$$A = 4 \cdot \pi \cdot r^2 = 4 \cdot \pi \cdot 55\text{ nm}^2 = 691.15\text{ nm}^2$$

- maximum number of ApoE3 molecules per liposomal surface:

$$\frac{691.15\text{ nm}^2}{73.70\text{ nm}^2} = \sim 9\text{ molecules}$$

Calculation of ApoE3 Molecules per Liposome According to the Concentration

- calculation of the number of lipids per liposome (assumption of an unilamellar vesicle composed of phosphatidylcholine)

$$N_{tot} = 17.69 \cdot \left[\left(\frac{d}{2} \right)^2 + \left(\frac{d}{2} + 5 \right)^2 \right]$$

- whereas 5 (nm) is the thickness of the bilayer and d is the diameter of the liposome (after conjugation: 125.1 nm)

$$N_{tot} = 17.69 \cdot \left[\left(\frac{125\text{ nm}}{2} \right)^2 + \left(\frac{125\text{ nm}}{2} + 5 \right)^2 \right] = 127\,589.125$$

- calculation of the number of liposomes per milliliter:

$$N_{lipo} = \frac{M_{lipid} \cdot N_A}{N_{tot} \cdot 1000}$$

- whereas N_A is the Avogadro constant and M_{lipid} molar lipid concentration

$$N_{lipo} = \frac{10.19 \cdot 10^{-3} \frac{\text{mol}}{\text{L}} \cdot 6.02 \cdot 10^{23} \frac{1}{\text{mol}}}{127\,589.125 \cdot 1000} = 4.81 \cdot 10^{13} \frac{\text{liposomes}}{\text{mL}}$$

$$N_{lipo} = 48.1 \cdot 10^{12} \frac{\text{liposomes}}{\text{mL}} = 48.1 \text{ billion liposomes/mL}$$

- calculation of the amount of ApoE3 with $c_m = 2.39 \mu\text{g/mL} \hat{=} 0.00239 \text{ mg/mL}$

$$n = \frac{0.00239 \text{ g} \cdot 10^{-3}}{34\,400 \frac{\text{g}}{\text{mol}}} = 6,95 \cdot 10^{-11} \text{ mol referred to 1 mL}$$

- calculation of the number of ApoE3 molecules in 1 mL:

$$N_{ApoE3} = n \cdot N_A = 6,95 \cdot 10^{-11} \text{ mol} \cdot 6.02 \cdot 10^{23} \frac{1}{\text{mol}}$$

$$N_{ApoE3} = 4.1825 \cdot 10^{13} \text{ molecules/mL}$$

- calculation of ApoE3 molecules per liposome:

$$\frac{N_{ApoE3}}{N_{lipo}} = \frac{4.1825 \cdot 10^{13}}{48.1 \cdot 10^{12}} = 0.8695 \text{ ApoE3/liposome}$$

Fragmented Fractionated Heparin

Calculation for ffHep Conjugation to Liposomes

DSPE-PEG1k-NH₂

- lipid film with a molar concentration of 20 mM; 1 mL were used for conjugation; volume of the 10 mg/mL stock solution of DSPE-PEG1k-NH₂ $V_{NH_2} = 0.1819 \text{ mL}$

- therefore: $m_{NH_2} = 1.819 \text{ mg}$ DSPE-PEG5k-NHS in 1 mL of liposomes;

$$m_{NH_2} = 9.095 \text{ mg DSPE-PEG5k-NHS in 5 mL of liposomes}$$

- required mass of ffHep using a mass ratio of 1:3 for conjugation $\rightarrow m_{ffHep} = 27.285 \text{ mg}$

- calculation of the required amount of NaCNBH₃ (CN) using 50-fold molar excess

$$n_{NH_2} = \frac{9.095 \cdot 10^{-3} \text{ g}}{1819 \frac{\text{g}}{\text{mol}}} = 5 \cdot 10^{-6} \text{ mol}$$

$$n_{CN} = n_{NH_2} \cdot 50 = 2.5 \cdot 10^{-4} \text{ mol}$$

- CN-solution has a concentration of $c_n = 6.4 \text{ mol/L}$ in PBS

$$6.4 \text{ mol} = 1000 \text{ mL}$$

$$2.5 \cdot 10^{-4} \text{ mol} = x \rightarrow x = 0.039 \text{ mL} \hat{=} 39.1 \mu\text{L}$$

- Calculation of the required amount of Succinic anhydride (SA) using a 20-fold molar excess

$$n_{SA} = n_{NH_2} \cdot 20 = 1 \cdot 10^{-4} \text{ mol}$$

- SA-solution has a concentration of $c_n = 0.5 \text{ mol/L}$ in 1,4-Dioxan

$$0.5 \text{ mol} = 1000 \text{ mL}$$

$$1 \cdot 10^{-4} \text{ mol} = y \rightarrow y = 0.2 \text{ mL} \hat{=} 200 \mu\text{L}$$

DPPE

- lipid film with a molar concentration of 20 mM; 1 mL were used for conjugation; volume of the 3 mg/mL stock solution of DPPE $V_{DPPE} = 0.2307 \text{ mL}$

- therefore: $m_{DPPE} = 0.6921 \text{ mg}$ DPPE in 1 mL of liposomes; $m_{DPPE} = 3.4605 \text{ mg}$ DSPE-PEG5k-NHS in 5 mL of liposomes

- required mass of ffHep using a mass ratio of 1:3 for conjugation $\rightarrow m_{ffHep} = 10.3815 \text{ mg}$

- calculation of the required amount of NaCNBH_3 (CN) using 50-fold molar excess

$$n_{DPPE} = \frac{3.4605 \cdot 10^{-3} \text{ g}}{691.96 \frac{\text{g}}{\text{mol}}} = 5 \cdot 10^{-6} \text{ mol}$$

$$n_{CN} = n_{DPPE} \cdot 50 = 2.5 \cdot 10^{-4} \text{ mol}$$

- CN-solution has a concentration of $c_n = 6.4 \text{ mol/L}$ in PBS

$$6.4 \text{ mol} = 1000 \text{ mL}$$

$$2.5 \cdot 10^{-4} \text{ mol} = x \rightarrow x = 0.039 \text{ mL} \hat{=} 39.1 \mu\text{L}$$

- calculation of the required amount of Succinic anhydride (SA) using a 20-fold molar excess

$$n_{SA} = n_{DPPE} \cdot 20 = 1 \cdot 10^{-4} \text{ mol}$$

- SA-solution has a concentration of $c_n = 0.5 \text{ mol/L}$ in 1,4-Dioxan

$$0.5 \text{ mol} = 1000 \text{ mL}$$

$$1 \cdot 10^{-4} \text{ mol} = y \rightarrow y = 0.2 \text{ mL} \hat{=} 200 \mu\text{L}$$

DOPS

- lipid film with a molar concentration of 20 mM; 1 mL were used for conjugation; volume of the 10 mg/mL stock solution of DOPS $V_{DOPS} = 0.0810 \text{ mL}$

- therefore: $m_{DOPS} = 0.81 \text{ mg}$ DSPE-PEG5k-NHS in 1 mL of liposomes; $m_{DOPS} = 4.05 \text{ mg}$ DOPS in 5 mL of liposomes

- required mass of ffHep using a mass ratio of 1:3 for conjugation $\rightarrow m_{ffHep} = 12.15 \text{ mg}$

- calculation of the required amount of NaCNBH_3 (CN) using 50-fold molar excess

$$n_{DOPS} = \frac{4.05 \cdot 10^{-3} g}{810.83 \frac{g}{mol}} = 5 \cdot 10^{-6} mol$$

$$n_{CN} = n_{DOPS} \cdot 50 = 2.5 \cdot 10^{-4} mol$$

- CN-solution has a concentration of $c_n = 6.4 mol/L$ in PBS

$$6.4 mol = 1000 mL$$

$$2.5 \cdot 10^{-4} mol = x \rightarrow x = 0.039 mL \hat{=} 39.1 \mu L$$

- calculation of the required amount of Succinic anhydride (SA) using a 20-fold molar excess

$$n_{SA} = n_{DOPS} \cdot 20 = 1 \cdot 10^{-4} mol$$

- SA-solution has a concentration of $c_n = 0.5 mol/L$ in 1,4-Dioxan

$$0.5 mol = 1000 mL$$

$$1 \cdot 10^{-4} mol = y \rightarrow y = 0.2 mL \hat{=} 200 \mu L$$

A9 Buffers, Lipid Films and Dilutions

Buffers

The following equations are used as a basis for calculating the weigh-in of the substances for the production of lipid films:

$$c_n = \frac{n}{V}$$

- c_n is the concentration [mol/L]
- n is the amount of substance [mol]
- V is the volume [L]

$$n = \frac{m}{M_W}$$

- n is the amount of substance [mol]
- m is the mass of a substance [g]
- M_W is the molecular weight of the substance [g/mol]

$$c_n = \frac{c_m}{M_W}$$

- c_m is the massconcentration [g/L]
- c_n is the concentration [mol/L]
- M_W is the molecular weight of the substance [g/mol]

Phosphate Buffer

Calculation of the base and acid concentration using the Henderson-Hasselbalch equation:

$$pH = pk_a + \log \frac{[A^-]}{[HA]}$$

Table A 9.1: Weigh-ins for the preparation of the phosphate buffer.

Calculation for 500 mL; 10 mM with pH 7.4	
1. Acid (Sodium dihydrogen phosphate)	2. Base (Disodium hydrogen phosphate)
$M_W = 119.98 \frac{g}{mol}$	$M_W = 141.96 \frac{g}{mol}$
$n_{Base} = 3.92 \cdot 10^{-3} \frac{mol}{L} \times 0.5 L$	$n_{Base} = 6.08 \cdot 10^{-3} \frac{mol}{L} \times 0.5 L$
$n_{Base} = 1.96 \cdot 10^{-3} mol$	$n_{Base} = 3.04 \cdot 10^{-3} mol$
$m_{Base} = 1.96 \cdot 10^{-3} mol \times 119.98 \frac{g}{mol}$	$m_{Base} = 3.04 \cdot 10^{-3} mol \times 141.96 \frac{g}{mol}$
$m_{Base} = 0.2352 g$	$m_{Base} = 0.4316 g$

Histidine – Sodium chloride Buffer

Table A 9.2: Weigh-ins for the preparation of the histidine-sodium chloride buffer.

Calculation for 1000 mL; 10 mM, 0.3 osmol/L with pH 7.4	
1. L-Histidine	2. Sodium chloride
$M_W = 155.16 \frac{g}{mol}$	Sodium chloride dissociates in water
$c_m = 0.01 \frac{mol}{L} \times 155.16 \frac{g}{mol}$	into two osmotically active particles:
$c_m = 1.5516 g/L$	$c_{osmol_{soll}} = \frac{0.29 \frac{osmol}{L}}{2} = 0.145 \frac{osmol}{L}$
$m_{His} = 1.5516 g \text{ for } 1 L$	$c_{osmol_{soll}} = 0.145 \frac{osmol}{L}$
<u>Osmolarity:</u>	$M_W = 58.44 \frac{g}{mol}$
$c_{osmol_{soll}} = 0.3 osmol/L$	$c_m = 0.145 \frac{mol}{L} \times 58.44 L$
L-Histidine does not dissociate in water	$c_m = 8.4738 g/L$
and therefore only has one osmotically	$m_{NaCl} = 8.4738 g \text{ for } 1 L$
active particle:	
$0.01 \frac{mol}{L} = 0.01 osmol /L$	
This concentration is subtracted from the desired osmolarity of 0.3 osmol/L. This results in an osmotic concentration of 0.29 osmol/L, which has to be adjusted by adding NaCl.	

Tris Buffer

Table A 9.3: Initial weight for the preparation of Tris buffer.

Calculation for 200 mL; 0.10 M with pH 8.0
$M_W = 121.1 \frac{g}{mol}$
$c_m = 0.1 \frac{mol}{L} \times 121.1 \frac{g}{mol}$
$c_m = 12.11 \frac{g}{L}$
For 200 mL:
$m = 2.422 g$

Lipid Stock Suspension for PFC/W Nanoemulsions

The following information applies to all preparations of lipid stock solutions:

Volume: $V = 3 \text{ mL}$

Concentration: $c_{n_{\text{sol}}} = 150 \text{ mM}$

Table A 9.4: Summary of all molecular weights of the used lipids.

Substance	Molecular weight [g/mol]
E80	762.00
DMPC	677.93
DPPC	734.04
DSPC	790.15
DPPG	744.95
DPPE	691.96
DPPA	648.89
DOPS	810.03
LiRh DHPE	1333.81
DSPE-PEG1k-RB	2258.00
Cholesterol	386.65

Exemplary calculation for a 3 mL of a 150 mM lipid film containing E80:Chol with 95:5 mol%:

Table A 9.5: Exemplary calculation for the initial weights of the lipids for the thin film preparation.

Calculation for 3 mL; 150 mM	
1. E80	2. Cholesterol
$c_{n_{\text{E80}}} = 150 \text{ mM} \times 0.95$	$c_{n_{\text{Chol}}} = 150 \text{ mM} \times 0.05$
$c_{n_{\text{E80}}} = 142.5 \text{ mM}$	$c_{n_{\text{Chol}}} = 7.5 \text{ mM}$
$M_{W_{\text{E80}}} = 762.00 \frac{\text{g}}{\text{mol}}$	$M_{W_{\text{Chol}}} = 386.65 \frac{\text{g}}{\text{mol}}$
$n_{\text{E80}} = 142.5 \cdot 10^{-3} \frac{\text{mol}}{\text{L}} \times 0.003 \text{ L}$	$n_{\text{Chol}} = 7.5 \cdot 10^{-3} \frac{\text{mol}}{\text{L}} \times 0.003 \text{ L}$
$n_{\text{E80}} = 4.275 \cdot 10^{-4} \text{ mol}$	$n_{\text{Chol}} = 2.25 \cdot 10^{-5} \text{ mol}$
$m_{\text{E80}} = 4.275 \cdot 10^{-4} \text{ mol} \times 762.00 \frac{\text{g}}{\text{mol}}$	$m_{\text{Chol}} = 2.25 \cdot 10^{-5} \text{ mol} \times 386.65 \frac{\text{g}}{\text{mol}}$
$m_{\text{E80}} = 0.32576 \text{ g}$	$m_{\text{Chol}} = 0.00822 \text{ g}$

Table A 9.6: Summary of all initial weights of the lipids for various thin film preparations.

Composition PL:Chol:X	Molar ratio [mol%]	$m_{PL}[g]$	$m_{Chol}[g]$	$m_X[g]$
E80:Chol	95:5	0.32586	0.00870	
	90:10	0.30861	0.01740	
	80:20	0.27432	0.03480	
	70:30	0.24003	0.05220	
	60:40	0.20574	0.06960	
E80:Chol:LiRh	59.4:39.6:01	0.10184	0.03445	0.00300
DMPC:Chol	60:40	0.18304	0.06960	
DSPC:Chol	60:40	0.21334	0.06960	
DPPA:Chol	60:40	0.17520	0.06960	
DPPE:Chol	60:40	0.18683	0.06960	
DPPG:Chol	60:40	0.20114	0.06960	
DPPC:Chol	70:30	0.23122	0.05220	
	60:40	0.19819	0.06960	
DPPC:Chol:DOPS	65:30:5	0.21471	0.05220	0.01823
DPPC:Chol:DSPE-PEG1k-RB	69.9:30:01	0.23089	0.05220	0.00060

Lipid Stock Suspensions for W/PFC Nanoemulsion

The following information applies to all preparations of lipid stock solutions:

Volume: $V = 600 \mu L$

Concentration: $c_{n_{soll}} = 300 mM$

Table A 9.7: Initial weights of the lipids for the thin film preparation.

Composition PL:Chol:X	Molar ratio [mol%]	$m_{PL}[g]$	$m_{Chol}[g]$	$m_X[g]$
DMPC:Chol	60:40	0.07322	0.02784	
DMPC:Chol:DOPS	55:40:5	0.06712	0.02784	0.00729

Dilution of Phospholipid Stock Suspension for PFC/W Nanoemulsion Preparation

The following equation is used as a basis for calculating the dilution of the lipid stock suspension for the preparation of the PFC/W nanoemulsion with different total lipid concentrations:

$$c_1 \cdot V_1 = c_2 \cdot V_2$$

- c_1 is the concentration of the first solution/suspension [mol/L]
- V_1 is the volume of the first solution/suspension [L]
- c_2 is the concentration of the second solution/suspension [mol/L]
- V_2 is the volume of the second solution/suspension [L]

Table A 9.8: Volumes of the lipid stock suspension and buffer for the preparation of the dilutions.

Concentration [mM]	Volume of 150 mM Stock Suspension [mL]	Volume of Buffer [mL]
2.5	0.25	14.75
5	0.5	14.5
7.5	0.75	14.25
10	1	14
15	1.5	13.5

Lipid Stock Solutions

All stock solutions, except for DPPE and DOPS, are produced based on Ethanol 99.5 % Ph. Eur. The stock solutions of DPPE and DOPS are prepared based on chloroform (unstabilized).

Table A 9.9: Initial weights of the liposome components for their organic stock solutions.

Substance	Molecular weight [g/mol]	Concentration [mg/mL]	Volume [mL]	Mass [mg]
DPPC	734.04	30	25	750
DOPS	810.33	10	5	50
DPPE	691.96	3	5	15
DPSE-PEG1k-NH ₂	1819.00	10	5	50
DSPE-PEG2k	2780.38	30	25	750
DSPE-PEG5k-Mal	5937.25	10	5	50
DSPE-PEG5k-NHS	5890.00	10	5	50
DSPE-PEG5k-Glu	5981.00	10	5	50
DSPE-PEG5k-c(RGD)	6482.00	10	5	50
Cholesterol	386.65	10	25	250
DiD	933.68	15	1	15

Lipid Films for Symmetric Liposomes

Volume [mL] of the organic stock solution of each component for a total liposomal volume of 5 mL with a total lipid concentration of 20 mM.

Table A 9.10: Volume of organic stock solutions for the various liposomal formulations.

Substance	Control	mPEG	GLU	NHS**	APG	Mal	ApoE3***	c(RGD)	NH ₂ ****	DPPE****	DOPS****
DPPC	1.4656	1.3433	1.2210	1.2210	1.2210	1.3408	1.3408	1.2210	1.3457	1.3457	1.3457
DPPE*										1.1533	
DOPS*											0.4052
DSPE-PEG2k		0.4634	0.4634	0.4634	0.4634	0.4634	0.4634	0.4634			
DPSE-PEG1k-NH ₂									0.9095		
DSPE-PEG5k-Mal						0.0594	0.0594				
DSPE-PEG5k-NHS				2.9450	2.9450						
DSPE-PEG5k-Glu			2.9905								
DSPE-PEG5k-c(RGD)								3.2410			
Cholesterol	1.5466	1.5466	1.5466	1.5466	1.5466	1.5466	1.5466	1.5466	1.5466	1.5466	1.5466
DiD	0.0062	0.0062	0.0062	0.0062	0.0062	0.0062	0.0062	0.0062			

* Stock solutions based on chloroform instead of ethanol

** NHS liposomes serve as precursors for the post-conjugation of 4-Amino- β -glucopyranoside for the preparation of APG liposomes

*** Mal 0.1 mol% liposomes serve as precursors for the post-conjugation of Apolipoprotein E3 for the preparation of ApoE3 liposomes

**** NH₂ or DPPE or DOPS liposomes serve as precursors for the post-conjugation of fractionated fHep for the preparation of fHep-modified liposomes

Dilutions for Uptake and Cytotoxicity Testing

A volume of 500 μL is prepared for each dilution.

Table A 9.11: Volumes of the liposomal suspension and culture medium for the preparation of the dilutions.

Type of liposomes	Initial concentration of liposomes [mM]	Diluted concentration [mM]	Final concentration in the well [μM]	Volume of liposomal suspension [μL]	Volume of DMEM [μL]
Control	11.74	10	1000	425.9	74.1
		5	500	212.9	287.1
		1	100	42.6	457.4
mPEG	11.28	10	1000	443.3	56.7
		5	500	221.6	278.4
		1	100	44.3	455.7
GLU	14.20	10	1000	352.1	147.9
		5	500	176.1	232.9
		1	100	35.2	646.8
NHS	11.46	10	1000	436.3	63.7
		5	500	218.2	281.8
		1	100	43.6	456.4

APG	12.81	10	1000	390.3	109.7
		5	500	195.2	304.8
		1	100	39.0	461.0
Mal	11.46	10	1000	436.3	63.7
		5	500	218.2	281.8
		1	100	43.6	456.4
ApoE3	10.19	10	1000	490.7	9.3
		5	500	245.3	254.7
		1	100	49.1	450.9
c(RGD)	11.49	10	1000	435.2	64.8
		5	500	217.2	282.4
		1	100	43.5	465.5

A10 Calibration Curves

The following graphs are examples of the calibration curves for various single experiments of those methods.

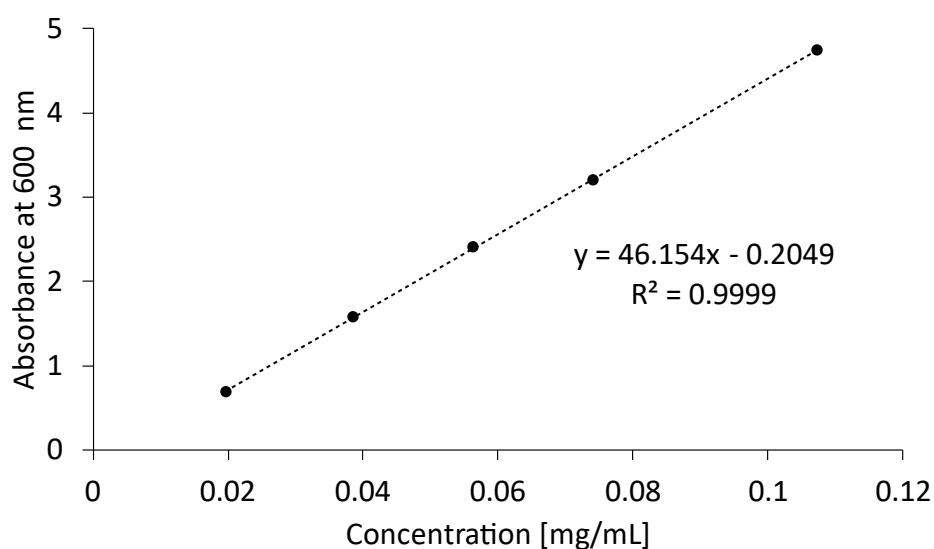


Figure A 10.1: Calibration curve of the LabAssay™ Cholesterol Kit for the calculation of the cholesterol concentration in the samples.

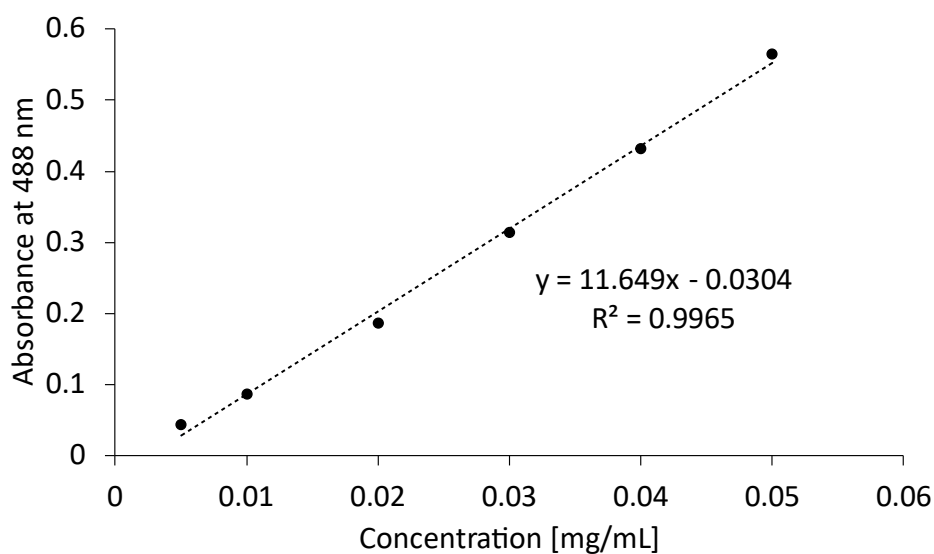


Figure A 10.2: Calibration curve of the color complex of DPPC and ammonium ferrothiocyanate in chloroform according to the Stewart Assay.

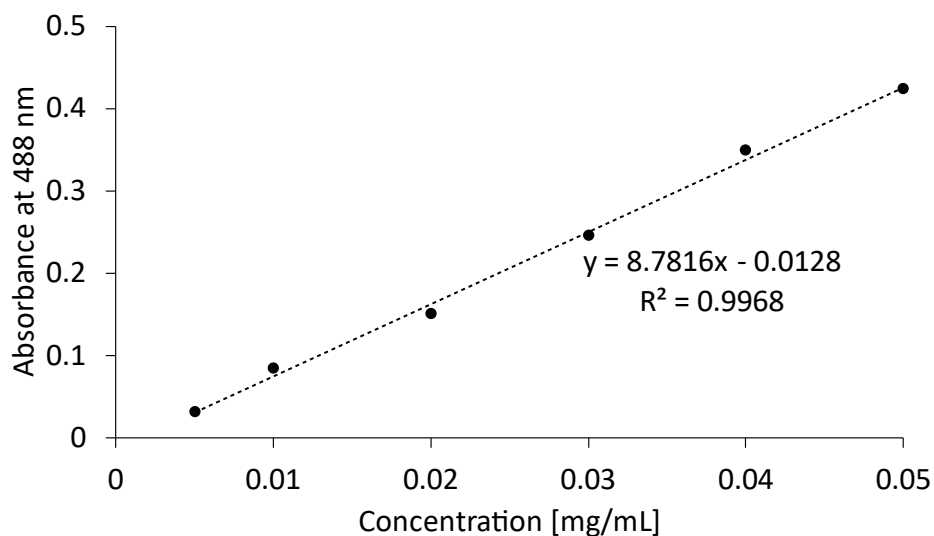


Figure A 10.3: Calibration curve of the color complex of DPPC:DMPC (70:60 mol%) and ammonium ferrothiocyanate in chloroform according to the Stewart Assay.

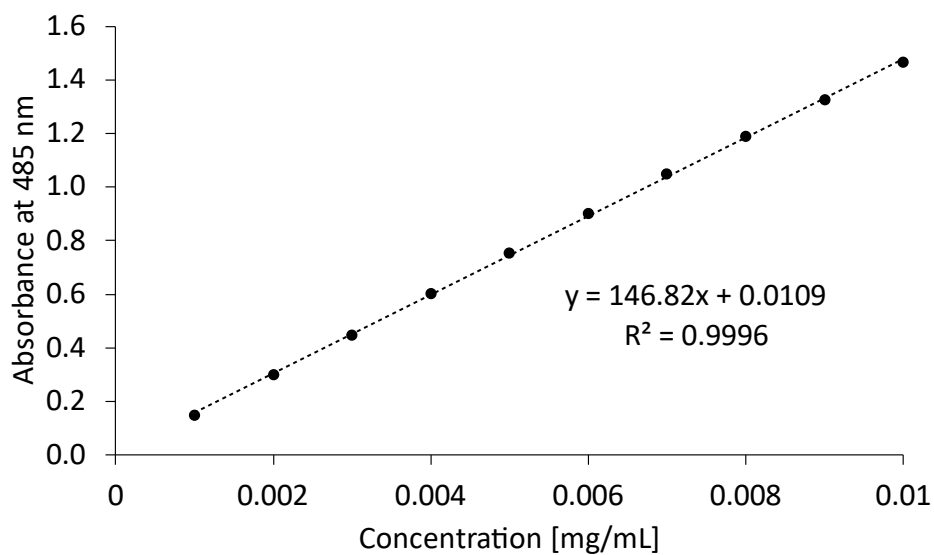


Figure A 10.4: Calibration curve of fluorescein sodium in His/NaCl buffer pH 7.4 for quantification of FluNa and the subsequent determination of the encapsulation efficiency of asymmetric liposomes.

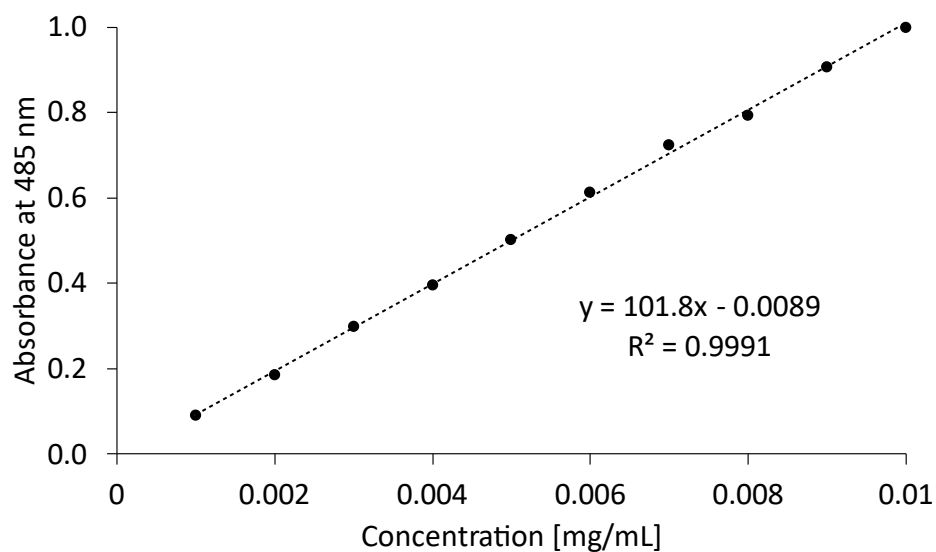


Figure A 10.5: Calibration curve of fluorescein sodium in Triton X-100 2 % (v/v) for quantification of FluNa and the subsequent determination of the encapsulation efficiency of asymmetric liposomes.

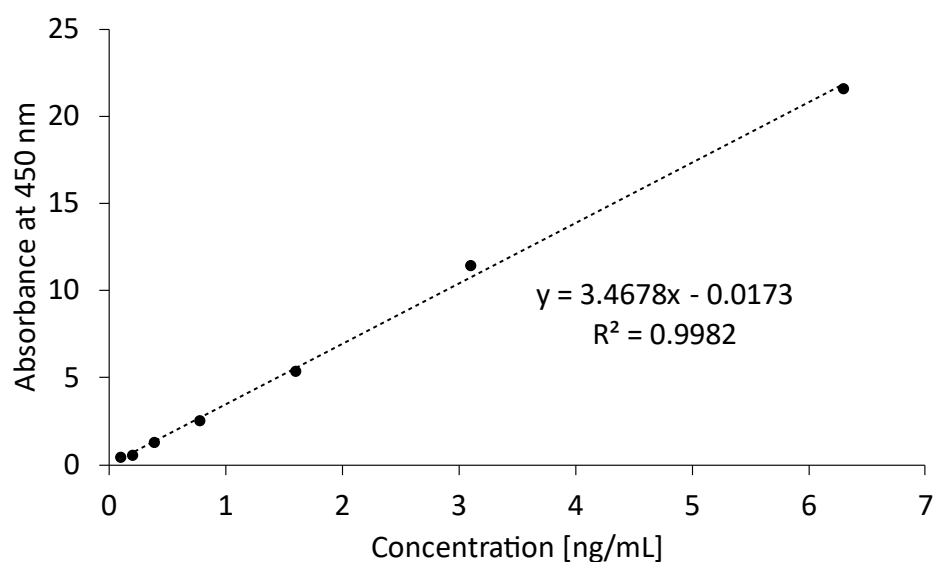


Figure A 10.6: Calibration curve of Apolipoprotein E of the Human Apo E ELISA^{BASIC} Kit for the calculation of the Apo E3 concentration on the liposomal surface.

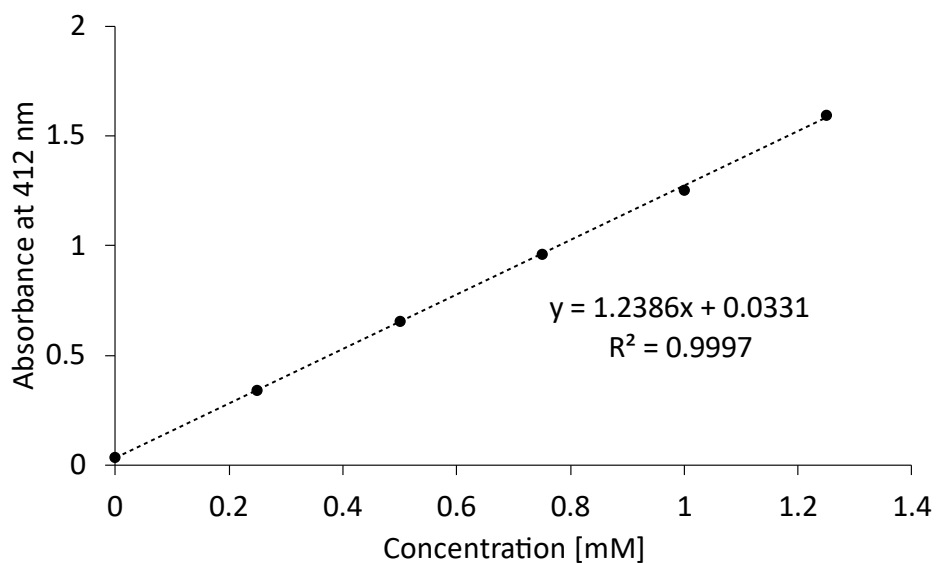


Figure A 10.7: Calibration curve of cysteine monohydrate in Tris buffer pH 8.0 for calculation of sulfhydryl-groups according to the Ellman's test.

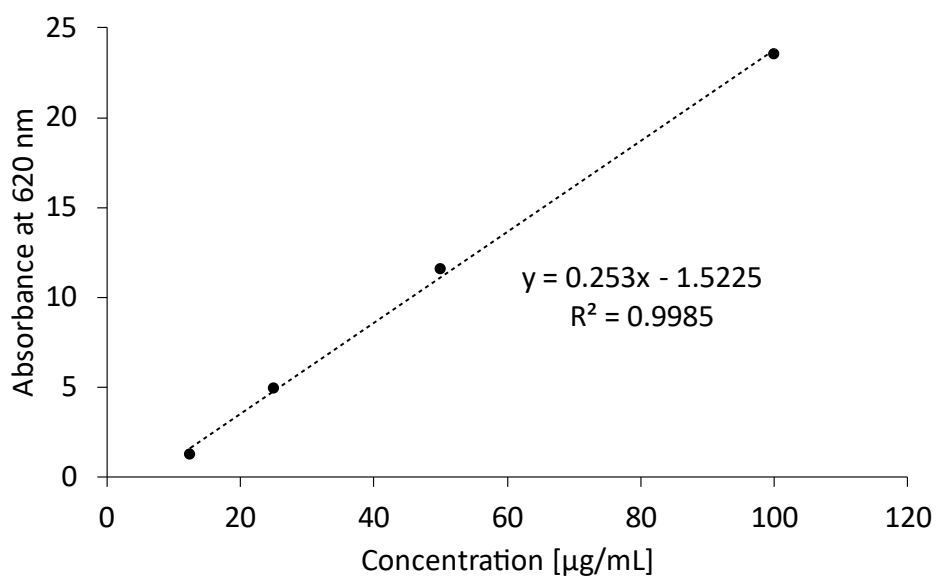


Figure A 10.8: Calibration curve of fragmented heparin in PBS pH 7.4 of the Alcian Blue Assay for the calculation of heparin of the liposomal surface.

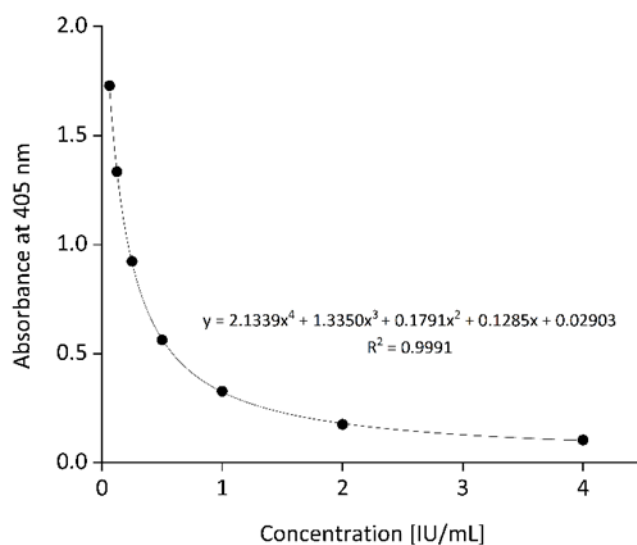


Figure A 10.9: Calibration curve of the heparin standard for the Factor Xa Assay for the calculation of the heparin activity.

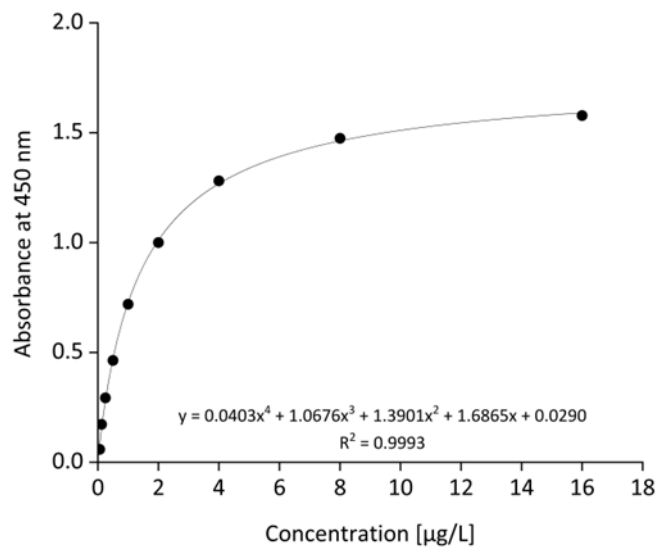


Figure A 10.10: Calibration curve of pooled Zymosan-activated plasma for the calculation of the complement factor C3a in plasma using an ELISA.

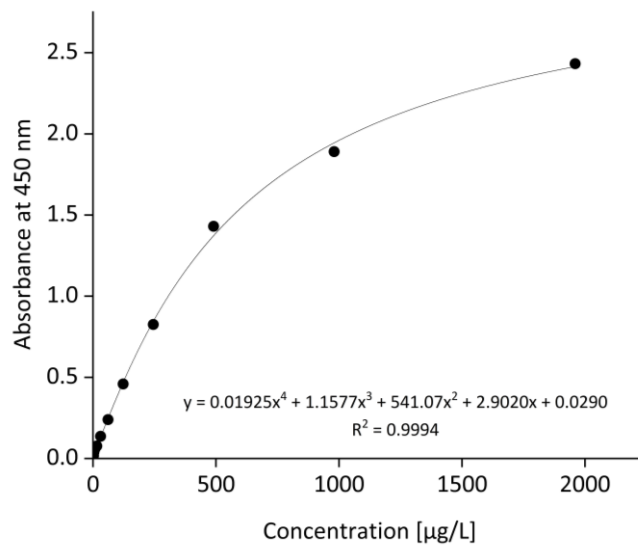


Figure A 10.11:Calibration curve of pooled Zymosan-activated plasma for the calculation of the complement factor C5b-9 in plasma using an ELISA.

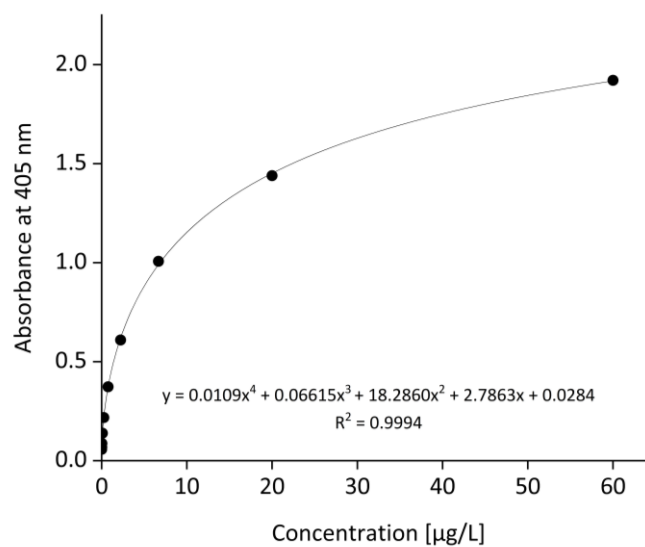


Figure A 10.12:Calibration curve of the complement factor #1 for the calculation of the thrombin-antithrombin concentration in plasma using an ELISA.

Abbreviation List

Abbreviation	Description
AB	Alcian Blue 8 GS
ABC effect	Accelerated blood clearance
ABC transporter	ATP binding cassette transporter
AF	Ammonium ferro thiocyanate solution
AMT	Adsorptive-mediated transporter
AP	Alternative pathway
API	Active pharmaceutical ingredient
ApoE3	Apolipoprotein E3
APS	Ammonium peroxydisulfate
BBB	Blood-brain barrier
BBTB	Blood-brain tumor barrier
BCEC	Brain capillary endothelial cell
bEnd.3	Endothelial cells
BM	Basement membrane
BSA	Bovine serum albumin
Chol	Cholesterol
CMC	Critical micelle concentration
CMT	Carrier-mediated transporters
CNS	Central nervous system
CP	Classical pathway
CPP	Cell penetrating peptide
DAMPs	Damage-associated molecular patterns
DAOS	<i>N</i> -Ethyl- <i>N</i> -(2-hydroxy-3-sulfopropyl)-3,5-dimethoxyanilin

DCR	Derived count rate
ddH ₂ O	Double distilled water
DiD	1,1-Dioctadecyl-3,3,3,3-tetramethylindodicarbocyanine
DLS	Dynamic light scattering
DMEM	<i>Dulbecco's Modified Eagle Medium</i>
DMF	Dimethylformamide
DMPC	1,2-Dimyristoyl- <i>sn</i> -glycerol-3-phosphocholine
DPBS	Dulbecco's phosphate-buffered saline
DPPA	1,2-Dipalmitoyl- <i>sn</i> -glycero-3-phosphate
DPPC	1,2-Dipalmitoyl- <i>sn</i> -glycerol-3-phosphocholine
DPPE	1,2-Dipalmitoyl- <i>sn</i> -glycero-3-phosphoethanolamin
DPPG-Na	1,2-Dipalmitoyl- <i>sn</i> -glycero-3-phosphoglycerol
DOPS	1,2-Dioctadecenoyl- <i>sn</i> -glycero-3-phosphatidylserine
DSPC	1,2-Distearoyl- <i>sn</i> -glycerol-3-phosphocholine
DSPE-PEG ₁₀₀₀ -RB	1,2-Distearoyl- <i>sn</i> -glycero-3-phosphoethanolamine- <i>N</i> -(poly(ethylene glycol))-Rhodamine B
DSPE-PEG ₂₀₀₀	1,2-Distearoyl- <i>sn</i> -glycero-3-phosphoethanolamine- <i>N</i> -[(polyethylene glycol)]
DSPE-PEG ₂₀₀₀ -NH ₂	1,2-Distearoyl- <i>sn</i> -glycero-3-phosphoethanolamine- <i>N</i> -[amino(polyethylene glycol)]
DSPE-PEG ₅₀₀₀ -c(RGD)	1,2-Distearoyl- <i>sn</i> -glycero-3-phosphoethanolamine- <i>N</i> -[amino(polyethylene glycol)] – cyclic RGD
DSPE-PEG ₅₀₀₀ -Glu	1,2-Distearoyl- <i>sn</i> -glycero-3-phosphoethanolamine- <i>N</i> -(polyethylene glycol) -Glucose
DSPE-PEG ₅₀₀₀ -Mal	1,2-Distearoyl- <i>sn</i> -glycero-3-phosphoethanolamine- <i>N</i> -[maleimide(polyethylene glycol)]
DSPE-PEG ₅₀₀₀ -NHS	1,2-Distearoyl- <i>sn</i> -glycero-3-phosphoethanolamine- <i>N</i> -[succinimidyl(polyethylene glycol)]
DTAC	Dodecyl trimethyl ammonium chloride
E80	Egg yolk phospholipid with 80 % phosphatidylcholine
EDTA	Ethylenediamine tetraacetic acid
EE	Encapsulation efficiency
Ellman's reagent	5,5'-Dithiobis-(2-nitrobenzoic acid)
EPR	Enhanced permeability and retention
F1 – F9	Fraction 1 to 9
FACS	Fluorescence Activated Cell Sorting

FBS	Fetal bovine serum
fHep	Fragmented heparin
ffHep	Fragmented fractionated heparin
FluNa	Fluorescein sodium
Glu	Glucose
GLU	4-Aminophenyl-D-glucopyranoside
GLUT1	Glucose transporter 1
GLUTs	Glucose transporters
GUV	Giant unilamellar vesicle
HCl	Hydrochloric acid
LiRh DHPE	Lissamine™ Rhodamine B 1,2-Dihexadecanoyl-sn-Glycero-3-Phosphoethanolamine, Triethylammonium Salt
LLOQ	Lower limit of quantification
LNP	Lipid nanoparticle
LP	Lectin pathway
LRP1	Low density lipoprotein receptor-related protein 1
LUV	Large unilamellar vesicle
Mal	Maleimide
MASPs	Mannose-binding lectin-associated serine proteases
MBL	Mannose-binding lectins
MFI	Mean fluorescent intensity
MLV	Multilamellar vesicle
mol%	Mol percent
MRI	Magnetic resonance imaging
MVV	Multivesicular vesicle
MWCO	Molecular weight cut off
NaOH	Sodium hydroxide
2-NBDG	2-Deoxy-2-[(7-nitro-2,1,3-benzoxadiazol-4-yl)amino]-D-glucose
NEAA	Nonessential amino acids
OLV	Oligolamellar vesicle
O/W	Oil-in-water
PA	Phosphate
PAGE	Polyacrylamide gel electrophoresis

PAMPs	Pathogen-associated molecular patterns
PBS	Phosphate buffered saline
PC	Phosphatidylcholine
Pdl	Polydispersity index
PE	Phosphatidylethanolamine
PE-mAb	Phycoerythrin coupled monoclonal antibody
PEG	Polyethylene glycol
PFC	Perfluorocarbon
PFDC	Perfluoro-1,3-dimethylcyclohexan
PFC/W	Perfluorocarbon-in-water
PFD	Perfluorodecalin
PFH	Perfluoroheptan
PFOB	Perfluorooctoylbromid
PG	Phosphatidylglycerol
PI	Phosphatidylinositol
PL	Phospholipid
PPHP	Perfluoroperhydrophenanthrene
PRRs	Pattern recognition receptors
PS	Polystyrene
PVA	Polyvinyl alcohol
RI	Refractive index
RMT	Receptor-mediated transporters
RR	Recovery rate
SD	Standard deviation
SDS	Sodium dodecyl sulfate
SEC	Size exclusion chromatography
SLC	Solute carriers
SM	Sphingomyelin
SUV	Small unilamellar vesicle
TAT	Thrombin-Antithrombin
TCEP	Tris-(2-carboxyethyl)-phosphine hydrochloride
TEER	Transendothelial electrical resistance

TEMED	<i>N,N,N',N'</i> -Tetramethylethylenediamine
TJ	Tight junction
T _m	Transition temperature
TMB	3,3',5,5'-Tetramethylbenzidine
Traut's reagent	2-Iminothiolan
U-87 MG	Glioblastoma astrocytoma cells
UFH	Unfractionated Heparin
UV	Ultraviolet
VIS	Visible
v/v	Volume per volume
W/O	Water-in-oil
w/v	Weight per volume
W/PFC	Water-in-perfluorocarbon
Z-Ave	Z-Average
ZP	Zeta potential

List of Symbols

Latin Letters

Symbol	Unit	Description
A	$[-]$	Baseline of the autocorrelation function
A	$[m^2]$	Surface Area
A_{ApoE3}	$[nm^2]$	Volume of an ApoE3 molecule
A_i	$[m^2]$	Cross-sectional area
$A_{Liposomes}$	$[nm^2]$	Volume of a liposome
A_{Test}	$[-]$	Absorbance Test Sample
$A_{Total\ Blank}$	$[-]$	Absorbance Total Blank
B	$[-]$	Amplitude of the autocorrelation function
CC	$[1/mL]$	Cell count per mL
c_L	$[mM]$	Total lipid concentration
c_m	$[g/L]$	Mass concentration
c_n	$[mol/L] = [M]$	Concentration
D	$[m^2/s]$	Diffusion coefficient
d	$[cm]$	Thickness of the cuvette
d	$[nm]$	Diameter of a liposome
D	$[nm]$	Z-averaged particle size
D_i	$[m]$	Characteristic length of the channel
DF	$[-]$	Dilution factor
EE	$[\%]$	Encapsulation efficiency
E_{kin}	$[kJ]$	Kinetic energy
E_γ	$[kg \cdot m^2/s^2]$	Energy through interfacial tension

F	[N]	Power
FI	[/]	Fluorescence Intensity
$f(ka)$	[/]	Henry's function
g	[m/s ²]	Gravitational acceleration
$g(\tau)$	[/]	Autocorrelation function
h	[m]	Height of the cylindrical protein
I	[a. u.]	Intensity (absorbance)
$I(q)$	[a. u.]	Intensity (absorbance) as a function of the scattering vector
I_0	[a. u.]	Initial intensity
I_t	[/]	Mean fluorescence intensity at a certain time point
k	[/]	Constant defined as saturation half-time $t_{1/2}$ multiplied with $\ln(2)$
k_b	[kg · m ² /s ²]	Boltzmann constant
m	[g]	Mass
M	[g/mol]	Molar mass of the entire molecule
M_l	[g/mol]	Molar mass of the lipophilic part
M_w	[g/mol]	Molecular weight
n	[mol]	Amount of substance
n	[/]	Quantity
N_A	[1/mol]	Avogadro constant
N_{ApoE3}	[1/mL]	Number of ApoE3 molecules per mL
$N_{Liposomes}$	[1/mL]	Number of liposomes per mL
N_{tot}	[1/liposome]	Total number of lipids per liposome
p	[/]	Significance level
P	[bar]	Pressure
pH	[/]	Potential hydrogenii
pk_a	[/]	Acid dissociation constant
q	[1/nm]	Scatter vector
Q	[m ³ /s]	Volume flow
r_h	[nm]	Hydrodynamic radius
R	[J/mol · K]	Ideal gas constant
Re_i	[/]	Reynolds number at a specific cross-section

RR	[%]	Recovery rate
SV	[mL]	Sample volume
t	[s]	Time
t	[h]	Time
Δt	[s]	Duration of outflow
$t_{1/2}$	[h]	Saturation half-time
T	[K]	Temperature
T_m	[°C]	Phase transition temperature
TV	[mL]	Total assay volume
\bar{u}_i	[m/s]	Mean flow velocity
U_E	[$\mu\text{m} \cdot \text{cm}/V \cdot \text{s}$]	Electrophoretic mobility
V	[L] = [dm^3]	(Stroke) Volume
V_D	[% (v/v)]	Volume of the dispersed phase
x_{chol}	[mol%]	Molar percentage of cholesterol
$Z - Ave$	[nm]	Diameter based on total average value

Greek Letters

Symbol	Unit	Description
Γ	[mol/m ²]	Gibbs adsorption isotherm
ρ	[kg/m ³]	Density
ε	[$(\frac{\text{mL}}{\text{mol}})(\frac{1}{\text{cm}})$]	Millimolar extinction coefficient
ε	[F/m]	Dielectric constant
η	[Pa · s]	Dynamic viscosity
ν	[m ² /s]	Kinetic viscosity
σ	[N/m]	Interfacial energy
γ	[mN/m]	Interfacial tension
λ	[nm]	Wavelength
τ	[s]	Time interval
ζ	[mV]	Zeta potential

List of Publications and Conferences

Scientific Publications

Lubitz LJ, Rieger H, Leneweit G – Laminar and turbulent flow effects in high-pressure homogenization of liposomes and perfluorocarbon nanoemulsion – *Scientific Reports* (2024); doi: 10.1038/s41598-024-78550-9.

Lubitz LJ, Rieger H, Leneweit G – Emulsifying mechanisms of phospholipids in high-pressure homogenization of perfluorocarbon nanoemulsions – under revision at *Soft Matter* (2024); doi: 10.1039/D4SM00828F.

Lubitz LJ, Haffner MP, Rieger H, Leneweit G – Elevated cellular uptake of succinimide- and glucose-modified liposomes for blood-brain barrier transfer and glioblastoma therapy – *Biomedicines* (2024); doi: 10.3390/biomedicines12092135.

Lubitz LJ, Haffner MP, Rieger H, Leneweit G – Increased cellular uptake of ApoE3- or c(RGD)-modified liposomes for glioblastoma therapy depending on the target cells – *Pharmaceutics* (2024); doi: 10.3390/pharmaceutics16091112.

Mellinger A, Lubitz L, Gazaille C, Leneweit G, Bastiat G, Lépinoux-Chambaud C, Eyer J – The use of liposomes functionalized with the NFL-TBS.40–63 peptide as a targeting agent to cross the in vitro blood-brain barrier and target glioblastoma cells - *International Journal of Pharmaceutics* (2023); doi: 10.1016/j.ijpharm.2023.123421.

Parts of this thesis have already been presented

Lubitz LJ, Ebert R, Rieger H, Nilsson B, Nisson-Ekdahl K, Leneweit G – Alternatives to avoid the “PEG dilemma” in liposomal targeting - fragmented heparin as a promising coating for lowered immunogenicity and improved hemocompatibility (Poster) – March 2024; PBP World Meeting 2024 in Vienna, Austria

Lubitz LJ, Rieger H, Leneweit G – Optimization process of a PFC-nanoemulsion for further use as outer layer of asymmetric liposomes (Poster and oral speech) – October 2023; CLINAM 14/2023 in Basel, Switzerland

Lubitz LJ, Haffner MP, Rieger H, Leneweit G – Investigation of surface modifications on liposomal drug delivery systems for active targeting towards the blood-brain barrier and glioblastoma multiforme (Poster) – May 2023; 22nd Barrier- and Transport Days in Bad Herrenalb, Germany

Lubitz LJ, Haffner MP, Rieger H, Leneweit G – small-molecule ligand on a liposomal drug delivery system for active targeting towards the blood-brain barrier and glioblastoma multiforme (Poster) – March 2023; Doctoral Conference of the DPhG in Bonn, Germany